# Accreting Black Hole Systems as Classical Analogue Gravity Models

Pratik Tarafdar

Thesis submitted for the degree of Doctor of Philosophy (Science)
in Physics (Theoretical)

Department of Physics
University of Calcutta, India
2019

*To all well-wishers without whom*
*this thesis would have been completed earlier...*

# Acknowledgements

It is an equally pleasant and arduous task to pen down a statement of gratitude; to look back upon so many years filled with joy, brimming with thrill, rejuvenating with success, striking hard with failures and disappointments, only to shine bright with new hopes and dreams. The real journey began a long time ago, but first let me take a stroll down those lanes of memory which lead me up to the gates of my college. It was where I got my first peek into the vast and dynamic world of scientific research. It was a rare fortune to be guided by the most enthusiastic and sincere team of teachers one can hope for. The name of Prof. Suparna Roy Chowdhury deserves a very special mention in this context. Not only did she encourage an undergraduate student to visit professional research institutes at an early age, but also continues to stay by his side till date as an earnest well-wisher, while he makes his way through numerous ups and downs in life. I suppose, friends are particularly the most delicious ingredients in this course. And what could be better than a friend who would be the worst partner in crimes, at the same time as being the best partner in studies. Abhishek Chowdhury was such a friend with whom hours could be spent discussing an insanely broad collection of topics. As a matter of fact, these discussions played a crucial role in the ignition of my scientific inquisition. I used to wait eagerly for vacations to visit Prof. Biman Nath at RRI and to learn something new while working on exciting astrophysical projects. I have more than a sense of gratitude towards him for his suggestions and assistance during some of the most vital junctures in my career so far. It was during my visits to RRI that I gained the acquaintance of Darshana Joshi, which gradually developed into an amazingly beautiful bond of trust, love and affection. The impression of her grace, compassion and vibrance shall remain everlasting. My postgraduate years turned out to be exceedingly effervescent, meeting a multitude of vivacious friends with extremely large scopes of interest. Hobbies got cultivated and passions were set free. Among such friends, I would like to thank Avradeep Pal, Abhishek Shankaran, Joydev Manna, Tathagata Kar, Ranjit Gulvady (we knew each other at college, but this was when our friendship grew even stronger!) and so many more that, if mentioned, would fill up the entire thesis. Hence with deepest apologies for not naming the rest, let me proceed to my years as a research scholar. In all times to come, I can proudly claim to have befriended during those early days of Ph.D., a phenomenon named Suman Dutta – a king at heart with an inextinguishable flame. It has been impossible for me to escape the impact of the tremendous amount of positive energy this person can unbelievably induce into anyone. Soumyakanti Bose has been one of the warmest persons I have met during this period. Suman and Soumya together have driven me consistently to keep all my worries at bay. I must admit that the daily routines of a Ph.D. student can be heavily monotonous. The tenure spans such an extended and pivotal period when life, with its arsenal of hardships,

takes the firm decision of maturing a person into a tough and resolute individual. The experience, although ultimately beneficial, can at times be excruciatingly painful and depressing. I am indebted to Ansuman Dey, Injamamul Arief, Shubhadipa Das, Debmalya Mukhopadhyay, Shubhasish Chakrabarty, Sauri Bhattacharyya, Sandip Saha, Anindita Mandal, Pratap Mukherjee, Shantanu Naval, Utsab Chatterjee and Anisha Chandra, for all the night-long sessions filled with laughter and music that have been my oases for so many years. It shall never be enough to thank Prof. Tapas K. Das, as it is not meant to be just a formal gesture of gratitude towards the supervisor, for he has been much more than that. Prof. Das has been a friend, philosopher and guide to me. His considerate and caring nature is beyond comparison. Since the very first day, he made me feel like a part of his own family. Co-incidentally, we have been to the same college for B.Sc., to the same research institute for Ph.D. and we even share our birthday! Surely, the match was made in heaven. I am immensely obliged to Prof. Amitabha Lahiri, who is my main supervisor at the S. N. Bose National Centre for Basic Sciences. He has literally been a saviour to me and without him, this thesis might have never been published. I am thankful to my groupmates, Md. Arif Sheikh, Satadal Datta, Susovan Maity, Pathikrit Banerjee, Arpan Krishna Mitra and Karan Fernandes. I am also grateful to Dr. Sankhashubhra Nag, Dr. Sonali Saha Nag, Dr. Odele Straub, Dr. Sourav Bhattacharya, Dr. Paramita Barai, Dr. Safiqul Islam, Dr. Nandan Roy, Dr. Soumini Choudhury, Deepika Ananda and Ivleena Firdousi. I would like to extend my heartfelt gratitude to Prof. Jayanta K. Bhattacharjee, Prof. Pinaki Majumdar, Prof. Satchitananda Naik, Prof. Subinay Dasgupta, Prof. Anirban Kundu, Prof. Biswajit Chakrabarty and Mr. Sunish Kumar Deb for their valuable advice and constant encouragement. A very special thanks to Ms. Nibedita Konar, Ms. Chandrakana Chatterjee and Ms. Moumita Banik for their guidance and prompt assistance in sorting through confusingly large piles of official procedures. I remain indebted to the academic, administrative and technical staff of S. N. B. N. C. B. S., Kolkata, and Harish-Chandra Research Institute, Allahabad, for their generous support.

And finally, I feel helpless and afraid while attempting to thank those who cannot be thanked. It is not completely right to say that these people are beyond formal obligations. The gratitude I have expressed so far has also not been formal. However, there are feelings that can simply never attain fulfilling expressions. I have already mentioned that this journey had begun a long time back. It was when my teachers had been grooming me as a child for this day, some of whom I have lost and may never be able to thank again. It is very rightly said that teaching is a thankless job. I was endowed with good teachers not only in school, but also outside it. Mr. Madhablal Chatterjee is still my reason to read books pertaining to any subject I can lay my hands upon. The impression of his immensely wide spectrum of knowledge got etched on my mind at a very young age. It has been a beautiful experience to grow together with my cousins, Diya Banerjee, Hirak Banerjee, Pritam Lahiri and Arindam Lahiri. Hirak, with his indomitable spirit for query has been a perennial source of motivation behind my career in research. I have had the blessings of my elders to strive forward. I dare not thank my parents who had laid each brick of my foundation with utmost care and dedication, and yet, have been tolerating my mood swings and frustrations while I fight my way ahead to ensure a better future for myself. And last of all, I cannot reserve just a small ‘thank you’ for Shauri, whose smile shines as a beacon of hope, always giving me the necessary strength to ride through darkness.

# Contents

# List of Publications

1. Tarafdar, P., Das, T. K., *Influence of the geometric configuration of accretion flow on the black hole spin dependence of relativistic acoustic geometry*, International Journal of Modern Physics D (2018), 27, 1850023.

2. Tarafdar, P., Das, T. K., *Influence of matter geometry on shocked flows-I: Accretion in the Schwarzschild metric*, New Astronomy (2018), 62, 1-14.

3. Tarafdar, P., Ananda, D. B., Nag, S., Das, T. K., *Influence of matter geometry on shocked flows-II: Accretion in the Kerr metric*,
arXiv:1612.06882 (2017).

4. Tarafdar, P., Das, T. K., *Dependence of acoustic surface gravity on geometric configuration of matter for axially symmetric background flows in the Schwarzschild metric*, International Journal of Modern Physics D (2015), 24, 1550096.

# List of Figures

# Chapter 1

# Introduction

## 1.1 Black holes

Black holes are the mathematical vacuum solutions of Einstein's field equations in general relativity. In the classical context, a black hole consists of a physical singularity in space-time which is hidden inside a boundary from the rest of the universe. The boundary is known as the event horizon, and it is censored in the sense that once anything falls into it, it can never escape out of it. The purview of 'anything' even consists of light and other forms of electromagnetic radiation. Typically, a black hole is characterized by three intrinsic properties – mass ($M_{BH}$), angular momentum ($J_{BH}$) and charge ($Q_{BH}$). Based on these properties black holes are formally categorized into the following types –

1. $M_{BH} \neq 0$, $J_{BH} = 0$, $Q_{BH} = 0$ – Schwarzschild black hole (uncharged, non-rotating).
2. $M_{BH} \neq 0$, $J_{BH} \neq 0$, $Q_{BH} = 0$ – Kerr black hole (uncharged, rotating).
3. $M_{BH} \neq 0$, $J_{BH} = 0$, $Q_{BH} \neq 0$ – Reissner-Nordström black hole (charged, non-rotating).
4. $M_{BH} \neq 0$, $J_{BH} \neq 0$, $Q_{BH} \neq 0$ – Kerr-Newman black hole (charged, rotating).

However, the Reissner-Nordström and Kerr-Newman solutions do not carry any physical significance in the astrophysical context due the following reason. An astrophysical black hole is surrounded by an environment of super-heated ionized gases. The ambient rotating charged plasma is expected to neutralize any net charge carried by the black hole. The time-scale of this charge neutralization has been found to be roughly of the order of $M_{BH}/M_{\odot}$ $\mu$sec (see Hughes [2005]). This time-scale is negligibly small compared to any significant time-scale of observations related to the black hole properties. Hence, Kerr and – in certain special cases – Schwarzschild solutions are of more interest to the astrophysicists studying black hole related phenomena.

The second scheme of classification for black holes is based on their mass. The first category of black holes consists of those with masses comparable to that of a star ($M_{BH} \approx$ a few times $M_{\odot}$). Such black holes are termed as 'stellar-mass' black holes. The formation of stellar-mass black holes can be theoretically explained by the process self-gravitational collapse of a massive star at the end of its life-cycle. The second category consists of black holes which are about a million times more massive than the sun. Such black holes are known to exist at the centre of each galaxy. Due to their gigantic mass, they are termed

as 'supermassive' black holes. It is impossible for a black hole of such a great mass to be formed by the gravitational collapse a star. As a matter of fact, the process behind the origin of a supermassive black hole is not yet well understood. Various theories have been proposed in this context. They might be formed through the monolithic collapse of early proto-spheroid gaseous masses originated at the time of galaxy formation. They might be formed by the merging of numerous smaller black holes. The runaway growth of a seed black hole by accretion in a specially favoured high-density environment might also lead to the formation of super massive black holes. The formation, growth and evolution of such gargantuan black holes is still a problem which needs to be investigated (see Rees [1984], Rees [2002], Haiman and Quataert [2004] and Begelman et al. [2006]). There is a possible third category of black holes known as 'intermediate-mass' black holes, but their existence is a debatable issue at present.

## 1.2 Accreting black hole systems

Gravitational capture of surrounding fluid by massive astrophysical objects is known as accretion. In our work, we shall deal with the accretion of matter by compact astrophysical objects – black holes, in particular. There is a basic difference between accretion onto a black hole and that onto other massive compact objects such as neutron stars and white dwarfs. Neutron stars and white dwarfs possess a hard surface and hence the infall of matter is terminated by direct collision with either the hard surface or the outer boundary of the magnetosphere, resulting in a luminous energy release from the surface. On the other hand, black holes do not have any hard surface. The infinitely dense and massive singular point is guarded by the boundaries of an event horizon. The region beyond the event horizon leading to the central singularity of the black hole is beyond our present knowledge of science. Thus, the accreting matter does not face any hard obstruction and ultimately dives through the event horizon from where radiation is prohibited to escape according to the rules of classical physics. Hence, the emergence of luminosity in this case occurs on matter's way towards the black hole event horizon. The efficiency of such accretion processes is marked by this luminosity of the dissipated energy. It may also be looked upon as a measure of the fractional conversion of the gravitational binding energy of matter to the emergent radiation. This emergent flux is much higher for black holes compared to the neutron stars and white dwarfs. The extraction of gravitational energy from black hole accretion is believed to power energy generation mechanisms in X-ray binaries, quasars and active galactic nuclei. Various aspects of accretion processes onto compact objects have been elaborately discussed in a number of review articles, e.g. Pringle [1981], Chakrabarti [1996b], Wiita [1999], Lin and Papaloizou [1996], Blandford [1999], Abramowicz [1998], and monographs by Frank et al. [1992] and Kato et al. [1998].

### 1.2.1 Classification of black hole accretion

Accretion processes can be broadly categorised into two different classes depending on the geometry of flow. Accreting fluid with no intrinsic angular momentum falls onto the central gravitating source in a spherically symmetric configuration (Bondi [1952]). Thus, all accretion-related variables depend on the radial distance of a fluid element from the event horizon. However, fluids with definite intrinsic angular momentum are thrown into circular orbits around the compact object. The matter falls inward spirally when excess

amount of the angular momentum gets transported off due to viscous stress in the fluid. This rotational spiral motion leads to the formation of flat rotating disc-like structures around the event horizon, known as accretion discs. The thermal spectrum and structure of such discs depend on specific sets of values corresponding to various flow parameters.

Accretion of matter by a black hole is almost essentially transonic. Except for supersonic stellar winds acting as the feeders of accretion, all matter which is far away from the black hole starts to fall in with subsonic velocities. However, due to immensely high space-time curvatures near the event horizon, the infalling matter has to cross the horizon with a dynamical velocity approaching that of light. Now, the maximum attainable sound speed for a relativistic fluid with the steepest possible equation of state is $c/\sqrt{3}$. Hence, black hole accretion has to cross the sonic barrier at some point in the flow. It is the only physically acceptable solution for accretion onto black holes (Novikov and Thorne [1973]). Later, Liang and Thomson [1980] showed that similar transonic behaviour is also observed for thin disc accretion in general.

Thus, based on the aforementioned schemes of categorisation according to flow configuration and transonicity, black hole accretion can be classified into the following types –

1. **Spherical mono-transonic accretion:**

   The first attempt at the investigation of matter falling onto massive astrophysical objects was made by Hoyle and Lyttleton [1939]. They had calculated the accretion rate of pressure-less matter onto a moving star. This was later followed by the seminal work of Bondi [1952], who had formulated a theory of stationary, spherically symmetric, transonic accretion of polytropic Newtonian fluid onto a central static gravitating compact astrophysical object. The general relativistic generalisation of this work for accretion of polytropic perfect fluid onto a Schwarzschild black hole was reported by Michel [1972]. A number of transonicity related aspects of this work were addressed by Begelman [1978] and Moncrief [1980]. General relativistic spherical accretion of fluids with other general equations of state have been studied by Shapiro [1973a], Shapiro [1973b], Blumenthal and Mathews [1976], Brinkmann [1980] etc. The back-reaction of accreting matter on the background space-time metric, i.e. a self-gravitating model, was considered by Malec [1999] and it was compared with an accreting system without self-gravity, reporting enhanced accretion without back-reaction. The behaviour of mono-transonic spherical accretion very close to the event horizon was also studied in both general relativistic (Das [2002]) and pseudo-Schwarzschild (Das and Sarkar [2001]) frameworks. However, all the aforementioned works have concluded that stationary, spherically-symmetric accretion onto a black hole is essentially mono-transonic in nature. Only one transonic surface is formed in the accretion sphere for such flow configurations over all possible sets of the astrophysically relevant flow parameters. Although shocks may be formed in supersonic regimes of a fluid accreting with spherical symmetry (Bisnovatyi-Kogan et al. [1971], Meszaros and Ostriker [1983], Protheroe and Kazanas [1983], Chang and Ostriker [1985], Kazanas and Ellison [1986], Babul et al. [1989], Park [1990b], Park [1990a], Jones and Ellison [1991]), but such shocks cannot bring the flow down to a subsonic

regime, and hence the possibility of formation of a second transonic surface gets eliminated.

2. **Axisymmetric multi-transonic disc accretion:**

Spherically symmetric configuration of accretion was found to have several shortcomings. For such flows, the radial velocity of the infalling fluid turned out to be too high to account for the extreme brightness of quasars and active galactic nuclei. Astrophysicists had to put forth various ideas to compensate for such missing luminosities, including dissipation due to magnetic fields (Shvartsman [1971b], Shvartsman [1971a], Shapiro [1973b], Shapiro [1973a]). However, none of the proposed theories were suitable enough to stand firm in favour of the spherical accretion models. Then it was realised that accretion in the form of rotation around the central compact object might be helpful in solving this mystery. An accreting fluid with some intrinsic angular momentum with respect to the compact object will have smaller values of the infall velocity (in regions not very close to the event horizon) and also higher densities compared to a spherically accreting fluid. Owing to higher infall time-scales, dissipative forces acting within the fluid (instabilities due to turbulence or magnetic fields), would be able to dissipate energy and angular momentum of the flow before it finally falls through the horizon. Thus the accreting matter would radiate with higher efficiency. While the theoreticians were still struggling with the limitations of the spherical model, the existence of possible disc-like structures around one of the components in binary systems were already being reported and it was being suggested that matter should accrete in the form of discs (Prendergast and Burbidge [1968], Lynden-Bell [1969]). Robinson [1976] provided an analysis of the cataclysmic variables and came up with strong evidence in support of accretion discs around white dwarfs in binaries. In the meanwhile, Shakura and Sunyaev [1973] and Novikov and Thorne [1973] had originally conceived the idea of thin-disc accretion via Roche lobes in binary systems. The height of such thin-discs was assumed to be very small compared to the radial distance at any point on the disc. The angular momentum of thin-discs was required to be Keplarian and the radial velocity was required to be negligible compared to the orbital velocity of the discs. Although such assumptions led to an elegant set of flow equations which could be solved analytically, however the model had its own constraints. Fairly large amount of viscosity was required in the flow to transport the high amount of angular momentum and thus allow the fluid to fall towards its accretor. The origin and nature of such significant amount of viscosity in thin accretion discs was difficult to explain (Wiita [1999] and references therein). While microscopic transport mechanisms (ionic, molecular and radiative viscosity) were too small to account for the necessary dissipation, related observations were extremely challenging to make, and hence the responsibilities were usually levied upon small-scale turbulences and magnetic instabilities (Balbus and Hawley [1998]). Moreover, the thin-disc assumptions are often invalid in the inner regions of the disc. Close to the event horizon, where matter falls in supersonically with very high velocities, pressure due to the emitted radiation is sufficient to puff the disc up to greater thickness. This radiation pressure leads to deviation of the flow angular momentum from its Keplerian distribution. The first model incorporating a thick-disc in the inner regions joining a

thin-disc continuously in the outer regions, was introduced by Paczyński and Wiita [1980] through a pseudo-Newtonian scheme for the gravitational potential around a Schwarzschild black hole. Later, models for fully general relativistic self-gravitating thick-discs supported by radiation pressure in the inner regions were proposed by Wiita [1982] and Lanza [1992]. But the thick-disc model also had several inconsistencies. Recently, theoreticians have settled for a compromise between purely radial (spherical) and purely rotating flow by incorporating a self-consistent 'advection' term which might account for both radial and angular velocities along with the corresponding radiative terms (Hōshi and Shibazaki [1977], Liang and Thomson [1980], Ichimaru [1977], Paczynski and Bisnovatyi-Kogan [1981], Abramowicz and Zurek [1981], Muchotrzeb and Paczynski [1982], Muchotrzeb [1983], Fukue [1987], Chakrabarti [1989], Abramowicz [1998], Narayan and Yi [1994], Chakrabarti [1996]).

Now, unlike spherical accretion, the number of sonic points in accretion discs may turn out to be more than one for certain given values of the accretion parameters. Generally some sonic points are characterised by smooth flow while some occur due to shock discontinuities in the flow. Such flows are known as 'multi-transonic' flows and shall form the main constituent of our work. The investigation of multi-transonic flows was initiated by Abramowicz and Zurek [1981]. Their work was followed by a number of subsequent publications in this field (Fukue [1987], Chakrabarti [1989], Chakrabarti [1996], Kafatos and Yang [1994], Yang and Kafatos [1995], Pariev [1996], Peitz and Appl [1997], Lasota and Abramowicz [1997], Lu et al. [1997], Das [2004], Barai et al. [2004], Abraham et al. [2006], Das et al. [2007]). All the above works, except Barai et al. [2004], primarily dealt with low angular momentum sub-Keplerian inviscid flow around a non- rotating black hole or prograde flow around a rotating black hole. Barai et al. [2004] reported that high angular momentum retrograde flows can exhibit multi-transonicity as well. The study of low angular momentum sub-Keplerian flows is of practical significance as such flows may be considered as theoretical models for OB stellar wind accretion by detached binary systems (Illarionov and Sunyaev [1975], Liang and Nolan [1984]), semi-detached low-mass non-magnetic binaries (Bisikalo et al. [1998]), and accretion of matter from slowly rotating stellar clusters at galactic centres by supermassive black holes (Illarionov [1988], Ho [1999] and references therein). Flow instabilities such as turbulence and shocks can generate low angular momentum flow even in standard Keplerian discs (Igumenshchev and Abramowicz [1999] and references therein).

3. **Non-axisymmetric disc accretion:**

Unlike axisymmetric discs, accretion discs with a tilted alignment of rotation with respect to the direction of spin of the central compact object can also be formed in general. The component of a strongly coupled binary system feeding matter may exert tidal forces on the accretion disc. Moreover, such misaligned discs experience torques owing to Lense- Thirring effect (Lense and Thirring [1918]) close to the horizon. This leads to precession of the inner plane of the discs. The differential nature of precession may also cause dissipative effects. Now, if the Lense-Thirring effect overcomes the internal viscous forces, then the orbital angular momentum of the inner plane of the disc gradually gets aligned with the central rotating black hole

spin. This phenomena is widely known in astrophysical literature as the 'Bardeen-Petterson effect' (Bardeen and Petterson [1975]). The radius of the inner disc plane which gets aligned due to the effect is termed as 'transition radius'. It can be derived by balancing the precession effect with the inward viscous drift. Owing to such partial alignment of non-axisymmetric discs, they appear to be warped. Significant warping of the disc is expected to impose effects which will be reflected in the corresponding emergent spectrum. It can also potentially influence the directionality of the jets rushing out from the inner planes of the accretion discs in quasars and micro-quasars (Maccarone [2002], Lu and Zhou [2005] and references therein). Efforts have been made to formulate systems of equation describing such warped discs as a collection of annuli with increasing radii and a smooth variation in the alignment of the orbital angular momentum of the disc (Petterson [1977], Kumar [1988], Demianski and Ivanov [1997], and references therein). Scheuer and Feiler [1996] had estimated the time scale required for the alignment of a misaligned disc with the spin of its central rotating black hole. The geometry of such discs have also been generated numerically using 3D SPH codes in the Newtonian (Nelson and Papaloizou [2000]) as well as general relativistic framework (Fragile and Anninos [2005]). However, since the transonic length scale is much smaller compared to that of the transition radius as estimated by Bardeen and Petterson [1975], we can safely ignore such non-axisymmetric effects in our work.

## 1.3 Black hole thermodynamics and Hawking radiation

Black holes in general relativity – or any other gravitational theory with field equations directly following from a diffeomorphism covariant Lagrangian – exhibit several aspects of resemblance with classical thermodynamic systems within the framework of classical physics (Wald [1984], Wald [1994], Brown [1995], Hehl et al. [1998], Wald [2001]). A considerable number of important works (Bekenstein [1972b], Bekenstein [1972a], Bekenstein [1973], Bardeen et al. [1973], Bekenstein [1975], Israel [1976], Bekenstein [1980]) have showed that general relativistic black holes obey certain laws which have analogies in classical thermodynamics. Such an analogy leads to the idea of 'surface gravity' of a black hole. The quantity is found to be constant for a given black hole. It is analogous to the Zeroth law of thermodynamics which suggests the constancy of temperature for a body in thermal equilibrium. In addition, the value of surface gravity has to be non-zero. No finite number of operations can lead to a zero value of the surface gravity. This is analogous to the fact that the temperature of a system can never be reduced to absolute zero (see Hehl et al. [1998] for discussions). It was also derived via black hole uniqueness theorem (Heusler [1996] and references therein) that entropy in classical thermodynamics is analogous to a constant multiple of the surface area of an event horizon.

Stephen Hawking, in his revolutionary paper published in 1975 (Hawking [1975]), used quantum field theoretic calculations in curved space-time to show that the physical temperature and entropy of black hole has finite non-zero value (see Page [2005] and Padmanabhan [2005] for excellent reviews of black hole thermodynamics and Hawking radiation). A linear quantum field, initially in its vacuum state, propagating against the dynamical background of classical space-time describing gravitational collapse leading to the formation of Schwarzschild black hole was considered. The vacuum expectation value of the

energy-momentum tensor of this field was found to be negative near the horizon. This negative energy flux decreases black hole mass. The outgoing mode of the quantum field contains particles. The expected number of these outgoing particles was observed to be corresponding with radiation from a finite-sized perfect black body. Hence, the radiation spectrum had to be of thermal nature, and the respective temperature was termed as the Hawking temperature. The Hawking temperature of a black hole turns out to be inversely proportional to its mass. A rough estimate reveals that $T_H$ for stellar mass black holes would be around $10^7$ times cooler than the cosmic microwave background radiation ($\approx 2.73$ K). Supermassive black holes would radiate at even lower temperatures. Thus, $T_H$ would be detectable only for hypothetical black holes with very small size and mass, known as 'primordial black holes'. Such black holes were proposed to have been formed just seconds after the big bang due to fluctuation-induced gravitational collapse of highly dense regions of *radiation-dominated* universe. The lower stable bound for the mass of such black holes has been estimated to be around $10^{15}$ gm. Although, depending on the model, such black holes can have masses of the order of $10^{-5}$ gm, but primordial black holes with masses lower than the stable bound will have evaporation time-scales (due to Hawking radiation) that are much smaller than the age of our universe, and hence will have ceased to exist by now. The size of primordial black holes with lower stable bounds of mass would roughly be of the order of $10^{-13}$ cm and the corresponding $T_H$ can be calculated to be approximately $10^{11}$ K, which is comparable with the macroscopic temperature of matter accreting onto stellar mass or supermassive black holes. However, the existence of primordial black holes is yet to be established, and at present, experimentally achievable resolutions are unable to detect temperatures as small as the theoretically calculated Hawking temperatures of stellar mass black holes. On the other hand, due to infinite gravitational redshift caused at the event horizon, the emergent Hawking radiation is expected to possess trans-Planckian frequencies whose corresponding wavelengths are beyond the Planck scale. Hence, effective low-energy theories cannot self-consistently deal with the Hawking radiation (see Parentani [2002] for further details). The nature of physics at such ultra-short distances is also not well understood. Hence, several fundamental issues like the statistical interpretation of black hole entropy, and the physical origin of the outgoing mode of the quantum field, still remain unresolved (Wald [2001]).

The aforementioned difficulties motivated physicists to look for an analogous theory whose effects can be perceived through experimentally realisable physical systems. The theory of an analogue Hawking phenomenon can create the possibility to verify some basic features of black hole physics in the laboratory. Several works have attempted to propose condensed matter or optical analogues of event horizon. Such analogue theories can have prospective utilities in the investigation of quasi-normal modes (Berti et al. [2004], Cardoso et al. [2004]), acoustic super-radiance (Basak and Majumdar [2003], Basak [2005], Lepe and Saavedra [2005], Slatyer and Savage [2005], Cherubini et al. [2005], Kim et al. [2005], Federici et al. [2006], Choy et al. [2006]), FRW cosmology inflationary models (Barceló et al. [2005]), quantum gravity and sub-Planckian models of string theory (Parentani [2002]). However, in our work, we concentrate upon the formalism behind classical analogue systems. The 'classical analogue systems' refer to the examples where analogue effects are studied in classical fluids.

## 1.4 Analogue gravity and acoustic geometry

Establishment of appropriate equivalences between propagating perturbations within an inhomogeneous dynamical continuum and certain kinematical features of spacetime as perceived in the general theory of relativity led to the formulation of analogue gravity phenomena (Unruh [1981],Visser [1998],Barceló et al. [2005]). For instance, the linearized equation of acoustic perturbations propagating in a transonic fluid flow, i.e. the wave equation, when casted in a covariant form, is found to resemble the d'Alembertian equation of propagation of a linear massless scalar field in a given background space-time. Thus, an analogous metric can be extracted out of the wave equation whose components shall depend on the dynamics and thermodynamical variables of the fluid flow along with properties of the background physical space-time. Such a metric is termed as an 'acoustic metric'. The acoustic metric represents a pseudo-Reimannian analogue of space-time which is seen by the propagating acoustic perturbation. This metric has various properties which have respective analogies in physical space-time geometry. Just as the Schwarzschild or Kerr metric possess their respective horizons and ergo-regions, so does the acoustic metric. It can be shown that the acoustic metric has a corresponding acoustic horizon, where the flow experiences transonicity, i.e. the flow undergoes a 'smooth' transition from subsonic to supersonic. The adjective 'smooth' is important as such transitions can also occur due to discontinuous jumps in the flow variables via shocks, whose significance will be discussed later. However, such locations of discontinuous transonicity are not designated as acoustic horizons. Acoustic perturbations propagating at sound velocity – a thermodynamic property of the fluid – are unable to catch up with the fluid in the region where it flows at supersonic velocities. Thus, the transonic boundary acts as an impenetrable barrier for sound waves. Acoustic waves generated anywhere within the 'acoustic ergo-region' propagating in any direction will remain trapped inside. Similarly, acoustic perturbations generated outside the analogue ergo-region will never be able to cross the transonic barrier. This is the reason why acoustic horizons are also known as 'dumb holes'. An acoustic horizon is to sound waves, what an event horizon is to electromagnetic waves.

Around four decades back, in the year 1981, a new age in physics began with the reporting of a revolutionary result by W. G. Unruh in a pioneering scientific article (Unruh [1981]). Unruh showed that the behaviour of normal modes near the acoustic horizon implies that the acoustic black hole will emit sound waves with a thermal spectrum that has a characteristic temperature given by

$$T = \frac{\hbar}{2\pi k_B} \frac{\partial u}{\partial r}\Big|_{r_s} \tag{1.1}$$

where $k_B$ is Boltzmann's constant, $r_s$ is the acoustic horizon or the 'sonic horizon' or the 'sonic point' (these terms will be used synonymously henceforth) and $u$ is the bulk radial velocity of the embedding fluid normal to the acoustic horizon. This equation has an uncanny resemblance with the expression for temperature of Hawking radiation given by

$$T_H = \frac{\hbar c^3}{8\pi k_B G M_{BH}}, \tag{1.2}$$

where $c$ and $M_{BH}$ are the velocity of light and mass of the black hole respectively. Owing to this resemblance, the temperature of the outgoing phonon spectrum reported by Unruh is now termed as the 'analogue Hawking temperature' ($T_{AH}$). It is evident that Hawking

temperature is inversely proportional to the mass of the black hole, whereas the analogue Hawking temperature is proportional to the space gradient of the advective flow velocity of the fluid at the acoustic horizon.

We know that the Hawking temperature can be written in terms of the surface gravity near the event horizon as

$$T_H = \frac{\hbar}{2\pi k_B}\kappa_G \tag{1.3}$$

where $\kappa_G$ is the surface gravity near the event horizon. Consequently, a quantity termed as acoustic surface gravity ($\kappa$) can be analogously defined near the acoustic horizon.

Unruh, in his work, had considered the transonic flow of a classical non-relativistic fluid in Newtonian gravity, with a uniform sound speed all throughout the flow. This would imply that the fluid is isothermal in nature. However, flow with a more general polytropic equation of state would require its characteristic sound speed to have spatial dependence like the flow velocity itself. The acoustic surface gravity for an analogue system where a propagating acoustic perturbation is embedded in a classical polytropic fluid flowing transonically on a Minkowskian background space-time, can be calculated as (Visser [1998])

$$\kappa = \left[\frac{1}{2c_s}\frac{\partial}{\partial\eta}\left(c_s^2 - u^2\right)\right]_{r_s} \tag{1.4}$$

where $c_s$ is the position-dependent sound speed (the speed of linear propagation of the embedded perturbation in general) and $\partial/\partial\eta$ is derivative normal to the acoustic horizon.

The acoustic perturbations propagate along timelike curves for both fluid flow under the influence of Newtonian gravity in flat Minskowskian space-time, as well as its general relativistic counterpart. Phonons corresponding to the acoustic propagation construct null geodesics with respect to the acoustic metric, and generate a null surface at the acoustic horizon (points where the flow becomes transonic). A more general expression for the acoustic surface gravity in curved space-time is given by (Bilic [1999],Abraham et al. [2006],Wald [1984]),

$$\kappa = \left[\frac{\sqrt{|\chi^\mu\chi_\mu|}}{(1-c_s^2)}\frac{\partial}{\partial\eta}\left(u - c_s\right)\right]_{r_s} \tag{1.5}$$

where $\chi^\mu$ is a Killing field with respect to the physical space-time metric and gradient $\partial/\partial\eta = \eta^\mu\partial_\mu$. The algebraic expression corresponding to $|\chi^\mu\chi_\mu|$ can be evaluated once the background space-time metric describing the fluid flow as well as certain quantities relevant to the propagation of the perturbation in a specified geometry are defined.

## 1.5 Astrophysics & analogue gravity

Acoustic black holes are the hydrodynamic analogues of general relativistic black holes. Such analogues possess acoustic horizons at local transonic points. We have also seen that analogue black holes emit an analogue Hawking radiation characterised by an analogue Hawking temperature. The primary importance of studying analogue black holes is that it might be possible to synthesize them experimentally in laboratories. If possible, this would be of immense assistance in the investigation of various properties of the black hole event horizon. It might to possible to explore the experimental manifestations of Hawking

radiation. Although the analogue Hawking temperature would be still extremely small and hard to detect in the presence of flow instabilities such as turbulence, but as Unruh had stated in his seminal article – "It is, however, a much simpler experimental task than creating a $10^{-8}$-cm black hole."

As evident from discussions in the previous section, it is imperative that in order to calculate the analogue surface gravity and the analogue Hawking temperature for a classical analogue system, a precise knowledge of the exact location of the sonic horizon, the velocity and sound speed of the flow at the acoustic horizon, and the spatial derivatives of such velocities, shall be required. Hence, a hydrodynamic system, for which such quantities can be calculated, may be chosen to represent a classical analogue gravity model.

Now, the boundary of the analogue ergo-region and the acoustic horizon do not coincide in general. Therefore, any random configuration of transonic flow may not be suitable for being considered as a classical analogue model. However, this condition is satisfied in some specific stationary geometries (Visser [1998], Bilic [1999]) –

1. A spherically symmetric configuration of stationary flow, where the fluid radially falls into a point-sink at the origin.

   In such cases, the flow velocity will only consist of components that are radial and hence perpendicular at each point on the acoustic horizon. Thus, there shall be no difference between boundary of the corresponding ergo-region and the sonic horizon. While discussing the various categories of black hole accretion in section 1.2.1 we have already encountered a very suitable example of such fluid flow configuration in the astrophysical literature. Stationary, spherically symmetric accretion onto a Schwarzschild black hole or any non-rotating compact astrophysical object had been studied by the astrophysicists since many years. This kind of astrophysical flow is known as 'Bondi accretion', as it was investigated for the first time by Hermann Bondi (Bondi [1952]).

2. An axisymmetric configuration of stationary flow, where fluid radially falls into a point-sink placed at the origin.

   Here also, the flow velocity comprises of non-zero components which are perpendicular everywhere on the acoustic horizon. Therefore, the acoustic horizon coincides with the boundary of the ergo-region. Again, well-studied examples of such hydrodynamic configuration exist in the astrophysical literature as already discussed in detail in section 1.2.1. Matter, while accreting onto a non-rotating or rotating compact astrophysical object – such as a black hole or a neutron star – generally settles in flat disc-like structures rotating around the centre, owing to some angular momentum initially carried by the flow. Such rotating discs of matter around a black hole or neutron star are known as 'accretion discs'. With appropriate coordinate transformations of the velocity components, the flow can be formulated in co-rotating frames, such as to transform the fluid motion into an axially-symmetric two-dimensional configuration with zero angular momentum falling radially into a point-sink.

Thus, we gather that since astrophysical accretion onto compact objects is essentially

transonic for both spherical (Bondi [1952]) and axisymmetric (Liang and Thomson [1980]) flows, and that the surface of transonicity co-incides with the boundary of the acoustic ergo-region for the two aforementioned configurations, hence accretion of astrophysical fluid by compact astrophysical objects turns out to be a very suitable candidate of classical analogue systems. Things become even more interesting in this case, as these are the only available physical systems in which analogue horizons are simultaneously present beside actual event horizons. Investigation of practical manifestations of the imprint of one on the other might possess a potential of immense academic significance.

## 1.6 Connection to dynamical systems

This work is primarily concerned with stationary flows, and hence it might seem surprising to try and draw any connection with the theory of dynamical systems. However, the dynamical systems theory endows us with a rich plethora of elegant analytical methods to study the behaviour of critical points, or stationary points, or equilibrium points, or stable points, or fixed points of a system as they are called. Our work is about transonic astrophysical flows and hence a major portion of it deals with the derivation of results related to the sonic points of the system. If such stationary astrophysical hydrodynamic models may be cast in the form of equations leading to the critical points of a dynamical system, then derivation of the related critical point conditions almost always reveal direct correlations between the critical points and the sonic points of the accreting fluid. This connection immediately hints at the applicability of stability analysis related tools in the theory of dynamical systems to the seemingly unrelated theory of transonic astrophysical accretion. As a matter of fact, the approach of linear stability analysis of fixed points in problems of general fluid dynamics has been in practice for quite some time (Bohr et al. [1993]). Analytical methods from the theory of dynamical systems have been borrowed in the context of investigating general accretion problems (Ray and Bhattacharjee [2002], Afshordi and Paczyński [2003], Chaudhury et al. [2006], Mandal et al. [2007]). Even few earlier works have explored this approach while studying the problem of astrophysical accretion (Matsumoto et al. [1984], Muchotrzeb and Czerny [1986], Abramowicz and Kato [1989]). In our work, we have utilized various mathematical aspects of such formalisms and have tried to provide new insights into the problem.

## 1.7 Summary of work

Now that the foundation has been laid, the whole content of this thesis will be organized according to the following scheme –

### Chapter 2: The Model

In the second chapter, we elaborate our model of axisymmetric, low angular momentum, inviscid, transonic accretion onto a black hole. We look for an appropriate physical system which might be fit for the application of our analytical assumptions. We argue that the general relativistic hydrodynamic equations in our model are, to a great extent, capable of modelling flows close to the event horizon of the supermassive black hole at our own galactic centre.

We describe the prominent features of the galactic centre Sagittarius A*. Various necessary system parameters are selected on the basis of a number of past and recent investigations related to the stellar environment of the galactic centre, and the central compact supermassive gravitating source. Mathematical construction of the physical space-time around a rotating black hole which shall act as the background of the physical accretion flow is formulated. Kinematics of the relativistic fluid is detailed, and all the transformations leading to an axisymmetric flow in co-moving co-ordinates are derived in a step-by-step manner.

Our study involves the comparision of flow properties firstly on the basis of thermodynamic equations of state of the fluid. Relativistic derivations of expressions for various thermodynamic variables corresponding to polytropic and isothermal fluids are presented. The second basis of our comparative analysis involves different axisymmetric disc geometries. Throughout this thesis, our endeavour has been to critically compare and discuss the trends of variation of flow variables with the flow parameters for three separate disc structures, viz. constant height discs (CH), quasi-spherical or conical flow discs (CF) and discs in vertical hydrostatic equilibrium (VE). We have elaborated upon such flow geometries and have provided the related derivations for heights of the polytropic and isothermal discs held by hydrostatic equilibrium in the vertical direction.

Finally, the equations characterising our model are formulated. Relativistic continuity equation and components of the relativistic Euler equation for the specific fluid motions considered are derived. Since this work primarily deals with stationary flow configurations, hence the corresponding stationary integral solutions of the above equations and the expressions for various conserved quantities are calculated.

### Chapter 3: Critical Points of the Flow

In the third chapter, we shall concentrate on the concept of 'critical points'. Critical points, or stable points, or equilibrium points, or fixed points, are important in the theory of dynamical systems, as they often signify phase separations in a dynamical system. Hence the study of their behaviour is of great interest. As mentioned in the previous section, analysis of the transonic accretion model from such a perspective reveals correlations between the transonic and critical contours.

We shall derive such critical conditions for three different disc geometries corresponding to two separate equations of state, and thus obtain the specific relations between the stationary sonic points and the stationary critical points for each of the six cases. To state more precisely, the critical conditions relate the flow velocity ($u$) with the sound velocity ($c_s$) at the critical points. The velocities are functions of the radial distance ($r$), and an intermediate step leading to the critical conditions gives us the expressions for the spatial gradients of the velocities ($dc_s/dr$ and $du/dr$). Numerical integration of the gradients generate the actual phase space plots, however, we shall postpone the discussion of this numerical aspect of our problem to a more appropriate chapter, and shall only present the analytical derivation of the expressions for the gradients at the critical points which would be necessary to calculate the initial conditions for the numerical integrations to be carried out later.

We shall develop a formalism in order to solve for the the location of critical points ($r_c$) for a given set of the accretion parameters viz. specific energy ($\mathcal{E}$), specific flow angular momentum ($\lambda$), polytropic index ($\gamma$) and black hole spin ($a$) for polytropic flows, and bulk flow temperature ($T$), flow angular momentum ($\lambda$) and black hole spin ($a$) for isothermal flows. The formalism will help us in plotting parameter space diagrams and investigating the physically admissible ranges of the flow parameters for different types of transonic accretion to occur for various flow configurations being considered.

### Chapter 4: Classification of Critical Points

In the fourth chapter, the connection of the astrophysical problem of black hole accretion to the theory of dynamical systems becomes more clear, as we present a scheme based on the tools of linear stability analysis. Such an analysis can be used for a qualitative prediction of the nature of those critical points obtained in the previous chapter. The scheme is based on purely analytical methods. Generation of the actual phase-space trajectories while resorting to numerical integration algorithms is not required to identify the categories of the various critical points of the system (nodes, spirals, saddles, centres etc.).

The scheme involves linearization of the expressions for space gradients of the squares of the flow velocity ($du^2/dr$) following the introduction of small first order perturbations in the flow variables in close neighbourhood of the critical points. The resultant perturbative equations can be parametrized with respect to some suitable mathematical parameter to provide a first order autonomous set of differential equations. When written down in matrix notation, the eigenvalues of the co-efficient matrix of the set of equations are obtained and a specific function ($\Omega^2$) of the eigenvalues is defined such that it depends exclusively on the critical point location ($r_c$), either explicitly or implicitly (via $u_c$ and $c_{sc}$). Thus, once the critical point locations for a given flow configuration are obtained following the formalisms established in the previous chapter, the corresponding values of $\Omega^2$ can be readily calculated and such values will turn out to be the indicators of the types of the respective critical points.

Since specific ranges of values of $\Omega^2$ characterise specific kinds of critical points, hence plots of $\Omega^2$ vs. other system parameters shall depict a complete picture of the critical behaviour of the given system over entire parameter domains. Transition of the nature of the flow from mono-transonic to multi-transonic can be visualised as bifurcations in the system. Such 'bifurcation diagrams' provide an elegant dynamic picture of the behaviour of critical points corresponding to the stationary flow along a given accretion parameter. These are extremely simple yet highly rich data-banks containing lots of information and capable of throwing light on the system from a wide scope of angles.

### Chapter 5: Discontinuities in the Flow

In the fifth chapter, we attempt to formulate the conditions for discontinuities in the flow. We shall discuss the importance of such discontinuities in the context of multi-transonic accretion. We shall also emphasize upon the physical arguments supporting the feasibility of the generation of discontinuities in our flow model in the form of shocks.

The mathematical treatment of the 'shock-problem' is grounded on the conservation of certain quantities across the shock surface, viz. the particle number, flow momentum, energy (in case of polytropic flow) and some equivalent of energy known as 'quasi-specific' energy ($\xi$, in case of isothermal flow). These conservation rules are written down in the form of the relativistic Rankine-Hugoniot conditions. We shall further assume that the shocks are stationary and the shock-width is infinitesimally small. Physical arguments in favour of such assumptions will be presented. Expanding the Rankine-Hugoniot conditions for six separate flow configurations, we shall combine the conditions for each, cancelling terms on both sides of the shock with explicit $r$-dependence (due to infinitesimally-thin-shock assumption) and retaining only the implicitly $r$-dependent ($u$ and $c_s$-dependent) terms. Thus, we shall obtain expressions corresponding to a single mathematical quantity ($S_h$) which will be termed as the 'shock-invariant' quantity. The shock-invariant quantity has the unique property of remaining unaltered exclusively across shock locations, and hence serves as a weapon to hunt for shocks across phase trajectories joining separate branches of flow.

We shall finally be required to use elaborate numerical integration schemes to generate the phase space plots for different configurations of flow over different sets of values of the accretion parameters selected from the parameter space diagrams obtained in chapter 3 allowing for multi-'critical' (note the use of 'critical' instead of 'transonic') solutions. While generating the phase trajectories we shall check for the invariance of $S_h$ at a given $r$, across all possible flow branches passing through that $r$. Positive results of this check shall indicate the radial distances at which the formation of a relativistic Rankine-Hugoniot shock is permitted. Shocks are essential for the super-sonic to sub-sonic transition of the flow and another subsequent transonicity to occur as the fluid starts accelerating again. Hence, it will allow us to construct more specific parameter space diagrams that will depict the parameter domains pertaining to actual physical multi-'transonic' solutions. The ratio of various flow variables – shock strength, compressibility, energy dissipation (for isothermal shocks) etc. – will be calculated across such shock locations. The variation of such quantitites with the accretion parameters will be traced in order to investigate the nature and comparative effect of shocks on the different types of flow configurations being considered in our work. It will also be reported that isothermal shocks are capable of dissipating significantly large amounts of gravitational energy of the accreting fluid.

### Chapter 6: Quasi-terminal Values

The sixth chapter will deal with the nature of flow variables at extreme close vicinities of the event horizon. Such values will be termed as 'quasi- terminal' values and shall be denoted by $V_\delta$, where $V$ is the corresponding variable (Mach number, pressure, density, temperature etc.) and $\delta$ is an extremely small fraction of the gravitational radius ($\sim 0.0001$) signifying the radial distance from the event horizon at which the quasi-terminal values are obtained.

We shall investigate the variation of quasi-terminal values with the accretion parameters – the black hole spin in particular – for three separate disc geometries and two different thermodynamic equations of state. A comparative analysis of multi-transonic accretion for all such configurations shall involve a careful study of the common parameter re-

gions corresponding to multi-transonic stationary flow solutions obtained in the previous chapter. Discrepancies reported in the variational trends of flow related variables will be established as side-effects of insignificant overlap in parameter regions corresponding to multi-transonic solutions. Comparative analysis of the variation of $V_\delta$ for mono-transonic accretion over almost entire astrophysical ranges of the accretion parameters will reveal common global behaviours for all configurations. Variation with respect to black hole spin will also bring forth stark asymmetries in the distribution of $V_\delta$ over positive and negative spins, thus hinting towards a possible observational signature of distinction between prograde and retrograde flows.

In the last section, we shall explain how all the calculations presented and all the results reported in the previous chapters converge together to play a vital role in the realisation of a greater goal – simulating the shadow image of an event horizon. A large number of such images constructed over various combinations of the parameter values and flow configurations might serve as theoretical charts for comparision with actual images of the galactic-centre event horizon being captured by earth-sized Very Long Baseline Interferometer (VLBI) arrays such as the Event Horizon Telescope (EHT). The first ever recorded shadow image of a galactic centre black hole (SMBH at the centre of M87, weighing approximately 6.5 billion Suns and 55 million light years away from us) has already been released by the EHT-ESO collaboration on the 10th of April, 2019, and similar images of Sagittarius A* are awaited. We present a glimpse into the overall scheme of such ongoing collaborations at a variety of larger scales, of which this work is a primary constituent.

### Chapter 7: Acoustic Black Holes

In the final chapter, we shall connect all the dots and utilize the results obtained regarding galactic centre black hole accretion to study the system as a unique classical analogue gravity model with the co-existence of both acoustic horizons and event horizon. Our attempt would be to investigate the effects of the event horizon and curved background space-time on the analogue effects of transonic fluid flow, which, except for a few preceding works, have been mainly studied so far, either for quantum fluid analogues with nothing to do regarding considerations of real space-time, or for classical non-relativisitc fluid flow in flat physical space-time.

Among the various analogue effects, our specific attention will be towards 'analogue surface gravity' ($\kappa$) and the corresponding 'analogue Hawking temperature' ($T_{AH}$). First of all, we shall consider the continuity and Euler eqution for a barotropic, inviscid, Newtonian fluid in irrotational flow in a flat background space-time. We shall derive the expression for the 'acoustic metric' ($G_{\mu\nu}$) through the comparision of a covariant formulation of the equation of propagation of a linear perturbation in the velocity potential of the fluid with an equation describing the propagation of perturbations in a linear massless scalar field with a $(3+1)$ dimensional background Lorentzian geometry. Then we shall establish the corresponding analogues of general relativistic properties and concepts of an actual space-time metric, such as 'ergo-regions', 'trapped surfaces' and 'event horizons', leading to the detailed derivation of the expressions for the analogue surface gravity and the respective analogue Hawking temperature.

Next, along exactly similar lines, we shall derive the acoustic metric for barotropic, inviscid, irrotational flow of a relativistic fluid in a general curved background space-time. The methods used would remain the same, only the framework of calculations would be fully relativistic allowing for such extreme conditions as highly energetic flows with relativistic velocities in significantly strong gravity regions. Gravitational analogues related to real physical space-time metric shall be established, and corresponding expressions for analogue surface gravity and analogue Hawking temperature will be calculated.

Finally, our knowledge regarding the analytical formalisms to derive and calculate the analogue surface gravity at the acoustic horizons will be used to study the variation of $\kappa$ with various accretion parameters. A comparision of the variation pattern of the location of acoustic horizons (i.e. the sonic points $r_s$) and their respective acoustic surface gravity ($\kappa$) with any given accretion parameter will reveal the influence of the curvature of background space-time upon the analogue acoustic space-time. It will provide a definitive picture of the gravity-analogue gravity correspondence in the present context. Further, the variational trends of $\kappa$ will be comparatively analysed for different types of astrophysical black hole accretion discs pertaining to astrophysical fluids with different thermodynamic equations of state. Variation of $\kappa$ for both multi-transonic accretion over intrinsically limited parameter domains, and mono-transonic accretion over entire astrophysical parameter domains will be reported. Thus, this work will establish accreting astrophysical black hole systems as the natural examples of classical analogue models.

# Chapter 2

# The Model

**Summary**

- ✓ *Description of the physical model – the accretor.*
- ✓ *Configurations of the background physical space-time metric.*
- ✓ *Thermodynamic properties of the accreting fluid.*
- ✓ *Necessary equations related to the fluid and its dynamics.*
- ✓ *Various flow geometries for comparative analysis.*

## 2.1 The accretor

Our work deals with axisymmetric, low angular momentum, inviscid, multi-transonic accretion. As discussed in the previous chapter, for rotating matter to fall spirally towards the event horizon, the angular momentum supporting the fluid in its rotational orbit against gravitational pull of the accretor, is required to be gradually transported out of the system. For an accretion disc to be thin, the necessary angular momentum is high and the proposed mechanisms of angular momentum transport could not account for the dissipation of such high values. Moreover, in regions close to the event horizon, due to relativistic supersonic velocities of the fluid, the resulting radiation pressure on the disc is bound to invalidate most of the assumptions regarding a thin-disc configuration. Hence, in order to study the flow properties in close proximity of the event horizon – which is the principle motivation behind the general relativistic treatment in our work – we need to consider a black hole accretion model with low, sub-Keplerian values of the flow angular momentum. This consideration does away with the necessity of dissipation of the excess rotational energy for the fluid to accrete onto the central gravitating source, and in turn, justifies our inviscid assumption.

However, in order to choose physically appropriate values of parameters of the system such as mass of the accretor and its accretion rate, specific energy (for polytropic fluids) or temperature (for isothermal fluids) and the range of specific angular momentum of the

flow, we need to look for actual accreting systems to which our assumptions may apply. Accretion onto stellar-mass black holes due to the tidal rupture of companion stars, initially in mutual orbits as binary systems, is supposed to be characterised by a Keplerian distribution of angular momentum. Such accretion occurs via Roche lobe accompanied by a thin rapidly rotating disc. In case of low-mass X-ray binaries, accretion occurs through an inner Lagrange point and the circularisation radius is quite significant compared to the Roche radius ($\approx 10^4\ R_g$, where $R_g$ is the gravitational radius). In case of high-mass X-ray binaries the circularisation radius of accretion flow turns out to be less ($\approx 10^3\ R_g$), but it is large enough for inflow to occur only via angular momentum transport. Hence stellar mass black holes do not turn out to be suitable candidates for our cause. But there exists another kind of black holes which are often fed by matter with significantly low instrinsic angular momentum. These are monstrous black holes now known to be lurking at the centre of each galaxy. Their mass ranges from millions to billions of Suns. It is because of their enormous mass and gravitational radius, that these are called 'super-massive' black holes (SMBHs).

The appetite of a galactic centre super-massive black hole along with the availability of feeding material, together determine the activity of the central region of a galaxy. Some of the galactic centres are extremely active, spewing out huge amounts of particles in the form of relativistic jets, over distances that are orders of magnitude larger than the dimensions of the host galaxy itself. These are known as bright 'active galactic nuclei' (AGNs). Quasars and Seyfert 1 galaxies fall into the category of such bright AGNs. In such cases, the accreting material either originates from the neighbouring stars (as stellar winds) or from the gaseous phase of the galactic material. The bright AGNs with very high radiative efficiencies show evidences of high angular momentum flow near the galactic centres. The accretion discs are prominent and comparable with those of the binary systems discussed above. Hence such luminous and highly active galactic centres also do not fit in our requirements.

Fortunately, neither all galactic centres have a rich environment to feed, nor all galactic-centre black holes are as heavy as those associated with quasars. Many galaxies have a weakly active centre with low radiative efficiency. It might be tempting to model the accretion phenomenon occuring at such galactic centres using Bondi flow, i.e. spherically symmetric radial flow. However, it has been reported that pure Bondi flow has radiative efficiencies that are too low to agree with the observed luminosities corresponding to most of the weakly active galaxies (Moscibrodzka [2006]). Thus a reasonable analytical modelling can be achieved in such cases by breaking the spherical symmetry and yet avoiding the angular momentum trasport problem due to slow rotation of the disc. Hence, these galaxies with low angular momentum flows in the central region and feebly feeding supermassive black holes, are going to be the focus of our investigation. And interestingly, we do not even need to look far for the best possible candidate.

Sagittarius A* (Sgr A*) is a compact and decently bright astronomical radio source, which resides at the centre of our own resident galaxy and is thought to be a spinning supermassive black hole. The galactic-centre environment of the Milky Way is extremely suitable for the application of a low angular momentum, inviscid, axisymmetric, general relativistic hydrodynamic model (Moscibrodzka et al. [2006]). It is located near the border of the con-

stellations Sagittarius and Scorpius. It is approximately 26000 light years away from the solar system and hence offers the largest available angular resolution for a supermassive black hole from the earth. Over the years, astronomers have been zeroing in on the mass of Sgr A* by meticulously studying the orbit of the stars around it. The mass we shall be using in our work follows the widely accepted recent estimate (Ghez et al. [2008], Gillessen et al. [2009]), which is around $4.3 \times 10^6\ M_\odot$. The mass accretion rate has been taken to be $4.6 \times 10^{-6}\ M_\odot$ per year, in accordance with the latest studies of stellar winds from stars near the galactic centre (Moscibrodzka et al. [2006], Czerny et al. [2007], Marrone et al. [2007], Ferrière [2009], Genzel et al. [2010]).

Sgr A* is an interesting candidate for the investigation of accretion processes onto supermassive black holes due to some of its observational features that are unique. The observed luminosities and the radiative spectrum of Sgr A* do not comply with those predicted by the standard thin disk model proposed by Shakura and Sunyaev (Shakura and Sunyaev [1973]). The luminosity predicted by the Shakura-Sunyaev model turns out to be orders of magnitudes higher than what is observed. In order to address such inconsistency, attempts had been made to apply the spherical Bondi flow (Bondi [1952]) and advection-dominated accretion flow (ADAF) (Narayan and Yi [1994],Narayan and Yi [1995]) for modelling hydrodynamics around Sgr A*. The main parameter demarcating these models is the angular momentum of the flow. While Bondi accretion possesses no net angular momentum, ADAF corresponds to high values of the same. However, both models lead to highly advected flows with radiative efficiencies that are much lower than the observed results (Okuda and Molteni [2012]). The Bondi model can indeed describe the environment around Sgr A* in detail (Melia [1992],Melia et al. [2001]) and is often used to estimate the mass accretion rate, however the model works only when the Bondi radius is smaller than that of the inner-most stable circular orbit (ISCO). Also, it cannot be extended to regions in close proximity to the event horizon owing to obvious limitations due to oversimplicity of the model. The ADAF model serves as a work-around to such limitations, however it leads to considerably high angular momentum flow at the outer boundary and since most the heat is advected into the flow, the flow temperatures tend to be extremely high and consequently, the resultant radiative efficiency turns out to be significantly lower than its observed values.

## 2.2 The physical space-time metric

A (3+1) stationary axisymmetric space-time is considered with two commuting Killing fields. The local timelike Killing field $\xi^\mu \equiv (\partial/\partial t)^\mu = \delta^\mu_t$ generates stationarity and $\phi^\mu \equiv (\partial/\partial\phi)^\mu = \delta^\mu_\phi$ generates axial symmetry. The Boyer-Lindquist line element on the equatorial plane of the space-time metric for an uncharged, rotating black hole is given by,

$$ds^2 = g_{\mu\nu}dx^\mu dx^\nu = -\frac{r^2 A}{\Delta}dt^2 + \frac{A}{r^2}(d\phi - \omega dt)^2 + \frac{r^2}{\Delta}dr^2 + dz^2, \tag{2.1}$$

where

$$\Delta = r^2 - 2r + a^2 \tag{2.2}$$

$$A = r^4 + r^2a^2 + 2ra^2 \tag{2.3}$$

$$\omega = \frac{2ar}{A}, \tag{2.4}$$

where $\omega$ represents the rate of frame dragging by the black hole, $a$ being the Kerr parameter which in turn is related to the spin angular momentum $J$ of the black hole through the relation $a = Jc/GM^2$, where $-1 < a < 1$. Calculations have been carried out using natural units, i.e. $G = M = c = 1$. Thus, all masses are measured in units of $M$, distances are measured in units of $GM/c^2$, times are measured in units of $GM/c^3$ and all velocities are scaled in units of $c$, where $G$ is the universal gravitational constant, $M$ is the mass of the respective black hole and $c$ is the velocity of light. Thus, on the equatorial plane, the horizon is located at the outer boundary of $g^{rr} = \Delta/r^2 = 0$, i.e. $r_+ = 1 + \sqrt{1 - a^2}$.

## 2.3 Relativistic kinematics of the fluid

The accreting fluid has been considered from different frames of reference which transform according to the prescriptions of (Taub [1978], Gammie and Popham [1998], Popham and Gammie [1998], Novikov and Thorne [1973]). The first frame is the *Boyer-Lindquist frame (BLF)* that has been used to define the background space-time metric. The co-ordinates of this frame make it extremely convenient to deal with the calculations for an axisymmetric disc. Although, singularities can be handled efficiently using other co-ordinate prescriptions (such as Eddington-Finkelstein co-ordinates (Misner et al. [1973])), however such issues are of less astrophysical significance in our problem, and hence BLF is much more favourable in the present context. The next frame is designated as a *locally non-rotating frame (LNRF)* which is an orthonormal tetrad basis located at some constant $z$ and $r$ but at $\phi = \omega t +$ constant. Bardeen et al. [1972] have illustrated explicit transformations between the BLF and LNRF. In the next step, the LNRF is given an azimuthal Lorentz-boost such that it starts co-rotating with the fluid. This new frame is known as the *co-rotating frame (CRF)*. Finally, the CRF is given another Lorentz-boost, but this time in the radial direction, such that the frame is at rest with respect to the fluid spiralling inwards to fall into the horizon. Hence this final frame is named *local rest frame (LRF)*. $v^\mu$ is the 4-velocity of the accreting fluid in this frame which is a unit vector field tangent to the flow streamline. The 4-velocity can be expressed in terms of the 3-velocity components $u^i$ as follows (Landau and Lifshitz [1994], Bilic [1999]),

$$v^\mu = \frac{1}{\sqrt{1-u^2}}\left(\frac{1}{\sqrt{g_{00}}} - \frac{g_{0j}u^j}{g_{00}}; u^i\right) \tag{2.5}$$

$$v_\mu = \frac{1}{\sqrt{1-u^2}}\left(\sqrt{g_{00}}; \frac{g_{0i}}{\sqrt{g_{00}}} - g'_{ij}u^j\right), \tag{2.6}$$

where, $u$, which is the norm of the 3-velocity of the flow on its equatorial plane, is conventionally termed as the 'advective velocity', and $g'_{ij}$ is the induced three-dimensional spatial metric given by,

$$g'_{ij} = \frac{g_{0i}g_{0j}}{g_{00}} - g_{ij}, \tag{2.7}$$

and hence,

$$u^2 = g'_{ij}u^iu^j \tag{2.8}$$

with $i$ and $j$ running over the spatial indices 1, 2 and 3.
A set of hypersurfaces, $\{\Sigma_u\}$, is defined by,

$$u^2 - c_s^2 = 0, \tag{2.9}$$

where $c_s$ is a constant, $0 \leq c_s < c$. Considering a two-dimensional axisymmetric flow in a stationary axisymmetric space-time and using the notation $u^i = \left(u^r, u^\phi, u^z\right)$ where $u^z = 0$, the 4-velocity is given by,

$$v^\mu = \frac{1}{1-u^2}\left(\frac{1}{\sqrt{g_{00}}} - \frac{g_{0\phi}u^\phi}{g_{00}}, u^r, u^\phi, 0\right), \tag{2.10}$$

$$v_\mu = \frac{1}{1-u^2}\left(\sqrt{g_{00}}, -g_{rr}u^r, \frac{g_{0\phi}}{\sqrt{g_{00}}} - \left(\frac{g_{0\phi}^2}{g_{00}} - g_{\phi\phi}\right)u^\phi, 0\right). \tag{2.11}$$

Hence, the 'advective velocity' can be expressed as,

$$u^2 = u_\parallel^2 - g_{rr}u^r u^r, \tag{2.12}$$

where, $u_\parallel^2 = \left(\frac{g_{0\phi}^2}{g_{00}} - g_{\phi\phi}\right)u^\phi u^\phi$.
For axially symmetric flows in the co-rotating frame, $u^\phi = 0$, and as a consequence, the tangential component $u_\parallel$ vanishes. Since the 4-velocities at each point may be decomposed into normal and tangential components with respect to the hypersurface $\{\Sigma_u\}$, therefore in the co-rotating frame of reference, $u_\phi = 0$ implies that the normal component $u_\perp = u$. The specific angular momentum (angular momentum per unit mass) $\lambda$ of the flow is given by

$$\lambda = -v_\phi/v_t, \tag{2.13}$$

The transition to a co-rotating frame is accomplished by the co-ordinate transformation

$$d\phi = d\phi' + \Omega dt, \tag{2.14}$$

where, using eqn.(2.13), the angular velocity $\Omega$ of the flow is given by

$$\Omega = \frac{v^\phi}{v^t} = \frac{g^{\mu\phi}v_\mu}{g^{\mu t}v_\mu} = \frac{g^{t\phi}v_t + g^{\phi\phi}v_\phi}{g^{tt}v_t + g^{\phi t}v_\phi} = \frac{g^{t\phi}v_t - \lambda g^{\phi\phi}v_t}{g^{tt}v_t - \lambda g^{\phi t}v_t} = \frac{g^{t\phi} - \lambda g^{\phi\phi}}{g^{tt} - \lambda g^{\phi t}}. \tag{2.15}$$

Hence, the normalization condition $v^\mu v_\mu = -1$ leads to the expression for the time component of $v_\mu$ given by

$$v_t = \sqrt{\frac{g_{t\phi}^2 - g_{tt}g_{\phi\phi}}{(1-\lambda\Omega)(1-u^2)(g_{\phi\phi} + \lambda g_{t\phi})}}. \tag{2.16}$$

## 2.4 Equations of the flow

The accreting fluid is considered to be a perfect fluid with energy-momentum tensor

$$T^{\mu\nu} = (p+\epsilon)v^\mu v^\nu + pg^{\mu\nu} \tag{2.17}$$

where $p$, $\epsilon$ and $\rho$ are isotropic pressure, total mass-energy density and rest mass density of the fluid respectively. Other relevant features of the fluid include its thermodynamic

properties (equation of state) and geometry of the flow. These have been detailed separately in subsequent sections.
The two basic equations used in our analysis are the energy-momentum conservation equations,

$$T^{\mu\nu}_{;\nu} = 0 \tag{2.18}$$

and the baryon number conservation equations,

$$(\rho v^{\mu})_{;\nu} = 0 \tag{2.19}$$

respectively. Stationary solutions of the above equations lead to the first integrals of motion for the system. The first integrals thus obtained can be broadly identified as -

- the specific energy ($\mathcal{E}$) or the quasi-specific energy ($\xi$) depending on the equations of state - polytropic or isothermal, respectively, and
- a reduced form of the mass accretion rate ($\dot{M}$), which is interpreted as the accretion rate of entropy ($\dot{\Xi}$).

The exact algebraic form of the preliminary equations, the first integrals and the respective stationary solutions depend on the equations of state, the geometry of the flow and are also subject to the choice of co-ordinates for the background space-time metric, which have been elaborated accordingly in the subsequent chapters.

## 2.5 Equations of state

The equation of state,

$$p = K\rho^{\gamma} \tag{2.20}$$

describes *polytropic accretion*, where the polytropic index $\gamma$ (ratio of the specific heats $C_p$ and $C_v$) is assumed to be constant for the steady state flow. If validity of the Clapeyron equation for an ideal gas is assumed in addition, i.e.,

$$p = \frac{k_B}{\mu m_p}\rho T, \tag{2.21}$$

where $\mu$ is the mean molecular mass of fully ionized Hydrogen atom, $m_H \sim m_P$ is the mass of the Hydrogen atom, $\kappa_B$ is the Boltzmann constant and $T$ is the locally measured temperature, then the entropy per particle is given by (Landau and Lifshitz [1959]),

$$\sigma = \frac{1}{\gamma - 1}\log K + \frac{\gamma}{\gamma - 1} + \text{constant} \tag{2.22}$$

where the constant depends on the chemical constituents of the accreting fluid. Therefore, the proportionality constant $K$ in eq.(2.20) is considered as a measure of the specific entropy of the accreting fluid when additional entropy is not generated. The specific enthalpy $h$ is formulated as

$$h = \frac{p + \epsilon}{\rho}, \tag{2.23}$$

where,

$$\epsilon = \rho + \frac{p}{\gamma - 1} \tag{2.24}$$

signifies the total internal energy density of the relativistic fluid.
The adiabatic sound speed $c_s$ for the relativistic fluid at constant entropy is defined by

$$c_s^2 = \left(\frac{\partial p}{\partial \epsilon}\right)_{\text{constant entropy}} \tag{2.25}$$

$$\implies c_s^2 = K\gamma\rho^{\gamma-1}\left(\frac{\partial \rho}{\partial \epsilon}\right)$$
$$\implies \rho = \left(\frac{c_s^2}{\gamma K}\right)^{\frac{1}{\gamma-1}}\left(\frac{\partial \epsilon}{\partial \rho}\right)^{\frac{1}{\gamma-1}} \tag{2.26}$$

Differentiating eqn.(2.24) w.r.t. $\epsilon$,

$$1 = \frac{\partial \rho}{\partial \epsilon} + \frac{1}{\gamma-1}\frac{\partial p}{\partial \epsilon}$$
$$\implies \frac{\partial \rho}{\partial \epsilon} = 1 - \frac{c_s^2}{\gamma-1} = \frac{\gamma-(1+c_s^2)}{\gamma-1} \tag{2.27}$$

Substituting eqn.(2.27) in eqn.(2.26),

$$\rho = \left(\frac{c_s^2}{\gamma K}\right)^{\frac{1}{\gamma-1}}\left(\frac{\gamma-1}{\gamma-(1+c_s^2)}\right)^{\frac{1}{\gamma-1}} \tag{2.28}$$

Using the above relations, the expression for the specific enthalpy at constant entropy in terms of $c_s$ is given by

$$h = \frac{\gamma-1}{\gamma-(1+c_s^2)} \tag{2.29}$$

Similar expressions for the pressure, total internal energy density and temperature in terms of $c_s$ are obtained as,

$$p = K^{\frac{-1}{\gamma-1}}\left(\frac{c_s^2}{\gamma}\right)^{\frac{\gamma}{\gamma-1}}\left(\frac{\gamma-1}{\gamma-(1+c_s^2)}\right)^{\frac{\gamma}{\gamma-1}} \tag{2.30}$$

$$T = \frac{\mu m_P}{k_B}\left(\frac{c_s^2}{\gamma}\right)\left(\frac{\gamma-1}{\gamma-(1+c_s^2)}\right) \tag{2.31}$$

$$\epsilon = \left(\frac{c_s^2}{\gamma K}\right)^{\frac{1}{\gamma-1}}\left(\frac{\gamma-1}{\gamma-(1+c_s^2)}\right)^{\frac{1}{\gamma-1}}\left[1+\frac{1}{\gamma}\left(\frac{c_s^2}{\gamma-(1+c_s^2)}\right)\right]. \tag{2.32}$$

We have also investigated the isothermal accretion flow, with the equation of state given by

$$p = \rho c_s^2 \tag{2.33}$$

Comparing with the Clapeyron equation,

$$\rho c_s^2 = \frac{\mathcal{R}}{\mu}\rho T = \frac{\rho \kappa_B T}{\mu m_H} \tag{2.34}$$

$$c_s^2 = \frac{\kappa_B T}{\mu m_H} \tag{2.35}$$

where $\mathcal{R}$ is the universal gas constant, $\kappa_B$ is the Boltzmann constant, $T$ is the flow temperature, $\mu$ is the mean molecular mass of fully ionized hydrogen and $m_H \sim m_P$ is Hydrogen atom mass approximated to be equal to the mass of proton, respectively.

## 2.6 The first integrals of motion

### 2.6.1 Integral stationary solution of the linear momentum conservation equation

Contracting eq.(2.18) with $\phi^\mu$, where $\phi^\mu \equiv (\partial/\partial\phi)^\mu = \delta^\mu_\phi$,

$$\begin{aligned}
\phi_\mu T^{\mu\nu}_{;\nu} &= 0 \\
\phi_\mu \left[(p+\epsilon)v^\mu v^\nu + p g^{\mu\nu}\right]_{;\nu} &= 0 \\
\phi_\mu \left[(p+\epsilon)v^\mu v^\nu\right]_{;\nu} + \phi_\mu p_{,\nu} g^{\mu\nu} &= 0 \\
\phi_\mu \left[(p+\epsilon)v^\mu v^\nu\right]_{;\nu} + p_{,t} g^{\phi t} + p_{,\phi} g^{\phi\phi} &= 0
\end{aligned}$$

Since, for stationary axisymmetric flows, $p_{,t} = p_{,\phi} = 0$,

$$\begin{aligned}
\phi_\mu \left[(p+\epsilon)v^\mu v^\nu\right]_{;\nu} &= 0 \\
\left[\phi_\mu h v^\nu\right]_{;\nu} &= 0
\end{aligned} \tag{2.36}$$

where, the condition for baryon number conservation (eqn.(2.19)) has been considered and the isentropic specific enthalpy $h$ is given by eqn.(2.23). Thus, one obtains $hv_\phi$, the angular momentum per baryon, which is constant throughout the flow.
Similarly, contracting eq.(2.18) with $\xi^\mu$, where $\xi^\mu \equiv (\partial/\partial t)^\mu = \delta^\mu_t$,

$$\begin{aligned}
\xi_\mu \left[(p+\epsilon)v^\mu v^\nu + p g^{\mu\nu}\right]_{;\nu} &= 0 \\
\left[\xi_\mu h v^\nu\right]_{;\nu} &= 0
\end{aligned} \tag{2.37}$$

The constant quantity, $hv_t$, is the relativistic version of the Bernoulli's constant. It can be identified with $\mathcal{E}$, the total specific energy of the ideal GR fluid (see, e.g., Das and Czerny [2012] and references therein) scaled in units of the rest mass energy. The corresponding expression for conserved energy $\mathcal{E}$ is therefore given by

$$\mathcal{E} = hv_t = \frac{\gamma - 1}{\gamma - (1 + c_s^2)} \sqrt{\frac{g_{t\phi}^2 - g_{tt} g_{\phi\phi}}{(1 - \lambda\Omega)(1 - u^2)(g_{\phi\phi} + \lambda g_{t\phi})}} \tag{2.38}$$

It is clear that the expression for $\mathcal{E}$ depends on space-time geometry. It does not depend on matter geometry. Since the flow has been assumed to be non self-gravitating, hence the accreting fluid does not back-react on the space-time metric itself. In case of isothermal flow, energy gets dissipated in order to maintain a constant temperature. Thus, the total specific energy is not conserved. Integration of the relativistic Euler equation leads to an entirely different algebraic form to define the first integral of motion which cannot be identified with the total energy of the system. The energy-momentum conservation equation obtained by setting the 4-divergence (covariant derivative w.r.t. $\nu$) of eqn.(2.18) to be zero is,

$$p_{,\nu}(g^{\mu\nu} + v^\mu v^\nu) + (p + \epsilon) v^\nu v^\mu_{;\nu} = 0 \tag{2.39}$$

Using eqn.(2.33), the general relativistic Euler equation for isothermal flow becomes,

$$\frac{c_s^2}{\rho} \rho_{,\nu}(g^{\mu\nu} + v^\mu v^\nu) + v^\nu v^\mu_{;\nu} = 0 \tag{2.40}$$

Using the irrotationality condition $\omega_{\mu\nu} = 0$, where $\omega_{\mu\nu} = l^\alpha_\mu l^\beta_\nu v_{[\alpha;\beta]}$,
$\omega_{\mu\nu}$ being the vorticity of the fluid, $l^\alpha_\mu$ being the projection operator in the normal direction

of $v^\mu$
$l^\alpha_\mu = \delta^\alpha_\mu + v^\alpha v_\mu$, and $v_{[\alpha;\beta]} = \frac{1}{2}(v_{\beta;\alpha} - v_{\alpha;\beta})$, we obtain,

$$\partial_\nu(v_\mu \rho^{c_s^2}) - \partial_\mu(v_\nu \rho^{c_s^2}) = 0 \tag{2.41}$$

Taking the time component, we thus observe that for an irrotational isothermal flow, $v_t \rho^{c_s^2}$ turns out to be a conserved quantity. The square of this quantity is defined as the *quasi-specific energy*, which is a first integral in this case and is given by,

$$\xi = v_t^2 \rho^{2c_s^2} \tag{2.42}$$

It must not be confused with the total conserved specific energy $\mathcal{E}$.

### 2.6.2 Integral stationary solution of the mass conservation equation

The mass conservation equation (2.19) gives

$$\frac{1}{\sqrt{-g}}(\sqrt{-g}\rho v^\mu)_{,\mu} = 0, \tag{2.43}$$

where $g \equiv \det(g_{\mu\nu})$. This implies $\left[(\sqrt{-g}\rho v^\mu)_{,\mu} d^4x = 0\right]$, where $\sqrt{-g}d^4x$ is the covariant volume element. We assume that $v^\theta$ (in spherical polar co-ordinates)/ $v^z$ (in cylindrical co-ordinates) are relatively negligible when compared to the transformed radial velocity component $v^r$. Using such assumption we obtain $\partial_r(\sqrt{-g}\rho v^r)\mathrm{d}r\mathrm{d}\theta\mathrm{d}\phi = 0$, for stationary flow in spherical polar co-ordinates, and $\partial_r(\sqrt{-g}\rho v^r)\mathrm{d}r\mathrm{d}z\mathrm{d}\phi = 0$, in cylindrical co-ordinates. The equations are integrated for $\phi$ ranging from 0 to $2\pi$ and $\theta$ ranging from $-H_\theta$ to $H_\theta$, or $z$ ranging from $-H_z$ to $H_z$, where $\pm H_\theta$ and $\pm H_z$ are the corresponding values of the co-ordinates above and below the equatorial plane in spherical or cylindrical co-ordinate systems, respectively, for local half thickness $H$, to obtain a quantity $\dot{M}$, which is constant throughout the flow when $\theta = \frac{\pi}{2}$ (i.e. on the equatorial plane). Physically, $\dot{M}$ signifies the amount of mass flowing per unit time through a given cross-section of the disc at a radial distance $r$ and hence it represents the 'mass accretion rate'. The expression for $\dot{M}$ is different for different matter geometry configurations. A generalized expression for $\dot{M}$ may be written as

$$\dot{M} = \rho v^r \mathcal{A}(r) \tag{2.44}$$

where $\mathcal{A}(r)$ represents the 2D surface area through which the steady state inbound mass flux is calculated.

## 2.7 Geometric configurations of the flow

Investigations have been carried out for three different geometric configurations of axially symmetric flow, as described below:

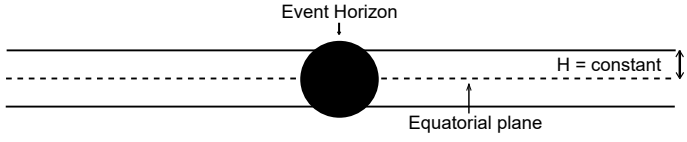


Figure 2.1: Accretion disc with constant height

1. In the simplest possible set up, the thickness of the accretion flow is usually assumed to be space invariant, i.e., for the stationary state, one deals with an accretion disc with constant thickness ($H \equiv constant$). Such a disc resembles a cross section of a right circular cylinder with constant height (Fig. 2.1).

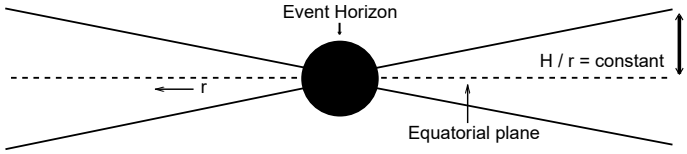


Figure 2.2: Quasi-spherical disc

2. In the next variant, the flow is considered to be quasi-spherical in shape, where the ratio of the radial distance at a point and the local half thickness at that particular point remains invariant for all $r$ ($H \equiv \Lambda r$, $\Lambda$ being a constant) (Fig. 2.2). Quasi-spherical flow, or the conical flow, as is it called in the literature (e.g. Nag et al. [2012], Bilić et al. [2014]), is considered to be ideal-most to model low angular momentum, advection dominated, inviscid accretion.

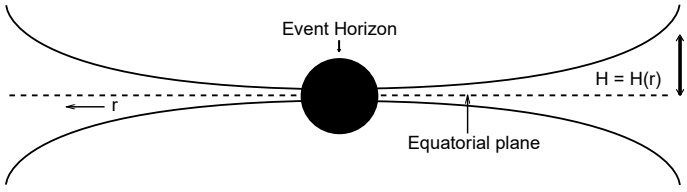


Figure 2.3: Disc held by hydrostatic equilibrium in the vertical direction

3. A rather non-trivial axially symmetric accretion configuration requires the matter to be in hydrostatic equilibrium along the vertical direction. In such a configuration, the local flow thickness becomes a non-linear function of radial distance, as well as of the advective velocity and the local radial sound speed ($H \equiv H(r, u, c_s)$) (Fig. 2.3). In order to derive the disc height in our work, we have followed the prescription laid down by (Abramowicz et al. [1997]) whose calculations can accommodate for thin disc and quasi-spherical geometry involving stationary flows and also involve equations that do not introduce unphysical singularities in the final vertical equation as in (Novikov and Thorne [1973], Riffert and Herold [1995], Abramowicz et al. [1996]).

- **Derivation of disc height for polytropic flows**

  The equation of disc thickness (**Abramowicz et. al. 1997**) takes the following final form with thin-disc approximation,

$$-2\frac{p_0}{\rho_0} + \left(\frac{H}{r}\right)^2 \frac{\mathscr{L}_*^2}{r^2} = 0 \tag{2.45}$$

  where,

$$\mathscr{L}_*^2 = \lambda^2 v_t^2 - a^2(v_t - 1). \tag{2.46}$$

  The subscript '0' would denote values on equatorial plane of the disc. Since we are interested in stationary solutions along equatorial planes of the discs,

all dynamical and thermodynamic flow variables upon the plane are defined as quantities integrated vertically along the disc height, as

$$v_0 = \int_{-H}^{+H} v(z)dz \tag{2.47}$$

where $v(z)$ is the distribution of a flow-related variable along the vertical direction $z$, $H$ is the half-thickness of the disc, and the subscript 0 indicates the value of the respective quantity upon the equatorial plane.

Using eqn.(2.28) and eqn.(2.30),

$$\frac{p_0}{\rho_0} = \left(\frac{c_s^2}{\gamma}\right)\left(\frac{\gamma-1}{\gamma-(1+c_s^2)}\right) \tag{2.48}$$

Substituting in eqn.(2.45),

$$H^2 = 2\left(\frac{c_s^2}{\gamma}\right)\left(\frac{\gamma-1}{\gamma-(1+c_s^2)}\right)\frac{r^4}{\lambda^2 v_t^2 - a^2(v_t-1)} \tag{2.49}$$

- **Derivation of disc height for isothermal flows**

Eqn.(2.45) holds for all thin axisymmetric discs in vertical hydrostatic equilibrium irrespective of the equation of state of the fluid. Hence, the corresponding disc height for isothermal flows can be calculated by substituting for the ratio of pressure and density from the isothermal equation of state (Tarafdar et al. [2017]).

$$\begin{aligned} H^2 &= 2\frac{p_0}{\rho_0}\frac{r^4}{\mathscr{L}_*^2} = \frac{2c_s^2 r^4}{\lambda^2 v_t^2 - a^2(v_t-1)} \\ &= \frac{2\kappa_B r^4 T}{\mu m_H(\lambda^2 v_t^2 - a^2(v_t-1))} \end{aligned} \tag{2.50}$$

Now that we are equipped with all the necessary knowledge regarding the background space-time, the accreting fluid itself and its fundamental equations, we proceed to elaborate the methods to solve for stationary transonic solutions and analyse their nature, in the following chapters.

# Chapter 3

# Critical Points of the Flow

**Summary**

- ✓ *What are critical points?*
- ✓ *Derivation of critical point conditions for all flow configurations*
- ✓ *Drawing a generic parameter space diagram for transonic accretion using the critical point conditions*
- ✓ *Comparative analysis of parameter space diagrams for different types of flow*

## 3.1 Critical points

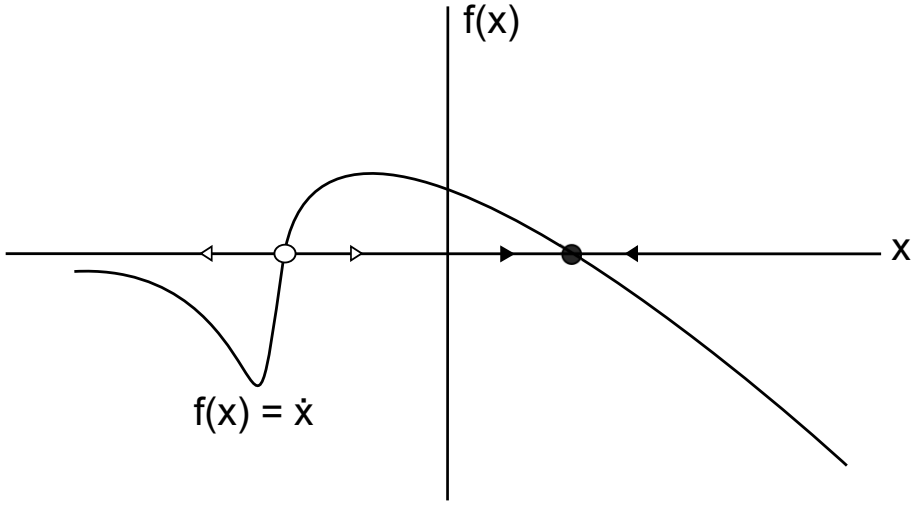


Figure 3.1: Critical points on a phase plot

Let us consider the function $\dot{x} = f(x)$ depicted in fig. 3.1 which represents the velocity of a particle plotted against its position in one dimension. Such figures are known an *phase-space plots*. Conventionally, positive velocity would indicate that the particle is moving along the x-axis, i.e. to the right. Similarly, negative velocity will correspond to the moving of the particle to its left. While passing through a *phase point* located

anywhere on the $f(x) > 0$ and $f(x) < 0$ curves, the particle proceeds in a unique direction. However, it encounters two opposite directions at *phase points* lying on the x-axis. All possible *phase trajectories* either converge onto these points or diverge from them. A system resting on such a point, on being subjected to small local perturbations, would either re-stabilize to its unperturbed state or de-stabilize away from it. Such values of $x$ where $f(x) = 0$ are called *fixed points* or *stable points* or *critical points* of the system. To avoid any confusions, we would like to inform the reader that these terms will be used synonymously throughout the thesis in our context.

The number of dynamical physical systems and their respective phase space plots are innumerably large. Depending on dimensions of the system, the natures of stable points in its phase space are equally diverse. There are nodal points, centre-type points, spiral points and saddle points as depicted in the following figures.

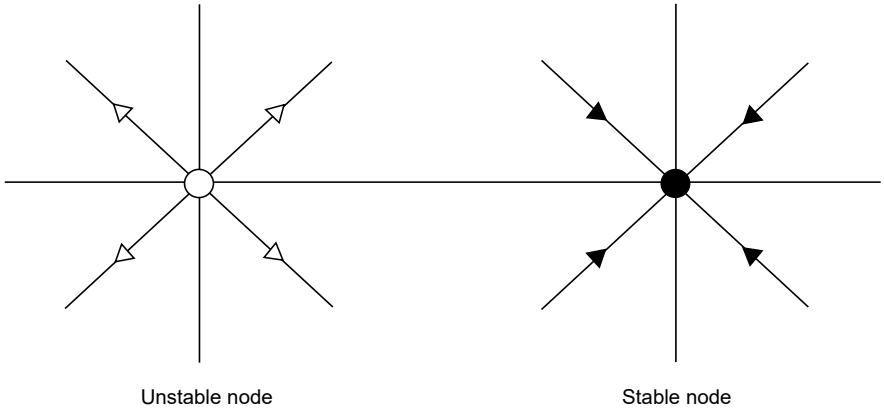


Figure 3.2: Nodal stable points

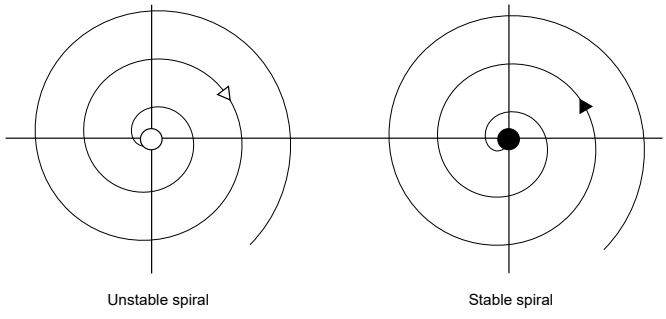


Figure 3.3: Spiral-type stable points

Fig. 3.2 illustrates the simplest type of critical points which are known as *nodes*. The phase trajectories either direct towards such points or radiate out of them. The former kinds are termed as stable nodes and the latter are termed as unstable nodes. Fig. 3.3 shows phase points which are very similar to nodes, save for the nature of the trajectories which in this case either spiral in or out of the critical points classified as stable or unstable *spirals* respectively. Fig. 3.4 depicts a combination of two different critical points. The point on the left is called a *centre-type* critical point. Such points are forbidden to phase trajectories and the system keeps oscillating around them. The equilibrium points of conservative simple harmonic oscillators are typical examples of centre-type critical points. The point shown to the right rests upon a very delicate equilibrium. Depending on the

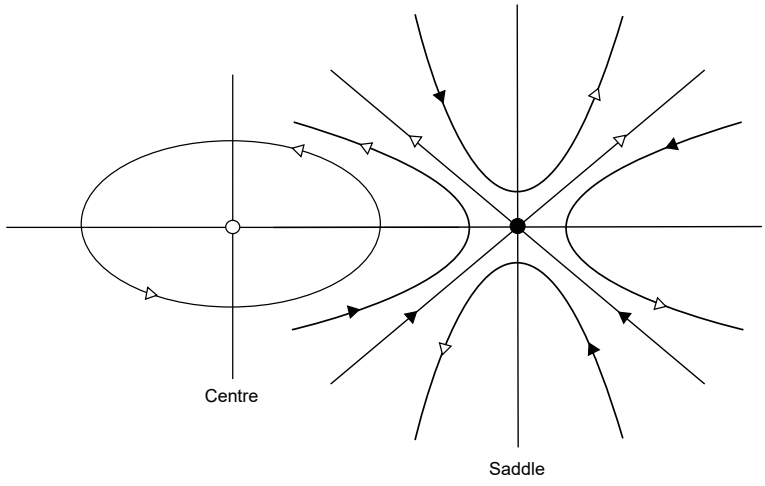


Figure 3.4: A centre-type and a saddle point

direction of perturbation, the system might either return to the stable point or fly away from it. These points are known as *saddles* due to their metastable nature. The phase portraits pertaining to the physical systems of our interest display similar combinations of centre and saddle, as will be shown in the subsequent chapters.

## 3.2 Derivation of critical point conditions for polytropic accretion

In this section, we derive the conditions satisfied at the critical points of polytropic flow with constant height discs (hereafter CH), quasi-spherical or conical discs (hereafter CF) and discs in vertical hydrostatic equilibrium (hereafter VE). Before delving into the detailed calculations which are quite involved, we would like to break down and summarise the whole formalism into the following basic steps –

1. We write down the equations for the conserved *specific energy* ($\mathcal{E}$) and the conserved *mass accretion rate* ($\dot{M}$) pertaining to the specific flow. It may be noted that $\mathcal{E}$ remains the same for CH, CF and VE discs. Disc geometry only influences $\dot{M}$ due to its dependence on the area of cross section through which influx of matter occurs.

2. We differentiate the equations for $\mathcal{E}$ and $\dot{M}$ with respect to radial distance $r$, and solve simultaneously to obtain expressions for the spatial gradients of the advective velocity $u$ and sound speed $c_s$.

3. Expression for spatial gradient of the advective velocity is of the form $du/dr = \mathcal{N}(r, u, c_s)/\mathcal{D}(r, u, c_s)$. Integrating $du/dr$ with proper initial conditions generates the corresponding phase space plots. Since velocity and their gradients at specific radial distances cannot be readily known without actual numerical integration, hence the initial conditions required for carrying out the integration are fixed using the values of $u$, $c_s$ and $du/dr$ at the critical points $r_c$ given by the critical point conditions. These conditions are obtained by equating $\mathcal{N}$ and $\mathcal{D}$ simultaneously to zero. It is a standard method that has been borrowed from the theory of dynamical systems and their stability (Jordan and Smith [1999]). Setting the numerator and denominator

to zero simultaneously ensures a smooth and continuous physical transonic flow. For multitransonic flows, the continuity is broken at locations of shock. This issue will be dealt with separately in later chapters.

Now that the formalism for derivation of critical point conditions has been laid, we can safely proceed towards the corresponding calculations for three different disc geometries (Barai et al. [2004], Tarafdar et al. [2017], Tarafdar and Das [2018b]).

### 3.2.1 Discs with constant height

The expression for specific energy ($\mathcal{E}$) is obtained by substituting for the metric elements in eqn.(2.38) –

$$\mathcal{E} = \frac{\gamma - 1}{\gamma - (1 + c_s^2)} \sqrt{\frac{(r-2)\left(r^3 + a^2(r+2)\right)}{(1-u^2)\left(r^4 - \lambda^2\left(4a^2 + r(r-2)\right) + a^2 r(r+2)\right)}} \tag{3.1}$$

As mentioned earlier, this expression depends only upon the space-time geometry. It is independent of the configuration of the disc, and hence remains unaltered for CH, CF and VE discs. Using eqn.(2.44), the mass accretion rate for an accretion disc with constant height can be written down as

$$\dot{M}_{CH} = 4\pi\sqrt{\Delta} H \rho \sqrt{\frac{u^2}{1-u^2}} \tag{3.2}$$

where $H$ is the radius independent constant half thickness of the accretion disc, $\rho = \left[\frac{c_s^2(\gamma-1)}{\gamma K(\gamma-1-c_s^2)}\right]^{\frac{1}{\gamma-1}}$ and $\Delta$ is given by eqn.(2.3). The corresponding entropy accretion rate may be obtained through the transformation $\dot{\Xi} = \dot{M}(K\gamma)^{\frac{1}{\gamma-1}}$ as,

$$\dot{\Xi}_{CH} = 4\pi\sqrt{\Delta} H \left[\frac{c_s^2(\gamma-1)}{\gamma - 1 - c_s^2}\right]^{\frac{1}{\gamma-1}} \sqrt{\frac{u^2}{1-u^2}} \tag{3.3}$$

The idea of 'entropy accretion rate' was initially proposed by Abramowicz and Zurek [1981] and Blaes [1987] in order to calculate the stationary solutions for low angular momentum non-relativistic transonic accretion under the influence of Paczyński and Wiita [1980] pseudo-Newtonian potential onto a non-rotating black hole. It is a *quasi-constant* multiple of the mass accretion rate. We use the term quasi-constant due to the fact that although mass accretion rate is a universal constant in the absence of creation or annihilation of matter in the system, but the *entropy accretion rate* remains constant throughout the flow only as long as the specific entropy per particle (characterised by the quantity $K = p/\rho^\gamma$) remains locally unchanged. This condition is violated at the location of shock in case of multi-transonic accretion and $\dot{\Xi}$ jumps discretely to a higher value as will be illustrated in later chapters where flow discontinuities have been discussed.
Differentiating eqns.(3.1) and (3.3) w.r.t $r$ and solving simultaneously, the space gradients of the acoustic and dynamical velocities can be computed as:

$$\frac{dc_s}{dr} = \frac{\mathcal{N}_1^{CH}}{\mathcal{D}_1^{CH}} \tag{3.4}$$

$$\frac{du}{dr} = \frac{\mathcal{N}_2^{CH}}{\mathcal{D}_2^{CH}} \tag{3.5}$$

where $\mathcal{N}_1^{CH} = \frac{-2u}{2(1-u^2)}\frac{du}{dr} - \frac{f'}{2f}$, $\mathcal{D}_1^{CH} = \frac{2c_s}{\gamma-1-c_s^2}$, $\mathcal{N}_2^{CH} = u(1-u^2)\left[\frac{r-1}{\Delta}c_s^2 - \frac{f'}{2f}\right]$, $\mathcal{D}_2^{CH} = u^2 - c_s^2$, $f = \frac{\Delta}{B}$, $B = g_{\phi\phi} + 2\lambda g_{t\phi} + \lambda^2 g_{tt} = (r^3 + a^2(r+2) - \lambda^2(r-2))/r$ and $f'$ denotes the space derivative of $f$, i.e., $\frac{df}{dr}$.
Equating $\mathcal{N}_2^{CH}$ and $\mathcal{D}_2^{CH}$ to zero, the critical point conditions are obtained as,

$$u^2|_{r_c} = c_s^2|_{r_c} = \frac{f'}{2f}|_{r_c}\frac{\Delta_c}{r_c - 1} \tag{3.6}$$

Inserting the critical point conditions in the expression of the conserved specific energy (eqn.(3.1)), one can solve the corresponding algebraic equation for a specific set of values of $[\mathcal{E}, \lambda, \gamma, a]$, to obtain the values of the critical points $r_c$. $u$ and $c_s$ at $r_c$ can subsequently be calculated by using eqn.(3.6). The values of $du/dr$ and $dc_s/dr$ at the critical points are also required as initial values for the integration to plot the phase diagrams. This can be achieved in steps by applying L'Hospital's rule to eqn.(3.5) and solving for the resultant quadratic equation in $du/dr$ in terms of $r_c$ and the values of $u$ and $c_s$ at $r_c$ corresponding to the given accretion parameters. The critical gradient of sound speed can then be computed easily by plugging the derived expression of $du/dr$ at $r_c$. For polytropic CH discs, the following expressions are obtained –

$$\frac{du}{dr}|_{r_c} = -\frac{\beta_{CH}}{2\alpha_{CH}} \pm \frac{1}{2\alpha_{CH}}\sqrt{\beta_{CH}^2 - 4\alpha_{CH}\Gamma_{CH}} \tag{3.7}$$

$$\frac{dc_s}{dr}|_{r_c} = \frac{\mathcal{N}_1}{\mathcal{D}_1}|_{r_c} \tag{3.8}$$

where, the co-efficients $\alpha_{CH}$, $\beta_{CH}$ and $\Gamma_{CH}$ are given by,

$$\alpha_{CH} = \frac{\gamma - 3c_s^2 + 1}{(c_s^2-1)^2}|_{r_c},$$

$$\beta_{CH} = \frac{2c_s(r-1)\left(c_s^2 - \gamma + 1\right)}{(c_s^2-1)(a^2+(r-2)r)}|_{r_c},$$

$$\Gamma_{CH} = \frac{2\left(c_s^2-1\right)(r-1)^2}{(a^2+(r-2)r)^2}|_{r_c} - \frac{c_s^2-1}{a^2+(r-2)r}|_{r_c} + \frac{c_s^2(r-1)^2\left(-c_s^2+\gamma-1\right)}{(a^2+(r-2)r)^2}|_{r_c} -$$

$$\left[\begin{array}{c} -\frac{a^2\lambda^4\left(a^2(r+2)+r^3\right)}{\left(a^2(r+2)+\lambda^2 r\right)^2} + \frac{2a^2\lambda^4(r-2)\left(a^2+\lambda^2\right)\left(a^2(r+2)+r^3\right)}{\left(a^2(r+2)+\lambda^2 r\right)^3} - \frac{a^2\lambda^4(r-2)\left(a^2+3r^2\right)}{\left(a^2(r+2)+\lambda^2 r\right)^2} \\ + \frac{\lambda^4\left(a^2+\lambda^2\right)\left(r^3-a^2\left(r^2-8\right)\right)}{\left(a^2(r+2)+\lambda^2 r\right)^2} + \frac{\lambda^4 r\left(2a^2-3r\right)}{a^2(r+2)+\lambda^2 r} - 2a^2 r + 4a\lambda r + 5r^4 \\ \hline r^4\left(-\frac{\lambda^4(r-2)\left(a^2(r+2)+r^3\right)}{r^3\left(a^2(r+2)+\lambda^2 r\right)} + \frac{2a^2}{r} + a^2 - \frac{4a\lambda}{r} + r^2\right) \end{array}\right]_{r_c}$$

$$+ \frac{4\left(-\frac{a^2\lambda^4(r-2)\left(a^2(r+2)+r^3\right)}{\left(a^2(r+2)+\lambda^2 r\right)^2} - a^2r^2 + \frac{\lambda^4\left(a^2\left(r^2-8\right)-r^3\right)}{a^2(r+2)+\lambda^2 r} + 2a\lambda r^2 + r^5\right)}{r^5\left(-\frac{\lambda^4(r-2)\left(a^2(r+2)+r^3\right)}{r^3\left(a^2(r+2)+\lambda^2 r\right)} + \frac{2a^2}{r} + a^2 - \frac{4a\lambda}{r} + r^2\right)}|_{r_c} +$$

$$\left[\begin{array}{c} 2\left(2a^5\lambda r^2(r+2)^2 + 4a^3\lambda^3 r^3(r+2) + 2a^2\lambda^2 r^3(r+2)\left(r^3-a^2\right) + \lambda^6(-r)\left(r^3-a^2\left(r^2-8\right)\right)\right. \\ \left. +\lambda^4\left(a^4(r-3)(r+2)^2 - 3a^2r^4 + r^7\right) + a^4r^2(r+2)^2\left(r^3-a^2\right) + 2a\lambda^5 r^4\right)^2 \\ \hline r^2\left(a^2(r+2)+\lambda^2 r\right)^2\left(a^4(r+2)^2r^2 - 4a^3\lambda(r+2)r^2\right. \\ \left. +a^2(r+2)\left(r^5+\lambda^2r^3-\lambda^4(r-2)\right) - 4a\lambda^3r^3 + \lambda^2r^6 - \lambda^4(r-2)r^3\right)^2 \end{array}\right]_{r_c}$$

### 3.2.2 Discs with quasi-spherical geometry

The expressions for mass and entropy accretion rates for quasi-spherical flow (CF) are given by,

$$\dot{M}_{CF} = 4\pi\sqrt{\Delta}\Lambda r\rho\sqrt{\frac{u^2}{1-u^2}} \tag{3.9}$$

and

$$\dot{\Xi}_{CF} = 4\pi\sqrt{\Delta}\Lambda r\left[\frac{c_s^2(\gamma-1)}{\gamma-1-c_s^2}\right]^{\frac{1}{\gamma-1}}\sqrt{\frac{u^2}{1-u^2}}\ , \tag{3.10}$$

where $\Lambda$ is the solid angle subtended by the accretion disc at the horizon. Differentiating eqns.(3.1) and (3.10) w.r.t $r$, the space gradients of sound speed and flow velocity are obtained as,

$$\frac{dc_s}{dr} = \frac{\mathcal{N}_1^{CF}}{\mathcal{D}_1^{CF}} \tag{3.11}$$

and

$$\frac{du}{dr} = \frac{\mathcal{N}_2^{CF}}{\mathcal{D}_2^{CF}}\ , \tag{3.12}$$

where $\mathcal{N}_1^{CF} = \mathcal{N}_1^{CH}$, $\mathcal{D}_1^{CF} = \mathcal{D}_1^{CH}$, $\mathcal{N}_2^{CF} = u(1-u^2)\left[\frac{2r^2-3r+a^2}{\Delta r}c_s^2 - \frac{f'}{2f}\right]$ and $\mathcal{D}_2^{CF} = \mathcal{D}_1^{CF}$. Hence, the corresponding critical point condition comes out to be

$$u^2|_{r_c} = c_s^2|_{r_c} = \frac{f'}{2f}|_{r_c}\frac{\Delta_c r_c}{2r_c^2-3r_c+a^2} \tag{3.13}$$

Substituting the critical point conditions in the expression of the conserved specific energy, one can solve the corresponding algebraic equation for a specific set of values of $[\mathcal{E},\lambda,\gamma,a]$, to obtain the values of the critical points $r_c$.

Using techniques discussed in the previous subsection, expressions for the velocity gradients at critical points may be obtained as,

$$\frac{du}{dr}|_{r_c} = -\frac{\beta_{CF}}{2\alpha_{CF}} \pm \frac{1}{2\alpha_{CF}}\sqrt{\beta_{CF}^2 - 4\alpha_{CF}\Gamma_{CF}} \tag{3.14}$$

$$\frac{dc_s}{dr}|_{r_c} = \frac{\mathcal{N}_1^{CF}}{\mathcal{D}_1^{CF}}|_{r_c} \tag{3.15}$$

where, the co-efficients $\alpha_{CF}$, $\beta_{CF}$ and $\Gamma_{CF}$ are given by,

$\alpha_{CF} = \alpha_{CH}$,

$\beta_{CF} = \frac{2c_s(a^2+r(2r-3))\left(c_s^2-\gamma+1\right)}{(c_s^2-1)r(a^2+(r-2)r)}|_{r_c}$,

$\Gamma_{CF} = -\frac{c_s^2-1}{a^2+(r-2)r}|_{r_c} + \frac{2\left(c_s^2-1\right)(r-1)^2}{(a^2+(r-2)r)^2}|_{r_c} + \frac{c_s^2}{r^2}|_{r_c} + \frac{c_s^2(r-1)\left(a^2+r(2r-3)\right)\left(c_s^2-\gamma+1\right)}{(c_s^2-1)r(a^2+(r-2)r)^2}|_{r_c}$

$+ \frac{c_s^2\left(-c_s^2+\gamma-1\right)}{r^2}|_{r_c} + \frac{c_s^2(r-1)\left(-c_s^2+\gamma-1\right)}{r(a^2+(r-2)r)}|_{r_c} + \frac{c_s^4(r-1)\left(a^2+r(2r-3)\right)\left(-c_s^2+\gamma-1\right)}{(c_s^2-1)r(a^2+(r-2)r)^2}|_{r_c}$

$$- \left[\begin{array}{c} -\frac{a^2\lambda^4\left(a^2(r+2)+r^3\right)}{\left(a^2(r+2)+\lambda^2r\right)^2} + \frac{2a^2\lambda^4(r-2)\left(a^2+\lambda^2\right)\left(a^2(r+2)+r^3\right)}{\left(a^2(r+2)+\lambda^2r\right)^3} - \frac{a^2\lambda^4(r-2)\left(a^2+3r^2\right)}{\left(a^2(r+2)+\lambda^2r\right)^2} \\ + \frac{\lambda^4\left(a^2+\lambda^2\right)\left(r^3-a^2\left(r^2-8\right)\right)}{\left(a^2(r+2)+\lambda^2r\right)^2} + \frac{\lambda^4r\left(2a^2-3r\right)}{a^2(r+2)+\lambda^2r} - 2a^2r + 4a\lambda r + 5r^4 \\ \hline r^4\left(-\frac{\lambda^4(r-2)\left(a^2(r+2)+r^3\right)}{r^3\left(a^2(r+2)+\lambda^2r\right)} + \frac{2a^2}{r} + a^2 - \frac{4a\lambda}{r} + r^2\right) \end{array}\right]_{r_c}$$

$$+\frac{4\left(-\frac{a^2\lambda^4(r-2)\left(a^2(r+2)+r^3\right)}{\left(a^2(r+2)+\lambda^2 r\right)^2}-a^2r^2+\frac{\lambda^4\left(a^2\left(r^2-8\right)-r^3\right)}{a^2(r+2)+\lambda^2 r}+2a\lambda r^2+r^5\right)}{r^5\left(-\frac{\lambda^4(r-2)\left(a^2(r+2)+r^3\right)}{r^3\left(a^2(r+2)+\lambda^2 r\right)}+\frac{2a^2}{r}+a^2-\frac{4a\lambda}{r}+r^2\right)}\Big|_{r_c}$$

$$+\left[\frac{\begin{array}{r}2\left(2a^5\lambda r^2(r+2)^2+4a^3\lambda^3r^3(r+2)+2a^2\lambda^2r^3(r+2)\left(r^3-a^2\right)+\lambda^6(-r)\left(r^3-a^2\left(r^2-8\right)\right)\right.\\ \left.+\lambda^4\left(a^4(r-3)(r+2)^2-3a^2r^4+r^7\right)+a^4r^2(r+2)^2\left(r^3-a^2\right)+2a\lambda^5r^4\right)^2\end{array}}{\begin{array}{c}r^2\left(a^2(r+2)+\lambda^2r\right)^2\left(a^4(r+2)^2r^2-4a^3\lambda(r+2)r^2\right.\\ \left.+a^2(r+2)\left(r^5+\lambda^2r^3-\lambda^4(r-2)\right)-4a\lambda^3r^3+\lambda^2r^6-\lambda^4(r-2)r^3\right)^2\end{array}}\right]_{r_c}.$$

### 3.2.3 Flow in hydrostatic equilibrium along the vertical direction

The mass accretion rate for flows in hydrostatic equilibrium in the vertical direction is given by,

$$\dot{M}_{VE}=4\pi\sqrt{\Delta}H(r)\rho\sqrt{\frac{u^2}{1-u^2}} \tag{3.16}$$

The disc height (eqn.(2.49)) derived in section 2.7 can be written as,

$$H(r)=\sqrt{\frac{2}{\gamma}}r^2\left[\frac{c_s^2(\gamma-1)}{(\gamma-1-c_s^2)F}\right]^{\frac{1}{2}} \tag{3.17}$$

where $F=\lambda^2v_t^2-a^2(v_t-1)$.
The corresponding entropy accretion rate is obtained as,

$$\dot{\Xi}_{VE}=4\pi ur^2\left[\frac{c_s^2(\gamma-1)}{\gamma-1-c_s^2}\right]^{\frac{\gamma+1}{2(\gamma-1)}}\left[\frac{2\Delta}{\gamma(1-u^2)F}\right]^{\frac{1}{2}} \tag{3.18}$$

Differentiating eqns.(3.1) and (3.18) w.r.t $r$, space gradients of $c_s$ and $u$ can be derived as,

$$\frac{dc_s}{dr}=\frac{\mathcal{N}_1^{VE}}{\mathcal{D}_1^{VE}} \tag{3.19}$$

$$\frac{du}{dr}=\frac{\mathcal{N}_2^{VE}}{\mathcal{D}_2^{VE}} \tag{3.20}$$

where,
$\mathcal{N}_1^{VE}=\frac{(2\lambda^2u_t-a^2)u_t}{2F}\left[\frac{u}{1-u^2}\frac{du}{dr}+\frac{P1}{2}\right]-\frac{1}{u(1-u^2)}\frac{du}{dr}-\frac{\Delta'}{2\Delta}-\frac{2}{r}$,
$\mathcal{D}_1^{VE}=\frac{\gamma+1}{c_s(\gamma-1-c_s^2)}$,
$\mathcal{N}_2^{VE}=\frac{2c_s^2}{\gamma+1}\left(-\frac{P1v_t\left(2\lambda^2v_t-a^2\right)}{4F}+\frac{\Delta'}{2\Delta}+\frac{2}{r}\right)-\frac{P1}{2}$,
$\mathcal{D}_2^{VE}=\frac{u}{1-u^2}-\frac{2c_s^2}{\gamma+1}\frac{1}{(1-u^2)u}\left(1-\frac{u^2v_t\left(2\lambda^2v_t-a^2\right)}{2F}\right)$,
$P1=\frac{\Delta'}{\Delta}+\frac{d\Omega}{dr}\frac{\lambda}{1-\Omega\lambda}-\frac{g'_{\phi\phi}+\lambda g'_{t\phi}}{g_{\phi\phi}+\lambda g_{t\phi}}=\frac{2r\left(a^4+2a^2(r-2)r+r^4\right)-2\lambda^2\left(4a^4+a^2r(8r-13)+(r-2)^2r^2\right)}{r(a^2+(r-2)r)(-\lambda^2(4a^2+(r-2)r)+a^2(r+2)r+r^4)}$.
This provides the corresponding critical conditions as,

$$u^2|_{r_c}=\frac{\mathrm{P1}}{\frac{\Delta'}{\Delta}+\frac{4}{r}}|_{r_c} \tag{3.21}$$

$$c_s^2|_{r_c}=\frac{(\gamma+1)\left(2Fu^2\right)}{2\left(2F-u^2v_t\left(2\lambda^2v_t-a^2\right)\right)}|_{r_c} \tag{3.22}$$

The corresponding velocity gradients at critical points are derived as,

$$\frac{du}{dr}|_{r_c} = -\frac{\beta_{VE}}{2\alpha_{VE}} \pm \frac{1}{2\alpha_{VE}}\sqrt{\beta_{VE}^2 - 4\alpha_{VE}\Gamma_{VE}} \tag{3.23}$$

$$\frac{dc_s}{dr}|_{r_c} = \frac{\mathcal{N}_1^{VE}}{\mathcal{D}_1^{VE}}|_{r_c}. \tag{3.24}$$

The co-efficients $\alpha_{VE}$, $\beta_{VE}$ and $\Gamma_{VE}$ are given by,
$\alpha_{VE} = \frac{1+u^2}{(1-u^2)^2} - \frac{2nD_2D_6}{2n+1}$, $\beta_{VE} = \frac{2nD_2D_7}{2n+1} + \tau_4$, $\Gamma_{VE} = -\tau_3$,
where,
$n = \frac{1}{\gamma-1}$, $D_2 = \frac{c_s^2}{u(1-u^2)}\left(1 - D_3\right)$, $D_6 = \frac{3u^2-1}{u(1-u^2)} - \frac{D_5}{1-D_3} - \frac{\left(1-nc_s^2\right)u}{nc_s^2(1-u^2)}$,
$D_7 = \frac{1-nc_s^2}{nc_s^2}\frac{P1}{2} + \frac{D_3D_4v_tP1}{2(1-D_3)}$, $\tau_3 = \frac{2n}{2n+1}\left(c_s^2\tau_2 - \frac{v_tP1v_1}{2nv_t}\left(1-nc_s^2\right) - c_s^2v_5v_t\frac{P1}{2}\right) - \frac{P1'}{2}$,
$\tau_4 = \frac{2n}{2n+1}\frac{v_tu}{1-u^2}\left(\frac{v_1}{nv_t}\left(1-nc_s^2\right) + c_s^2v_5\right)$, $v_1 = \frac{\Delta'}{2\Delta} + \frac{2}{r} - \left(2\lambda^2v_t - a^2\right)v_t\frac{\mathrm{P1}}{4F}$,
$D_3 = \frac{u^2v_t\left(2\lambda^2v_t-a^2\right)}{2F}$, $D_4 = \frac{1}{v_t} + \frac{2\lambda^2}{2\lambda^2v_t-a^2} - \frac{2\lambda^2v_t-a^2}{F}$, $D_5 = D_3\left(\frac{2}{u} + \frac{D_4v_tu}{1-u^2}\right)$, $\tau_2 = \tau_1 - \frac{v_t\left(2\lambda^2v_t-a^2\right)}{4F}P1'$, $v_5 = \left(2\lambda^2v_t - a^2\right)\frac{P1}{4F}v_4$,
$\tau_1 = \frac{1}{2}\left(\frac{\Delta''}{\Delta} - \frac{(\Delta')^2}{\Delta^2}\right) - \frac{2}{r^2}$, $v_4 = \frac{v_3}{(2\lambda^2v_t-a^2)F}$, $v_3 = \left(4\lambda^2v_t - a^2\right)F - \left(2\lambda^2v_t - a^2\right)^2v_t$.

Note that $u^2 \neq c_s^2$ at the critical points. Hence, the critical points and the sonic points (transonic radius where $u = c_s$) do not appear to be isomorphic for discs in vertical hydrostatic equilibrium. The issue of locating sonic points may be resolved in two different ways:

a) The time-dependent Euler equation and the continuity equation can be linearly perturbed to find out the corresponding wave equation which describes the propagation of the acoustic perturbation through the background fluid space-time. The speed of propagation of such perturbation can be taken as the effective adiabatic sound speed. The critical points become the sonic points for such effective acoustic velocity. This treatment requires dealing with time-dependent perturbation techniques, which is beyond the scope of this present work. For related calculations, one may refer to Bollimpalli et al. [2017], where such techniques have been applied for accretion in the Schwarzschild metric.

b) The solutions for stationary trajectories in phase-space may be obtained through numerical integration of the spatial gradients of flow velocities starting from the critical points, to figure out the radial distance where the Mach number becomes equal to unity, i.e. the corresponding sonic point. We shall follow this approach in our present work.

Determining the locations of transonicity is crucial to our work, and its importance shall be evident when we discuss the relevance of acoustic horizons in the context of analogue gravity in later chapters.

### 3.2.4 Parameter space for polytropic accretion - Comparative analysis for different disc geometries

As already mentioned, substituting the critical point conditions in eqn.(3.1) for a given set of the accretion parameters, viz. specific energy $\mathcal{E}$, specific angular momentum $\lambda$, ratio of specific heats $\gamma$ and black hole spin parameter $a$, we numerically solve the resultant algebraic equation for the critical points $r_c$. It is important to note that with the exceptions

of a few very special cases, the algebraic equations are of highly non-linear nature and hence, cannot be solved analytically.

$\mathcal{E}$ is scaled by the rest mass energy and is inclusive of the rest mass energy. Thus, $\mathcal{E}$ signifies a flow which has no thermal energy at infinity. Such an initial boundary condition is unphysical for the generation of acoustic perturbation. Setting $\mathcal{E} < 1$ would also lead to a configuration with a negative energy initial state that would need a physical mechanism for dissipative extraction of energy in order to get a solution consisting of positive energy states. Presence of such dissipation cannot fit in the inviscid flow model considered for our work. Now, almost all solutions with $\mathcal{E} > 1$ are permissible in theory. However, $\mathcal{E} > 2$ would signify extremely large initial values of the thermal energy of the fluid which is not a common trait for accreting black hole systems. Therefore, $1 < \mathcal{E} < 2$ should be a reasonable choice of range in the present model. $\lambda = 0$ signifies a spherically symmetric configuration, whereas $\lambda > 4$ (for $G = M = c = 1$ scaling) corresponds to flows beyond the Keplerian regime where multi- criticalbehaviour does not show up in general. Therefore, in our work we shall consider the physical range of $\lambda$ to be $0 < \lambda \leq 4$. For isothermal accretion, the polytropic index $\gamma = 1$. Now, whereas $\gamma < 1$ is not a realistic value in accretion astrophysics, $\gamma > 2$ would signify super-dense matter with considerably large magnetic field in addition to a direction dependent anisotropic pressure. Since we are not dealing with general relativistic magneto- hydrodynamic equations in the present context, hence our choice of values for $\gamma$ shall be constrained as $1 < \gamma < 2$. Moreover, throughout black hole accretion literature, the realistic bounds for the polytropic index are $\gamma = 4/3$ (for ultra- relativistic flows) and $\gamma = 5/3$ (for purely non- relativistic flows) (Refer Frank et al. [1992] for further references). Hence we shall fix the range for $\gamma$ as $4/3 \leq \gamma \leq 5/3$. The range for $a$ spans all possible values between the values of Kerr parameters corresponding to maximally rotating black holes for the prograde and the retrograde flows. In this context, it is important to mention that prograde flows are those rotating in the same direction as the black hole, whereas retrograde flows are those rotating in the opposite direction of the black hole. And in order to distinguish between the two, we shall alter the sign of $a$, maintaining $\lambda$ to be always positive, which is a standard practice in black hole accretion theory. Hence the obvious choice for $a$ would be $-1 \leq a \leq 1$. Although an upper limit for $a$ has been set to 0.998 in some works (Thorne [1974]) by considering the influence of the interaction of the accreting material with the accretor on the evolution of mass and spin of the black hole. However, in our work, we shall not consider such interactions. Hence, the astrophysical limits of the flow parameters shall be given by $\left[1 < \mathcal{E} < 2, 0 < \lambda \leq 4, \frac{4}{3} \leq \gamma \leq \frac{5}{3}, -1 \leq a \leq 1\right]$ (Das et al. [2015]).

For polytropic accretion in the Schwarzschild and Kerr metrics, the parameter space is three and four dimensional respectively. For convenience, we deal with a two dimensional parameter space in both cases. ${}^4C_2$ and ${}^3C_2$ such spaces may be obtained respectively for Schwarzschild and Kerr space-times. In the present context, we concentrate on the $[\mathcal{E} - \lambda]$ parameter space for fixed values of $[\gamma, a]$.

Figure 3.5 shows the $[\mathcal{E} - \lambda]$ parameter space for polytropic accretion in quasi- spherical disc geometry for $[\gamma = 1.35, a = 0.1]$. Similar diagrams can be generated for the two other geometries as well. $\mathrm{A_1A_2A_3A_4}$ represents the region of $[\mathcal{E}, \lambda]$ for which the corresponding polynomial equation in $r_c$ along with the corresponding critical point conditions

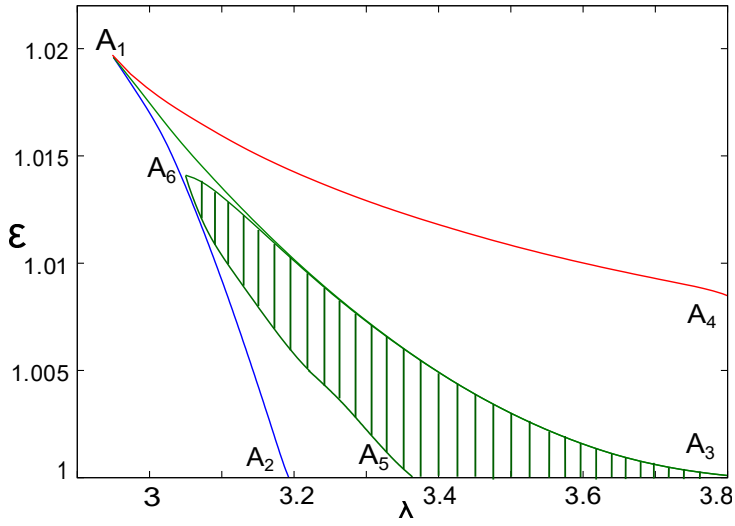


Figure 3.5: $\mathcal{E}$-$\lambda$ plot for quasi-spherical disc geometry ($\gamma = 1.35$ and $a = 0.1$)

provides three real positive roots lying outside $r_+$, where $r_+ = 1 + \sqrt{1 - a^2}$, $a$ being the Kerr parameter. Values of $r_c$ inside the region $\mathrm{A_1A_2A_3}$ are characterised by the condition $\dot{\Xi}_{\rm inner} > \dot{\Xi}_{\rm outer}$ and represent multi-critical accretion solutions.

Region $\mathrm{A_1A_3A_4}$ represents a subset of $[\mathcal{E}, \lambda, \gamma, a]_{\rm mc}$ (where 'mc' stands for 'multi-critical') for which $\dot{\Xi}_{\rm inner} < \dot{\Xi}_{\rm outer}$. This condition represents the wind or outflow solutions. The boundary $\mathrm{A_1A_3}$ between these two regions represents the value of $[\mathcal{E}, \lambda, \gamma, a]$ for which multi-critical accretion is characterized by $\dot{\Xi}_{\rm inner} = \dot{\Xi}_{\rm outer}$. In such caes, the transonic solutions passing through the inner and the outer critical points are completely degenerate, leading to the formation of a heteroclinic orbit[1] on the phase portrait. Such flow patterns may be subject to turbulence and various other forms of instabilities.

The region $\mathrm{A_3A_5A_6}$ (shaded in green), is a subspace of $\mathrm{A_1A_2A_3}$ which allows shock formation. For the time being, this is being mentioned for the sake of a comprehensive picture of a complete generic parameter space diagram. The analytical techniques required for computing this region will be discussed later in chapter 5. It has been already mentioned that multi-transonic flows must encounter shocks to be brought down discontinuously from supersonic to subsonic regimes. This is essential for the second transonicity to occur. Hence it is this subspace, which represents real physical multi-transonic accretion, where the stationary transonic solutions passing through the outer sonic point join the stationary transonic solutions constructed through the inner sonic point through discontinuous energy preserving shocks of Rankine-Hugoniot type. Such shocked multi-transonic solutions contain two smooth transonic transitions (from sub- to super-) at two regular sonic points (of saddle type) and a discontinuous transition (from super- to sub-) at the shock location.

Figure 3.5 contains a lot of information about the specific flow. However in order to compare various flow related variables corresponding to different disc geometries, first of all, it is required to spot the common range of parameters over which all the disc geome-

[1]Heteroclinic orbits are the trajectories defined on a phase portrait which connects two different saddle type critical points. Integral solution configuration on phase portrait characterized by heteroclinic orbits are topologically unstable (Jordan and Smith [1999], Strogatz [2001]).

tries have multitransonic accretion solutions. While comparing flow profiles, we will be required to choose values of accretion parameters from such specific regions of overlap, failing which, a comparision will be physically meaningless.

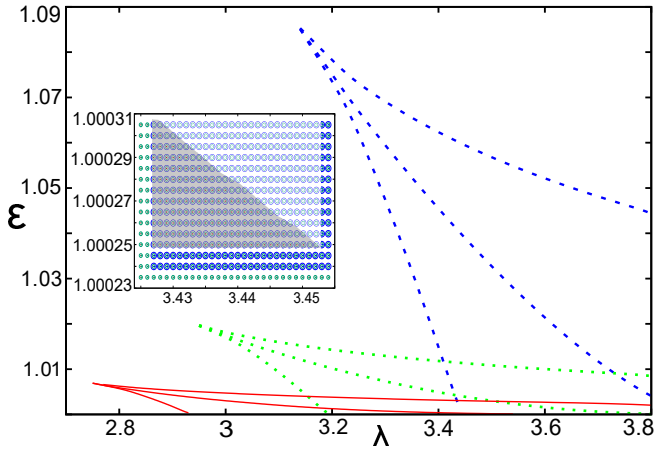


Figure 3.6: Comparision of $\mathcal{E}$-$\lambda$ plot for three different flow geometries ($\gamma = 1.35$ and $a = 0.1$). Constant height disc, quasi-spherical flow and flow in vertical hydrostatic equilibrium represented by blue dashed lines, green dotted lines and red solid lines respectively. Shaded region in the inset depicts $[\mathcal{E}, \lambda]$ space overlap with multicritical solutions for all three models.

In figure 3.6, for the same values of $[\gamma, a]$ as in figure 3.5, we compare the parameter spaces for three different flow geometries. The common region for which multiple critical points are formed for all three flow geometries are shown in the inset. It is observed that the window of overlapping parameters available is extremely small. After scanning over different combinations of the accretion parameters, we could find that the overlap is maximum for non-rotating black holes, and it continues to decrease with increasing values of the black hole spin. In particular, with increasing values of $a$, the multi-transonic solutions shift towards lower values of the specific flow angular momentum $\lambda$ and higher values of the specific energy $\mathcal{E}$. The apparent correlation between angular momentum of the flow and spin parameter of the central gravitating black hole in this context is particularly interesting. We shall try to investigate this correlation and understand its implications in chapter 5 where the analytics of flow discontinuities are discussed in detail.

## 3.3 Derivation of critical conditions for isothermal accretion

Isothermal equations of state and the integral solutions of the corresponding relativistic Euler and continuity equations were presented in sections 2.5 and 2.6 of the previous chapter. The isothermal parameter space is smaller due to a constant value of the polytropic index ($\gamma = 1$). The expression for conserved specific energy derived in the case of polytropic accretion is replaced by constant temperature for isothermal flows. Comparision of the isothermal equation of state with the Clapeyron equation (eqn.(2.35)) implies a constant value of the sound speed once temperature of the flow is fixed.

One might argue that the critical point conditions and all other relevant equations for the isothermal case can be readily obtained by substituting $\gamma = 1$ in the previous results. However the logic is misleading as the effects of an entirely different thermodynamics influence the basic levels of the formulation. Concepts such as specific enthalpy and specific

energy are not defined in the isothermal regime. It is a separate physics altogether. After doing the calculations, although comparisons might suggest a match upon substitution of $\gamma$ with a constant for some results, but most of the results are found to be different. This motivates us further to study the isothermal cases separately, and as will be seen in the later chapters, it leads to some important findings.

### 3.3.1 Discs with constant height

The mass accretion rate is given by,

$$\dot{M}^{iso}_{CH} = 4\pi\sqrt{\Delta}H\rho\sqrt{\frac{u^2}{1-u^2}} \tag{3.25}$$

where, H is the constant half thickness of the disc and $\rho$ is substituted in terms of the constant *quasi-specific energy* $\xi$ derived in eqn.2.42 as,

$$\rho = (\xi v_t^{-2})^{\frac{1}{2c_s^2}} \tag{3.26}$$

Defining $\dot{\Xi}^{iso}_{CH} = \dot{M}^{iso}_{CH}\xi^{-\frac{1}{2c_s^2}}$ as a constant multiple of the mass accretion rate, we obtain,

$$\dot{\Xi}^{iso}_{CH} = 4\pi\sqrt{\Delta}Hv_t^{-\frac{1}{c_s^2}}\sqrt{\frac{u^2}{1-u^2}} \tag{3.27}$$

Substituting for $v_t$ from eqn.(2.16) and differentiating $\dot{\Xi}^{iso}_{CH}$ w.r.t $r$, the radial gradient of the advective velocity is derived as,

$$\frac{du}{dr}|_{CH} = \frac{\frac{1-c_s^2}{2c_s^2}\frac{\Delta'}{\Delta} - \frac{1}{2c_s^2}\frac{B'}{B}}{\frac{1}{u} - \frac{u}{1-u^2}\frac{1-c_s^2}{c_s^2}} = \frac{\mathcal{N}^{iso}_{CH}}{\mathcal{D}^{iso}_{CH}} \tag{3.28}$$

where $\Delta$ and $B$ are entirely functions of $r$ and have their usual meanings. Note that since $dc_s/dr = 0$, we need to differentiate just a single expression to obtain the flow velocity gradient. Isothermal flows have less number of varying parameters to worry about and hence the calculations are way simpler than their polytropic counterparts.

Equating $\mathcal{N}^{iso}_{CH}$ and $\mathcal{D}^{iso}_{CH}$ to zero simultaneously, the critical point conditions are obtained as,

$$u_c^2|_{CH} = c_{sc}^2|_{CH} = 1 - \frac{B'}{B}\frac{\Delta}{\Delta'} \tag{3.29}$$

The idea to solve for $r_c$ in the isothermal case, is to substitute the critical point conditions in the isothermal Clapeyron equation (eqn. (2.35)) and then solve the resulting equation in $r_c$ for given values of flow temperature $T$. The $r_c$ equation for CH is therefore given by,

$$c_s^2 = \frac{\kappa_B T}{\mu m_H} = 1 - \frac{B'}{B}\frac{\Delta}{\Delta'} \tag{3.30}$$

Velocity gradient at critical points are obtained by applying l'Hospital's rule to eqn.(3.28) and solving for the resulting quadratic equation in $du/dr$,

$$\left(\frac{du}{dr}\right)_c|^{iso}_{CH} = -\sqrt{\frac{\beta^{iso}_{CH}}{\Gamma^{iso}_{CH}}} \tag{3.31}$$

where,

$\Gamma^{iso}_{CH} = \frac{2}{c_{s_c}^2(1-c_{s_c}^2)}$,

$\beta^{iso}_{CH} = \beta^{(1)}_{CH} + \beta^{(2)}_{CH} + \beta^{(3)}_{CH} - \beta^{(4)}_{CH} - \beta^{(5)}_{CH}$,

$\beta^{(1)}_{CH} = \frac{2(1-c_{s_c}^2)(1-r_c)^2}{c_{s_c}^2(c_{s_c}^2+r_c(r_c-2))^2}$,

$\beta^{(2)}_{CH} = \frac{c_{s_c}^2-1}{c_{s_c}^2(c_{s_c}^2+r_c(r_c-2))}$,

$\beta^{(3)}_{CH} = \frac{\beta^{(31)}_{CH}}{r_c^4 c_{s_c}^2(c_{s_c}^2+\frac{2c_{s_c}^2}{r_c}+r_c^2-\frac{4c_{s_c}\lambda}{r_c}-\frac{(r_c-2)(r_c^3+c_{s_c}^2(r_c+2))\lambda^4}{r_c^3(c_{s_c}^2(r_c+2)+r_c\lambda^2)})}$,

$\beta^{(31)}_{CH} = -2c_{s_c}^2 r_c + 5r_c^4 + 4c_{s_c} r_c\lambda$
$+\frac{2c_{s_c}^2(r_c-2)(r_c^3+c_{s_c}^2(r_c+2))\lambda^4(c_{s_c}^2+\lambda^2)}{(c_{s_c}^2(r_c+2)+r_c\lambda^2)^3} - \frac{c_{s_c}^2(r_c-2)(c_{s_c}^2+3r_c^2)\lambda^4}{(c_{s_c}^2(r_c+2)+r_c\lambda^2)^2} - \frac{c_{s_c}^2(r_c^3+c_{s_c}^2(r_c+2))\lambda^4}{(c_{s_c}^2(r_c+2)+r_c\lambda^2)^2}$
$+\frac{(r_c^3-c_{s_c}^2(r_c^2-8))\lambda^4(c_{s_c}^2+\lambda^2)}{(c_{s_c}^2(r_c+2)+r_c\lambda^2)^2} + \frac{(2c_{s_c}^2-3r_c)r_c\lambda^4}{c_{s_c}^2(r_c+2)+r_c\lambda^2}$,

$$\beta^{(4)}_{CH} = \frac{4(-c_{s_c}^2 r_c^2 + r_c^5 + 2c_{s_c} r_c^2\lambda - \frac{c_{s_c}^2(r_c-2)(r_c^3+c_{s_c}^2(r_c+2))\lambda^4}{(c_{s_c}^2(r_c+2)+r_c\lambda^2)^2} + \frac{(-r_c^3+c_{s_c}^2(r_c^2-8))\lambda^4}{c_{s_c}^2(r_c+2)+r_c\lambda^2})}{c_{s_c}^2 r_c^5(c_{s_c}^2+\frac{2c_{s_c}^2}{r_c}+r_c^2-\frac{4c_{s_c}\lambda}{r_c}-\frac{(r_c-2)(r_c^3+c_{s_c}^2(r_c+2))\lambda^4}{r_c^3(c_{s_c}^2(r_c+2)+r_c\lambda^2)})},$$

$\beta^{(5)}_{CH} = \frac{\beta^{(51)}_{CH}}{\beta^{(52)}_{CH}}$,

$\beta^{(51)}_{CH} = 2\left[-c_{s_c}^6 r_c^2(r_c+2)^2 + 2c_{s_c} r_c^4\lambda^5 + 2c_{s_c}^5 r_c^2(r_c+2)^2\lambda\right.$
$+4c_{s_c}^3 r_c^3(r_c+2)\lambda^3 + r_c^4\lambda^4(r_c^3-\lambda^2)$
$+c_{s_c}^2 r_c\lambda^2(4r_c^5+2r_c^6-3r_c^3\lambda^2-8\lambda^4+r_c^2\lambda^4)$
$\left.+c_{s_c}^4(r_c+2)(2r_c^5+r_c^6-2r_c^3\lambda^2-6\lambda^4-r_c\lambda^4+r_c^2\lambda^4)\right]^2$,

$\beta^{(52)}_{CH} = \left[c_{s_c}^2 r_c^2(c_{s_c}^2(r_c+2)+r_c\lambda^2)^2\right]$
$\left[c_{s_c}^4 r_c^2(r_c+2)^2 - 4c_{s_c}^3 r_c^2(r_c+2)\lambda - 4c_{s_c} r_c^3\lambda^3\right.$
$\left.+r_c^3\lambda^2(r_c^3-(r_c-2)\lambda^2) + c_{s_c}^2(r_c+2)(r_c^5+r_c^3\lambda^2-(r_c-2)\lambda^4)\right]^2$.

### 3.3.2 Discs with quasi-spherical geometry

The mass accretion rate is given by,

$$\dot{M}^{iso}_{CF} = 4\pi\sqrt{\Delta}\Lambda r\rho\sqrt{\frac{u^2}{1-u^2}} \tag{3.32}$$

where $\Lambda$ is the solid angle subtended by the disc at the event horizon. Substituting for $\rho = (\xi v_t^{-2})^{\frac{1}{2c_s^2}}$, we obtain,

$$\dot{\Xi}^{iso}_{CF} = 4\pi\sqrt{\Delta}\Lambda r v_t^{-\frac{1}{c_s^2}}\sqrt{\frac{u^2}{1-u^2}} \tag{3.33}$$

Substituting for $v_t$ and differentiating eqn.(3.33) w.r.t $r$, the radial gradient of advective velocity is given by,

$$\frac{du}{dr}|^{iso}_{CF} = \frac{\frac{1-c_s^2}{2c_s^2}\frac{\Delta'}{\Delta} - \frac{1}{2c_s^2}\frac{B'}{B} - \frac{1}{r}}{\frac{1}{u} - \frac{u}{1-u^2}\frac{1-c_s^2}{c_s^2}} = \frac{\mathcal{N}^{iso}_{CF}}{\mathcal{D}^{iso}_{CF}} \tag{3.34}$$

Equating $\mathcal{N}^{iso}_{CF}$ and $\mathcal{D}^{iso}_{CF}$ simultaneously to zero, the critical point conditions are derived as,

$$u_c^2|^{iso}_{CF} = c_{s_c}^2|^{iso}_{CF} = \frac{\frac{\Delta'}{\Delta} - \frac{B'}{B}}{\frac{2}{r} + \frac{\Delta'}{\Delta}} \tag{3.35}$$

Solving the equation

$$\frac{k_B T}{\mu m_H} = \frac{\frac{\Delta'}{\Delta} - \frac{B'}{B}}{\frac{2}{r} + \frac{\Delta'}{\Delta}} \tag{3.36}$$

for specific values of the flow temperature $T$, we obtain the values of the corresponding critical points $r_c$.

Finally, applying l'Hospital's rule to eqn.(3.34), the expression for velocity gradient at critical points is obtained as,

$$\left(\frac{du}{dr}\right)_c |^{iso}_{CF} = -\sqrt{\frac{\beta^{iso}_{CF}}{\Gamma^{iso}_{CF}}} \tag{3.37}$$

where,

$\Gamma^{iso}_{CF} = \frac{2}{c_{s_c}^2(1-c_{s_c}^2)}$,
$\beta^{iso}_{CF} = \beta^{(0)}_{CF} + \beta^{(1)}_{CF} + \beta^{(2)}_{CF} + \beta^{(3)}_{CF} - \beta^{(4)}_{CF} - \beta^{(5)}_{CF}$,
$\beta^{(0)}_{CF} = -\frac{1}{r_c^2}$,
$\beta^{(1)}_{CF} = \frac{2(1-c_{s_c}^2)(1-r_c)^2}{c_{s_c}^2(c_{s_c}^2+r_c(r_c-2))^2}$,
$\beta^{(2)}_{CF} = \frac{c_{s_c}^2-1}{c_{s_c}^2(c_{s_c}^2+r_c(r_c-2))}$,
$\beta^{(3)}_{CF} = \frac{\beta^{(31)}_{CF}}{r_c^4 c_{s_c}^2(c_{s_c}^2+\frac{2c_{s_c}^2}{r_c}+r_c^2-\frac{4c_{s_c}\lambda}{r_c}-\frac{(r_c-2)(r_c^3+c_{s_c}^2(r_c+2))\lambda^4}{r_c^3(c_{s_c}^2(r_c+2)+r_c\lambda^2)})}$,
$\beta^{(31)}_{CF} = -2c_{s_c}^2 r_c + 5r_c^4 + 4c_{s_c} r_c \lambda$
$+\frac{2c_{s_c}^2(r_c-2)(r_c^3+c_{s_c}^2(r_c+2))\lambda^4(c_{s_c}^2+\lambda^2)}{(c_{s_c}^2(r_c+2)+r_c\lambda^2)^3} - \frac{c_{s_c}^2(r_c-2)(c_{s_c}^2+3r_c^2)\lambda^4}{(c_{s_c}^2(r_c+2)+r_c\lambda^2)^2} - \frac{c_{s_c}^2(r_c^3+c_{s_c}^2(r_c+2))\lambda^4}{(c_{s_c}^2(r_c+2)+r_c\lambda^2)^2}$
$+\frac{(r_c^3-c_{s_c}^2(r_c^2-8))\lambda^4(c_{s_c}^2+\lambda^2)}{(c_{s_c}^2(r_c+2)+r_c\lambda^2)^2} + \frac{(2c_{s_c}^2-3r_c)r_c\lambda^4}{c_{s_c}^2(r_c+2)+r_c\lambda^2}$,

$$\beta^{(4)}_{CF} = \frac{4(-c_{s_c}^2 r_c^2 + r_c^5 + 2c_{s_c} r_c^2 \lambda - \frac{c_{s_c}^2(r_c-2)(r_c^3+c_{s_c}^2(r_c+2))\lambda^4}{(c_{s_c}^2(r_c+2)+r_c\lambda^2)^2} + \frac{(-r_c^3+c_{s_c}^2(r_c^2-8))\lambda^4}{c_{s_c}^2(r_c+2)+r_c\lambda^2})}{c_{s_c}^2 r_c^5 (c_{s_c}^2 + \frac{2c_{s_c}^2}{r_c} + r_c^2 - \frac{4c_{s_c}\lambda}{r_c} - \frac{(r_c-2)(r_c^3+c_{s_c}^2(r_c+2))\lambda^4}{r_c^3(c_{s_c}^2(r_c+2)+r_c\lambda^2)})},$$

$\beta^{(5)}_{CF} = \frac{\beta^{(51)}_{CF}}{\beta^{(52)}_{CF}}$,
$\beta^{(51)}_{CF} = 2\left[-c_{s_c}^6 r_c^2(r_c+2)^2 + 2c_{s_c} r_c^4 \lambda^5 + 2c_{s_c}^5 r_c^2(r_c+2)^2\lambda\right.$
$+4c_{s_c}^3 r_c^3(r_c+2)\lambda^3 + r_c^4\lambda^4(r_c^3-\lambda^2)$
$+c_{s_c}^2 r_c\lambda^2(4r_c^5+2r_c^6-3r_c^3\lambda^2-8\lambda^4+r_c^2\lambda^4)$
$\left.+c_{s_c}^4(r_c+2)(2r_c^5+r_c^6-2r_c^3\lambda^2-6\lambda^4-r_c\lambda^4+r_c^2\lambda^4)\right]^2$,
$\beta^{(52)}_{CF} = \left[c_{s_c}^2 r_c^2(c_{s_c}^2(r_c+2)+r_c\lambda^2)^2\right]$
$\left[c_{s_c}^4 r_c^2(r_c+2)^2 - 4c_{s_c}^3 r_c^2(r_c+2)\lambda - 4c_{s_c} r_c^3\lambda^3 + r_c^3\lambda^2(r_c^3-(r_c-2)\lambda^2)\right.$
$\left.+c_{s_c}^2(r_c+2)(r_c^5+r_c^3\lambda^2-(r_c-2)\lambda^4)\right]^2$

The flow profile is then obtained by integrating the velocity gradient using critical point conditions and values of velocity gradients evaluated at the critical points.

### 3.3.3 Flow in vertical hydrostatic equilibrium

Tha mass accretion rate is given by,

$$\dot{M}^{iso}_{VE} = 4\pi\sqrt{\Delta}H(r)\rho\sqrt{\frac{u^2}{1-u^2}} \tag{3.38}$$

where the half thickness $H(r)$ is given by eqn.(2.50). Substituting for $\rho = (\xi v_t^{-2})^{\frac{1}{2c_s^2}}$,

$$\dot{\Xi}^{iso}_{VE} = 4\pi v_t^{-\frac{1}{c_s^2}}\sqrt{\frac{2c_s^2 r^4 \Delta u^2}{(1-u^2)(\lambda^2 v_t^2 - a^2(v_t-1))}} \tag{3.39}$$

Differentiating eqn.(3.39) w.r.t. $r$, the radial gradient of advective velocity is derived as,

$$\frac{du}{dr}|_{VE}^{iso} = \frac{c_s^2(\frac{\Delta'}{2\Delta} + \frac{2}{r} - (2\lambda^2 v_t - a^2)\frac{v_t P1}{4F}) - \frac{P1}{2}}{\frac{u}{1-u^2} - \frac{c_s^2}{u(1-u^2)}(1 - (2\lambda^2 v_t - a^2)\frac{u^2 v_t}{2F})} = \frac{\mathcal{N}_{VE}^{iso}}{\mathcal{D}_{VE}^{iso}} \tag{3.40}$$

where $\Delta$, $P1$ and $F$ have their usual meanings. Equating $\mathcal{N}_{VE}^{iso}$ and $\mathcal{D}_{VE}^{iso}$ to zero, the critical point conditions are calculated as,

$$u_c^2|_{VE}^{iso} = \frac{P1}{\frac{\Delta'}{\Delta} + \frac{4}{r}} \tag{3.41}$$

$$c_{sc}^{\ 2}|_{VE}^{iso} = \frac{2Fu_c^2}{2F - u_c^2 v_t(2\lambda^2 v_t - a^2)} = \frac{k_B T}{\mu m_H} \tag{3.42}$$

Substituting eqn.(3.41) in eqn.(3.42), and solving for $r$ given a specific set of $[T, \lambda, a]$, we get the values of the corresponding critical points $r_c$. Then, applying l'Hospital's rule to eqn.(3.40) and solving the resulting quadratic equation in $du/dr$, the critical gradient of flow velocity is obtained to be,

$$\left(\frac{du}{dr}\right)_c|_{VE}^{iso} = -\frac{\beta_{VE}^{iso}}{2\alpha_{VE}^{iso}} \pm \frac{1}{2\alpha_{VE}^{iso}}\sqrt{\beta_{VE}^{iso\ 2} - 4\alpha_{VE}^{iso}\Gamma_{VE}^{iso}} \tag{3.43}$$

where,
$\alpha_{VE}^{iso} = \frac{1+u_c^2}{(1-u_c^2)^2} - D_2 D_6$, $\beta_{VE}^{iso} = D_2 D_7 + \tau_4$, $\Gamma_{VE}^{iso} = -\tau_3$,
$D_2 = \frac{c_s^2}{u(1-u^2)}(1 - D_3)$, $D_6 = \frac{3u^2-1}{u(1-u^2)} - \frac{D_5}{1-D_3}$,
$D_7 = \frac{D_3 D_4 v_t P1}{2(1-D_3)}$, $\tau_3 = \left(c_s^2\tau_2 - c_s^2 v_5 v_t \frac{P1}{2}\right) - \frac{P1'}{2}$,
$\tau_4 = \frac{c_s^2 v_5 v_t u}{1-u^2}$, $v_1 = \frac{\Delta'}{2\Delta} + \frac{2}{r} - \left(2\lambda^2 v_t - a^2\right) v_t \frac{\mathrm{P1}}{4F}$,
$D_3 = \frac{u^2 v_t\left(2\lambda^2 v_t - a^2\right)}{2F}$, $D_4 = \frac{1}{v_t} + \frac{2\lambda^2}{2\lambda^2 v_t - a^2} - \frac{2\lambda^2 v_t - a^2}{F}$, $D_5 = D_3\left(\frac{2}{u} + \frac{D_4 v_t u}{1-u^2}\right)$, $\tau_2 = \tau_1 - \frac{v_t\left(2\lambda^2 v_t - a^2\right)}{4F} P1'$, $v_5 = \left(2\lambda^2 v_t - a^2\right)\frac{P1}{4F} v_4$,
$\tau_1 = \frac{1}{2}\left(\frac{\Delta''}{\Delta} - \frac{(\Delta')^2}{\Delta^2}\right) - \frac{2}{r^2}$, $v_4 = \frac{v_3}{(2\lambda^2 v_t - a^2)F}$, $v_3 = \left(4\lambda^2 v_t - a^2\right) F - \left(2\lambda^2 v_t - a^2\right)^2 v_t$.

Thus it is observed that even in the isothermal case, critical and sonic points do not overlap for discs in vertical hydrostatic equilibrium. Hence the sonic points are required to be obtained by numerically integrating eqn.(3.40), using eqn.(3.41) and eqn.(3.43) to calculate the initial conditions at the respective critical points.

### 3.3.4 Parameter Space for Isothermal Accretion

The isothermal parameter space is two and three dimensional in the case of Schwarzschild and Kerr metrics respectively. For visual convenience, we shall deal only with two-dimensional projections of the parameter space. Hence, isothermal flow around a non-rotating black hole will be characterised by a single parameter space diagram, i.e. $[T, \lambda]$, and that around a rotating black hole will have three such possible combinations $({}^3C_2)$, i.e. $[T, \lambda]$, $[\lambda, a]$ and $[a, T]$. The astrophysically significant limits for two of the parameters governing the flow are given by $[0 < \lambda < 4, -1 < a < 1]$. For the time being, we concentrate on $[T, \lambda]$ parameter space for a fixed value of $a$. A general $[T, \lambda]$ diagram for a given accretion disc geometry would look similar to the generic diagram for polytopic accretion shown in fig.3.5. So we are rather interested in comparing the parameter space diagrams

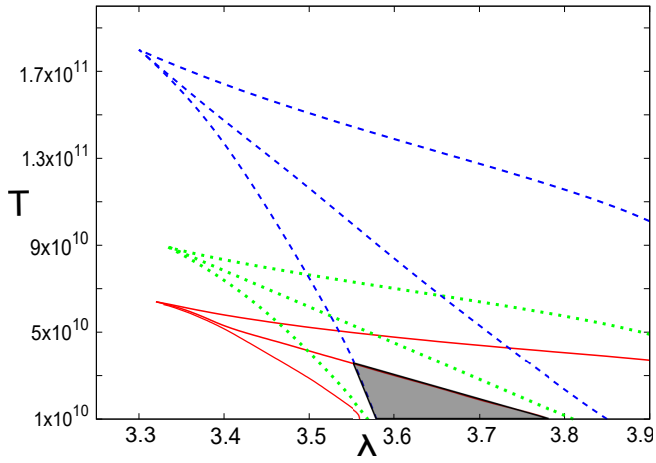


Figure 3.7: Comparision of $T$-$\lambda$ plot for three different flow geometries ($a = 0.1$, $T$ in Kelvin). Constant height disc, quasi-spherical flow and flow in vertical hydrostatic equilibrium represented by blue dashed lines, green dotted lines and red solid lines respectively. The shaded region allows for multicritical solution in all flow configurations.

for the three different flow geometries, in order to find a common region of overlap.

In figure 3.7, for $a = 0.1$, we compare the parameter spaces for three different flow geometries. The common domain for which multiple critical points are formed for all three flow geometries is depicted in the shaded region. The region of overlap, in contrast to figure 3.6, is found to be greater for isothermal flows. We have also observed once again, that increasing the value of $a$ leads to multicritical accretion at lower values of $\lambda$ and even higher values of $T$. As mentioned previously, the apparent correlation between black hole spin and the flow angular momentum in the context of multi-transonic accretion is interesting, and will be studied in detail, in the subsequent chapters.

# Chapter 4

# Classification of Critical Points

**Summary**

- ✓ *Outline of the scheme*
- ✓ *Defining an eigenvalue-based class indicator* – $\Omega^2$
- ✓ *Derivation of* $\Omega^2$ *for all flow configurations*
- ✓ *Bifurcation diagrams – A comparative analysis for different flows*

Transonic accretion may possess one or more critical points, depending on the set of flow parameters defined by the values of $[\mathcal{E}, \lambda, \gamma, a]$ (for polytropic flow) or $[T, \lambda, a]$ (for isothermal flow). As mentioned in section 3.1, the phase portraits corresponding to the physical system under investigation exhibit saddle-type points (for mono-transonic flows) and specifically ordered combinations of saddles and centres (for multi- transonic flows). The nature of a critical point could not be determined analytically so far. The exact phase trajectories through that point had to be constructed by numerical integration of the expressions for velocity gradients using the critical point conditions as initial values. A classification scheme was developed by Goswami et al. [2007] to accomplish such a task. The scheme has been borrowed from the theory of dynamical systems and can be immediately recognised by those who are familiar with the theory. In problems of general fluid dynamics – all of which are almost essentially non-linear – this approach for the linear stability analysis of fixed points is quite common (Bohr et al. [1993]). In the context of accretion studies (which, in its essence, is the study of a compressible fluid flow), this method has been effectively adopted before (Ray and Bhattacharjee [2002], Afshordi and Paczyński [2003], Chaudhury et al. [2006], Mandal et al. [2007]). Some earlier works in accretion had also made use of the general mathematical aspects of this approach (Matsumoto et al. [1984], Muchotrzeb and Czerny [1986], Abramowicz and Kato [1989]). The application of such techniques to our astrophysical model may lead to new perspectives and insights. Classification of critical points using this method for accretion around non-rotating black holes has been studied by Iram [2015]. We have tried to apply this analytical machinery to comprehend the critical behaviour of our solutions in terms of

*bifurcation diagrams* and to do an exhaustive study of various flow configurations around a rotating black hole (Tarafdar et al. [2017]). The formalism has been elaborated in the following section.

## 4.1 The general scheme

Once the location of a critical point is identified, a linearized study of the space gradients of the square of the advective velocities in the close neighbourhood of such a point may be carried out to develop a complete and rigorous mathematical scheme to understand whether a critical point is of saddle or centre type. Exact expressions will depend on the corresponding flow geometry and the equations of state.

Gradient of the square of advective velocity may be written as,

$$\frac{du^2}{dr} = f(r, u^2, c_s^2) \tag{4.1}$$

Parametrizing eqn.(4.1) with some variable $\tau$, we obtain

$$\frac{du^2}{d\tau} = f_1(r, u^2, c_s^2) \tag{4.2}$$

$$\frac{dr}{d\tau} = f_2(r, u^2, c_s^2). \tag{4.3}$$

$\tau$, which is a mathematical parameter, does not appear on the right hand sides of the equations. Therefore eqn.(4.2) and eqn.(4.3) represent our system as a set of first-order autonomous differential equations. Given that $r_c$ is a critical point, and $u_c$ and $c_{s_c}$ are the corresponding advective and acoustic velocities at $r_c$ respectively, we introduce arbitrarily small perturbations in $r$, $u$ and $c_s$ around their critical values,

$$r = r_c + \delta r, \tag{4.4}$$

$$u^2 = u_c^2 + \delta u^2, \tag{4.5}$$

$$c_s^2 = c_{s_c}^2 + \delta c_s^2. \tag{4.6}$$

At first we substitute eqn.(4.4), eqn.(4.5) and eqn.(4.6) in eqn.(4.2) and eqn.(4.3). Then using the critical point conditions and retaining only linear terms in $\delta u^2$ and $\delta r$, we obtain the following linearized forms,

$$\frac{d}{d\tau}(\delta u^2) = \mathcal{A}\delta u^2 + \mathcal{B}\delta r, \tag{4.7}$$

$$\frac{d}{d\tau}(\delta r) = \mathcal{C}\delta u^2 + \mathcal{D}\delta r. \tag{4.8}$$

Eqn.(4.7) and eqn.(4.8) can be written together in matrix notation as

$$\frac{d}{d\tau}\mathbf{y} = \mathbf{A}\mathbf{y}, \tag{4.9}$$

where $\mathbf{y} = \begin{pmatrix} \delta u^2 \\ \delta r \end{pmatrix}$ and $\mathbf{A} = \begin{pmatrix} \mathcal{A} & \mathcal{B} \\ \mathcal{C} & \mathcal{D} \end{pmatrix}$.
Using trial solutions of the form $exp(\Omega\tau)$, where $\Omega$ are the eigenvalues calculated by solving

the characteristic equation of the co-efficient matrix $\mathbf{A}$ ($\Omega$, in this context, should not be confused with angular velocity of the flow in eqn.(2.15)), the product of the eigenvalues of the system can be written as

$$\Omega_1\Omega_2 = \mathcal{AD} - \mathcal{BC}. \tag{4.10}$$

Then we define a quantity

$$\Omega^2 = -\Omega_1\Omega_2, \tag{4.11}$$

which is an exclusive function of $r_c$, $u_c^2$ and $c_{s_c}^2$. Since critical points and critical velocities are already known to us from previous calculations, the numerical value of $\Omega^2$ can be calculated easily. One can readily infer from the theory of linear stability analysis that $\Omega^2 > 0$ would correspond to a saddle-type critical point, and $\Omega^2 < 0$ would correspond to a centre-type critical point.

This is an elegant method for the qualitative visualisation of the dependence of transonicity on accretion parameters. Graphs depicting the variation of $\Omega^2$ with the parameters provide not only a visual representation of mono- critical to multi-critical transitions (*bifurcation diagrams*), but also give information regarding the nature of the respective fixed points. However, global understanding of the flow topology can only be achieved from the stationary integral solutions required to be obtained numerically.

Thus, stationary axisymmetric accretion in the Kerr metric can be described by a set of first order autonomous differential equations. Application of the above formalism to the system of equations reveals the nature of the critical points. Details of such analysis for various flow configurations have been presented in the following sections.

## 4.2 Polytropic flow

### 4.2.1 Discs with constant height

Using eqn.(3.4) and eqn.(3.5), the gradients of square of the sound speed and advective velocity can be written as,

$$\frac{dc_s^2}{dr} = (\gamma - 1 - c_s^2)\left[\frac{-1}{2(1-u^2)}\frac{du^2}{dr} - \frac{f'}{2f}\right] \tag{4.12}$$

$$\frac{du^2}{dr} = \frac{2\left[\frac{r-1}{\Delta}c_s^2 - \frac{f'}{2f}\right]}{\frac{1}{u^2}\left(\frac{1}{1-u^2}\right)(u^2 - c_s^2)} \tag{4.13}$$

The expression for $\frac{du^2}{dr}$ can be decomposed into two parameterized equations –

$$\frac{du^2}{d\tau} = 2\left[\frac{r-1}{\Delta}c_s^2 - \frac{f'}{2f}\right] \tag{4.14}$$

$$\frac{dr}{d\tau} = \frac{1}{u^2}\left(\frac{1}{1-u^2}\right)(u^2 - c_s^2). \tag{4.15}$$

$\tau$ does not explicitly appear on the right hand sides and hence, the above equations represent a first-order autonomous set of differential equations. Perturbation prescription around the fixed points is given by,

$$u^2 = u_c^2 + \delta u^2 \tag{4.16}$$

$$c_s^2 = {c_{s_c}}^2 + \delta c_s^2 \tag{4.17}$$

$$r = r_c + \delta r. \tag{4.18}$$

Substituting eqn.(4.16–4.18) in eqn.(4.14) and eqn.(4.15), one can derive a set of two autonomous first-order linear differential equations in the $\delta r - \delta u^2$ plane. $\delta c_s^2$ is expressed in terms of $\delta r$ and $\delta u^2$ as,

$$\frac{\delta c_s^2}{{c_{s_c}}^2} = (\gamma - 1 - {c_{s_c}}^2)\left[\frac{-1}{2u_c^2(1-u_c^2)}\delta u^2 - \frac{r_c - 1}{\Delta_c}\delta r\right]. \tag{4.19}$$

This form of $\delta c_s^2$ has been derived using the modified form (in terms of $u^2$ instead of $u$) of the mass accretion rate (eqn.(3.2)) and its corresponding expression for the entropy accretion rate (eqn.(3.3)). Through this procedure, a set of coupled linear equations in $\delta r$ and $\delta u^2$ will be obtained as

$$\frac{d}{d\tau}(\delta u^2) = \mathcal{A}_{CH}\delta u^2 + \mathcal{B}_{CH}\delta r \tag{4.20}$$

$$\frac{d}{d\tau}(\delta r) = \mathcal{C}_{CH}\delta u^2 + \mathcal{D}_{CH}\delta r \tag{4.21}$$

where,

$$\mathcal{A}_{CH} = \frac{(1-r_c)(\gamma - 1 - c_{s_c}^2)}{\Delta_c(1-u_c^2)} \tag{4.22}$$

$$\mathcal{B}_{CH} = 2\left[\frac{c_{s_c}^2}{\Delta_c} - \frac{(r_c-1)^2 c_{s_c}^2}{\Delta_c^2}(\gamma + 1 - c_{s_c}^2) - \frac{f''}{2f} + \frac{1}{2}\left(\frac{f'}{f}\right)^2\right] \tag{4.23}$$

$$\mathcal{C}_{CH} = \left[1 + \frac{(\gamma - 1 - c_{s_c}^2)}{2(1-u_c^2)}\right]\frac{1}{u_c^2(1-u_c^2)} \tag{4.24}$$

$$\mathcal{D}_{CH} = -\mathcal{A}_{CH} \tag{4.25}$$

Writing eqn.(4.20) and eqn.(4.21) in matrix notation and using trial solutions of the form $\exp(\Omega\tau)$, the product of eigenvalues of the co-efficient matrix can be expressed as,

$$\Omega_{CH_1}\Omega_{CH_2} = \mathcal{A}_{CH}\mathcal{D}_{CH} - \mathcal{B}_{CH}\mathcal{C}_{CH} \tag{4.26}$$

Consequently, $\Omega^2$ is given by

$$\Omega_{CH}^2 = \mathcal{B}_{CH}\mathcal{C}_{CH} - \mathcal{A}_{CH}\mathcal{D}_{CH} \tag{4.27}$$

Once the critical points and critical velocities are obtained, it is straightforward to calculate the numerical value corresponding to the expression for $\Omega^2$. It has been observed that the single critical point solutions are always of saddle type. This is obvious, otherwise monotransonic solutions would not exist. It is also observed that for multi-critical flow, the middle critical point is of centre type and the inner and the outer critical points are of saddle type. This will be explicitly shown in the subsequent sections.

### 4.2.2 Discs with quasi-spherical geometry

Using eqn.(3.11) and eqn.(3.12), the gradients of square of the sound speed and the advective velocity can be written as,

$$\frac{dc_s^2}{dr} = (\gamma - 1 - c_s^2)\left[\frac{-1}{2(1-u^2)}\frac{du^2}{dr} - \frac{f'}{2f}\right] \tag{4.28}$$

$$\frac{du^2}{dr} = \frac{2\left[\frac{(2r^2-3r+a^2)}{\Delta r}c_s^2 - \frac{f'}{2f}\right]}{\frac{1}{u^2}\left(\frac{1}{1-u^2}\right)(u^2-c_s^2)}. \tag{4.29}$$

The parameterized form of eqn.(4.29) is given by,

$$\frac{du^2}{d\tau} = 2\left[\frac{(2r^2-3r+a^2)}{\Delta r}c_s^2 - \frac{f'}{2f}\right] \tag{4.30}$$

$$\frac{dr}{d\tau} = \frac{u^2-c_s^2}{u^2(1-u^2)} \tag{4.31}$$

Eqn.(4.30) and eqn.(4.31) are expanded using the perturbation scheme in eqns.(4.16–4.18). Using modified forms of the eqn.(3.9) and eqn.(3.10), $\delta c_s^2$ is derived as

$$\frac{\delta c_s^2}{c_{s_c}^2} = (\gamma - 1 - c_{s_c}^2)\left[-\frac{1}{2u_c^2(1-u_c^2)}\delta u^2 - \frac{(2r_c^2-3r_c+a^2)}{\Delta_c r_c}\delta r\right]. \tag{4.32}$$

Thus, the coupled linear equations in $\delta r$ and $\delta u^2$ are given by,

$$\frac{d}{d\tau}(\delta u^2) = \mathcal{A}_{CF}\delta u^2 + \mathcal{B}_{CF}\delta r \tag{4.33}$$

$$\frac{d}{d\tau}(\delta r) = \mathcal{C}_{CF}\delta u^2 + \mathcal{D}_{CF}\delta r \tag{4.34}$$

where,

$$\mathcal{A}_{CF} = -\frac{(2r_c^2-3r_c+a^2)(\gamma-1-c_{s_c}^2)}{\Delta_c r_c(1-u_c^2)} \tag{4.35}$$

$$\mathcal{B}_{CF} = \frac{2(4r_c-3)c_{s_c}^2}{\Delta_c r_c} - \frac{f''}{f} + \left(\frac{f'}{f}\right)^2 - \frac{2c_{s_c}^2}{\Delta_c^2 r_c^2}(2r_c^2-3r_c+a^2)$$
$$\left[(3r_c^2-4r_c+a^2) + (\gamma-1-c_{s_c}^2)(2r_c^2-3r_c+a^2)\right] \tag{4.36}$$

$$\mathcal{C}_{CF} = \left[1 + \frac{(\gamma-1-c_{s_c}^2)}{2(1-u_c^2)}\right]\frac{1}{u_c^2(1-u_c^2)} \tag{4.37}$$

$$\mathcal{D}_{CF} = -\mathcal{A}_{CF}. \tag{4.38}$$

As discussed in the previous section, the expression for $\Omega^2$ in this case is given by

$$\Omega_{CF}^2 = -\Omega_{CF_1}\Omega_{CF_2} = \mathcal{B}_{CF}\mathcal{C}_{CF} - \mathcal{A}_{CF}\mathcal{D}_{CF} \tag{4.39}$$

### 4.2.3 Flow in hydrostatic equilibrium along the vertical direction

Using eqn.(3.19) and eqn.(3.20), the gradient of square of acoustic and advective velocities can be written as,

$$\frac{du^2}{dr} = \frac{\beta^2 c_s^2 \left[\frac{F_1'}{F_1} - \frac{1}{F}\frac{\partial F}{\partial r}\right] - \frac{f'}{f}}{\left(1 - \frac{\beta^2 c_s^2}{u^2}\right)\frac{1}{(1-u^2)} + \frac{\beta^2 c_s^2}{F}\left(\frac{\partial F}{\partial u^2}\right)} \tag{4.40}$$

where $F_1 = \Delta r^4$ and $\beta = \sqrt{\frac{2}{\gamma+1}}$.
The parameterized form of eqn.(4.40) is given by

$$\frac{du^2}{d\tau} = \beta^2 c_s^2 \left[\frac{F_1'}{F_1} - \frac{1}{F}\frac{\partial F}{\partial r}\right] - \frac{f'}{f} \tag{4.41}$$

$$\frac{dr}{d\tau} = \left(1 - \frac{\beta^2 c_s^2}{u^2}\right)\frac{1}{(1-u^2)} + \frac{\beta^2 c_s^2}{F}\left(\frac{\partial F}{\partial u^2}\right). \tag{4.42}$$

Using the perturbation scheme of eqns.(4.16–4.18) and modified forms of eqns.(3.16) and (3.18) we obtain,

$$\frac{\delta c_s^2}{c_{s_c}^2} = \mathcal{A}\delta u^2 + \mathcal{B}\delta r \tag{4.43}$$

where,

$$\mathcal{A} = -\frac{\gamma-1-c_{sc}^2}{\gamma+1}\left[\frac{1}{u_c^2(1-u_c^2)} - \frac{1}{F_c}\left(\frac{\partial F}{\partial u^2}\right)\Big|_c\right], \tag{4.44}$$

$$\mathcal{B} = -\frac{\gamma-1-c_{sc}^2}{\gamma+1}\left[\frac{F_1'(r_c)}{F_1(r_c)} - \frac{1}{F_c}\left(\frac{\partial F}{\partial r}\right)\Big|_c\right], \tag{4.45}$$

and the coupled linear equations in $\delta r$ and $\delta u^2$ given by,

$$\begin{aligned}
\frac{\mathrm{d}}{\mathrm{d}\tau}(\delta u^2) &= \beta^2 c_{\mathrm{sc}}^2\left[\frac{\mathcal{A}F_1'}{F_1} - \frac{\mathcal{A}\mathcal{C}}{F} + \frac{\mathcal{C}\mathcal{D}}{F^2} - \frac{\Delta_3}{F}\right]\delta u^2 \\
&\quad + \left[\frac{\beta^2 c_{\mathrm{sc}}^2 F_1'}{F_1}\left\{\mathcal{B} + \left(\frac{F_1''}{F_1'} - \frac{F_1'}{F_1}\right)\right\}\right. \\
&\quad - \frac{f'}{f}\left(\frac{f''}{f'} - \frac{f'}{f}\right) \\
&\quad \left. - \frac{\beta^2 c_{\mathrm{sc}}^2 \mathcal{C}}{F}\left(\mathcal{B} - \frac{\mathcal{C}}{F} + \frac{\Delta_4}{\mathcal{C}}\right)\right]\delta r
\end{aligned} \tag{4.46}$$

$$\begin{aligned}
\frac{\mathrm{d}}{\mathrm{d}\tau}(\delta r) &= \left[\frac{1}{\left(1-u_{\mathrm{c}}^2\right)^2} - \frac{\beta^2 c_{\mathrm{sc}}^2}{u_{\mathrm{c}}^2\left(1-u_{\mathrm{c}}^2\right)}\left\{\mathcal{A} + \frac{2u_{\mathrm{c}}^2 - 1}{\left(1-u_{\mathrm{c}}^2\right)^2}\right\}\right. \\
&\quad \left. + \frac{\beta^2 c_{\mathrm{sc}}^2 \mathcal{D}}{F}\left(\mathcal{A} - \frac{\mathcal{D}}{F} + \frac{\Delta_1}{\mathcal{D}}\right)\right]\delta u^2 \\
&\quad + \left[-\frac{\beta^2 c_{\mathrm{sc}}^2 \mathcal{B}}{u_{\mathrm{c}}^2\left(1-u_{\mathrm{c}}^2\right)}\right. \\
&\quad \left. + \frac{\beta^2 c_{\mathrm{sc}}^2 \mathcal{D}}{F}\left(\mathcal{B} - \frac{\mathcal{C}}{F} + \frac{\Delta_2}{\mathcal{D}}\right)\right]\delta r
\end{aligned} \tag{4.47}$$

where,
$\mathcal{C} = \left(\frac{\partial F}{\partial r}\right)\Big|_c$, $\mathcal{D} = \left(\frac{\partial F}{\partial u^2}\right)\Big|_c$,

$\Delta_1 = \frac{\partial}{\partial u^2}\left(\frac{\partial F}{\partial u^2}\right)\Big|_c$, $\Delta_2 = \frac{\partial}{\partial r}\left(\frac{\partial F}{\partial u^2}\right)\Big|_c$, $\Delta_3 = \frac{\partial}{\partial u^2}\left(\frac{\partial F}{\partial r}\right)\Big|_c$, $\Delta_4 = \frac{\partial}{\partial r}\left(\frac{\partial F}{\partial r}\right)\Big|_c$.
Thus, $\Omega^2$ can be derived as,

$$\Omega^2_{VE} = -\Omega_{VE_1}\Omega_{VE_2} = \beta^4 c^4_{s_c}\chi^2 + \xi_1\xi_2 \tag{4.48}$$

where, $\chi = \left[\frac{F_1'\mathcal{A}}{F_1} - \frac{\mathcal{A}\mathcal{C}}{F} + \frac{\mathcal{C}\mathcal{D}}{F^2} - \frac{\Delta_3}{F}\right] = \left[\frac{\mathcal{B}}{u_c^2(1-u_c^2)} - \frac{\mathcal{B}\mathcal{D}}{F} + \frac{\mathcal{C}\mathcal{D}}{F^2} - \frac{\Delta_2}{F}\right]$,
$\xi_1 = \frac{\beta^2 c^2_{sc} F_1'}{F_1}\left[\mathcal{B} + \frac{F_1''}{F_1'} - \frac{F_1'}{F_1}\right] - \frac{f'}{f}\left[\frac{f''}{f'} - \frac{f'}{f}\right] - \frac{\beta^2 c^2_{sc}\mathcal{C}}{F}\left[\mathcal{B} - \frac{\mathcal{C}}{F} + \frac{\Delta_4}{\mathcal{C}}\right]$, and
$\xi_2 = \frac{1}{(1-u_c^2)^2} - \frac{\beta^2 c^2_{sc}}{u_c^2(1-u_c^2)}\left[\mathcal{A} + \frac{2u_c^2-1}{u_c^2(1-u_c^2)}\right] + \frac{\beta^2 c^2_{sc}\mathcal{D}}{F}\left[\mathcal{A} - \frac{\mathcal{D}}{F} + \frac{\Delta_1}{\mathcal{D}}\right]$.

### 4.2.4 Variation of $\Omega^2$ with accretion parameters - A comparative analysis

The expressions for $\Omega^2$ derived in the previous subsections for three different polytropic flow geometries are ultimately functions of the critical point $r_c$. Computation of $r_c$ using methods elaborated in chapter 2 enables us to calculate this new quantity and check its sign to determine whether the corresponding critical point is a saddle or centre. However, a comparative study of the trends of variation of $\Omega^2$ with the various acccretion parameters can also turn out to be quite informative in this context.

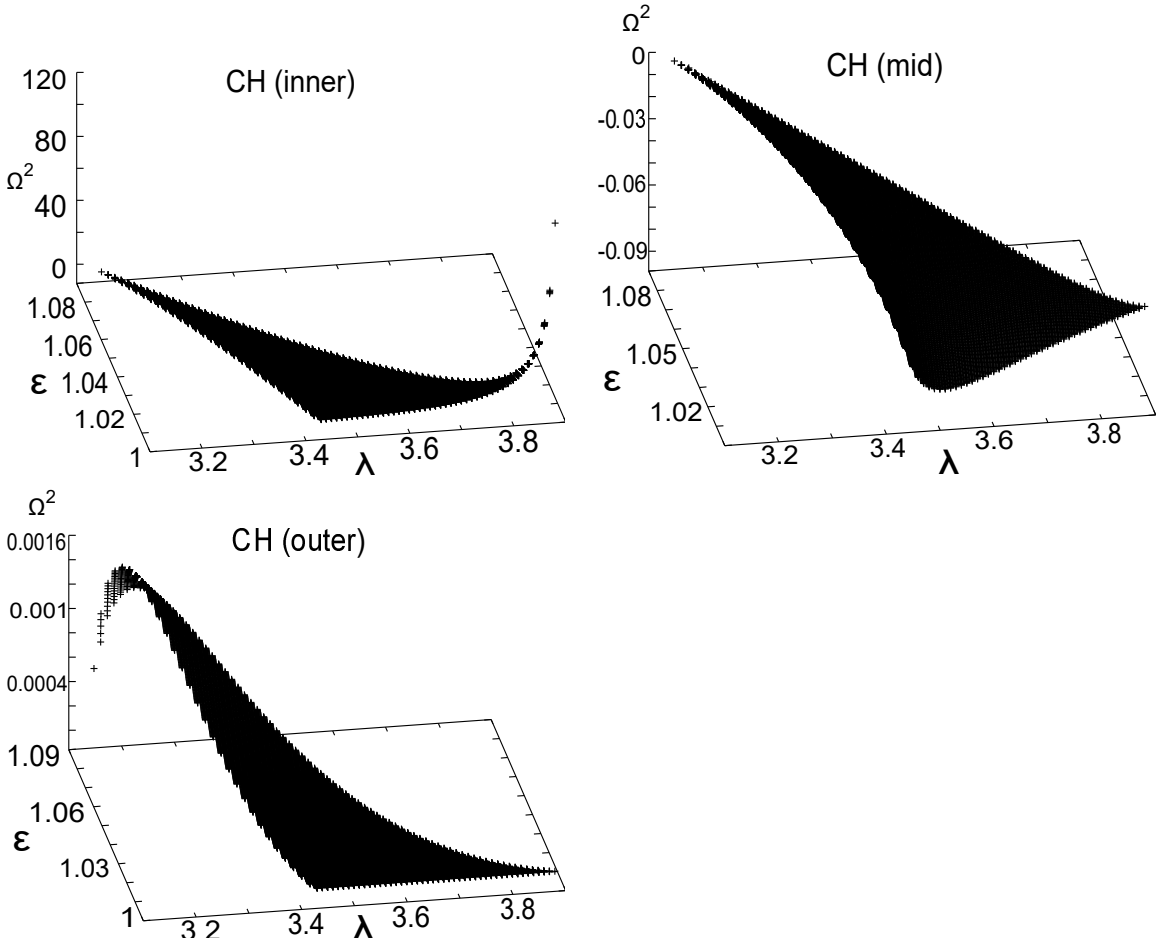


Figure 4.1: $\Omega^2$ vs. $[\mathcal{E} - \lambda]$ for constant height flow ($\gamma = 1.35$, $a = 0.1$).

Figure 4.1 consists of a panel of three different plots. All these diagrams depict the variation of $\Omega^2$ for constant height discs with the specific energy and specific angular

momentum of the flow. The first plot (left – upper row) shows the values of $\Omega^2$ for the inner critical points. The second (right – upper row) and third (left – lower row) plots correspond to the middle and outer critical points respectively. It is readily observed that the inner and outer critical points – which co-incide with the sonic points for polytropic constant height discs, as proved in the previous chapter – have positive values of $\Omega^2$ throughout the admissible parameter space, and hence are of saddle-type. Whereas, the middle critical point has negative values of $\Omega^2$ and therefore has to be a centre-type critical point through which, phase trajectories cannot pass. Thus, it is evident that physical flow can occur only through the outer and inner sonic points and not through the middle critical point. It is also observed that the values of $\Omega^2$ at the inner sonic points are higher by orders of magnitude than those at the outer sonic points. This definitely hints at a correlation between the quantity and the extent of the local space-time curvature around the respective critical points. Although a thorough treatment of this issue is beyond the scope of our present work, but our finding does point in a prospective direction for future investigations.

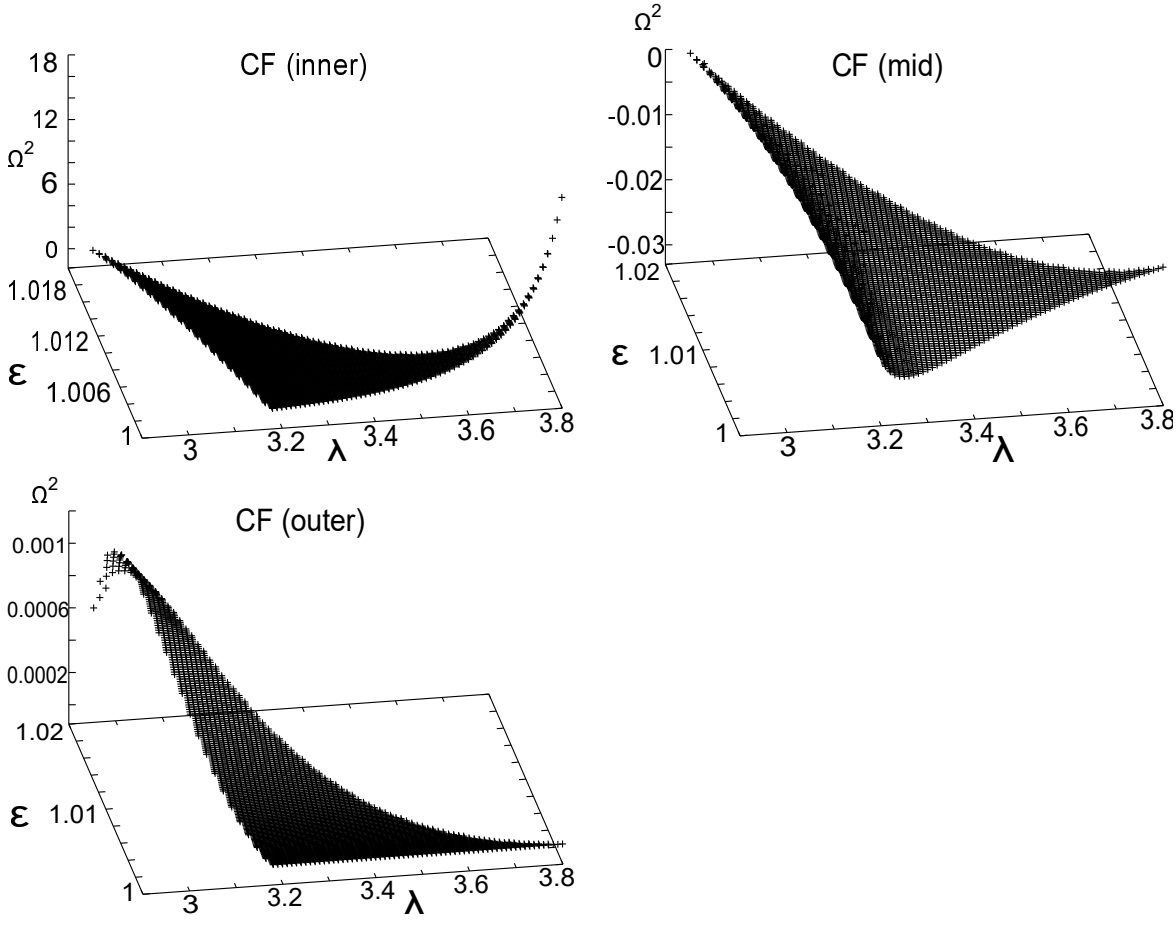


Figure 4.2: $\Omega^2$ vs. $[\mathcal{E} - \lambda]$ for quasi-spherical flow ($\gamma = 1.35$, $a = 0.1$).

Figure 4.2 depicts the variation of $\Omega^2$ with accretion parameters $[\mathcal{E} - \lambda]$ for flows with quasi-spherical geometry. Values of $\gamma$ and $a$ have been fixed at 1.35 and 0.1 respectively. The trends of variation are same as those that have been observed for accretion discs with a constant height. The inner and outer critical points – which are isomorphic with the sonic points for quasi-sperical flows as demonstrated in chapter 2 – are saddle-types, whereas the middle critical points are found to be centre-types. The only evident difference is in

terms of the magnitudes of $\Omega^2$ which are observed to be lower than the corresponding values for constant height discs. The apparent correlation between $\Omega^2$ and the strength of gravity at the critical points can be seen in this case as well.

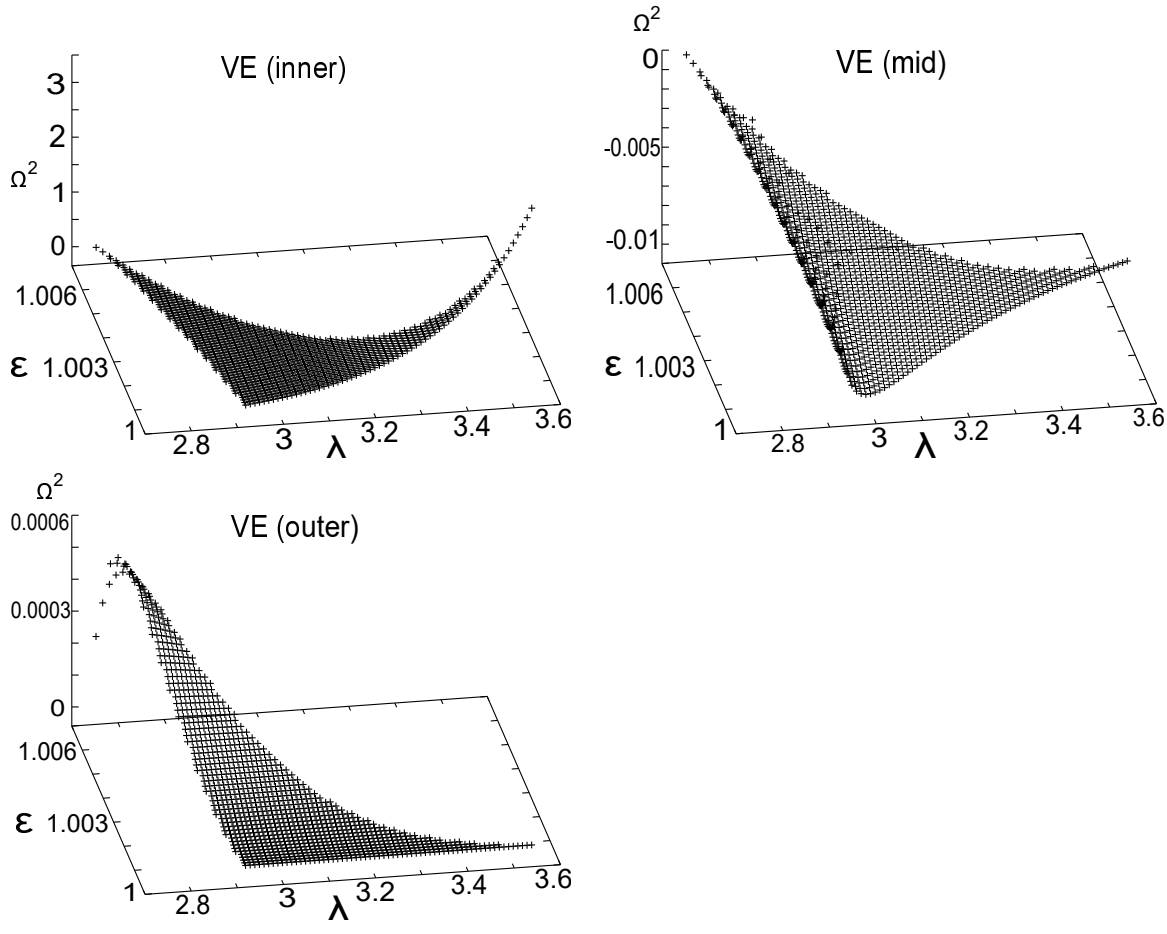


Figure 4.3: $\Omega^2$ vs. $[\mathcal{E} - \lambda]$ for flow in vertical hydrostatic equilibrium ($\gamma = 1.35$, $a = 0.1$).

Figure 4.3 shows the variation of $\Omega^2$ with $[\mathcal{E} - \lambda]$ for discs in hydrostatic equilibrium in the vertical direction. Trends of variation remain same as for the previous two flow geometries, except for the magnitudes which may be observed to have decreased further in this case. The inner and outer critical points – which are not the same as sonic points for VE discs – are saddle-type, whereas the middle critical point is of centre-type nature. Values at the inner critical points are much higher than those at the outer critical points, as have been observed in all the preceding cases.

Figure 4.4 presents an elegant tool for visualising the evolution of critical points with the system parameters. It can be immediately recognised as a *bifurcation diagram* in the terminology of dynamical systems theory. However, there is an essential difference. This improvised bifurcation diagram not only depicts the creation and annihilation of critical points with the variation of parameters in a system, but it also contains information about the nature of the respective critical points. In a qualitative sense, it gives us the dynamical picture of the phase trajectories as they evolve with a changing system parameter. The parameter space diagrams reported in the previous chapter could tell us about the number of critical points in a particular region of the parameter space. But the bifurcation diagram presented in figure 4.4 also helps us to understand the physical reasons behind

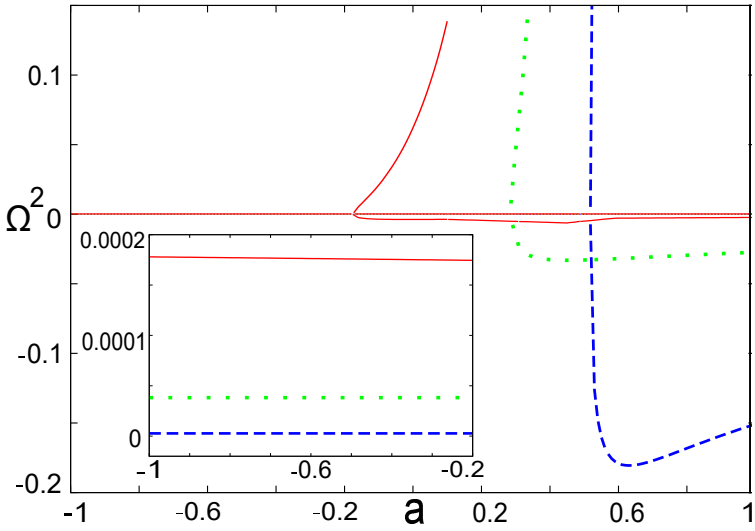


Figure 4.4: Comparision of $\Omega^2$ vs. $a$ for constant height flow (blue dashed lines), quasi-spherical flow (green dotted lines) and flow in vertical hydrostatic equilibrium (red solid lines)($\mathcal{E} = 1.003$, $\lambda = 3.0$, $\gamma = 1.35$). Inset shows a magnified view of the common monotransonic region for the three flow geometries.

the number of critical points in a parameter space region, as will be demonstrated for this particular plot.

We have depicted the dependence of transonicity on the entire physical range of black hole spin including retrograde flows (flows counter-rotating with the the central black hole) for a given set of the other parameters ($\mathcal{E} = 1.003$, $\lambda = 3.0$, $\gamma = 1.35$). The blue dashed lines, the green dotted lines and the red solid lines represent discs with constant height, quasi- spherical geometry and vertical hydrostatic equilibrium respectively. The magnified image in the inset shows that for the given values of $[\mathcal{E}, \lambda, \gamma]$, only one critical point exists almost over the entire range of negative Kerr parameter. The single positive values of $\Omega^2$ establish that the sole critical point is a saddle and hence we have a mono-transonic flow through the critical point. The extremely low magnitudes of the values indicate that the saddle-type critical points lie far away from the event horizon. As the system proceeds towards higher black hole spin, the single values bifurcate into three distinct values. This is the value of $a$ where, for the given values of the other parameters, the flow undergoes a transition from mono-transonic to multi-transonic. Two among the three branches have positive values of $\Omega^2$ pointing to saddle-type critical points, and the third branch lying below the zero-line corresponds to a centre-type middle critical point. The upper positive branch of the trident exhibits a sharp rise indicating that it is the inner critical point, possibly rushing towards the horizon with increasing $a$, until it enters the horizon not to be seen anymore on the diagram. The lower positive branch (middle branch of the trident) is a continuation of the monotransonic branch denoting the outer critical point. Hence if one can visualise the whole process in the phase space of the system, it will be realised that while the black hole spin consistently evolves from extremally retrograde to extremally prograde, at a particular value of spin, the a saddle-centre pair of critical points appears out of nowhere between the outer critical point and the horizon. Then the inner saddle-type critical point approaches the horizon and is ultimately lost into it, leaving us with two critical points, out of which physical flow can occur only through the outer saddle-type point. In other words, the flow reverts back to its mono-transonic state

and remains so until the black hole reaches its maximum possible co-rotational spin.

This picture is extremely useful as it reveals the complete life-cycle of the phase trajectories over full ranges of the system parameters, without requiring us to undertake the arduous task of constructing the numerically accurate phase diagrams through integration for a specific set of $[\mathcal{E}, \lambda, a, \gamma]$. The diagram also enables a comparison between the different disc geometries. It is evident that for polytropic flows, the bifurcation from mono-transonic to multi-transonic state occurs at lower values of black hole spin for discs in vertical hydrostatic equilibrium, whereas constant height discs undergo such bifurcations at higher values of $a$. Bifurcation in quasi-spherical discs is intermediate between the other two configurations.

In the next section, we present the derivation of expressions of $\Omega^2$ and its variation with the accretion parameters for various isothermal flow geometries.

## 4.3 Isothermal flow

Using the same techniques elaborated in the previous section, derivation of the product of eigenvalues for the first-order autonomous linear differential equations corresponding to isothermal accretion have been demonstrated for the three disc geometries in the following sub-sections.

### 4.3.1 Constant Height Flow

Using eqn.(3.28), the gradient of square of the advective velocity $u$ is obtained as,

$$\frac{du^2}{dr} = \frac{(1-c_s^2)\frac{\Delta'}{\Delta} - \frac{B'}{B}}{\frac{c_s^2}{u^2} - \frac{1-c_s^2}{1-u^2}}. \tag{4.49}$$

Parameterizing eqn.(4.49) using a mathematical parameter $\tau$, we get

$$\frac{du^2}{d\tau} = (1-c_s^2)\frac{\Delta'}{\Delta} - \frac{B'}{B} \tag{4.50}$$

$$\frac{dr}{d\tau} = \frac{c_s^2}{u^2} - \frac{1-c_s^2}{1-u^2} \tag{4.51}$$

Substituting the perturbation relations given by eqn.(4.16) and eqn.(4.18) (since $\delta c_s^2 = 0$) in eqn.(4.50) and eqn.(4.51), a first-order autonomous set of equations in the $\delta r$–$\delta u^2$ plane is derived as,

$$\frac{d}{d\tau}(\delta u^2) = \mathcal{B}_{CH}^{iso}\delta r \tag{4.52}$$

$$\frac{d}{d\tau}(\delta r) = \mathcal{C}_{CH}^{iso}\delta u^2 \tag{4.53}$$

such that,

$$\mathcal{B}_{CH}^{iso} = \frac{f_c^{'}}{f_c}\frac{a^2-1-(r_c-1)^2}{\Delta(r_c-1)} - \frac{f_c^{''}}{f_c} + \left(\frac{f_c^{'}}{f_c}\right)^2 \tag{4.54}$$

$$\mathcal{C}_{CH}^{iso} = \frac{1}{u_c^2(1-u_c^2)}, \tag{4.55}$$

where $f = \Delta/B$. Therefore, the expression for $\Omega^2$ for a constant height isothermal disc is given by,

$$\Omega^{iso}_{CH}{}^2 = -\Omega^{iso}_{CH_1}\Omega^{iso}_{CH_2} = \mathcal{B}^{iso}_{CH}\mathcal{C}^{iso}_{CH}. \tag{4.56}$$

Note that the constancy of acoustic velocity makes the whole calculation a lot simpler for isothermal flows.

### 4.3.2 Discs with quasi-spherical geometry

Using eqn.(3.34), the gradient of square of the advective velocity $u$ can be written as,

$$\frac{du^2}{dr} = \frac{(1-c_s^2)\frac{\Delta'}{\Delta} - \frac{B'}{B} - \frac{2c_s^2}{r}}{\frac{c_s^2}{u^2} - \frac{1-c_s^2}{1-u^2}} \tag{4.57}$$

Parameterizing eqn.(4.57) with $\tau$, we get

$$\frac{du^2}{d\tau} = (1-c_s^2)\frac{\Delta'}{\Delta} - \frac{B'}{B} - \frac{2c_s^2}{r} \tag{4.58}$$

$$\frac{dr}{d\tau} = \frac{c_s^2}{u^2} - \frac{1-c_s^2}{1-u^2} \tag{4.59}$$

Substituting the perturbation scheme from eqn.(4.16) and eqn.(4.18) in eqn.(4.58) and eqn.(4.59), we obtain the following set of first order autonomous differential equations in the $\delta r - \delta u^2$ plane,

$$\frac{d}{d\tau}(\delta u^2) = \mathcal{B}\delta r \tag{4.60}$$

$$\frac{d}{d\tau}(\delta r) = \mathcal{C}\delta u^2 \tag{4.61}$$

where,

$$\begin{aligned}\mathcal{B}^{iso}_{CF} &= \frac{f_c^{'}}{f_c(2r_c^2-3r_c+a^2)}(-\frac{\Delta_c}{r_c} + \frac{r_c}{\Delta_c}(a^2-1-(r_c-1)^2)) \\ &\quad -\frac{f_c^{''}}{f_c} + \left(\frac{f_c^{'}}{f_c}\right)^2 \qquad (4.62)\\ \mathcal{C}^{iso}_{CF} &= \frac{1}{u_c^2(1-u_c^2)}. \qquad (4.63)\end{aligned}$$

Therefore, the expression of $\Omega^2$ for discs with quasi-spherical geometry can be derived as,

$$\Omega^{iso}_{CF}{}^2 = -\Omega^{iso}_{CF_1}\Omega^{iso}_{CF_2} = \mathcal{B}^{iso}_{CF}\mathcal{C}^{iso}_{CF}. \tag{4.64}$$

### 4.3.3 Flow in vertical hydrostatic equilibrium

Using eqn.(3.40), the gradient of square of the advective velocity $u$ is obtained as,

$$\frac{du^2}{dr} = \frac{2uc_s^2(\frac{\Delta'}{2\Delta} + \frac{2}{r} - (2\lambda^2 v_t - a^2)\frac{v_t P1}{4F}) - \frac{P1}{2}}{\frac{u}{1-u^2} - \frac{c_s^2}{u(1-u^2)}(1-(2\lambda^2 v_t - a^2)\frac{u^2 v_t}{2F})} \tag{4.65}$$

where $\Delta$, $P1$ and $F$ have their usual meanings.

Parameterizing eqn.(4.65) with $\tau$, we get

$$\frac{du^2}{d\tau} = 2uc_s^2(\frac{\Delta'}{2\Delta} + \frac{2}{r} - (2\lambda^2 v_t - a^2)\frac{v_t P1}{4F}) - \frac{P1}{2} \tag{4.66}$$

$$\frac{dr}{d\tau} = \frac{u}{1-u^2} - \frac{c_s^2}{u(1-u^2)}(1 - (2\lambda^2 v_t - a^2)\frac{u^2 v_t}{2F}). \tag{4.67}$$

Substituting the perturbation scheme provided in eqn.(4.16) and eqn.(4.18), we derive

$$\frac{d}{d\tau}(\delta u^2) = \mathcal{A}_{VE}^{iso}\delta u^2 + \mathcal{B}_{VE}^{iso}\delta r \tag{4.68}$$

$$\frac{d}{d\tau}(\delta r) = \mathcal{C}_{VE}^{iso}\delta u^2 + \mathcal{D}_{VE}^{iso}\delta r, \tag{4.69}$$

such that,

$$\mathcal{A}_{VE}^{iso} = \frac{{c_{sc}}^2}{g_2}\left(\frac{(2\lambda^2 v_t - a^2){f_c}' {g_2}'}{2g_2\sqrt{(1-u_c^2)f_c}} - \delta_3\right) \tag{4.70}$$

$$\begin{aligned}\mathcal{B}_{VE}^{iso} = {c_{s_c}}^2\Bigg(&\frac{2}{\Delta_c} - \frac{4}{r_c^2} - \frac{4(r_c-1)^2}{\Delta_c^2} - \frac{\delta_4}{g_2} \\ &+ \left(\frac{(2\lambda^2 v_t - a^2){f_c}'}{2g_2\sqrt{(1-u_c^2)f_c}}\right)^2\Bigg) \\ &- \frac{f_c''}{f_c} + \left(\frac{f_c'}{f_c}\right)^2\end{aligned} \tag{4.71}$$

$$\mathcal{C}_{VE}^{iso} = \frac{u_c^4 - 2{c_s}_c^2 u_c^2 + {c_s}_c^2}{u_c^4(1-u_c^2)^2} + \frac{{c_s}_c^2\delta_1}{g_2} - \frac{{c_s}_c^2 {g_2}'^2}{g_2^2} \tag{4.72}$$

$$\mathcal{D}_{VE}^{iso} = -\mathcal{A}_{VE}^{iso} \tag{4.73}$$

where,
$g_2 = (\lambda v_t)^2 - v_t a^2 + a^2$,
$\delta_1 = \frac{2\lambda^2 f}{(1-u_c^2)^3} - \frac{3a^2}{4}\sqrt{\frac{f}{(1-u_c^2)^5}}$,
$\delta_3 = \frac{\lambda^2 f'}{(1-u_c^2)^2} - \frac{a^2 f'}{4\sqrt{f(1-u_c^2)^3}}$,
$\delta_4 = \frac{\lambda^2 f''}{1-u_c^2} - \frac{a^2}{4\sqrt{1-u_c^2}}\frac{2ff''-f'^2}{f^{\frac{3}{2}}}$.

Therefore, the expression of $\Omega^2$ for isothermal discs in vertical hydrostatic equilibrium can be written as,

$${\Omega_{VE}^{iso}}^2 = -\Omega_{VE_1}^{iso}\Omega_{VE_2}^{iso} = \mathcal{B}_{VE}^{iso}\mathcal{C}_{VE}^{iso} - \mathcal{A}_{VE}^{iso}\mathcal{D}_{VE}^{iso}. \tag{4.74}$$

### 4.3.4 Variation of $\Omega^2$ with accretion parameters – A comparative analysis

We follow the same line of arguments presented in subsection 4.2.4 to carry out a comparative analysis of the variation of $\Omega^2$ with the accretion parameters $[T, \lambda, a]$ for isothermal flow around rotating black holes.

Figure 4.5 shows the dependence of $\Omega^2$ for discs with constant height on the $[T, \lambda]$ parameter space. The value of the black hole spin parameter has been fixed at $a = 0.1$.

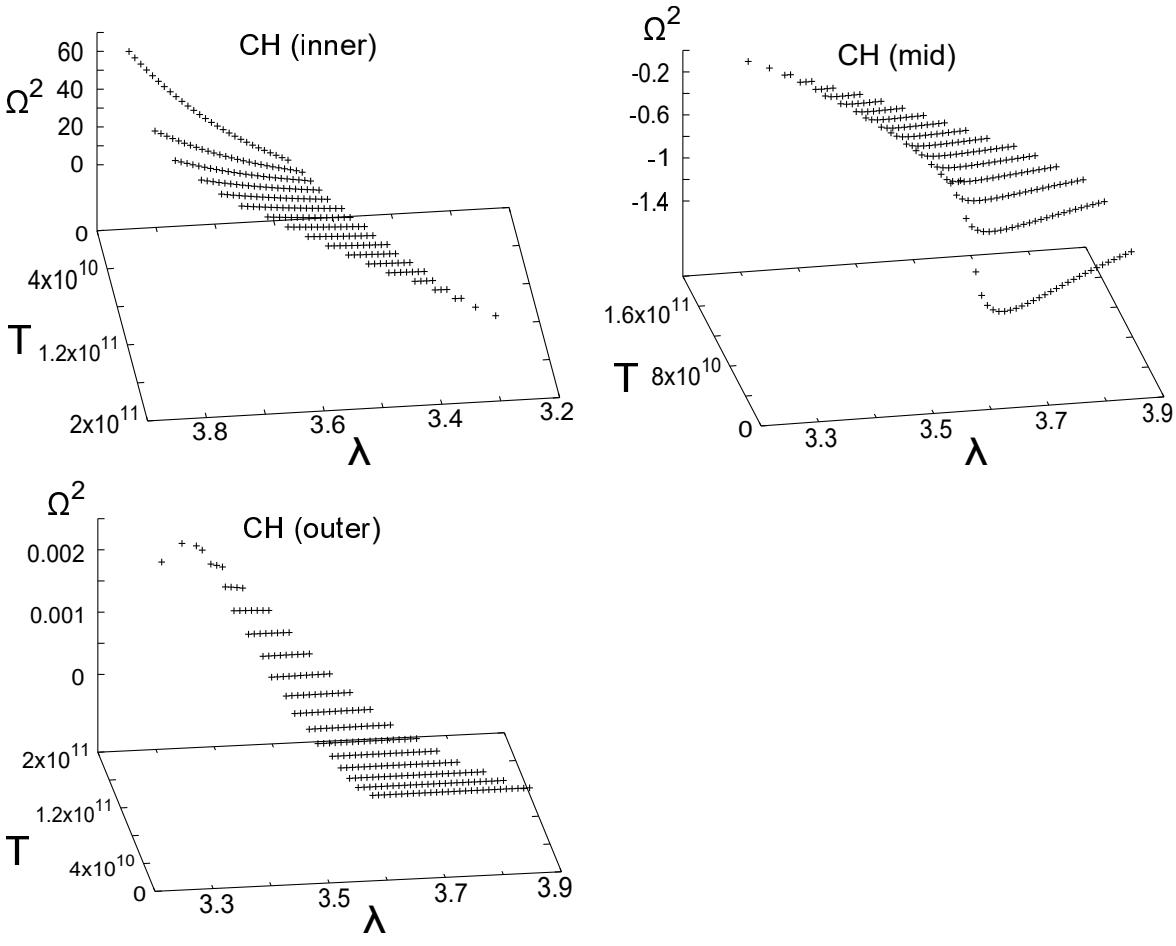


Figure 4.5: $\Omega^2$ vs. $[T - \lambda]$ for constant height flow ($a = 0.1$).

The choice of $a$ may seem adhoc to the reader at first. But there are reasons behind it. In fact, we are compelled to choose from a specific range of the fixed parameter due to non-availability of multi- transonic stationary flow solutions over a common region of the other parameters for all three disc geometries. And in order to draw physically meaningful inferences from the comparision of flow geometries, one needs to select values of the fixed parameters such that there is a considerable overlap of the other available parameters for the required kind of flow solution. After carefully studying the corresponding parameter space diagrams obtained in the previous chapter, we fix only upon such parameter values which allow for the scope to undertake a comparative analysis.

We observe from figure 4.5 that in accordance with polytropic accretion, multi- transonic isothermal flows are also characterised by two saddle-type critical points (inner and outer) and a centre-type middle critical point. The trend of variation is similar to the corresponding polytropic configuration, except for the absolute magnitude of $\Omega^2$ which is found to be lower in the isothermal case. The relative magnitudes of the quantity for inner and outer critical points – which are the same as inner and outer sonic points – are once again observed to be hinting at a correlation with the curvature of space-time at the critical point $r_c$.

Figure 4.6 depicts the variation of $\Omega^2$ with $[T, \lambda]$ for discs with quasi-spherical geometry. With two saddle-type critical points (co-incident with the sonic points) and one centre-

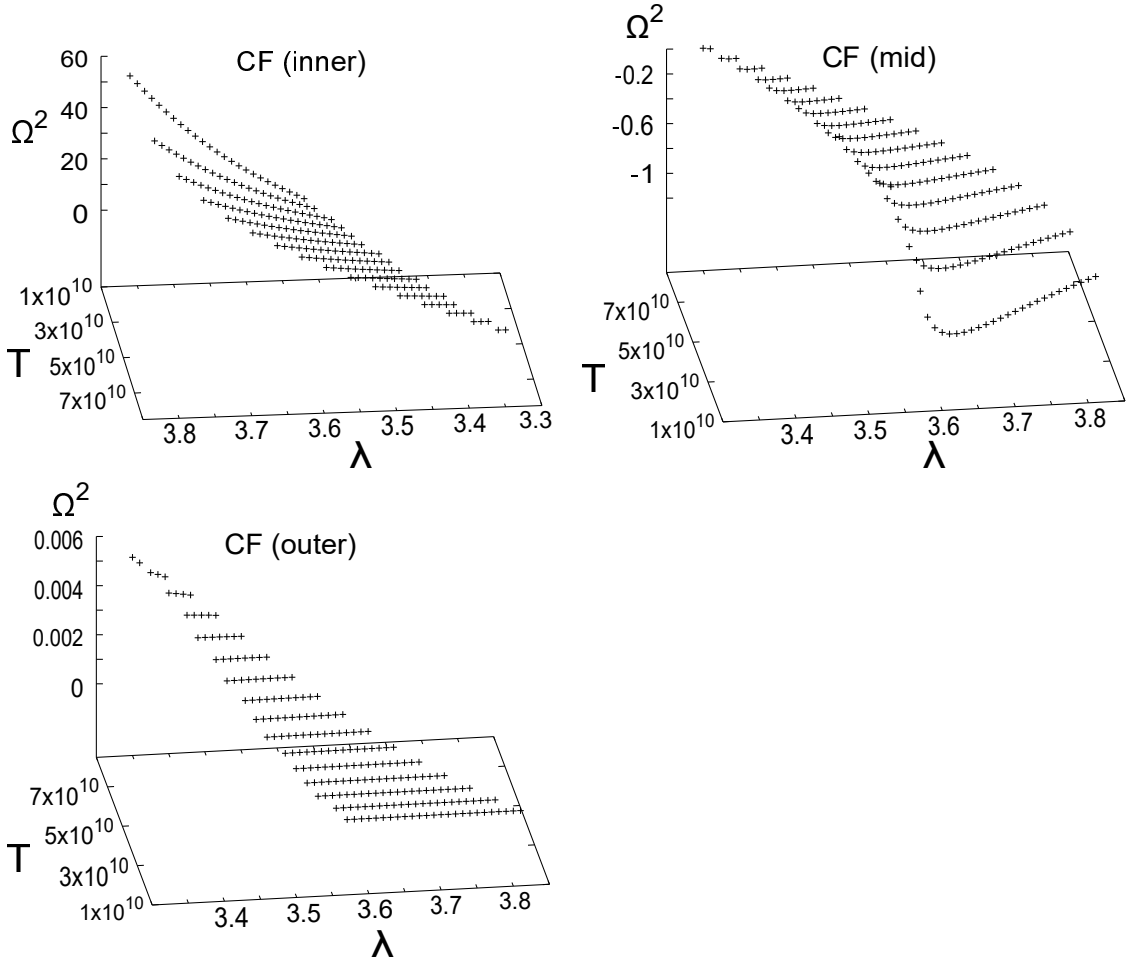


Figure 4.6: $\Omega^2$ vs. $[T - \lambda]$ for quasi-spherical flow ($a = 0.1$).

type middle critical point, the plots look almost indistinguishable from figure 4.5. The values of $\Omega^2$ seem to be very close, with the only difference being the temperature of the flow which is slightly lower than that for the constant height discs.

Variation of $\Omega^2$ corresponding to all the three critical points with $[T, \lambda]$ for discs in vertical hydrostatic equilibrium has been presented in figure 4.7. While very little difference is observed in the values for the saddle-type outer critical point and the centre- type middle critical point, the saddle-type inner critical point exhibits values of $\Omega^2$ which are much less than those for the CH and CF discs. The strength of gravity is higher at the inner critical points. And the variation of $\Omega^2$ also appears to respond accordingly to the sharp increase in space-time curvature near the event horizon.

Figure 4.8 is the bifurcation diagram depicting the values of $\Omega^2$ with a changing Kerr parameter for CH, CF and VE accretion discs. The values of flow temperature and flow angular momentum have been fixed at $T = 10^{10}$ Kelvin and $\lambda = 3.6$ respectively. Monotransonic flow through the outer saddle point is observed throughout the retrograde region. Following the bifurcation into three critical points (which do not co-incide with the sonic points for isothermal VE discs), the inner saddle point is driven towards the horizon with increasing $a$. As the inner critical point is lost inside the event horizon, we are left with the centre-type middle critical point (other partner of the saddle-centre pair created at bifurcation) which does not accommodate for any phase trajectories, and the outer saddle-type

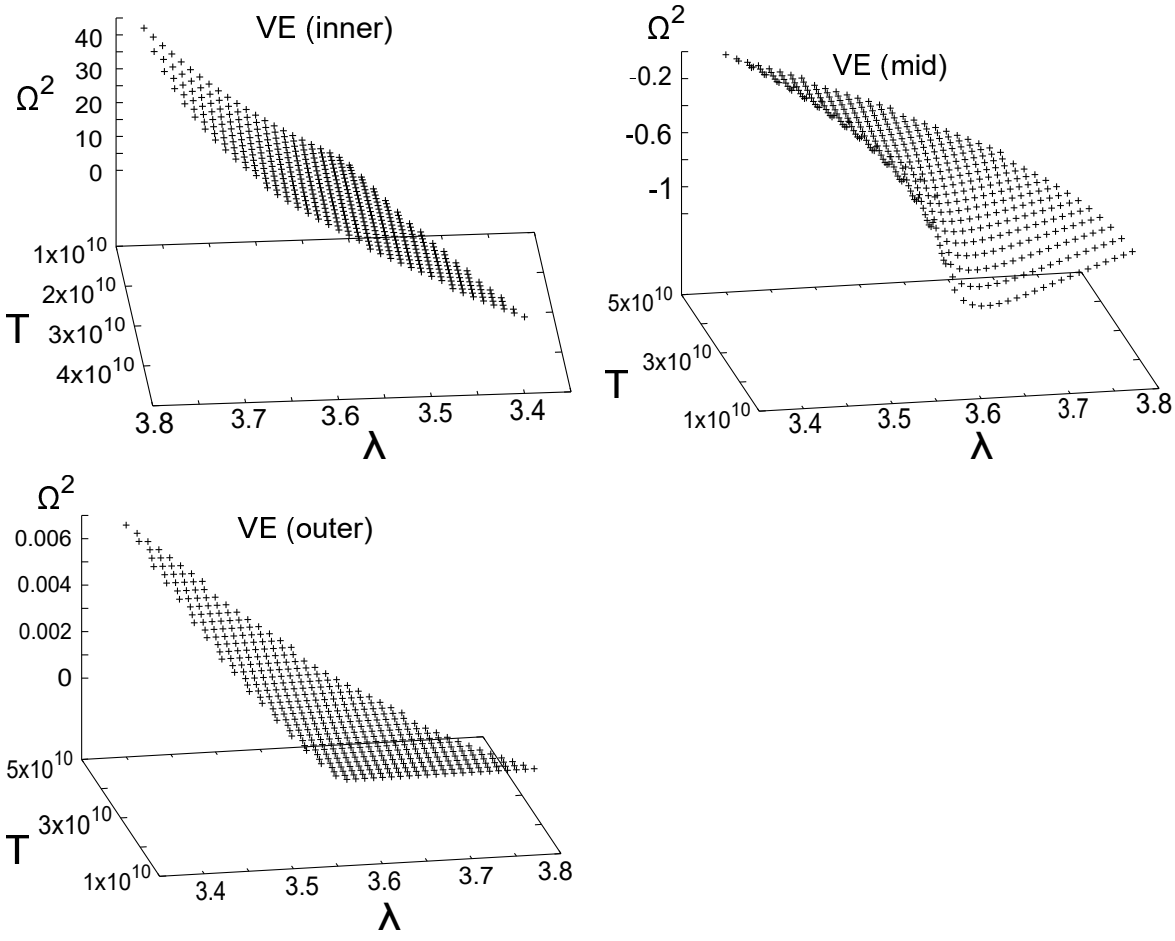


Figure 4.7: $\Omega^2$ vs. $[T - \lambda]$ for flow in vertical hydrostatic equilibrium ($a = 0.1$).

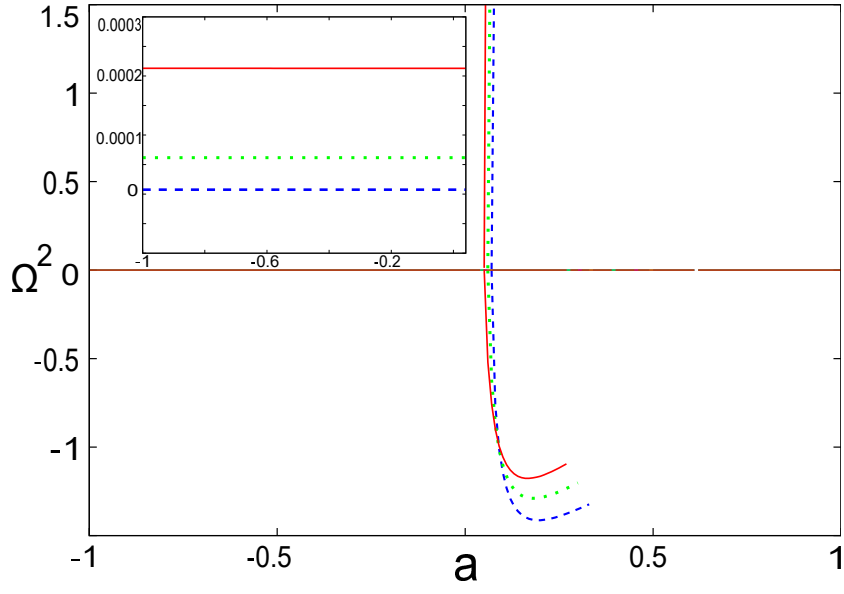


Figure 4.8: Comparision of $\Omega^2$ vs. $a$ for constant height flow (blue dashed lines), quasi-spherical flow (green dotted lines) and flow in vertical hydrostatic equilibrium (red solid lines)($T = 10^{10}$ K, $\lambda = 3.6$). Inset shows a magnified view of the common monotransonic region for the three flow geometries.

critical point through which accreting matter flows towards its ultimate mono-transonic fall into the event horizon.

A discontinuity is observed in the negative branch of $\Omega^2$ after a certain value of $a$ for each of the three different flow geometries. This is an indication of the fact that for the given set of $[T, \lambda]$, increasing the Kerr parameter beyond some value leads to disappearance of the centre-type middle critical point. This might occur due to penetration of the critical point into the horizon, or due to a gradual degeneration of the homoclinic orbit leading to its final separation into an upper mono-transonic accretion branch and a lower mono-transonic wind (or outflow) branch, or both. The bifurcation diagram does not contain sufficient information to confirm the actual reason for the given profile. Such an inquiry can only be answered through actual numerical integration to obtain the corresponding phase portrait. The following chapter will deal with the generation of phase portraits using numerical schemes to compute the integral solutions for various flow configurations.

So far, we have been talking about multi-transonic flows in terms of multiple critical points obtained mathematically by deriving the critical conditions using analytical recipes. In other words, we had been treating the terms 'multi-transonic' and 'multi-critical' synonymously. However, as we have already seen, critical points and sonic points are not necessarily the same. Critical points are mathematical derivatives, whereas sonic points are real physical locations on the flow. And none of the continuous phase trajectories pass through more than one sonic points. Hence, for a flow to be truly multi-transonic, it must be brought down from the supersonic branch of its phase trajectory to the subsonic branch of a separate trajectory. This can only be achieved through discontinuities in the flow. We address this issue in the next chapter.

# Chapter 5

# Discontinuities in the Flow

**Summary**

- ✓ *Relativistic Rankine-Hugoniot conditions*
- ✓ *Shock-invariant quantitites ($S_h$)*
- ✓ *Derivation of $S_h$ for all flow configurations*
- ✓ *Numerical integration scheme – Construction of phase portraits*
- ✓ *Hunting for shocks in the phase portraits*
- ✓ *Flow variables at shock vs. accretion parameters*

Discontinuities are often generated in supersonic astrophysical flows with an intrinsic angular momentum. The discontinuities in the form of physical shocks divert the flow to subsonic branches which eventually lead it through other sonic points in phase space. The reason behind generation of shocks may be attributed to the repulsive centrifugal barrier experienced by such flows. The barrier is sufficiently strong to hinder the infalling motion. The only way to bypass such an obstruction and continue along a stationary solution is through the introduction of shocks. Rotating, transonic astrophysical fluid flows are thus believed to be 'prone' to the phenomenon of shock formation.

It is also expected that shock formation in black- hole accretion discs might be a general phenomenon because shock waves in rotating astrophysical flows potentially provide an efficient mechanism for conversion of a significant amount of the gravitational energy into radiation by randomizing the directed inflow of the accreting fluid. Hence, shocks seem to play a crucial role in governing the overall dynamical and radiative processes taking place in astrophysical accretion. The study of steady, standing, stationary shock waves produced in black hole accretion discs has acquired an important status. A number of works have investigated the process (Fukue [1983], Hawley et al. [1984], Ferrari et al. [1985], Sawada et al. [1986], Spruit [1987], Chakrabarti [1989], Abramowicz and Chakrabarti [1990], Yang and Kafatos [1995], Chakrabarti [1996b], Lu et al. [1997], Caditz and Tsuruta [1998], Tóth

et al. [1998], Das [2002], Takahashi et al. [1992], Das et al. [2003], Das [2004], Chakrabarti and Das [2004], Fukumara and Tsuruta [2004], Abraham et al. [2006], Das et al. [2007]) For more details and an exhaustive list of references see, e.g., Chakrabarti [1996a] and Das [2002].

Generally, the issue of the formation of steady, standing shock waves in black-hole accretion discs is addressed in two different ways. Firstly, one can study the formation of Rankine-Hugoniot shock waves in a polytropic flow. Radiative cooling in this type of shock is quite inefficient. No energy is dissipated at the shock and the total specific energy of the accreting material is a shock- conserved quantity. Entropy is generated at the shock and the post-shock flow possesses a higher entropy accretion rate than its pre-shock counterpart. The flow changes its temperature permanently at the shock. Higher post-shock temperature puffs up the post-shock flow and a quasi-spherical, quasi-toroidal centrifugal pressure supported region is formed in the inner region of the accretion disc (see Das [2002] and references therein for further detail) which locally mimics a thick accretion flow. Secondly, one can concentrate on shock formation in isothermal accretion discs. The characteristic features of such shocks are different from the non-dissipative shocks. In isothermal shocks, the flow dissipates a part of its energy and entropy to keep the post-shock temperature equal to its pre-shock value. This maintains the vertical thickness of the flow before and after the shock. Simultaneous jumps in energy and entropy join the pre-shock supersonic flow to its post-shock subsonic branch. For detailed discussion and references see, e.g., Das et al. [2003] and Fukumara and Tsuruta [2004]. In the following sections, we shall construct the equations governing general relativistic Rankine-Hugoniot shock conditions for different flow configurations and derive their corresponding shock-invariant quantities (Tarafdar et al. [2017]).

## 5.1 Polytropic flow – Energy preserving shocks

### 5.1.1 Relativistic Rankine-Hugoniot conditions

The basic equations governing the flow are the energy and baryon number conservation equations which contain no dissipative terms and the flow is assumed to be inviscid. Hence, the shock produced in this way can only be of Rankine- Hugoniot type which conserves energy. The shock thickness must be very small in this case, otherwise non-dissipative flows will radiate energy through shock boundaries because of the presence of strong temperature gradients between the inner and outer boundaries of the shock. The relativistic Rankine-Hugoniot conditions can then be written as,

$$[[\rho v^r \mathcal{A}(r)]] = 0, \tag{5.1}$$

$$[[T_{t\mu} v^\mu]] = [[(p+\epsilon) v_t v^r]] = 0, \tag{5.2}$$

$$[[T_{\mu\nu} \eta^\mu \eta^\nu]] = [[(p+\epsilon) v^r v^r + p]] = 0, \tag{5.3}$$

where $[[f]]$ signifies the discontinuity in $f$ across the shock surface. If $f_-$ and $f_+$ denote the value of $f$ just before and after the shock respectively, then $[[f]] = f_+ - f_-$. $\eta_\mu$ is in a direction normal to the shock hypersurface. $v_t$, $v^r$ and $\mathcal{A}(r)$ have their usual meanings. $\mathcal{A}(r)$ is the only disc geometry dependent term, while all other terms depend

on the thermodynamics of the flow and the physical space-time background. For three different types of discs, $\mathcal{A}(r)$ is given by,

$$\mathcal{A}_{CH}(r) = 4\pi r H \tag{5.4}$$

$$\mathcal{A}_{CF}(r) = 4\pi\Lambda r^2 \tag{5.5}$$

$$\mathcal{A}_{VE}(r) = 4\pi r H(r) \tag{5.6}$$

All the above equations lead to a set of *shock-invariant quantities* ($S_h$) for three different flow configurations.

The *shock-invariant quantity* ($S_{\rm h}$) is defined as a quantity whose numerical value becomes equal on the integral solution branch passing through the outer sonic point and the branch passing through the inner sonic point, exclusively at the location(s) of physically allowed discontinuities obeying general relativistic Rankine Hugoniot conditions. Thus, once the expression for shock- invariant quantities are obtained, the corresponding shock locations can be evaluated by numerically checking for the condition

$$S_{\rm h}^{\rm out} = S_{\rm h}^{\rm in}, \tag{5.7}$$

where $S_{\rm h}^{\rm out}$ and $S_{\rm h}^{\rm in}$ are the shock-invariant quantities defined on the phase trajectories passing through the outer and the inner sonic points respectively.

Thus, by monitoring the invariance of $S_h$ while integrating along the flow, locations of shock ($r_{sh}$) and the ratios of different flow variables across shock can be determined. Then, the trend of their variation with various accretion parameters can be investigated.

### 5.1.2 Discs with constant height

Substituting eqn.(2.28), eqn.(2.30), eqn.(2.32) and eqn.(5.4) in eqns.(5.1–5.3) and cancelling all terms with an explicit $r$-dependence (the shocks have infinitesimally small thickness and hence $r_+ = r_-$) we get,

$$\left[\left[\frac{u}{\sqrt{1-u^2}}\left(\frac{c_s^2}{\gamma-1-c_s^2}\right)^{\frac{1}{\gamma-1}}\right]\right] = 0 \tag{5.8}$$

$$\left[\left[\frac{\gamma u}{c_s^2(1-u^2)}\left(\frac{c_s^2}{\gamma-1-c_s^2}\right)^{\frac{\gamma}{\gamma-1}}\right]\right] = 0 \tag{5.9}$$

$$\left[\left[\frac{1}{1-u^2}\left(\frac{c_s^2}{\gamma-1-c_s^2}\right)^{\frac{\gamma}{\gamma-1}}\left(\frac{\gamma u^2\Delta}{c_s^2}+r^2\left(1-u^2\right)\right)\right]\right] = 0 \tag{5.10}$$

Solving eqns.(5.8–5.10), we derive the following shock-invariant quantity for polytropic discs with constant height,

$$S_h\Big|_{CH} = \frac{u^2(\gamma\frac{\Delta}{r^2}-c_s^2)+c_s^2}{u\sqrt{1-u^2}(\gamma-1-c_s^2)}. \tag{5.11}$$

### 5.1.3 Discs with quasi-spherical geometry

Substituting eqn.(2.28), eqn.(2.30), eqn.(2.32) and eqn.(5.5) in eqns.(5.1–5.3), we get

$$\left[\left[\frac{u}{\sqrt{1-u^2}}\left(\frac{c_s^2}{\gamma-1-c_s^2}\right)^{\frac{1}{\gamma-1}}\right]\right]=0 \tag{5.12}$$

$$\left[\left[\frac{\gamma u}{c_s^2(1-u^2)}\left(\frac{c_s^2}{\gamma-1-c_s^2}\right)^{\frac{\gamma}{\gamma-1}}\right]\right]=0 \tag{5.13}$$

$$\left[\left[\frac{1}{1-u^2}\left(\frac{c_s^2}{\gamma-1-c_s^2}\right)^{\frac{\gamma}{\gamma-1}}\left(\frac{\gamma u^2\Delta}{c_s^2}+r^2\left(1-u^2\right)\right)\right]\right]=0 \tag{5.14}$$

Solving eqns.(5.12–5.14) and cancelling all terms with an explicit $r$-dependence, we obtain the expression of $S_h$ for polytropic discs with quasi-spherical geometry,

$$S_h\Big|_{CF}=\frac{u^2(\gamma\frac{\Delta}{r^2}-c_s^2)+c_s^2}{u\sqrt{1-u^2}(\gamma-1-c_s^2)}. \tag{5.15}$$

We note that the shock conditions and consequently the shock-invariant quantities are identical for CH and CF discs. This is due to the fact that the flow-geometry-dependent conditions differ either by multiples of constants or multiples of exclusively explicit functions of $r$. These factors get cancelled at the shock location(s), since $r_+ = r_-$. The equations representing energy and momentum conservation across shock remain same irrespective of the disc geometry.

### 5.1.4 Discs in vertical hydrostatic equilibrium

Substituting eqn.(2.28), eqn.(2.30), eqn.(2.32), eqn.(5.6) and eqn.(2.49) in eqns.(5.1–5.3), we get

$$\left[\left[\frac{u}{\sqrt{(1-u^2)F}}\left(\frac{c_s^2}{\gamma-1-c_s^2}\right)^{\frac{\gamma+1}{2(\gamma-1)}}\right]\right]=0 \tag{5.16}$$

$$\left[\left[\frac{\gamma u}{c_s^2(1-u^2)}\left(\frac{c_s^2}{\gamma-1-c_s^2}\right)^{\frac{\gamma}{\gamma-1}}\right]\right]=0 \tag{5.17}$$

$$\left[\left[\frac{1}{1-u^2}\left(\frac{c_s^2}{\gamma-1-c_s^2}\right)^{\frac{\gamma}{\gamma-1}}\left(\frac{\gamma u^2\Delta}{c_s^2}+r^2\left(1-u^2\right)\right)\right]\right]=0 \tag{5.18}$$

Solving eqns.(5.16–5.18) and cancelling all terms with an explicit $r$-dependence, $S_h$ for polytropic discs in vertical hydrostatic equilibrium is derived as,

$$S_h\Big|_{VE}=\frac{\sqrt{F}\{u^2(\gamma\frac{\Delta}{r^2}-c_s^2)+c_s^2\}}{uc_s\sqrt{(1-u^2)(\gamma-1-c_s^2)}}. \tag{5.19}$$

Now that the expressions of shock-invariant quantities for all three polytropic flow configurations have been derived explicitly, we can proceed to investigate the parameter space diagrams and look for the subsets of multi-critical solution regions which allow the formation of shocks (as depicted previously in figure 3.5), and hence represent real physical multi-transonic accretion. Then we use numerical integration schemes to generate the phase portraits with shock locations for specific sets of the flow parameters. The phase portraits subsequently enable us to undertake a comparative analysis of the pre- and post-shock ratios of relevant flow variables for the three disc geometries.

### 5.1.5 Phase portraits and flow variable ratios at shock

In the previous chapter, we illustrated that it is possible to understand the nature of the critical points through some local stability analysis, i.e., the methodology is applicable only in the close neighbourhood of the critical points. The global picture of the flow topology, however, can only be generated through the stationary integral solutions of the corresponding flow equations. Such solutions are obtained through numerical integration techniques. For a particular set of $[\mathcal{E}, \lambda, \gamma, a]$, one calculates the location of critical point(s). The values of $u$, $c_s$, $du/dr$ and $dc_s/dr$ on such critical points are then computed. Starting from critical points, the expressions corresponding to $du/dr$ and $dc_s/dr$ are then numerically integrated to obtain the radial Mach number vs. radial distance profile. For tran- sonic flow with multiple critical points, a stationary shock may form. For such flows, integral stationary subsonic solutions pass through the outer sonic point (associated with the saddle-type outer critical point) and become supersonic. The supersonic flow then encounters a discontinuous transition through shock and becomes subsonic once again. The location of the shock is determined by checking for the equality of the shock-invariant quantities at points along the supersonic and subsonic branches of two different phase trajectories. The post-shock subsonic flow then passes through the inner sonic point (corresponding to the saddle-type inner critical point) to become supersonic again and ultimately plunges into the event horizon.

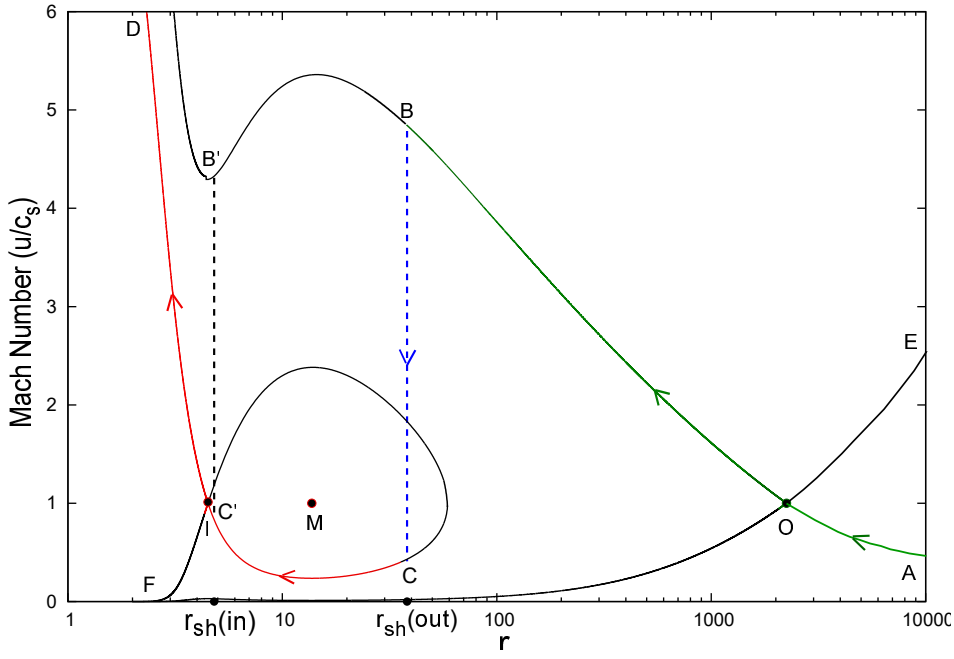


Figure 5.1: Phase-space portrait (Mach number vs. $r$ plot) for quasi-spherical disc ($\mathcal{E} = 1.0003$, $\lambda = 3.5$, $\gamma = 1.35$, $a = 0.1$). $r_{sh}^{in} = 4.805$, $r_{sh}^{out} = 38.15$, $r^{in} = 4.5$ (inner sonic point I), $r_{mid} = 13.712$ (mid sonic point M), $r_{out} = 2244.313$ (outer sonic point O).

Figure 5.1 shows the Mach number vs. radial distance phase portrait of a shocked multi-transonic flow for accretion in quasi- spherical geometry. Branch AOB (green curve) represents accretion through the outer sonic point O. The flow encounters a stable, standing, energy preserving shock at $r = r_{sh}^{out}$ whose location is obtained by using the scheme of equating shock-invariant quantities. It then jumps along the line of discontinuity BC (blue dashed curve). Thus being transformed into a subsonic, compressed and hotter flow,

it then approaches the event horizon moving along the line CC'ID (red curve), becoming supersonic once again while passing through the inner sonic point I. B'C' shows an unstable line of discontinuity which is inaccessible to physical flow. FOE represents the corresponding wind solution, while DIC'CF is a homoclinic orbit encompassing the middle critical point M.

Now that a generic phase-space diagram of the flow has been elaborated, we intend to know which region of the parameter space allows the construction of such phase portraits with the formation of physical shocks. For given values of $a$ and $\gamma$, we check the validity of relativistic Rankine-Hugoniot conditions for every set of $[\mathcal{E}, \lambda]$ which have an associated multi- critical accretion solution. It is observed that only for some subsets of such regions, the shock-invariant quantities calculated along the supersonic and subsonic solutions passing through the outer and the inner sonic points respectively, become equal at a particular radial distance, which is then designated as the shock location.

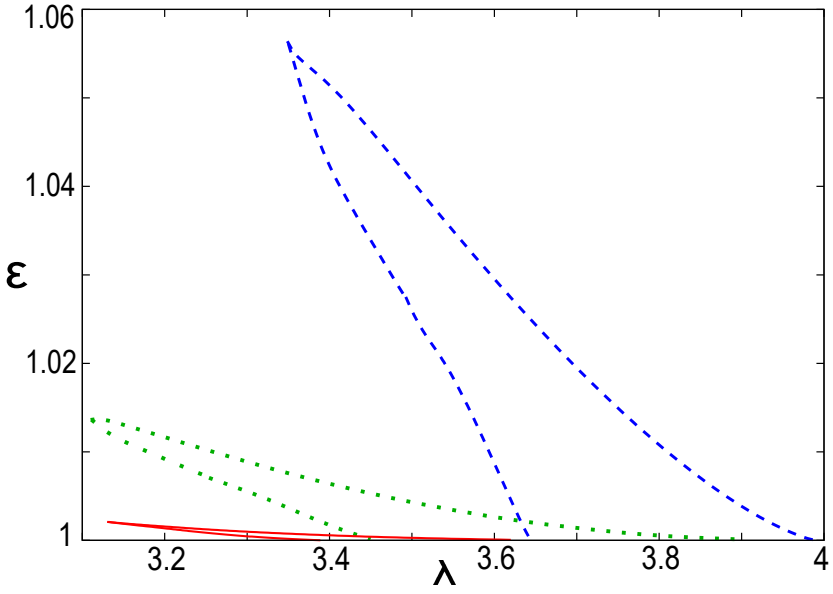


Figure 5.2: Comparison of $[\mathcal{E} - \lambda]_{\rm shock}$ plots for CH (blue-dashed curves), CF (green-dotted curves) and VE (red-solid curves) discs ($a = 0, \gamma = 1.35$).

In figures 5.2 and 5.3, we plot $[\mathcal{E}, \lambda]_{\rm shock}$ for various geometric configurations of flow around a non-rotating and a rotating black hole, respectively. It is observed that in case of a Schwarzschild black hole, for the given value of $\gamma$, a common region of $[\mathcal{E}, \lambda]_{\rm shock}$ for all three kinds of disc does not exist. Increasing the black hole spin parameter pushes the solutions towards lower values of flow angular momentum (note the correlation between $a$ and $\lambda$), and squeezes them closer, thus generating a tiny region of overlap. Therefore one may infer, that in order to perform a comparative analysis of the flow variable ratios across shocks (shock strength, compressibility etc.), low angular momentum, low energy, inviscid flows around rapidly co-rotating black holes need to be considered.

Figure 5.4 shows a magnified image of the common $[\mathcal{E}, \lambda]$ region for shocked multi-transonic accretion in discs with constant height, with quasi-spherical geometry and in vertical hydrostatic equilibrium. These overlapping parameter space domains are extremely important to our purpose. All the shock related flow properties for which the

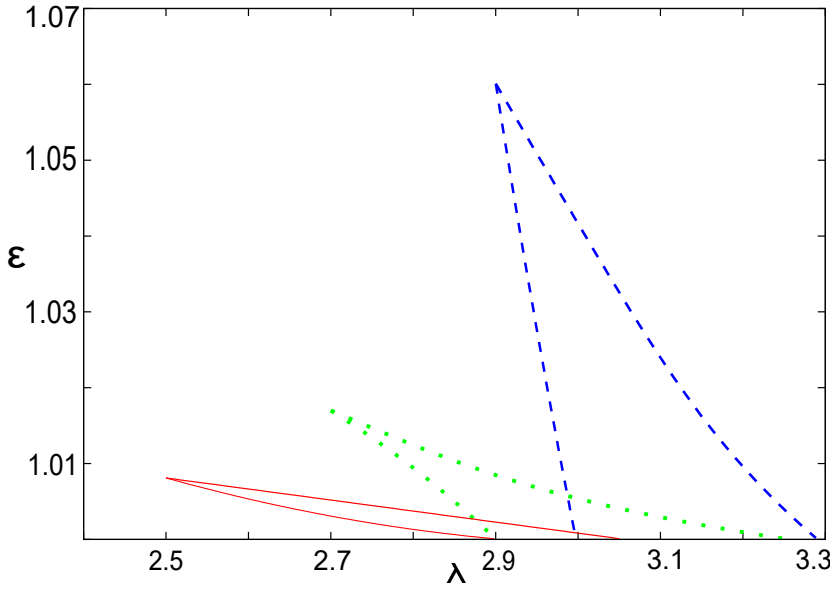


Figure 5.3: Comparison of $[\mathcal{E} - \lambda]_{\rm shock}$ plots for CH (blue-dashed curves), CF (green-dotted curves) and VE (red-solid curves) discs ($a = 0.57, \gamma = 1.35$).

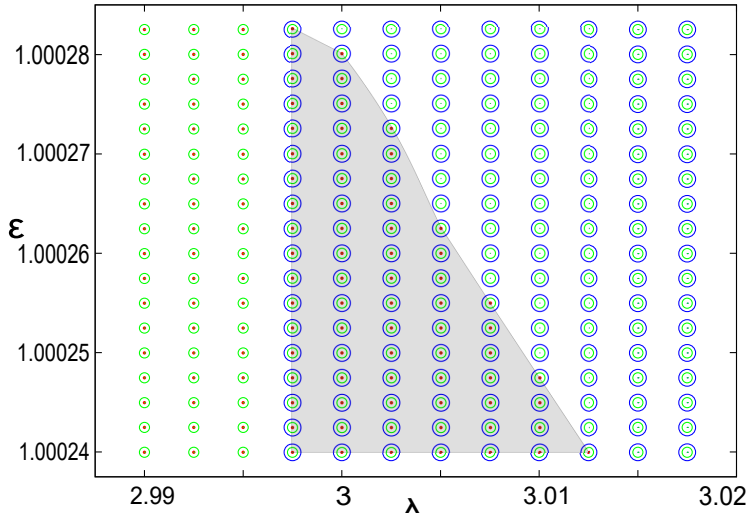


Figure 5.4: Shaded region depicts the common domain of $[\mathcal{E} - \lambda]_{\rm shock}$ for CH (blue circles), CF (green circles) and VE (red dots) discs ($a = 0.57, \gamma = 1.35$).

flow behaviour is to be compared for three different geometries, are to be characterized by $[\mathcal{E}, \lambda, \gamma, a]$ corresponding to these common regions only.

Figure 5.5 is crucial, as it depicts the anti-correlation between black hole spin $a$ and the flow angular momentum $\lambda$ in the context of formation of shocks. Even before the issue of flow discontinuities was addressed, all the results obtained in the previous chapters hinted at this connection. It can be seen that higher values of $a$ lead to multi-transonic solutions at lower values of $\lambda$ and vice versa. Moreover, it may be observed that a higher difference between $a$ and $\lambda$ leads to the generation of a greater shock-forming region on the parameter space. The only probable reason behind this observation seems to be an increase in the effective centrifugal potential barrier experienced by the flow, which must be proportional to $(\lambda - a)^2$. As already explained at the introduction of the chapter, a higher effective centrifugal barrier causes greater hindrance to the accreting matter. The only way around

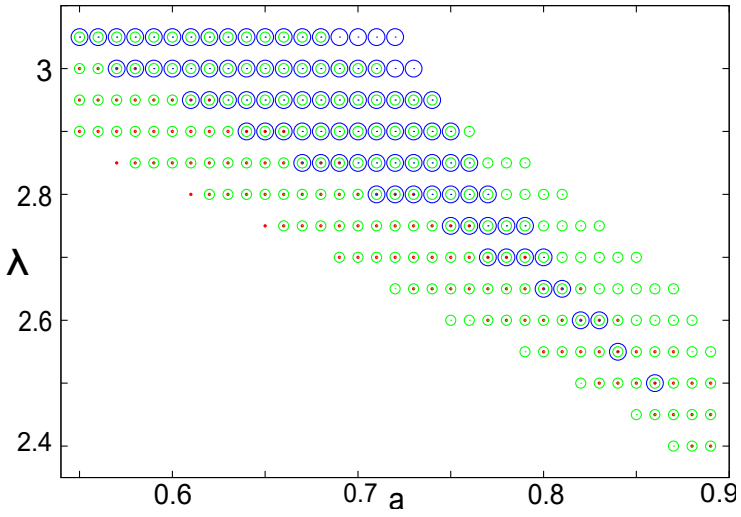


Figure 5.5: Overlap region of $[a, \lambda]$ ($\gamma = 1.35, \mathcal{E} = 1.00024$) which allows shock formation in CH discs (blue circles), CF discs (green circles) and VE discs (red dots).

such an impediment is to channel the matter through a shock onto the subsonic branch of a different phase trajectory, which eventually leads into the event horizon through a second sonic point. Thus, figure 5.5 strongly supports the hypothesis regarding formation of shocks due to centrifugal barriers in the flow. It is important to remember that application of Rankine-Hugoniot conditions provides an analytical tool to look for shocks by utilising few conservation rules at the shock boundaries. However, it does not grant any physical explanation to the phenomenon of shock-formation itself.

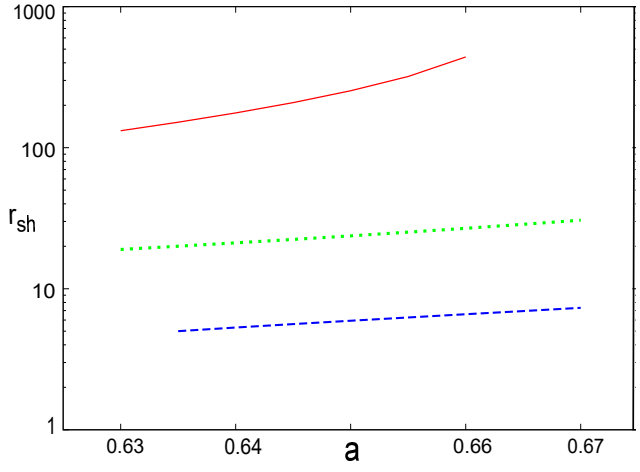


Figure 5.6: Shock location ($r_{sh}$) vs. $a$ plot ($\mathcal{E} = 1.00024, \lambda = 2.9, \gamma = 1.35$) for CH discs (dashed blue curve), CF discs (dotted green curve) and VE discs (solid red curve).

Figure 5.6 depicts the variation of shock- location ($r_{sh}$) with spin parameter $a$. The value of $\lambda$ in this figure and all subsequent figures illustrating other shock related quantities for polytropic flow has been chosen from the common region in figure 5.5 so as to ensure the maximum possible overlapping range of $a$ permissible for shocked accretion at the given value of $\mathcal{E}$ and $\gamma$ for all three flow geometries. The shock location is observed to shift further from the horizon as the black hole spin increases. This is what we may expect, as increasing Kerr parameter for a fixed angular momentum of the flow implies a stronger effective centrifugal barrier. Thus transonicity and shock formation are speculated to

occur in early phases of the flow at greater distances from the massive central source. A comparision of the models reveals the following trend at a given value of $a$,

$$r_{sh}(VE) > r_{sh}(CF) > r_{sh}(CH).$$

This indicates that flow in vertical hydrostatic equilibrium has to face much greater opposition than the other two disc geometries for the same amount of obstruction posed by rotation of the flow and spin of the black hole.

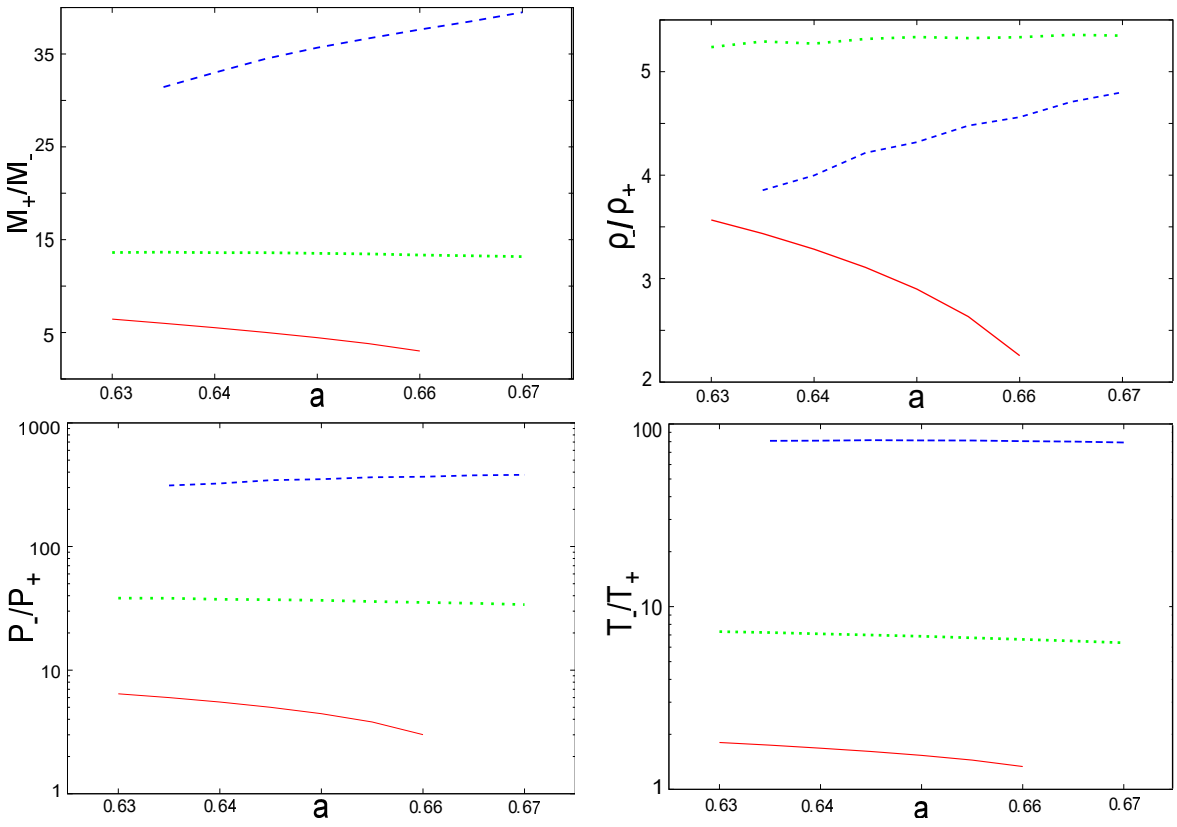


Figure 5.7: Variation of shock strength ($M_+/M_-$), compression ratio ($\rho_-/\rho_+$), pressure ratio ($P_-/P_+$) and temperature ratio ($T_-/T_+$) with black hole spin parameter $a$ ($\gamma = 1.35, \mathcal{E} = 1.00024, \lambda = 2.9$) for constant height flow (dashed blue lines), quasi-spherical flow (dotted green lines) and flow in hydrostatic equilibrium (solid red lines). Subscripts '+' and '-' represent pre and post shock quantities respectively.

It is also interesting to note from figure 5.7 that not only does the vertical equilibrium model experience maximum hindrance due to rotation, but it also exhibits the formation of shocks with the weakest strength, i.e. pre-shock to post-shock ratio of the Mach number ($M_+/M_-$), when compared with the other two models. The shocks are the strongest in case of discs with a constant height and intermediate in the case of quasi-spherical flows. The strengths are observed to decrease with $a$. This can be explained by the dependence of shock location on the spin parameter. Greater values of $r_{sh}$ point at decreasing curvature of physical space-time leading to diminishing influence of gravity. Thus the dropping of shock-strength with increasing $a$, i.e. a farther shock-location $r_{sh}$, demonstrates that weaker gravity amounts to the formation of weaker discontinuities in the flow and vice-versa. Naturally, waning shock strengths in turn lead to lower post- to pre-shock compression ($\rho_-/\rho_+$), pressure ($P_-/P_+$) and temperature ($T_-/T_+$) ratios, as observed in the figure. A seemingly anomalous behaviour is observed in the variation trend for constant height flow

geometry. In spite of a receding shock location, the shock strength increases, although behaviour of the other related ratios fall in line with our previous arguments. The reason behind such an anomaly will be revealed in the next chapter when we discuss the variation of *quasi-terminal* values for mono-transonic flow solutions available over the entire physical range of the Kerr parameter.

## 5.2 Isothermal flow – Dissipative shocks

### 5.2.1 Relativistic Rankine-Hugoniot conditions

Isothermal shocks are dissipative in nature. Constant temperature is maintained at the cost of energy liberated at the shock locations. In fact, such dissipative shocks prove to be an efficient mechanism for the extraction of gravitational energy of the accreting fluid in the form of radiation. Since energy is not conserved in isothermal flows, the relativistic Rankine-Hugoniot conditions are defined as the conservation of pre- and post-shock mass given by eqn.(5.1), conservation of pre- and post-shock flow momentum given by eqn.(5.3) and the conservation of pre- and post-shock *quasi-specific energy* given by,

$$\left[\left[v_t^2 \rho^{2c_s^2}\right]\right] = 0 \tag{5.20}$$

Applying the techniques described in the previous section, the *shock-invariant quantities* ($S_h$) for all three isothermal flow geometries are derived as under –

### 5.2.2 Discs with constant height

Substituting for $\rho$ from eqn.(2.44) in eqn.(5.20), we get

$$\left[\left[v_t^2 \left(\frac{\dot{M}}{v^r \mathcal{A}(r)}\right)^{2c_s^2}\right]\right] = 0. \tag{5.21}$$

Substituting for $\mathcal{A}(r)$ from eqn.(5.4), we obtain

$$\left[\left[\frac{(r-2)\left(r^3+a^2(r+2)\right)}{(1-u^2)\left(r^4-\lambda^2\left(4a^2+r(r-2)\right)+a^2 r(r+2)\right)}\left(\frac{\dot{M}\sqrt{1-u^2}}{u\sqrt{\Delta}4\pi r H}\right)^{2c_s^2}\right]\right] = 0. \tag{5.22}$$

Also, substituting for $\rho$ from eqn.(2.44), $p$ from eqn.(2.33) and $\mathcal{A}(r)$ from eqn.(5.4) in eqn.(5.3), we obtain

$$\left[\left[\frac{\dot{M}}{4\pi H}\left(\frac{u^2\Delta(c_s^2+1)+c_s^2(1-u^2)}{ur\sqrt{\Delta(1-u^2)}}\right)\right]\right] = 0. \tag{5.23}$$

Cancelling all constants and terms with an explicit $r$-dependence in eqn.(5.22) and eqn.(5.23), the shock-invariant quantity for isothermal constant height accretion discs is derived as,

$$S_h|_{CH}^{iso} = \left(\frac{u}{\sqrt{1-u^2}}\right)^{2c_s^2-1}(u^2\Delta + r^2 c_s^2(1-u^2)). \tag{5.24}$$

### 5.2.3 Discs with quasi-spherical geometry

Substituting for $\mathcal{A}(r)$ from eqn.(5.5) in eqn.(5.21), we obtain

$$\left[\left[\frac{(r-2)\left(r^3+a^2(r+2)\right)}{(1-u^2)\left(r^4-\lambda^2\left(4a^2+r(r-2)\right)+a^2r(r+2)\right)}\left(\frac{\dot{M}\sqrt{1-u^2}}{u\sqrt{\Delta}4\pi r^2\Lambda}\right)^{2c_s^2}\right]\right]=0. \tag{5.25}$$

Substituting for $\rho$ from eqn.(2.44), $p$ from eqn.(2.33) and $\mathcal{A}(r)$ from eqn.(5.5) in eqn.(5.3), we obtain

$$\left[\left[\frac{\dot{M}}{4\pi\Lambda}\left(\frac{u^2\Delta(c_s^2+1)+c_s^2(1-u^2)}{ur^2\sqrt{\Delta(1-u^2)}}\right)\right]\right]=0. \tag{5.26}$$

Cancelling all constants and terms with an explicit $r$-dependence in eqn.(5.25) and eqn.(5.26), the shock-invariant quantity for isothermal quasi-spherical accretion discs can be derived as,

$$S_h|^{iso}_{CF}=\left(\frac{u}{\sqrt{1-u^2}}\right)^{2c_s^2-1}(u^2\Delta+r^2c_s^2(1-u^2)) \tag{5.27}$$

### 5.2.4 Discs in vertical hydrostatic equilibrium

Substituting for $\mathcal{A}(r)$ from eqn.(5.6) and $H(r)$ from eqn.(2.50) in eqn.(5.21), we obtain

$$\left[\left[\frac{\dot{M}}{8\pi}\frac{v_t^{\frac{1}{c_s^2}}(\lambda^2v_t^2-a^2(v_t-1))\sqrt{1-u^2}}{u\sqrt{\Delta}r^5c_s^2}\right]\right]=0. \tag{5.28}$$

Substituting for $\rho$ from eqn.(2.44), $p$ from eqn.(2.33) and $\mathcal{A}(r)$ from eqn.(5.6) in eqn.(5.3), we obtain

$$\left[\left[\frac{\dot{M}}{4\pi}\frac{2c_s^2r^4}{\lambda^2v_t^2-a^2(v_t-1)}\left(\frac{u^2\Delta(c_s^2+1)+c_s^2(1-u^2)}{ur\sqrt{\Delta(1-u^2)}}\right)\right]\right]=0. \tag{5.29}$$

Cancelling all constants and terms with an explicit $r$-dependence in eqn.(5.28) and eqn.(5.29), the shock-invariant quantity for isothermal accretion discs in vertical hydrosatic equilibrium can be derived as,

$$S_h|^{iso}_{VE}=u^{2c_s^2-1}(u^2\Delta+r^2c_s^2(1-u^2)) \tag{5.30}$$

### 5.2.5 Phase portraits and flow variable ratios at shock

We now intend to see which region of the $T-\lambda$ space allows shock formation. For given values of $a$, we check the validity of relativistic Rankine-Hugoniot conditions for every set of $[T,\lambda]$ which have an associated multi-critical accretion solution. It is observed that only for some subset of such $[T,\lambda]$, the shock-invariant quantities calculated along the solution passing through the outer and the inner sonic points become equal at a particular radial distance, which is then designated as the shock location.

In figures 5.8 and 5.9, we plot the corresponding $[T,\lambda]_{\rm shock}$ for various geometric configurations of flow around a non-rotating and a rotating black hole, respectively. We plot the subsets of the $T-\lambda$ spaces for three different flow geometries at fixed values of $a=0$

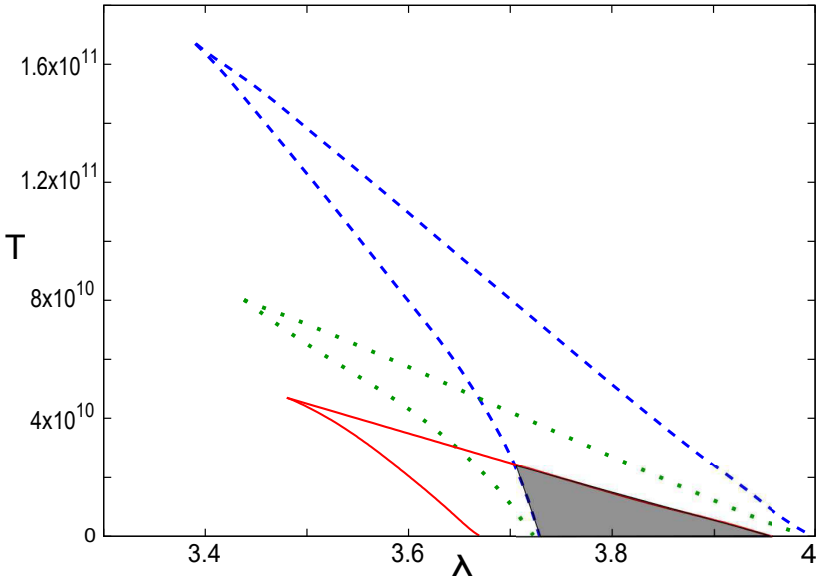


Figure 5.8: Comparision of $T - \lambda$ plot of allowed shocked multi-transonic accretion solutions for three different flow geometries ($a = 0$, $T$ in Kelvin). CH, CF and VE discs are represented by blue dashed, green dotted and red solid curves respectively. Shaded region depicts the overlapping domain of parameters for all the three geometries.

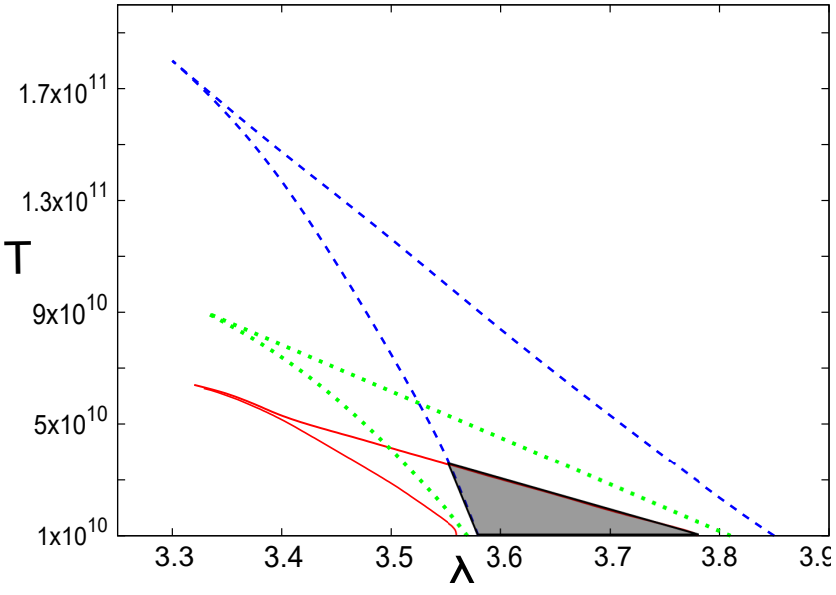


Figure 5.9: Comparision of $T - \lambda$ plot of allowed shocked multi-transonic accretion solutions for three different flow geometries ($a = 0.1$, $T$ in Kelvin). CH, CF and VE discs are represented by blue dashed, green dotted and red solid curves respectively. Shaded region depicts the overlapping domain of parameters for all the three geometries.

and $a = 0.1$, for which, value of the shock-invariant quantities $S_h$, when evaluated along the flow branches through inner and outer critical points, become equal at particular value(s) of $r$, which is the location of shock. The shaded region depicts overlap of shock-forming $[T, \lambda]$ parameter set of the three disc configurations. It is observed that unlike the polytropic case, isothermal accretion onto non- rotating black holes with different flow geometries have a significant region of overlap. Even for rotating black holes, the common region is much larger than its polytropic counterpart. An increase in black hole spin pushes the multi-transonic solutions towards lower values of the flow angular momentum.

Once the common region for shock formation is obtained, we investigate the variation

of shock location ($r_{sh}$), shock strength ($M_+/M_-$), compression ratio ($\rho_-/\rho_+$), pressure ratio ($P_-/P_+$) and quasi-specific energy dissipation ratio ($\xi_+/\xi_-$) (subscripts + and − have the same meanings as defined for polytropic accretion in the previous sections) with the black hole spin parameter $a$, also comparing the trends of variation for various disc geometries.

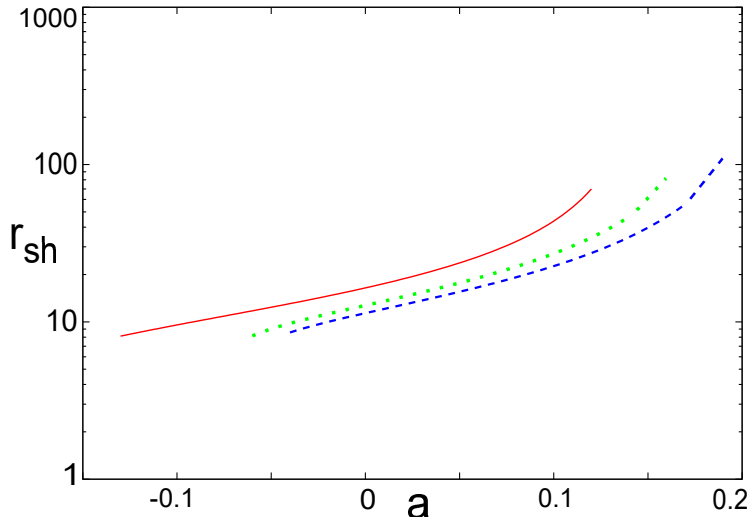


Figure 5.10: Shock location ($r_{sh}$) vs. $a$ plot ($T = 10^{10}$ K, $\lambda = 3.75$) for CH disc (dashed blue curve), CF disc (dotted green curve) and VE disc (solid red curve).

Figure 5.10 shows how the shock location ($r_{sh}$) varies with spin parameter $a$. The bulk ion temperature has been fixed at $10^{10}$ K and the value of has been selected accordingly ($\lambda = 3.75$) from the region of shock overlap observed in figure 5.9 so that the available range of $a$ is maximum. The same set of $[T, \lambda]$ has been used in all subsequent isothermal shock related plots. As already argued in the previous sections on polytropic flow, growth in strength of the effective centrifugal barrier due to increase in the difference between $\lambda$ and $a$ explains the formation of shock farther away from the gravitating source as the value of black hole spin is increased while fixing the value of specific angular momentum. Again, for a particular value of $a$, it is observed that

$$r_{sh}(VE) > r_{sh}(CF) > r_{sh}(CH),$$

which indicates that even in the case of an isothermal disc, flow in vertical hydrostatic equilibrium is exposed to the maximum resistance for the same centrifugal barrier faced by CH and CF geometry discs.

Figure 5.11 on comparing with figure 5.7 establishes the fact that irrespective of whether the flow is polytropic or isothermal, a gradual increase in black hole spin for a specific flow angular momentum shifts the shock location outwards by boosting the effective centrifugal barrier. A shock formed far away from the event horizon is weaker in strength owing to the eventual flattening of space-time. Moreover in both polytropic and isothermal cases, for a given $[a, \lambda]$, the strongest shocks are formed in constant height discs whereas discs in vertical hydrostatic equilibrium exhibit the weakest shocks. The same trend is consistently observed for all the relevant ratios across the discontinuity.

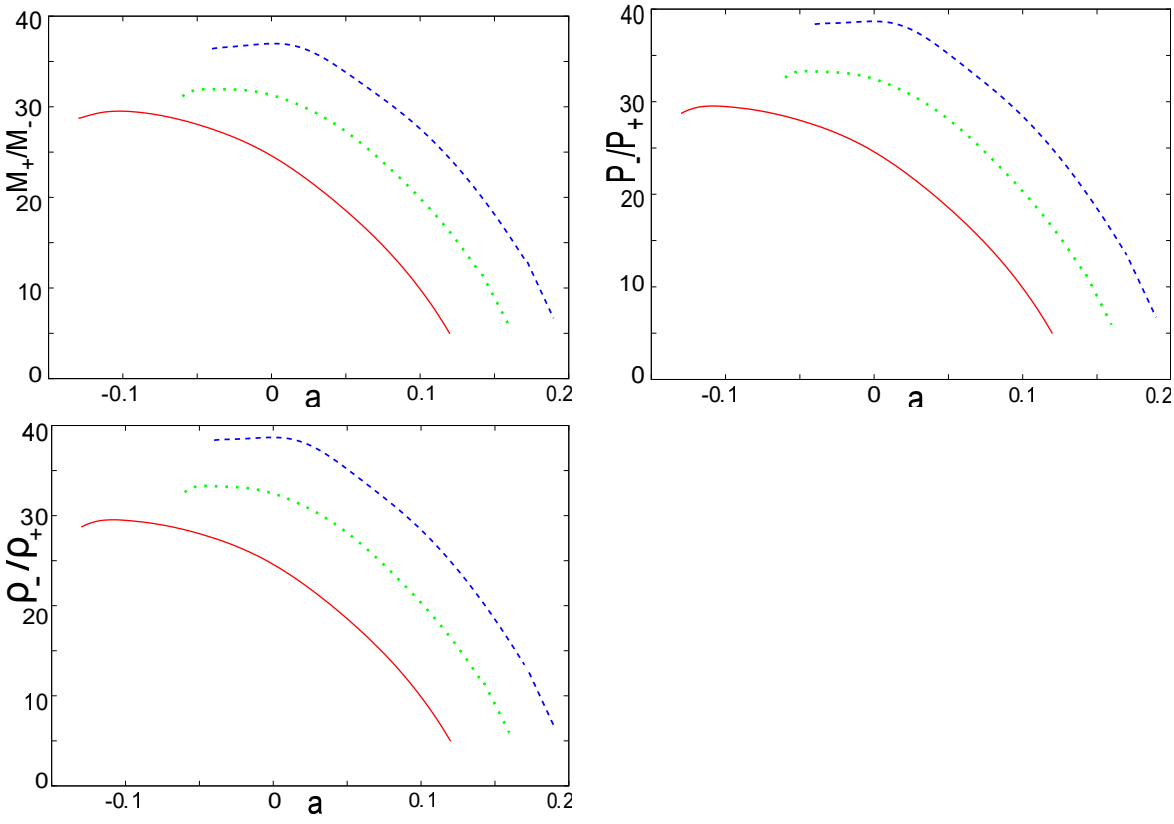


Figure 5.11: Variation of shock strength ($M_+/M_-$), compression ratio ($\rho_-/\rho_+$) and pressure ratio ($P_-/P_+$) with spin parameter $a$ ($\mathcal{E} = 10^{10}$ K, $\lambda = 3.75$) for CH (dashed blue curves), CF (dotted green curves) and VE discs (solid red curves). Subscripts '+' and '-' represent pre- and post- shock quantities respectively.

### 5.2.6 Powering flares through energy dissipated at shock

For the isothermal accretion onto a rotating black hole considered in the present work, we concentrate on dissipative shocks. Unlike the standing Rankine- Hugoniot type energy-preserving shocks studied for the polytropic flow, a substantial amount of energy is dissipated at the shock location to maintain the temperature invariance of the isothermal flow. As a consequence, the flow thickness does not change abruptly at the shock location and handling the pressure balance equation across the shock becomes more convenient as compared to that for the polytropic accretion. The amount of energy dissipated at the shock might make an isothermal shock to appear 'bright', since for inviscid, dissipationless flow considered in our work, accretion remains radiatively inefficient throughout. The type of low angular momentum inviscid flow we consider in the present work, is believed to be ideal to mimic the accretion environment of our galactic centre black hole (Moscibrodzka et al. [2006]). Sudden substantial energy dissipation from the shock surface may thus be conjectured to feed the X-ray and IR flares emanating from our galactic centre black hole (Baganoff et al. [2001], Genzel et al. [2003], Marrone et al. [2008], Czerny et al. [2010], Wang et al. [2013], Ponti et al. [2015], Karssen et al. [2017], Mossoux and Grosso [2017], Yuan et al. [2018]).

In our formalism, the ratios of the quasi-specific energies corresponding to the pre-shock and post-shock flows is assumed to be a measure of the amount of the dissipated energy at the shock surface. In figure 5.12, we plot such ratios for various ranges of the

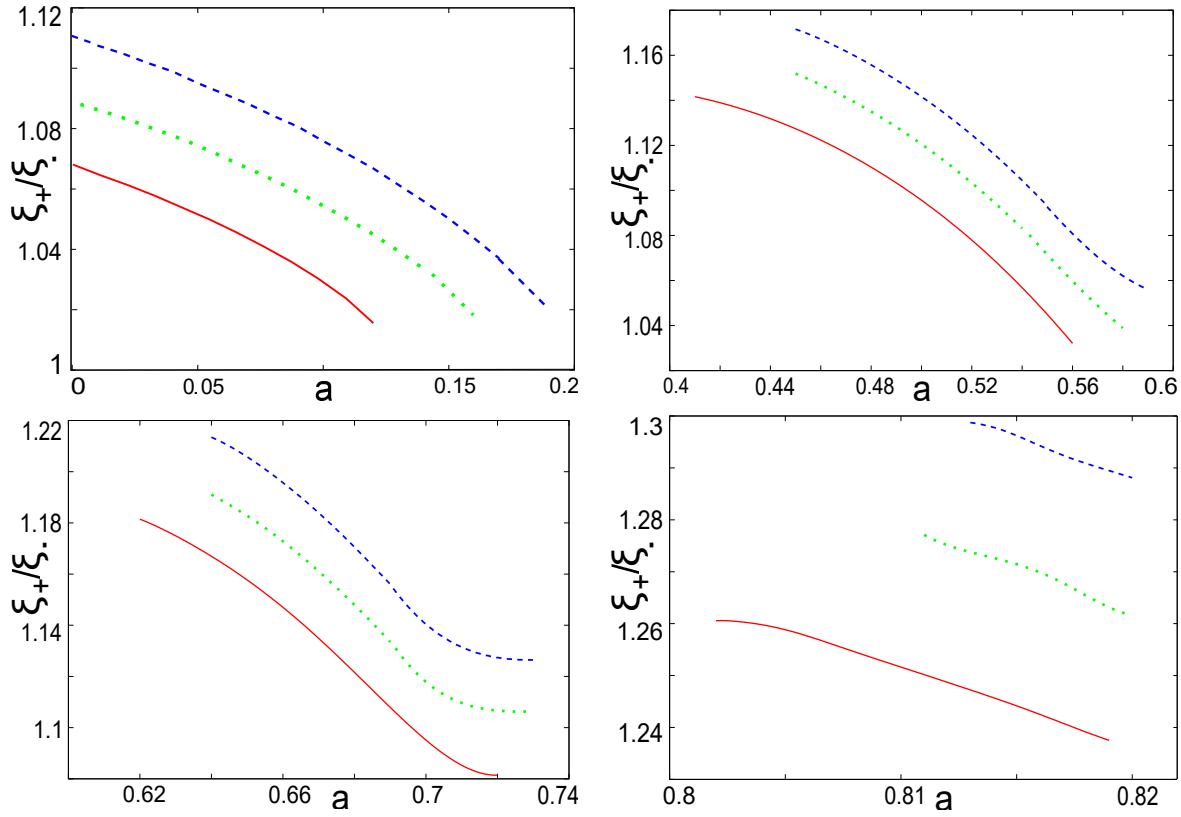


Figure 5.12: Variation of quasi-specific energy ratio ($\xi_+/\xi_-$) with black hole spin parameter a ($T = 10^{10}$ K). In order to obtain multi-critical domains with shock over four different ranges of $a$, four different values of $\lambda$ have been fixed at the given $T$ , i.e. $\lambda = 3.75$ (upper left), $\lambda = 3.25$ (upper right), $\lambda = 3.0$ (lower left), $\lambda = 2.7$ (lower right). CH, CF and VE flow have been represented by dashed blue, dotted green and solid red curves respectively. Subscripts '+' and '-' represent pre- and post-shock quantities respectively.

black hole spins for three different types of the geometries of the flow. The panel consists of four figures, each corresponding to a certain range of values of $a$. As already discussed, for a fixed value of $[\mathcal{E}, \lambda, \gamma]$ or $[T, \lambda]$, shock formation over a continuous range of the Kerr parameter spanning its entire physical domain $-1 > a > 1$, is allowed neither for polytropic nor isothermal accretion. Four different figures in the panel are thus characterised by four different sets of $[T, \lambda]$ as mentioned in the caption. The following interesting features are observed:

1. Depending on the initial conditions, substantial amount of energy gets liberated from the shock surface. Sometimes even as high as 30% of the rest mass may be converted into radiated energy, which is a huge amount. Hence the shock-generated dissipated energy can, in principle, be considered as a good candidate to explain the source of energy dumped into the flare. The length scale on the disc from which the flare may be generated also matches well with the shock location. Such 'flare-generating' length scales obtained in our theoretical calculations are thus, in good agreement with the observational works (Karssen et al. [2017]).

2. We also observe that the amount of dissipated energy anti-correlates with the shock location, which is perhaps intuitively obvious because closer the shock forms to the horizon, greater is the available gravitational energy to be converted into dissipated radiation. Following the same line of argument, the amount of dissipated energy anti-correlates with the flow angular momentum. The lower the angular momentum

of the flow, the closer to the horizon is the centrifugal pressure supported region formed. Such regions slow down the flow and break the flow behind it, and hence the shock is generated. The locations of such region are thus markers anticipating the region of the disc from which the flares may be generated.

It is imperative to study the influence of the black hole spin in determining the amount of energy liberated at the shock. What we have found here is that for prograde flow, such amount anti-correlates with the black hole spin. Thus, for a given flow angular momentum, slowly rotating black holes produce the strongest flares. Hence, for a given value of $[T, \lambda]$, if shocked multi-transonic accretion solutions exist over a positive span of $a$ including $a = 0$, then flares originating from the vicinity of a Schwarzschild black hole would consequently contain the maximum amount of energy. Hence, unlike the Blandford-Znajek mechanism (Blandford and Znajek [1977], Das and Czerny [2012], O' Riordan et al. [2016], Czerny and You [2016], Bambi [2017]), the amount of energy transferred to a flare is not extracted at the expense of black hole spin. Certain works based on the observational results argue that there is no obvious correlation between the black hole spin and the jet power (Fender et al. [2010], Broderick and Fender [2011] and references therein). Our present finding is in accordance with such arguments. In this connection, however, it is to be noted that BZ mechanism is usually associated with the electromagnetic energy extractions, whereas energy liberation at the shock is associated with the hydrodynamic flow. Hence no direct comparision can perhaps be made between the Blandford-Znajek process and the process considered in our work.

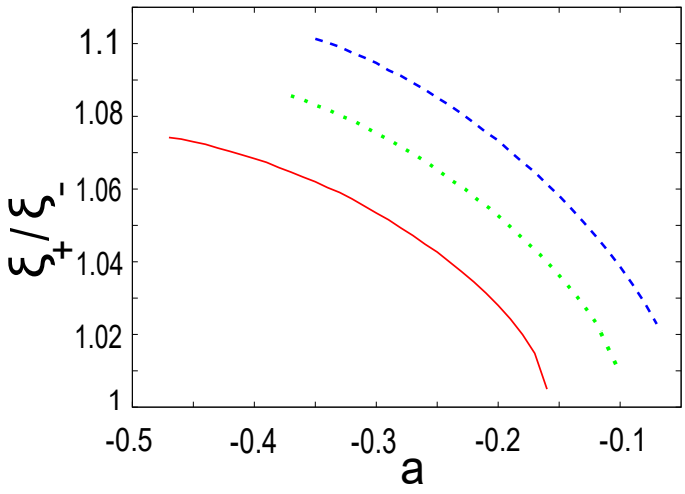


Figure 5.13: Variation of quasi-specific energy ratio ($\xi_+/\xi_-$) with $a$ ($T = 10^{10}$ K, $\lambda = 4.0$) for retrograde flow.

In recent years, the study of retrograde flow close to the Kerr black holes are also of profound interest (Garofalo [2013], Mikhailov et al. [2018] and references therein). Hence we study the spin dependence of the amount of energy dissipation at the shock. The result is shown in figure 5.13. Here we observe that the amount of dissipated energy is greater for faster counter-rotating black holes. For retrograde flow, the negative Kerr parameter essentially reduces the overall measure of the angular momentum of the flow and the effective angular momentum, which may explain such finding.

It is also observed that the amount of shock-dissipated energy is also influenced by the

geometric configuration of the flow. We find that axially symmetric flow with constant thickness produces the largest amount of liberated energy at shock, whereas the flow in hydrostatic equilibrium along the vertical direction generates the smallest amount. The quasi-spherical flow contributes at a rate which is intermediate between the rates for CH and VE discs. This feature remains unaltered for prograde as well as retrograde flows.

Now that the discontinuities have been discussed in detail, we shall try to proceed farther along the flow. When accreting matter becomes subsonic after overcoming the centrifugal barrier, it accelerates towards the inner sonic point. Once it is crossed, there is nothing to stop the resultant supersonic flow from plunging into the event horizon. In case of accretion onto hard, finite-sized compact objects such as neutron stars, more subsequent shocks can be formed before collision of the infalling matter with the surface of the accretor. However, black holes do not have a hard surface. Hence the inflow continues unhindered, attaining ultra-high values of velocity (approaching the speed of light), pressure, density and temperature (for polytropic flows) just before falling into the horizon. Considering appropriate radiative mechanisms, such values may be used to find the intensities of radiation for different frequencies in the close vicinity of the event horizon. Once the intensity of radiation emanating from the region is known, it can be integrated along various lines of sight using the ray-tracing techniques from numerical optics, to produce an image of the disc at the boundary of the horizon, which is nothing but an optically inverted shadow-image of the event horizon itself! In the next chapter, we shall focus on these terminal values of the flow variables. We prefer to call them 'quasi-terminal' values, as the fluid simply does not stop at the horizon, but is lost into oblivion, still accelerating towards the singularity.

# Chapter 6

# Quasi-terminal Values

**Summary**

- ✓ *Definition & significance of quasi-terminal values – $V_\delta$*
- ✓ *$V_\delta$ vs. a for multi-transonic flow configurations*
- ✓ *$V_\delta$ vs. a for mono-transonic flow configurations*
- ✓ *A glimpse of the horizon*

Accreting matter manifests extreme behaviour before plunging through the event horizon because it experiences the strong curvature of space-time close to the black hole. The spectral signature of such matter corresponding to such length scale helps to understand the key features of strong gravity space-time in close proximity of the horizon. It may also help in investigating the spectral signatures of black hole spin. The corresponding spectral profiles and the light curves can be used to construct the relevant black hole shadow images (Falcke et al. [2000], Takahashi [2004], Huang et al. [2007], Hioki and Maeda [2009], Zakharov et al. [2012], Straub et al. [2012]).

For a very small positive value of $\delta$ ($\sim 0.0001$), any flow variable $V_\delta$ measured at a radial distance $r_\delta = r_+ + \delta$ ($r_+$ is the radius of the horizon) will be termed as a 'quasi-terminal value' of the respective flow variable. In Das et al. [2015], dependence of $V_\delta$ on the Kerr parameter was studied for polytropic discs in hydrostatic equilibrium along the vertical direction. In the present work, we intend to generalize such work by computing $V_\delta$ for all three different matter geometries for both polytropic and isothermal flows. This generalization will be of paramount importance in understanding the geometric configuration of matter close to the horizon manifested through imaging of its shadow.

In what follows, we shall study the dependence of $[M, \rho, T, P]_{r_\delta}$ (for polytropic flow) and $[M, \rho, P]_{r_\delta}$ (for isothermal flow) on the Kerr parameter for shocked multi-transonic accretion with three different flow geometries to understand how the nature of such dependence gets influenced by the disc structure. In this context, we shall also investigate mono-

transonic flows which offer solutions over the entire range of Kerr parameter, from $-1$ to $+1$, with an aim to look for any general asymmetry in the variation trend of $V_\delta$ between co-rotating and counter-rotating accretion discs.

## 6.1 Polytropic flows

### 6.1.1 Dependence of $V_\delta$ on $a$ for multi-transonic accretion

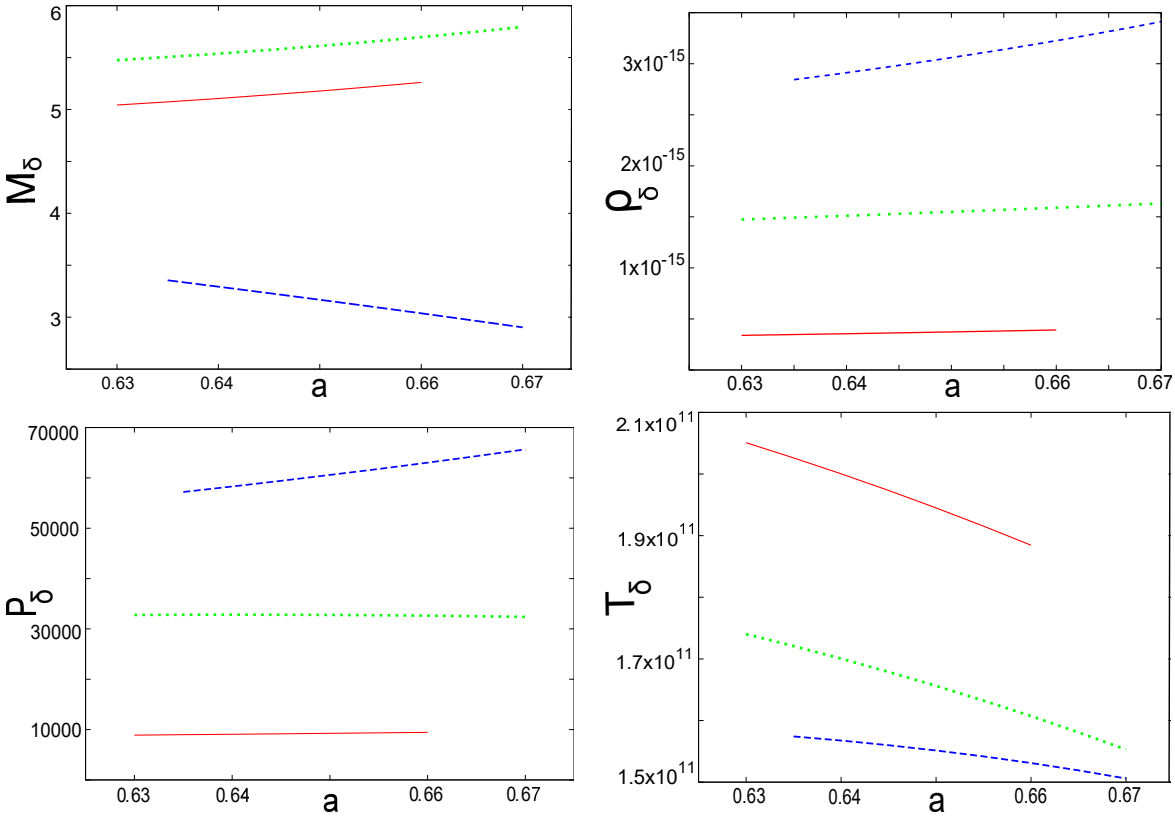


Figure 6.1: Variation of quasi-terminal values of Mach number ($M_\delta$), density ($\rho_\delta$), pressure ($P_\delta$) and temperature ($T_\delta$) with $a$ ($\gamma = 1.35, \mathcal{E} = 1.00024, \lambda = 2.9$) for CH (dashed blue curves), CF (dotted green curves) and VE (solid red curves) discs. Density and pressure are in CGS units of $g\ cm^{-3}$ and $dyne\ cm^{-2}$ respectively and temperature is in absolute units of Kelvin.

Figure 6.1 demonstrates how the quasi-terminal values pertaining to Mach number ($M_\delta$), density ($\rho_\delta$), pressure ($P_\delta$) and the bulk ion temperature ($T_\delta$) vary with black hole spin $a$. A given set of $[\mathcal{E}, \lambda, \gamma]$ is chosen such that a substantial range of $a$ is available for comparing any observable trend of variation in the common shock regime for all three disc configurations.

It may be noted that although a general course of dependence of the values may be observed within a local set of flow parameters for each geometry separately, however it is impossible to conclude about any global trends of such sort. This is primarily due to the reason that each permissible set of $[\mathcal{E}, \lambda, \gamma]$ offers an exclusively different domain of black hole spin for multi-transonic accretion to occur and an even narrower common window for the viability of general relativistic Rankine-Hugoniot shocks in different geometric configurations of the flow. Hence, in spite of the fact that physical arguments may be able to justify the observed results in certain cases, however similar specific attempts made in all

small local parameter regions may not only turn out to be futile, but also dangerously misleading.

The anomaly which was pointed out in section 5.1.5 of the previous chapter, is clearly an example of such an issue. However, there is absolutely no scope for scepticism regarding the universality or validity of our previous physical arguments. It is only that nature offers a few selected systems with an opportunity to peek into their global behaviour. We present such an instance in the following subsection.

### 6.1.2 Dependence of $V_\delta$ on $a$ for mono-transonic accretion

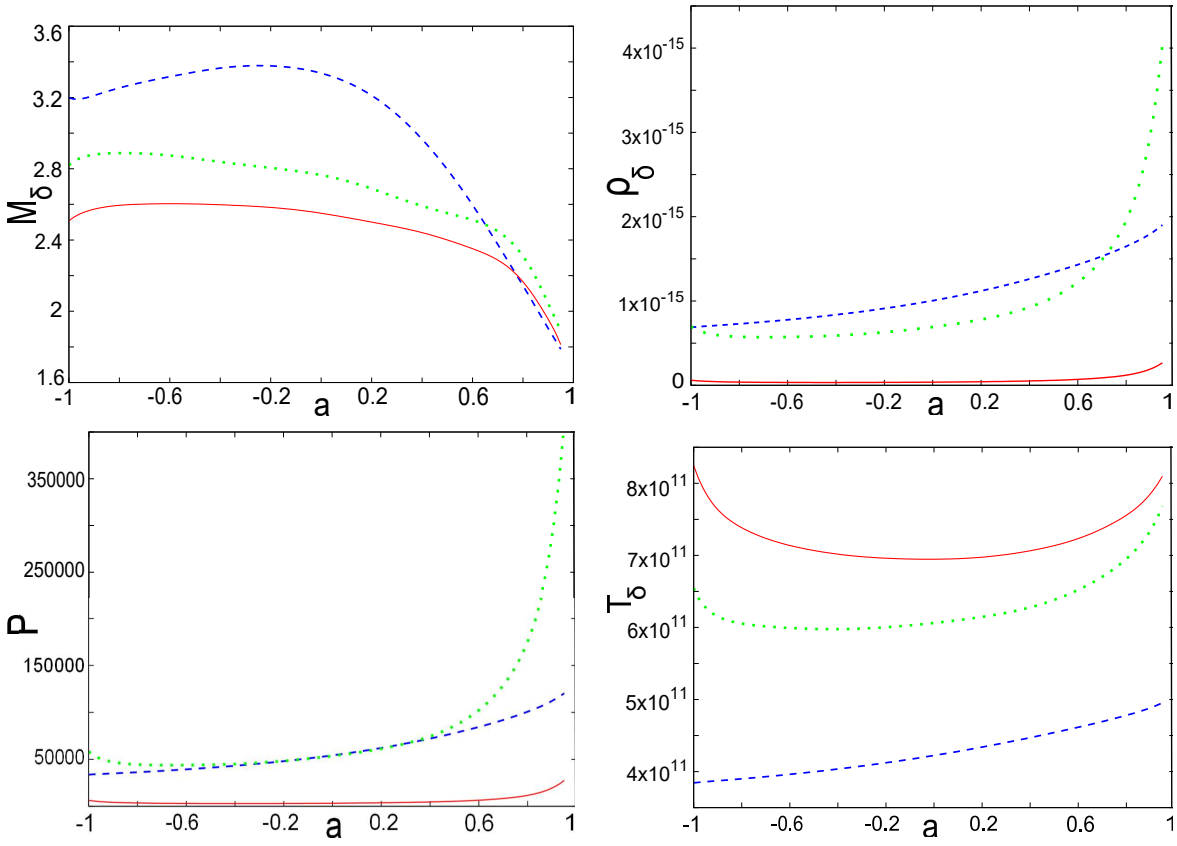


Figure 6.2: Variation of quasi-terminal values of Mach number ($M_\delta$), density ($\rho_\delta$), pressure ($P_\delta$) and temperature ($T_\delta$) with $a$ ($\gamma = 1.35, \mathcal{E} = 1.2, \lambda = 2.0$) for mono-transonic accretion with CH (dashed blue curves), CF (dotted green curves) and VE (solid red curves) discs. Density and pressure are in CGS units of $g\ cm^{-3}$ and $dyne\ cm^{-2}$ respectively and temperature is in absolute units of Kelvin.

In figure 6.2 we show the dependence of quasi-terminal values on black hole spin for mono-transonic accretion. It is observed that weakly rotating and substantially hot flows allow stationary mono-transonic solutions over the entire physical range of the Kerr parameter. A careful glance at the results reveals, that the reason behind the previously discussed anomaly in general spin-dependent behaviour of the corresponding physical quantities, are the essential intrinsic limitations in the possibility of observing their variation over the complete range of $a$. Since, for any given set of $[\mathcal{E}, \lambda, \gamma]$, shocked stationary multi-transonic accretion solutions for all disc configurations are allowed over a considerably small overlapping domain of $a$, one is only able to look through a narrow slit of the whole window. It is clearly evident from figure 6.2 that the quasi-terminal values indeed exhibit common

global trends of variation over $a$. However, while concentrating upon a small portion of spin, asymmetry in the shapes and distributions of such trends leads to crossovers and apparently non-correlative or anti-correlative mutual behaviours among the various disc geometries.

It is understandable to question the utility of results with such unavoidable constraints which are levied by nature itself. But sometimes, a curse is a blessing in disguise. In the present context, it is this very asymmetry, that turns out to be of supreme importance in pointing towards a prospective observational signature of the black hole spin. One may readily observe in figure 6.2 that the distributions of $V_\delta$ across $a$ exhibit clear distinctions between prograde and retrograde flows. The values of $V_\delta$ at $+a$ and $-a$ are distinctly separate. We must keep in mind, that feeding these values in appropriate radiative transfer processes (such as synchrotron, bremsstrahlung and Compton scattering) is the first step in the process of constructing a black hole shadow image. Hence, differences between black holes with co-rotating and counter-rotating spins visible on these plots are expected to reflect on the resulting shadow images, providing a direct way to distinguish between positive and negative spins. Generation of numerous shadow images of black holes with different values of spin, surrounded by accretion discs with different geometries, equations of state and flow parameters is a method which is being pursued by theoretical astrophysicists to create calibration charts that may be compared to actual images of the event horizon to be captured using extremely high-resolution telescopes in the upcoming decades.

## 6.2 Isothermal flows

### 6.2.1 Dependence of $V_\delta$ on $a$ for multi-transonic accretion

Variation of the quasi-terminal values of Mach number ($M_\delta$), density ($\rho_\delta$) and pressure ($P_\delta$) with spin parameter $a$ has been depicted in figure 6.3 for a given $T$ ($10^{10}$ K) and $\lambda$ (3.75). It is observed that although the variations are similar in nature to those for polytropic flow, but even in this case, limitations in the availability of a substantial range of spin for shocked multi-transonic solutions for all disc geometries, make it impossible to comment on the global trend with which such quantities vary in accordance to black hole spin or the disc configuration. Hence, we try to resolve this issue in the next subsection by looking at the case of mono-transonic isothermal flows.

### 6.2.2 Dependence of $V_\delta$ on $a$ for mono-transonic accretion

Figure 6.4 demonstrates the dependence of the quasi-terminal values of Mach number, density and pressure for mono-transonic isothermal flow on the Kerr parameter. Hot flows with low angular momentum exhibit stationary accretion solutions spanning the complete range of black hole spin. It is observed that the general spin-dependent behaviour of the corresponding physical quantities for three different flow geometries is comparatively well-behaved than the polytropic case, and is evenly consistent over different regions of $a$. The following trends

$$M_\delta^{iso}(CH) > M_\delta^{iso}(CF) > M_\delta^{iso}(VE), \tag{6.1}$$

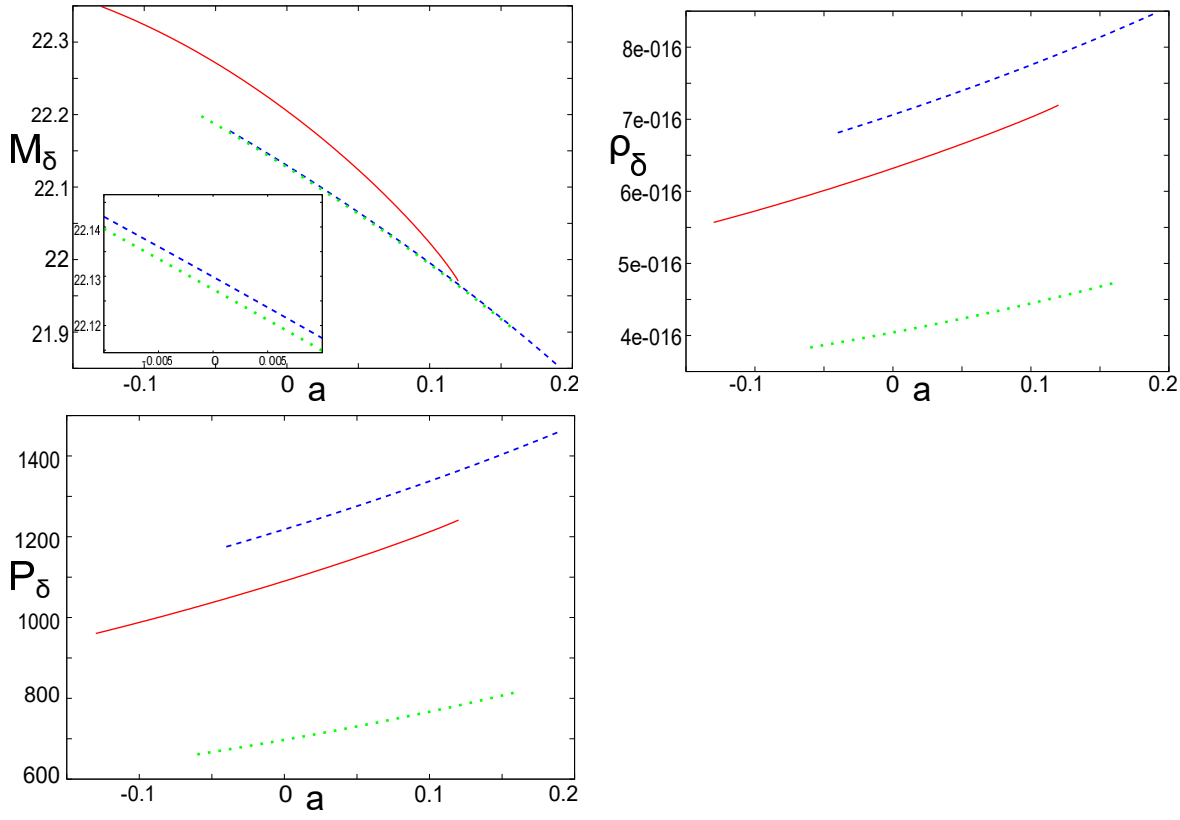


Figure 6.3: Variation of quasi-terminal values of Mach number ($M_\delta$), density ($\rho_\delta$) and pressure ($P_\delta$) with $a$ ($T = 10^{10}K, \lambda = 3.75$) for constant height flow (dashed blue lines), quasi-spherical flow (dotted green lines) and flow in hydrostatic equilibrium (solid red lines). Density and pressure are in CGS units of $g\ cm^{-3}$ and $dyne\ cm^{-2}$ respectively and temperature is in absolute units of Kelvin.

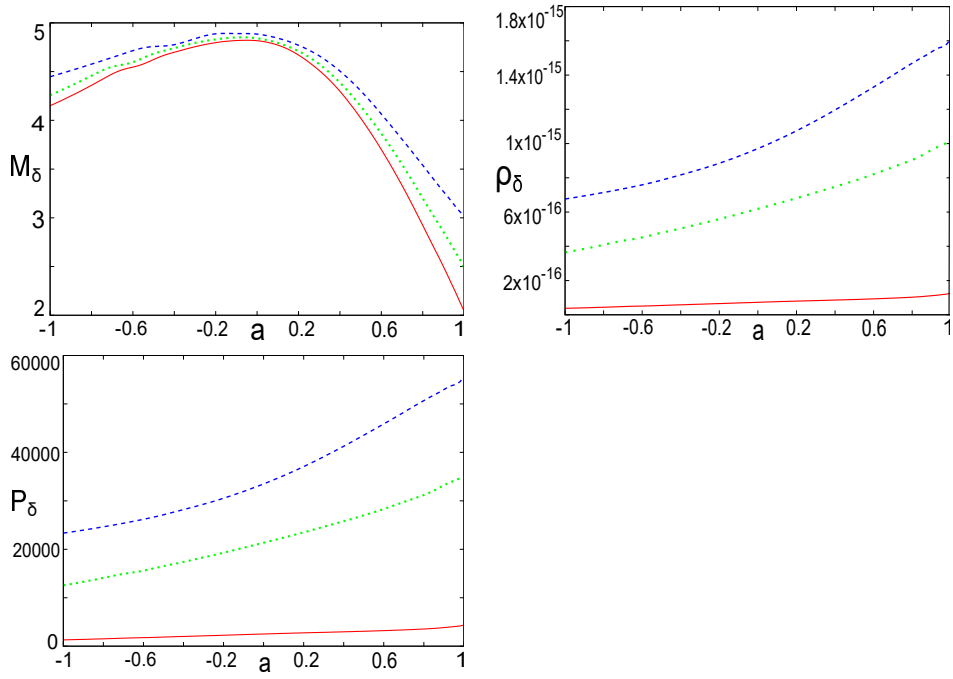


Figure 6.4: Variation of quasi-terminal values of Mach number ($M_\delta$), density ($\rho_\delta$) and pressure ($P_\delta$) with $a$ ($T = 2 \times 10^{11}K, \lambda = 2.0$) for monotransonic accretion in constant height flow (dashed blue lines), quasi-spherical flow (dotted green lines) and flow in hydrostatic equilibrium (solid red lines). Density and pressure are in CGS units of $g\ cm^{-3}$ and $dyne\ cm^{-2}$ respectively and temperature is in absolute units of Kelvin.

$$\rho_{\delta}^{iso}(CH) > \rho_{\delta}^{iso}(CF) > \rho_{\delta}^{iso}(VE), \tag{6.2}$$

$$P_{\delta}^{iso}(CH) > P_{\delta}^{iso}(CF) > P_{\delta}^{iso}(VE), \tag{6.3}$$

are observed throughout the physical range of the Kerr parameter. However, the intrinsic limitations on the range of spin for comparing the $V_{\delta}$ variations for different disc geometries still exist for multi-transonic flows. It is clear from figure 6.4 that quasi-terminal values possess common global trends of variation over $a$ for CH, CF and VE discs. The important observation in this context is the existence of an apparent asymmetry between prograde and retrograde flows. As mentioned in the case of polytropic accretion, such an asymmetry is exceedingly significant for the observation of black hole spin related spectral signatures.

## 6.3 A glimpse of horizon

Computation of quasi-terminal values helps us to understand spectral nature of the photons that are emanated from close proximity of the horizon. Hence, a study into the variation of the quasi-terminal values with $a$ is useful to understand how the black hole spin influences the the shape of the black hole shadow image. The importance of our present work is that –

It investigates the spin dependence of quasi-terminal values for different geometrical configurations and thermodynamic states of the disc.

It shows that prograde and retrograde flows are distinctly marked by asymmetric distributions of relevant quasi-terminal values over the entire theoretical range of black hole spin. This indicates that the constructed image of shadow will be different for the co- and counter rotating flows.

We also observe that the physical quantities responsible to construct the black hole spectra (velocity, density, pressure, temperature (for polytropic accretion) and quasi-specific energy (for isothermal accretion) of the flow) change abruptly at the shock location. This indicates that the discontinuous changes in the physical quantities should get manifested as a break in the corresponding spectral index, and will also show up during the procedure of black hole shadow imaging.

Our work is thus expected to predict how the shape of the image of the shadow might be governed by the dynamical and thermodynamic properties of the accretion flow along with the spin of black hole. Through the construction of such images (large multinational collaborative projects are underway, see e.g. figures 6.5), we will not only be able to provide a possible methodology to look for the observational signatures of black hole spin, but such images will also possibly shed light on the difference between the prograde and retrograde flows from an observational point of view. The Event Horizon Telescope (EHT) team is analysing petabytes of data being recorded by their VLBI instruments across the globe, with an effective baseline comparable with the radius of the earth. In fact, the first-ever shadow- image of a 6.5 billion solar mass supermassive black hole lurking at the centre of

the M87 galaxy – which is 55 million light years away from us – was publicly released by the EHT team on 10th of April, 2019! Although the number and resolution of the images will increase as new data pours in over further epochs of observation, however striking similarities with predictions made using Einstein's theory of gravity have already been observed. An image of the bright radio source at the centre of our own galaxy is still awaited.

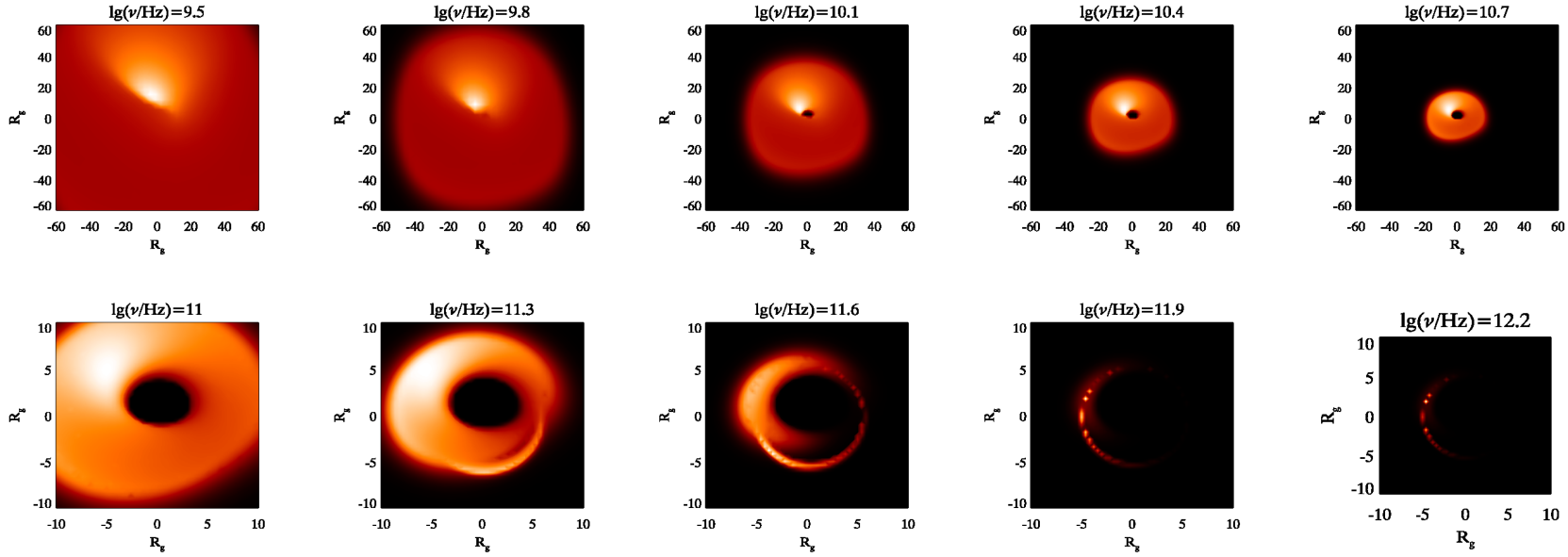


Figure 6.5: Simulated images of the galactic centre. X and Y axes represent radial distances from the galactic centre in terms of the gravitational radius ($R_g$) of the supermassive black hole. Each image corresponds to observation at a different radio-wavelength (Das & Huang 2019 (in preparation)). The accretion considered is mono-transonic. It is evident from the images by the absence of excess luminosity due to shock at any interim radius of the accretion disc. Shadows of the event horizon can be seen as photons emanated due to various radiative processes from different points on the disc are bent around the horizon due to warping of the space-time close to it. The relativistic beaming effect due to dragging of space-time by the rotating black hole can also be seen clearly. The images are obtained using a combination of relativistic radiative transfer codes and general relativistic ray-tracing techniques. The quasi-terminal values of the velocities and the thermodynamic variables obtained from the analytical models of the flow determine the value of the differential intensity of radiation at a given radial distance on the disc. Such values of intensity depend on the specific models of radiative transfer selected in accordance with the given process. Integration of the differential intensity of radiation – depending on the viewing angle and along various lines of sight – is achieved using GR ray-tracing codes which implement the gravitational lensing effects.

# Chapter 7

# Acoustic Black Holes

**Summary**

- ✓ *Acoustic black holes & analogue gravity*
- ✓ *Acoustic metric ($G_{\mu\nu}$) and acoustic surface gravity ($\kappa$)*
- ✓ *A classical model – transonic accretion*
- ✓ *Variation of $\kappa$ with accretion parameters for various flow configurations*

Although striking similarities exist between an ordinary thermodynamic system and a black hole, classical physics forbids black holes to radiate. Black hole radiation is a quantum phenomenon, and the introduction of quantum physics brings about significant changes in the scenario. The black hole radiation effect is known as Hawking effect, and the corresponding radiation and its associated temperature are termed as Hawking radiation and Hawking temperature, respectively. However, the observation of Hawking radiation for astrophysical black holes is beyond the scope of present day instruments due to extremely low temperatures. Moreover, such radiation may possess trans-Planckian frequencies due to gravitational red-shift close to the horizon. These challenges regarding experimental measurement of the Hawking effect motivated physicists to look for an analogue version of the phenomenon. Thus, a theory of analogue or 'acoustic' black holes was introduced.

## 7.1 Analogue gravity

Black holes in general relativity and any diffeomorphism covariant theory of gravity (with field equations directly following from a diffeomorphism covariant Lagrangian), resemble several aspects of classical thermodynamic systems within the classical physics framework (Wald [1984], Wald [1994], Brown [1995], Hehl et al. [1998], Wald [2001]). A number of significant works published during the early seventies (Bekenstein [1972b], Bekenstein [1972a], Bekenstein [1973], Bardeen et al. [1973], Bekenstein [1975], Israel [1976], Bekenstein [1980]) revealed that black holes in general relativity obey certain laws which are analogous to the classical laws of thermodynamics. Such an analogy leads to the

idea of 'surface gravity' of a black hole[1], which can be derived by computing the norm of the gradient of norms of the Killing fields evaluated at the event horizon, and is found to be constant for a given black hole (analogous to constant temperature of a body in thermal equilibrium, i.e. the 'Zeroth Law' of thermodynamics). Moreover, a zero value of surface gravity cannot be attained through any finite number of operations (analogous to the fact that the temperature of a system cannot be reduced to absolute zero, e.g. see discussions in Hehl et al. [1998]). It was found via black hole uniqueness theorem (Heusler [1996] and references therein) that classical thermodynamic entropy is analogous to a constant multiple of the surface area of a classical black hole.

However, the physical temperature of a black hole is absolute zero (see, e.g. Wald [2001]). Hence any physical connection between the surface gravity of a black hole and classical thermodynamic temperature cannot be established. But Stephen Hawking, in his revolutionary paper published in 1975 (Hawking [1975]), used quantum field theoretic calculations in curved space-time to show that the physical temperature and entropy of black hole has finite non-zero value (see Page [2005] and Padmanabhan [2005] for excellent reviews of black hole thermodynamics and Hawking radiation). A linear quantum field, initially in its vacuum state, propagating against the dynamical background of classical space-time describing gravitational collapse leading to the formation of Schwarzschild black hole was considered. The vacuum expectation value of the energy-momentum tensor of this field was found to be negative near the horizon. This negative energy flux decreases black hole mass. The outgoing mode of the quantum field contains particles. The expected number of these outgoing particles was observed to be corresponding with radiation from a finite-sized perfect black body. Hence, the radiation spectrum had to be of thermal nature, and the respective temperature – termed as the Hawking temperature – was computed as,

$$T_H = \frac{\hbar c^3}{8\pi k_B G M_{BH}} \tag{7.1}$$

where $G$, $\hbar$, $c$, $k_B$, $M_{BH}$ are the gravitational constant, reduced Planck constant, velocity of light, Boltzmann constant and black hole mass, respectively.

It is evident that the Hawking temperature of a black hole is inversely proportional to its mass. A rough estimate reveals that $T_H$ for stellar mass black holes would be around $10^7$ times cooler than the cosmic microwave background radiation ($\approx 2.73$ K). Supermassive black holes would radiate at even lower temperatures. Thus, $T_H$ would be detectable only for hypothetical black holes with very small size and mass, known as 'primordial black holes'. Such black holes were proposed to have been formed just seconds after the big bang due to fluctuation-induced gravitational collapse of highly dense regions of *radiation-dominated* universe. The lower stable bound for the mass of such black holes has been estimated to be around $10^{15}$ gm. Although, depending on the model, such black holes can have masses of the order of $10^{-5}$ gm, but primordial black holes with masses lower than the stable bound will have evaporation time-scales (due to Hawking radiation) that are much smaller than the age of our universe, and hence will have ceased to exist by now. The size of primordial black holes with lower stable bounds of mass would roughly be of the order of $10^{-13}$ cm and the corresponding $T_H$ can be calculated to be approximately

[1]Surface gravity may be defined as the acceleration measured by red-shift of light rays passing close to the horizon (Helfer [2003]).

$10^{11}$ K, which is comparable with the macroscopic temperature of matter accreting onto stellar mass or supermassive black holes. However, the existence of primordial black holes is yet to be established, and at present, experimentally achievable resolutions are unable to detect temperatures as small as the theoretically calculated Hawking temperatures of stellar mass black holes. On the other hand, due to infinite gravitational redshift caused at the event horizon, the emergent Hawking radiation is expected to possess trans-Planckian frequencies whose corresponding wavelengths are beyond the Planck scale. Hence, effective low-energy theories cannot self-consistently deal with the Hawking radiation (see Parentani [2002] for further details). The nature of physics at such ultra-short distances is also not well understood. Hence, several fundamental issues like the statistical interpretation of black hole entropy, and the physical origin of the outgoing mode of the quantum field, still remain unresolved (Wald [2001]).

The aforementioned difficulties motivated physicists to look for an analogous theory whose effects can be perceived through experimentally realisable physical systems. The theory of an analogue Hawking phenomenon can create the possibility to verify some basic features of black hole physics in the laboratory. Several works have attempted to propose condensed matter or optical analogues of event horizon. Such analogue theories can have prospective utilities in the investigation of quasi-normal modes (Berti et al. [2004], Cardoso et al. [2004]), acoustic super-radiance (Basak and Majumdar [2003], Basak [2005], Lepe and Saavedra [2005], Slatyer and Savage [2005], Cherubini et al. [2005], Kim et al. [2005], Federici et al. [2006], Choy et al. [2006]), FRW cosmology inflationary models (Barceló et al. [2005]), quantum gravity and sub-Planckian models of string theory (Parentani [2002]).

However, in our work, we concentrate upon the formalism behind classical analogue systems. The 'classical analogue systems' refer to the examples where analogue effects are studied in classical fluids, and not quantum fluids. Detailed description of such systems have been provided in the subsequent sections.

## 7.2 A classical analogue system

Recently, theoretical analogies have been predicted between acoustic perturbations in a fluid, and several kinematic features of space-time in general relativity. An effective metric, describing the geometry of a manifold in which acoustic perturbations propagate, can be constructed. Such a metric is termed as an 'acoustic metric'. Several properties of this effective geometry are analogous to the properties of curved space-time in general relativity. One of the most significant effects of analogue gravity is the 'classical black hole analogue'. An acoustic perturbation (sound wave), dragged by a transonic, classical, inhomogenous, dissipationless fluid, can never cross the 'sonic surface', which is a collection of transonic points in space-time. The location where the fluid becomes supersonic, behaves as a 'trapping' surface for the outgoing phonons. Thus, the sonic surface acts as an acoustic horizon and is found to mimic the electromagnetic event horizon in a number of ways. The acoustic horizon turns to be a null hypersurface generated by acoustic null geodesics (phonons). The acoustic horizon is found to feature an analogue of radiation with a quasi-thermal phonon spectra. Such radiation is considered an analogue of Hawking radiation, and the corresponding temperature is termed as the analogue Hawking temperature ($T_{AH}$). The terms 'analogue', 'acoustic' and 'sonic' will be used

synonymously henceforth, and classical systems in which, the effects of analogue radiation are manifested, will be termed as classical analogue systems.

In his pioneering work, Unruh [1981] simulated the behaviour of a linear quantum field in a classical gravitational field by the propagation of an acoustic perturbation in a convergent fluid flow. Considering the equation of motion for a transonic, barotropic, irrotational fluid, Unruh [1981] showed that the scalar field representing the acoustic perturbation satisfies a differential equation which is analogous to the equation of a massless scalar field propagating in a physical space-time metric. Such a metric has striking resemblance with Schwarzschild metric near the event horizon – which in this case turns out to be the sonic point or the 'acoustic horizon'. The behaviour of normal modes near the acoustic horizon indicates that an analogue radiation with a quasi-thermal spectrum will be emitted from the acoustic horizon and the temperature of such acoustic emission was calculated as (Unruh [1981]):

$$T_{AH} = \frac{\hbar}{4\pi k_B}\left[\frac{1}{c_s}\frac{\partial u_\perp^2}{\partial \eta}\right]_{r_s}, \tag{7.2}$$

where $r_s$ is the location of the sonic horizon, $c_s$ is the sound speed, $u_\perp$ and $\partial/\partial\eta$ are the components of advective velocity and derivative, respectively, normal to the acoustic horizon.

Note that the sound speed $c_s$ is constant indicating that an isothermal equation of state was used by Unruh to describe the fluid. This work was followed by a number of important works (Jacobson [1991], Unruh [1995], Visser [1998], Jacobson [1999], Bilic [1999]). Visser [1998] considered a general barotropic, inviscid, Newtonian fluid in irrotational flow and presented a general treatment of the associated classical analogue radiation. He stated that the equation of motion for the velocity potential describing an acoustic disturbance in the fluid would resemble the d'Alembertian equation of motion for a minimally coupled massless scalar field propagating in a $(3+1)$ dimensional Lorentzian geometry, given by

$$\Box\psi = \frac{1}{\sqrt{-G}}\partial_\mu\left(\sqrt{-G}G^{\mu\nu}\partial_\nu\psi\right) = 0, \tag{7.3}$$

where $\psi$ is the velocity potential of the propagating acoustic perturbation, and $G_{\mu\nu}$ is the so-called *acoustic metric*. It was shown that the acoustic metric for a point sink was conformally related to the Painlevé-Gullstrand-Lemaître form of the Schwarzschild metric (Painlevé [1921], Gullstrand [1922], Lemaître [1933]) and the following general expression for analogue temperature was obtained, where $c_s$ was free to depend on the spatial coordinates (Visser [1998]),

$$T_{AH} = \frac{\hbar}{4\pi k_B}\left[\frac{1}{c_s}\frac{\partial}{\partial\eta}\left(c_s^2 - u_\perp^2\right)\right]_{r_s}. \tag{7.4}$$

Moreover, in all the above classical analogue systems, the fluid is non-relativistic and it flows in the physical background of a flat Minkowski space-time. But the acoustic perturbation propagating through the non-relativistic fluid is coupled to an effective acoustic metric which is curved and hence may be qualitatively classified as pseudo-Riemannian in nature. These limitations were addressed by Bilic [1999], and the formalism was generalized for the flow of relativistic fluids with their respective acoustic metrics in the background of

a physically curved space-time. The expression for the corresponding analogue Hawking temperature was obtained as (Bilic [1999])

$$T_{AH} = \frac{\hbar}{2\pi k_B}\left[\frac{\sqrt{\chi^{\mu}\chi_{\mu}}}{1-c_s^2}\frac{\partial}{\partial\eta}\left|u_{\perp}-c_s\right|\right]_{r_s}, \tag{7.5}$$

where $\chi^{\mu}$ is the Killing vector corresponding to the curved background space-time metric. The detailed derivations for both classical non-relativistic flow in flat Minkowski space-time and classical relativistic flow in curved space-time have been presented in the subsequent sections.

## 7.3 Acoustic geometry in flat background space-time

The continuity and Euler equations for a barotropic, inviscid, Newtonian fluid in irrotational flow with velocity vector $\vec{u}$, density $\rho$ and pressure $p$ are given by,

$$\frac{\partial\rho}{\partial t} + \nabla.(\rho\vec{u}) = 0, \tag{7.6}$$

$$\rho\left[\frac{\partial\vec{u}}{\partial t} + (\vec{u}.\nabla)\vec{u}\right] = -\nabla p - \nabla\Phi. \tag{7.7}$$

where $\Phi$ is the potential associated with any external driving force. Eqn.(7.7) can be recast in the form,

$$\frac{\partial\vec{u}}{\partial t} = \vec{u}\times(\nabla\times\vec{u}) - \frac{\nabla p}{\rho} - \nabla\left(\frac{1}{2}u^2+\Phi\right). \tag{7.8}$$

Defining specific enthalpy $h$ such as $\nabla h = \nabla p/\rho$, velocity potential $\psi$ such that $\vec{u} = -\nabla\psi$ and implementing irrotationality of the flow, eqn.(7.8) can be written down as,

$$-\frac{\partial\psi}{\partial t} + h + \frac{1}{2}(\nabla\psi)^2 + \Phi = 0. \tag{7.9}$$

Introducing the following perturbation scheme –

$$\begin{aligned}
\rho &= \rho^0 + \rho^1 \\
p &= p^0 + p^1 \\
\vec{u} &= \vec{u^0} + \vec{u^1} \\
\psi &= \psi^0 + \psi^1 \\
h &= h^0 + h^1
\end{aligned} \tag{7.10}$$

where $\rho^0$, $p^0$, $u^0$, $\psi^0$ and $h^0$ denote unperturbed values of the corresponding flow variables – the continuity and Euler equations can be linearized to obtain

$$\begin{aligned}
\frac{\partial\rho^0}{\partial t} + \nabla.(\rho^0\vec{u^0}) &= 0 \\
\frac{\partial\rho^1}{\partial t} + \nabla.(\rho^1\vec{u^0} + \rho^0\vec{u^1}) &= 0
\end{aligned} \tag{7.11}$$

and,

$$-\frac{\partial\psi^0}{\partial t}+h^0+\frac{1}{2}(\nabla\psi^0)^2+\Phi=0$$
$$-\frac{\partial\psi^1}{\partial t}+\frac{p^1}{\rho^0}-\vec{u^0}.\nabla\psi^1=0. \tag{7.12}$$

From eqn.(7.12), we get

$$p^1=\rho^0\left(\frac{\partial\psi^1}{\partial t}+\vec{u^0}.\nabla\psi^1\right), \tag{7.13}$$

and hence, using the barotropic assumption,

$$\rho^1=\frac{\partial\rho}{\partial p}p^1=\frac{\partial\rho}{\partial p}\rho^0\left(\frac{\partial\psi^1}{\partial t}+\vec{u^0}.\nabla\psi^1\right). \tag{7.14}$$

Substituting eqn.(7.14) in eqn.7.11, and defining sound speed as $c_s^2=\partial p/\partial\rho$ at constant specific entropy, we obtain the equation for propagation of disturbance in $\psi$,

$$-\frac{\partial}{\partial t}\left[\frac{\rho^0}{c_s^2}\left(\frac{\partial\psi^1}{\partial t}+\vec{u^0}.\nabla\psi^1\right)\right]+\nabla.\left[\rho^0\nabla\psi^1-\frac{\rho^0}{c_s^2}\vec{u^0}\left(\frac{\partial\psi^1}{\partial t}+\vec{u^0}.\nabla\psi^1\right)\right]=0 \tag{7.15}$$

Then we are required to define a quantity $f^{\mu\nu}$ such that eqn.(7.15) is reduced to the following form describing the propagation of a linearized scalar potential $\psi^1$,

$$\partial_\mu(f^{\mu\nu}\partial_\nu\psi^1)=0. \tag{7.16}$$

From observation, one can readily define $f^{\mu\nu}$ as a $4\times4$ matrix given by,

$$f^{\mu\nu}=\frac{\rho^0}{c_s^2}\left[\begin{array}{c:c}-1 & -\vec{u}^0\\ \hdashline -\vec{u}^0 & (c_s^2\delta^{ij}-(u^0)^i(u^0)^j)\end{array}\right] \tag{7.17}$$

with latin indices running from 1 to 3.

From eqn.(7.17), the determinant of $f^{\mu\nu}$ is given by

$$det(f^{\mu\nu})=\left(\frac{\rho^0}{c_s^2}\right)^4\left[-(c_s^2-(u^0)^2)-(-\vec{u^0}).(-\vec{u^0})\right]\left[c_s^2\right]\left[c_s^2\right]=-\frac{(\rho^0)^4}{c_s^2}. \tag{7.18}$$

Now defining, $f^{\mu\nu}=\sqrt{-G}G^{\mu\nu}$,

$$det(f^{\mu\nu})=(\sqrt{-G})^4G^{-1}=G. \tag{7.19}$$

Therefore,

$$G=-\frac{(\rho^0)^4}{c_s^2};\ \sqrt{-G}=\frac{(\rho^0)^2}{c_s}. \tag{7.20}$$

Hence,

$$G^{\mu\nu}=\frac{1}{\sqrt{-G}}f^{\mu\nu}=\frac{1}{\rho^0c_s}\left[\begin{array}{c:c}-1 & -\vec{u}^0\\ \hdashline -\vec{u}^0 & (c_s^2\delta^{ij}-(u^0)^i(u^0)^j)\end{array}\right]. \tag{7.21}$$

The new effective acoustic metric $G_{\mu\nu}$ describes the *acoustic geometry* of the classical analogue system, and is given by the $4\times4$ matrix,

$$G_{\mu\nu}=\frac{\rho^0}{c_s}\left[\begin{array}{c:c}-(c_s^2-(u^0)^2) & -\vec{u}^0\\ \hdashline -\vec{u}^0 & I\end{array}\right] \tag{7.22}$$

where $I$ is the $3 \times 3$ identity matrix. Thus, in terms of the acoustic metric $G_{\mu\nu}$, the equation of propagation of acoustic perturbation (sound waves) in a barotropic, inviscid, Newtonian fluid (eqn.(7.15)) can be written down in the form of an equation describing the propagation of perturbations in a linear massless scalar field with a $(3+1)$ dimensional background Lorentzian geometry as,

$$\Box\psi^1 = \frac{1}{\sqrt{-G}}\partial_\mu\left(\sqrt{-G}G^{\mu\nu}\partial_\nu\psi^1\right) = 0. \tag{7.23}$$

In other words, the sound wave while propagating through the fluid, sees something analogous to a real physical pseudo-Riemannian $(3+1)$ space-time manifold described by $G_{\mu\nu}$.

The phenomenon is even more interesting as $G_{\mu\nu}$ does not only mimic space-time in the above dynamical equation, but it also manifests various other properties of real physical space-time, as we describe below –

The acoustic interval can be written as,

$$ds^2 = G_{\mu\nu}dx^\mu dx^\nu = \frac{\rho^0}{c_s}\left[-c_s^2dt^2 + \left(dx^i - (u^0)^i dt\right)\delta_{ij}\left(dx^j - (u^0)^j dt\right)\right]. \tag{7.24}$$

It is observed that $G_{\mu\nu}$ has a Lorentzian $(-+++)$ signature. General relativistic properties and concepts such as 'stable causality', 'proper time', 'ergo-regions', 'trapped surfaces', 'apparent horizon' and 'event horizon' are readily inherited by the acoustic metric.

Consider the following analogue of the time-translational Killing vector for a steady flow given by $\xi^\mu = (\partial/\partial t)^\mu = (1, 0, 0, 0)$. Therefore,

$$G_{\mu\nu}\xi^\mu\xi^\nu = -\frac{\rho^0}{c_s}(c_s^2 - (u^0)^2), \tag{7.25}$$

which changes sign immediately when $(u^0)^2 > c_s^2$, i.e., the fluid flow becomes supersonic. Thus, in analogy to the case of a spinning black hole whose ergo-region is defined by that region where space moves with superluminal velocities, for a steady transonic flow, the analogue ergo-region shall be defined by that region where the fluid moves supersonically. The boundary of such transonic region may be termed as the analogue ergo-sphere.

Now let us express the fluid velocity in the vicinity of the acoustic horizon in terms of components that are normal and tangential to the horizon,

$$\vec{u} = \vec{u}_\perp + \vec{u}_\parallel. \tag{7.26}$$

Henceforth, we shall drop the superscripts denoting unperturbed values for the sake of notational convenience.

Considering a vector field $L^\mu$ given by

$$L^\mu = (1; u^i_\parallel), \tag{7.27}$$

such that the spatial components of $L^\mu$ are tangential to a constant-time slice through the horizon. Thus, integral curves of $L^\mu$ would give us the acoustic horizon.

The norm of $L^\mu$ can be obtained as,

$$\begin{aligned} ||L||^2 &= G_{\mu\nu}L^\mu L^\nu \\ &= -\frac{\rho}{c_s}\left[-(c_s^2-u^2)-2\vec{u_\parallel}.\vec{u}+\vec{u_\parallel}.\vec{u_\parallel}\right] \\ &= -\frac{\rho}{c_s}\left[-(c_s^2-u^2)-u_\parallel^2\right] \\ &= \frac{\rho}{c_s}(c_s^2-u_\perp^2) \end{aligned} \tag{7.28}$$

By definition, $u_\perp = c_s$ at the acoustic horizon. Hence $L^\mu$ becomes a null vector field on the acoustic horizon, whose integral curves generate the horizon. Now, although $L^\mu$ is not normalized with an affine parameter, one can verify that these generators are in fact geodesics, and thus calculate the analogue surface gravity as follows –

$$(\vec{L}.\nabla)\vec{L} = -\vec{L}\times(\nabla\times\vec{L}) + \frac{1}{2}\nabla(L^2), \tag{7.29}$$

or, in the index notation,

$$L^\alpha\nabla_\alpha L^\mu = L^\alpha(\nabla_\alpha L_\beta - \nabla_\beta L_\alpha)g^{\beta\mu} + \frac{1}{2}\nabla_\beta(L^2)g^{\beta\mu}. \tag{7.30}$$

Now,

$$\begin{aligned} L_\mu &= G_{\mu\nu}L^\nu \\ &= \frac{\rho}{c_s}\left[\begin{array}{c:c} -(c_s^2-u^2) & -u^i \\ \hdashline -u^i & I \end{array}\right]\left[\begin{array}{c} 1 \\ u_\parallel^i \end{array}\right] \\ &= -\frac{\rho}{c_s}\left[\begin{array}{c} (c_s^2-u_\perp^2) \\ \vec{u}_\perp \end{array}\right] \end{aligned} \tag{7.31}$$

Therefore,

$$L^\alpha L_{[\beta,\alpha]} = \left[\begin{array}{c} \vec{u}_\parallel.\nabla\left[\frac{\rho}{c_s}(c_s^2-u_\perp^2)\right] \\ \nabla_j\left[\frac{\rho}{c_s}(c_s^2-u_\perp^2)\right] + u_\parallel^i(\frac{\rho}{c_s}u_\perp)_{[j,i]} \end{array}\right], \tag{7.32}$$

and

$$\nabla_\beta\left(L^2\right) = \left[\begin{array}{c} 0 \\ \nabla_j\left[\frac{\rho}{c_s}(c_s^2-u_\perp^2)\right] \end{array}\right]. \tag{7.33}$$

Since $u_\perp = c_s$ at the acoustic horizon, eqn.(7.32) and eqn.(7.33) become

$$\begin{aligned} L^\alpha L_{[\beta,\alpha]} &= -\frac{\rho}{c_s}\left[\begin{array}{c} 0 \\ \nabla_j(c_s^2-u_\perp^2) \end{array}\right] \\ \nabla_\beta\left(L^2\right) &= \frac{\rho}{c_s}\left[\begin{array}{c} 0 \\ \nabla_j(c_s^2-u_\perp^2) \end{array}\right] \end{aligned} \tag{7.34}$$

Hence from eqn.(7.30)

$$L^\alpha\nabla_\alpha L^\mu = \frac{1}{2c_s^2}\left[\begin{array}{c} u^j\nabla_j(c_s^2-u_\perp^2) \\ (c_s^2\delta^{ij}-u^iu^j)\nabla_j(c_s^2-u_\perp^2) \end{array}\right]. \tag{7.35}$$

Now, the gradient term has to be normal at the acoustic horizon, and therefore from eqn.(7.35), we get

$$L^{\alpha}\nabla_{\alpha}L^{\mu} = \frac{1}{2c_s}\frac{\partial}{\partial\eta}\left(c_s^2 - u_{\perp}^2\right)\begin{bmatrix} 1 \\ \vec{u}_{\parallel} \end{bmatrix} = \frac{1}{2c_s}\frac{\partial}{\partial\eta}\left(c_s^2 - u_{\perp}^2\right)L^{\mu}. \tag{7.36}$$

Comparing with the standard definition of surface gravity, we realise that the $L^{\mu}$ is not only a null generator of the acoustic horizon, but inspite of not being normalized with an affine parameter, it is also an analogue geodesic, and the analogue or 'acoustic' surface gravity is given by (Visser [1998]),

$$\kappa = \frac{1}{2}\frac{\partial}{\partial\eta}(c_s^2 - u_{\perp}^2)|_{r_s}. \tag{7.37}$$

The corresponding analogue Hawking temperature can be obtained as,

$$T_{AH} = \frac{\hbar\kappa}{2\pi k_B c_s} = \frac{\hbar}{4\pi k_B}\left[\frac{1}{c_s}\frac{\partial}{\partial\eta}(c_s^2 - u_{\perp}^2)\right]_{r_s}. \tag{7.38}$$

Note that in the above formalism $G_{\mu\nu}$ and $g_{\mu\nu}$ (real physical background space-time) appear to be decoupled. However, one needs to remember that $G_{\mu\nu}$ is explicitly dependent on the dynamical velocities of the fluid flow, which in the present non-relativistic case with flat background space-time do not seem to carry any impression of $g_{\mu\nu}$. But the scenario will change when relativistic flows in curved physical space-times are considered as the respective analogue models. This is the most important reason for us to deviate momentarily from the problem of astrophysical accretion and talk about analogue gravity. As the title of the thesis suggested in the very beginning, our aim has been to study black hole accretion as a classical analogue model. Black hole accretion is nothing but the relativistic flow of astrophysical fluids in curved space-time. Hence the corresponding acoustic geometry is bound to contain information about the background physical geometry which in turn imbibes information regarding black hole mass and spin.

## 7.4 Acoustic geometry in curved background space-time

First of all, basic relativistic fluid dynamics is formulated for a perfect gravitating relativistic fluid with four velocity $u_{\mu}$, pressure $p$, total mass-energy density $\epsilon$, particle number density $\rho$ and entropy density $s$. The energy-momentum tensor is then given by,

$$T_{\mu\nu} = (p + \epsilon)u_{\mu}u_{\nu} + pg_{\mu\nu} \tag{7.39}$$

$g_{\mu\nu}$ is the physical space-time metric, and the velocity normalization is given by $u_{\mu}u^{\mu} = g_{\mu\nu}u^{\nu}u^{\mu} = -1$.

The relativistic continuity equation is given by,

$$(\rho u^{\mu})_{;\mu} = \frac{1}{\sqrt{-g}}\partial_{\mu}(\sqrt{-g}\rho u^{\mu}) = 0, \tag{7.40}$$

and the energy-momentum conservation equation is given by,

$$T^{\mu\nu}_{\ ;\nu} = \partial_{\nu}p + u_{\mu}u^{\nu}\partial_{\nu}p + (p + \epsilon)u^{\nu}u_{\mu;\nu} = 0. \tag{7.41}$$

Now, given $h = (p + \epsilon)/\rho$ is the specific enthalpy of the fluid such that

$$dh = Td\left(\frac{s}{\rho}\right) + \frac{dp}{\rho}, \tag{7.42}$$

where $T$ is the flow temperature, eqn.(7.41) reduces to

$$u^{\nu}\left(hu_{\mu}\right)_{;\nu} - \partial_{\mu}h = 0. \tag{7.43}$$

Adding the irrotationality condition given by

$$\omega_{\mu\nu} = (\delta^{\rho}_{\mu} - u^{\rho}u_{\mu})(\delta^{\sigma}_{\nu} - u^{\sigma}u_{\nu})u_{[\rho;\sigma]} = 0, \tag{7.44}$$

the Euler's equation further simplifies to (Taub [1978])

$$\left(hu_{\mu}\right)_{;\nu} - \left(hu_{\nu}\right)_{;\mu} = 0. \tag{7.45}$$

Thus, the quantity $hu_{\mu}$ can be defined using a potential function $\psi$ such that

$$hu_{\mu} = \partial_{\mu}\psi. \tag{7.46}$$

Eqn.(7.46) is an analogue for potential flow in relativistic fluids. The perturbation scheme used to linearize the continuity and Euler's equations is given by,

$$\begin{aligned} h &= h + \delta h \\ \rho &= \rho + \delta\rho \\ u^{\mu} &= u^{\mu} + \delta u^{\mu} \\ \psi &= \psi + \delta\psi. \end{aligned} \tag{7.47}$$

The normalization condition for $u^{\mu}$ implies

$$g_{\mu\nu}u^{\mu}\delta u^{\nu} = 0. \tag{7.48}$$

Substituting eqn.(7.47) in eqn.(7.46),

$$\delta h g_{\mu\nu}u^{\nu} + h g_{\mu\nu}\delta u^{\nu} = \partial_{\mu}\delta\psi. \tag{7.49}$$

Multiplying eqn.(7.49) with $u^{\mu}$ and utilising the normalization condition for $u^{\mu}$ along with eqn.(7.48), we get

$$\delta h = -u^{\mu}\partial_{\mu}\delta\psi, \tag{7.50}$$

and substituting eqn.(7.50) in eqn.(7.49), we obtain

$$h\delta u^{\mu} = -g^{\mu\nu}\partial_{\mu}\delta\psi + u^{\mu}u^{\nu}\partial_{\mu}\delta\psi. \tag{7.51}$$

Defining $\delta\rho = (\partial\rho/\partial h)\delta h$, and substituting eqn.(7.50) and eqn.(7.51) in eqn.(7.40), we derive the following equation,

$$\partial_{\mu}\left[\frac{\rho}{h}\sqrt{-g}\left\{g^{\mu\nu} - \left(1 - \frac{h}{\rho}\frac{\partial\rho}{\partial h}\right)u^{\mu}u^{\nu}\right\}\partial_{\nu}\delta\psi\right] = 0. \tag{7.52}$$

A comparision of the above equation with eqn.(7.3) reveals that eqn.(7.52) is identical to an equation describing the propagation of a massless scalar field $\delta\psi$ in the background of a $(3+1)$ pseudo-Riemannian geometry which is characterised by a metric $G_{\mu\nu}$, such that

$$\sqrt{-G}G^{\mu\nu} = \frac{\rho}{h}\sqrt{-g}\left[g^{\mu\nu} - \left(1 - \frac{h}{\rho}\frac{\partial\rho}{\partial h}\right)u^{\mu}u^{\nu}\right]. \tag{7.53}$$

Hence, $G_{\mu\nu}$ is the effective analogue or 'acoustic' metric for fluid flow in curved space-time.

Now from eqn.(7.42) for a process with constant specific entropy, the speed of propagation of the acoustic perturbation is given by

$$c_s^2 = \frac{\partial p}{\partial \rho} \equiv \frac{\rho}{h}\frac{\partial h}{\partial \rho}. \tag{7.54}$$

Therefore

$$f^{\mu\nu} = \sqrt{-G}G^{\mu\nu} = \frac{\rho}{h}\sqrt{-g}\left[g^{\mu\nu} - \left(1 - c_s^{-2}\right)u^\mu u^\nu\right] \tag{7.55}$$

or,

$$G^{\mu\nu} = \frac{1}{\sqrt{-G}}f^{\mu\nu} = \frac{\rho\sqrt{-g}}{h\sqrt{-G}}\left[g^{\mu\nu} - \left(1 - c_s^{-2}\right)u^\mu u^\nu\right]. \tag{7.56}$$

Hence acoustic metric $G_{\mu\nu}$ should be given by

$$G_{\mu\nu} = k\left[g_{\mu\nu} - (1 - c_s^2)u_\mu u_\nu\right] \tag{7.57}$$

where $k$ is a conformal factor.

Using eqn.(7.56), eqn.(7.57) and the normalization condition for $u^\mu$, we obtain

$$\begin{aligned} G^{\mu\gamma}G_{\gamma\nu} &= k\frac{\rho\sqrt{-g}}{h\sqrt{-G}}\left[g^{\mu\nu} - \left(1 - c_s^{-2}\right)u^\mu u^\nu\right]\left[g_{\mu\nu} - (1 - c_s^2)u_\mu u_\nu\right] \\ &= k\frac{\rho\sqrt{-g}}{h\sqrt{-G}}\delta^\mu_\nu. \end{aligned} \tag{7.58}$$

In a general co-moving co-ordinate system, the 4-velocity of the stationary fluid flow is along the time-translation Killing vector $\xi = (1; \vec{0})$, whose unit vectors are given by,

$$t^\mu = \frac{\xi^\mu}{\sqrt{\xi^\nu\xi_\nu}} = \frac{\delta^\mu_0}{\sqrt{g_{00}}}, \tag{7.59}$$

and

$$t_\mu = \frac{\xi_\mu}{\sqrt{\xi^\nu\xi_\nu}} = \frac{g_{\mu 0}}{\sqrt{g_{00}}}. \tag{7.60}$$

Therefore

$$\begin{aligned} G &= k^4 det\left[g_{\mu\nu} - (1 - c_s^2)u_\mu u_\nu\right] \\ &= k^4 det\left[g_{\mu\nu} - (1 - c_s^2)\frac{g_{\mu 0}g_{\nu 0}}{g_{00}}\right] \\ &= k^4 g c_s^2 \end{aligned} \tag{7.61}$$

Thus, from eqn.(7.58)

$$k = \frac{\rho}{hc_s}, \tag{7.62}$$

and hence the acoustic metric for relativistic fluid flow in curved space-time is given by,

$$G_{\mu\nu} = \frac{\rho}{hc_s}\left[g_{\mu\nu} - (1 - c_s^2)u_\mu u_\nu\right]. \tag{7.63}$$

Defining the boundary of ergo-region as the hypersurface on which norm of the time-translation Killing vector changes its sign, we have

$$\xi^2 = G_{\mu\nu}\xi^\mu\xi^\nu = \frac{\rho}{hc_s}\left[g_{00} - (1 - c_s^2)u_0 u_0\right]. \tag{7.64}$$

In order to find $u_0$ let us define $u_\mu$ as a combination of two components, one parallel to $t_\mu$ and the other orthogonal to $t_\mu$, i.e.

$$u_\mu = \gamma t_\mu + (g_{\mu\nu} - t_\mu t_\nu)u^\nu \tag{7.65}$$

where $g_{\mu\nu} - t_\mu t_\nu$ is the orthogonal projection operator and $\gamma = t^\mu u_\mu$. Therefore from eqn.(7.59),

$$u_0 = \gamma\sqrt{g_{00}}. \tag{7.66}$$

Since $\gamma$ can also be written in terms of the advective velocity $u$ as $\gamma^2 = \frac{1}{1-u^2}$, hence

$$\xi^2 = \frac{\rho g_{00}}{h c_s}\left[\frac{c_s^2 - u^2}{1-u^2}\right]. \tag{7.67}$$

Therefore the ergo-region for $G_{\mu\nu}$ describing acoustic geometry in curved space-time is also bounded by the hypersurface $\Sigma_{c_s} \equiv c_s^2 - u^2 = 0$, as it was for acoustic geometry in flat space-time. The normal to $\Sigma_{c_s}$ is given by $n \propto \partial_\mu u^2$. The 4-velocity of the fluid can be decomposed into normal and tangential components w.r.t $\Sigma_{c_s}$ as

$$\begin{aligned} u^\mu &= \gamma_\perp u_\perp n^\mu + (g^{\mu\nu} + n^\mu n^\nu)u_\nu \\ &= \gamma_\perp u_\perp n^\mu + \gamma_\perp L^\mu, \end{aligned} \tag{7.68}$$

where

$$L^\mu = \frac{1}{\gamma_\perp}(g^{\mu\nu} + n^\mu n^\nu)u_\nu \tag{7.69}$$

is the time-like unit vector representing a displacement in $\Sigma_{c_s}$ along the projection of $u^\mu$. The norm of $L^\mu$ can be calculated as

$$||L||^2 = G_{\mu\nu}L^\mu L^\nu \equiv \left[1 - (1-c_s^2)\gamma_\perp^2\right] = \gamma_\perp^2(c_s^2 - u_\perp^2). \tag{7.70}$$

It is evident that $L^\mu$ is a null vector on the acoustic horizon and represents the component of flow velocity which is tangential to $\Sigma_{c_s}$. Thus the integral curves of $L^\mu$ would generate the acoustic horizon.

Now we construct the Killing vector $\chi^\mu$ as

$$\chi^\mu = \xi^\mu + \Omega\phi^\mu, \tag{7.71}$$

where $\xi^\mu$ is the time-translation Killing vector and $\phi^\mu = \delta^\mu_\phi$ (in an appropriately transformed coordinate system) is the generator of isometry group of displacements on the horizon. $\Omega$ is analogous to the horizon angular velocity of a Kerr black hole, and is chosen such that $\chi^\mu$ becomes parallel to $L^\mu$ and hence is null on the acoustic horizon. Thus in the given co-ordinate system $L^\mu$ takes the form

$$L^\mu = \gamma_\parallel\left(\frac{1}{\sqrt{g_{00}}} - \frac{g_{0\phi}u_\phi}{g_{00}}; u_\phi, 0, 0\right). \tag{7.72}$$

Since this $L^\mu$ has to be parallel to $\chi^\mu$ on the horizon, we set

$$\chi^\mu = \sqrt{\chi^\nu\chi_\nu}L^\mu, \tag{7.73}$$

where

$$\sqrt{\chi^\nu\chi_\nu} = \frac{1}{\gamma_\parallel}\left(\frac{1}{\sqrt{g_{00}}} - \frac{g_{0\phi}u_\phi}{g_{00}}\right)^{-1}. \tag{7.74}$$

From eqn.(7.70) and eqn.(7.73),

$$||\chi||^2 = \gamma_\perp^2 (c_s^2 - u_\perp^2)\chi^\nu \chi_\nu. \tag{7.75}$$

Now, the acoustic surface gravity may be calculated using (Wald [1984])

$$G^{\mu\nu}\partial_\nu ||\chi||^2 = -2\kappa\chi^\mu. \tag{7.76}$$

Since $\chi^\mu$ is null at the horizon, therefore $\partial_\nu ||\chi||^2$ at the horizon will be given by

$$\partial_\nu ||\chi||^2_{r_h} = n_\nu \frac{\partial}{\partial n}||\chi||^2. \tag{7.77}$$

Therefore, from eqn.(7.76)

$$G^{\mu\nu} n_\nu \frac{\partial}{\partial n}||\chi||^2 = 2\kappa\chi^\mu \tag{7.78}$$

where $\partial/\partial n = \partial^\mu n_\mu$. From eqn.(7.69) and eqn.(7.73), we obtain

$$G^{\mu\nu} n_\nu = n^\mu - \frac{1}{u_\perp \gamma_\perp} u^\mu = -\frac{1}{u_\perp}\frac{\chi^\mu}{\sqrt{\chi^\nu \chi_\nu}}. \tag{7.79}$$

Substituting eqn.(7.75) and eqn.(7.79) in eqn.(7.78), the analogue or acoustic surface gravity for relativistic fluid flow in curved space-time can be calculated as (Bilic [1999])

$$\kappa = \left[\frac{\sqrt{\chi^\nu \chi_\nu}}{1 - c_s^2}\frac{\partial}{\partial n}|u_\perp - c_s|\right]_{r_s}. \tag{7.80}$$

Note that surface gravity remains unaffected by the conformal factor in the acoustic metric, and hence all conformal factors were dropped in the above calculations leading to an expression for $\kappa$. The corresponding analogue Hawking temperature can be readily written down as,

$$T_{AH} = \frac{\hbar}{2\pi k_B}\left[\frac{\sqrt{\chi^\nu \chi_\nu}}{1 - c_s^2}\frac{\partial}{\partial n}|u_\perp - c_s|\right]_{r_s}. \tag{7.81}$$

Now that we are equipped with the expressions for $\kappa$ simply in terms of the physical metric elements, the advective flow velocities, the sound speed and their spatial derivatives, we proceed to apply this whole analogue formalism of relativistic flow in curved space-time to the general relativistic model of axisymmetric, low angular momentum, inviscid accretion onto a supermassive black hole at the galactic centre that has been so elaborately discussed throughout this book. In the subsequent sections, we shall calculate the value of the acoustic surface gravity at the acoustic horizons (transonic surfaces) of the accretion discs and investigate its variation with various accretion parameters for various flow configurations.

## 7.5 Variation of $\kappa$ - polytropic accretion

We concentrate on the equatorial slice of a disc formed by general relativistic hydrodynamic, low angular momentum, inviscid, axisymmetric accretion onto both non-rotating and spinning supermassive astrophysical black holes. Owing to the transonic nature of accretion (both mono-transonic and multi-transonic), the configuration leads to an interesting acoustic geometry where multiple acoustic horizons may be formed. We shall calculate the acoustic surface gravity for such horizon(s), which is the characteristic feature of the perturbative manifold, and study how the sonic point location and the acoustic

surface gravity depend on various accretion parameters which are the characteristic features of the background fluid continuum for both polytropic and isothermal equations of state and for three different disc geometries around a Schwarzschild black hole (Tarafdar and Das [2015]). Similarly, we shall also study the dependence of the acoustic surface gravity and the sonic point location on the spin angular momentum of a rotating astrophysical black hole, with different flow geometries and equations of state (Tarafdar and Das [2018a]).

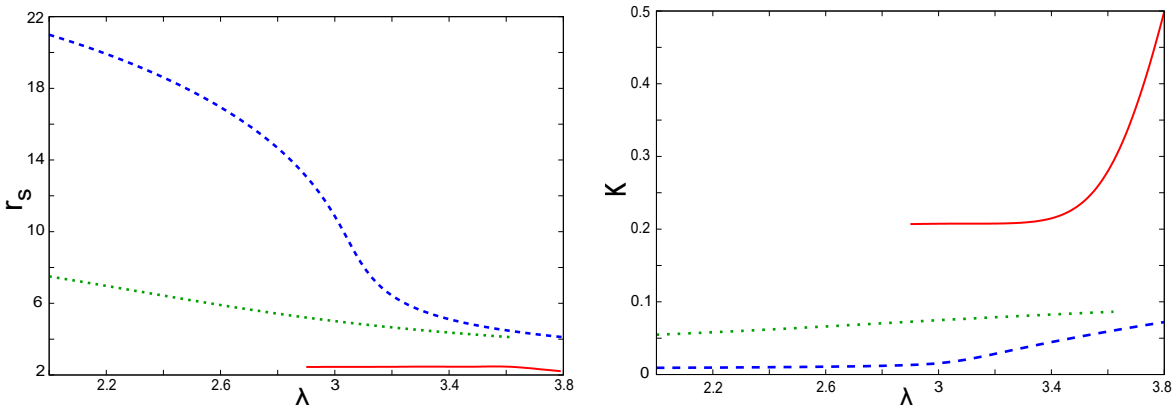


Figure 7.1: (a) $r_s - \lambda$ and (b) $\kappa - \lambda$ plots ($\mathcal{E} = 1.12, \gamma = 4/3, a = 0$) for monotransonic polytropic accretion. Blue dashed curve, green dotted curve and red solid curve represent CH, CF and VE flows respectively.

In figure 7.1(a), for a fixed set of $[\mathcal{E} = 1.12, \gamma = 4/3, a = 0]$, we plot the location of the inner-type acoustic horizon (the inner sonic point $r_s$) as a function of the specific angular momentum $\lambda$ of the flow for mono-transonic stationary accretion solution for three different disc geometries around a Schwarzschild black hole. It is observed that the location of the acoustic horizon anti-correlates with $\lambda$. This is somewhat obvious because for greater amount of rotational energy content of the flow, accretion starts with smaller advective velocity and has to approach very close to the event horizon to acquire the dynamical velocity sufficiently large to smoothly surpass the acoustic velocity.

For a specified initial boundary condition describing the flow, one observes

$$r_s^{CH} > r_s^{CF} > r_s^{VE}. \tag{7.82}$$

This indicates that for the same set of $[\mathcal{E}, \lambda, \gamma]$, the acoustic horizon for accretion discs in hydrostatic equilibrium along the vertical direction, forms at the closest proximity of the Schwarzschild black hole event horizon and hence the relativistic acoustic geometry at the neighbourhood of such acoustic horizons are subjected to considerably curved spacetime. One thus intuitively concludes that among all three flow configurations considered in this work, the Hawking-like effects may perhaps be more pronounced for axisymmetric background flow in hydrostatic equilibrium along the vertical direction. This intuitive conclusion is further supported by results presented in figure 7.1(b), where we have studied the variation of the acoustic surface gravity $\kappa$ as a function of the flow angular momentum $\lambda$ for the same set of initial boundary conditions and same range of $\lambda$ for which figure 7.1(a) has been obtained. For identical values of $[\mathcal{E}, \lambda, \gamma, a]$, one obtains

$$\kappa^{VE} > \kappa^{CF} > \kappa^{CH}. \tag{7.83}$$

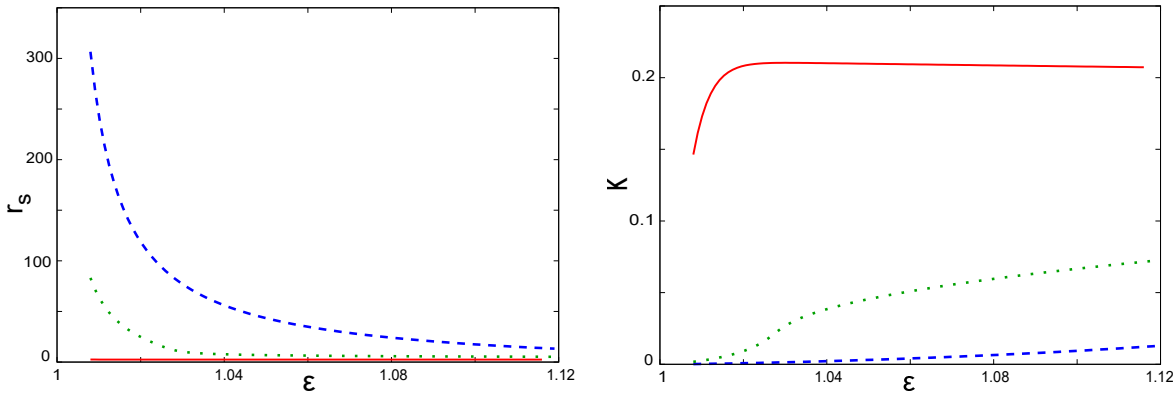


Figure 7.2: (a) $r_s - \mathcal{E}$ and (b) $\kappa - \mathcal{E}$ plots ($\lambda = 2.89, \gamma = 4/3, a = 0$) for monotransonic polytropic accretion. Blue dashed curve, green dotted curve and red solid curve represent CH, CF and VE flows respectively.

For a fixed value of $[\lambda = 2.89, \gamma = 4/3, a = 0]$, the variation of the location of the inner acoustic horizons (the inner sonic points $r_s$) as a function of the specific flow energy $\mathcal{E}$ is plotted in figure 7.2(a). $r_s$ anti-correlates with $\mathcal{E}$ for obvious reasons. At a large distance away from the accretor, the total specific energy is essentially determined by the thermal energy of the flow, a large value of $\mathcal{E}$ ('hot' accretion) corresponds to a high value of the sound speed $c_s$ to begin with. The subsonic to supersonic transition takes place quite close to the black hole where the bulk flow velocity (the advective velocity $u$) becomes large enough to overtake the sound speed. Once again, flow in vertical hydrostatic equilibrium produces the acoustic horizons located at a relatively stronger gravity region. The analogue effect should be more pronounced for such geometric configuration of the flow. Results presented in figure 7.2(b), where the acoustic surface gravity $\kappa$ has been plotted as a function of the specific energy of the flow for the same set of $[\lambda, \gamma, a]$ used to draw figure 7.2(a), assert such conclusion.

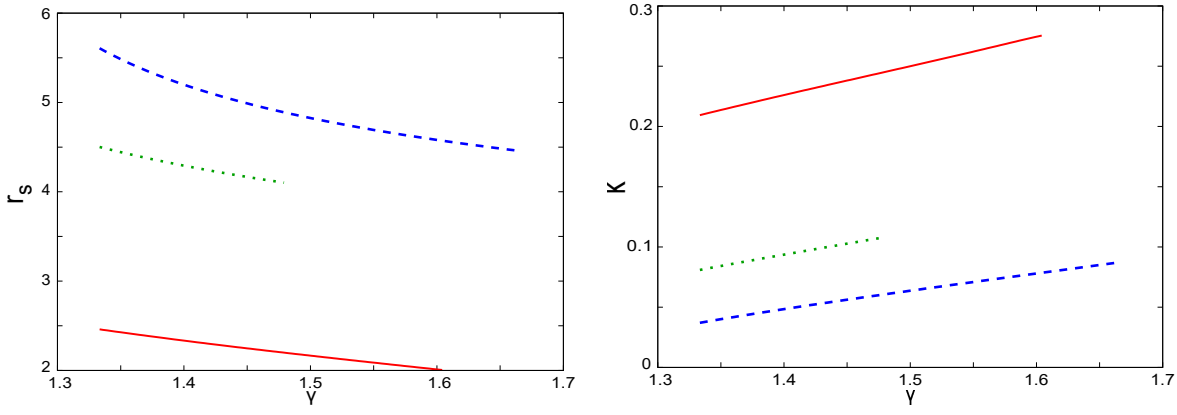


Figure 7.3: (a) $r_s - \gamma$ and (b) $\kappa - \gamma$ plots ($\mathcal{E} = 1.12, \lambda = 3.3, a = 0$) for monotransonic polytropic accretion. Blue dashed curve, green dotted curve and red solid curve represent CH, CF and VE flows respectively.

For a fixed value of $[\mathcal{E} = 1.12, \lambda = 3.3, a = 0]$, in figure 7.3(a), we find that the location of the acoustic horizon anti-correlates with $\gamma$ and hence the acoustic surface gravity $\kappa$ co-relates with $\gamma$ as expected (figure 7.3(b)). Similar results can be obtained for any set of $[\mathcal{E}, \lambda, a]$ for which mono-transonic stationary accretion passing through the inner type sonic point can be obtained for all three flow configurations considered in this work. Here too the acoustic surface gravity for accretion discs in vertical hydrostatic equilibrium is

maximum (compared to CF and CH discs). We thus obtain

$$r_s^{CH} > r_s^{CF} > r_s^{VE} \tag{7.84}$$

and,

$$\kappa^{VE} > \kappa^{CF} > \kappa^{CH} \tag{7.85}$$

in this case as well.

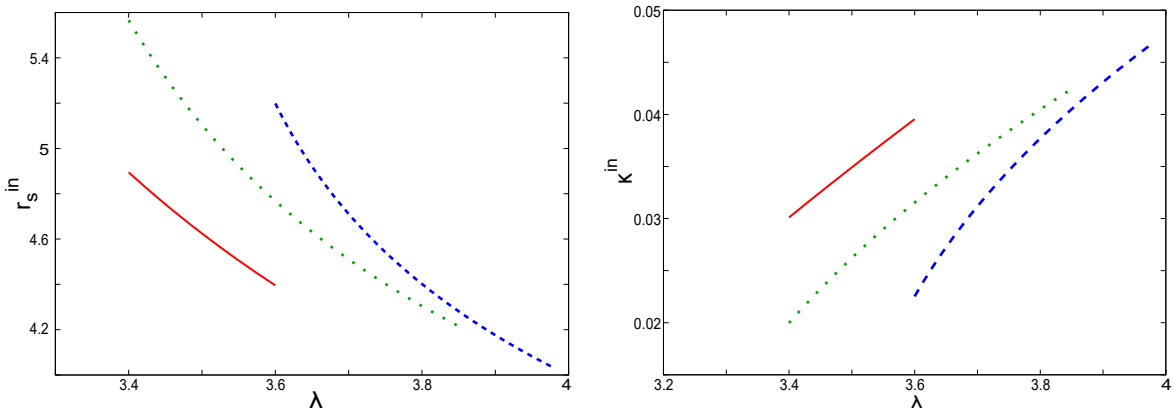


Figure 7.4: (a) $r_s^{in} - \lambda$ and (b) $\kappa^{in} - \lambda$ plots ($\mathcal{E} = 1.00025, \gamma = 4/3, a = 0$) for multi-transonic polytropic accretion. Blue dashed curve, green dotted curve and red solid curve represent CH, CF and VE flows respectively.

Figure 7.4(a) and figure 7.4(b) depict the dependence of the inner sonic point $r_s^{in}$ and its corresponding analogue surface gravity $\kappa^{in}$, respectively, on the specific angular momentum of shocked multi-transonic accretion flow around a non-rotating black hole. It was already observed from figure 5.2 in chapter 5, that no overlapping parameter region of shocked multi-transonic stationary flow solutions for different discs could be obtained for Schwarzschild background space-time geometry. The absence of overlapping $\lambda$ for the given values of $\mathcal{E}$, $\gamma$ and $a$ is also reflected in figure 7.4. However, one can readily note that $r_s^{in}$ anti-correlates with $\lambda$, and consequently $\kappa^{in}$ correlates with $\lambda$. The usual comparative trend given by,

$$r_s^{in}(CH) > r_s^{in}(CF) > r_s^{in}(VE) \tag{7.86}$$

and

$$\kappa^{in}(VE) > \kappa^{in}(CF) > \kappa^{in}(CH), \tag{7.87}$$

is also consistently maintained.

Now, since we are dealing with shocked multi-transonic accretion, therefore the presence of the second acoustic horizon (the outer sonic point $r_s^{out}$) has to be considered as well. Figure 7.5(a) and 7.5(b) portray the dependence of $r_s^{out}$ and $\kappa^{out}$, respectively, on $\lambda$ given $[\mathcal{E} = 1.00025, \gamma = 4/3, a = 0]$ for CH, CF and VE discs. The first observation is that VE discs correspond to the lowest radial distances of outer sonic points and the highest values of analogue surface gravity at the outer sonic horizons. The second observation relates acoustic geometry to the physical space-time geometry. As we have seen in the previous sections, the effect of $g_{\mu\nu}$ gets manifested in the components of $G_{\mu\nu}$ and in the consequent expression for acoustic surface gravity, in case of transonic relativistic fluid flow in the background of curved space-time. This effect clearly reflects in the figures 7.5(a) and 7.5(b), where values of $\kappa$ corresponding to the outer sonic points – which are far away from the event horizon and hence in a nearby region of effectively flat space-time – are

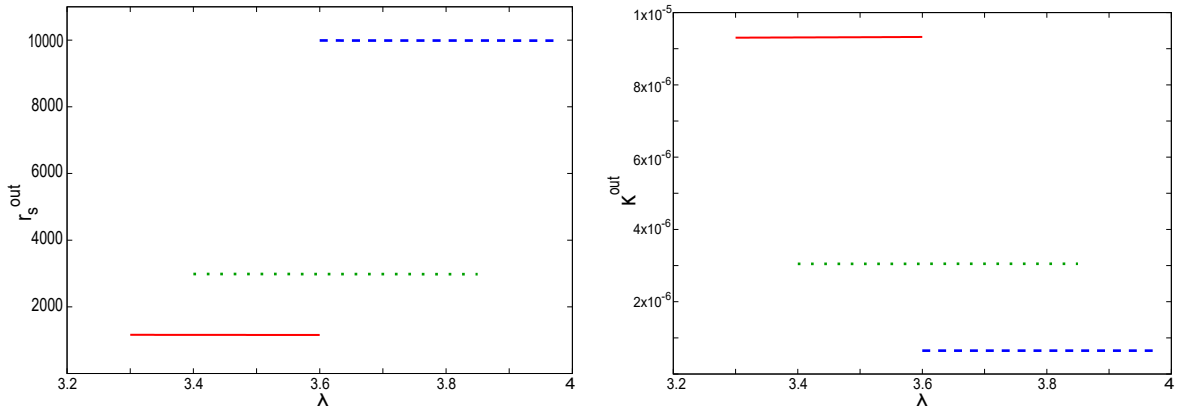


Figure 7.5: (a) $r_s^{out} - \lambda$ and (b) $\kappa^{out} - \lambda$ plots ($\mathcal{E} = 1.00025, \gamma = 4/3, a = 0$) for multi-transonic polytropic accretion. Blue dashed curve, green dotted curve and red solid curve represent CH, CF and VE flows respectively.

extremely low as compared to those on the inner sonic points in regions with significantly high space-time curvatures.

The results previously presented in this section corresponded to the variation of acoustic surface gravity with various accretion parameters for different polytropic accretion disc geometries around a non-rotating black hole. Next, we would like to investigate the variation of the location of the sonic points and the respective $\kappa$ with the black hole spin for relativistic, transonic, polytropic flows in Kerr space-time.

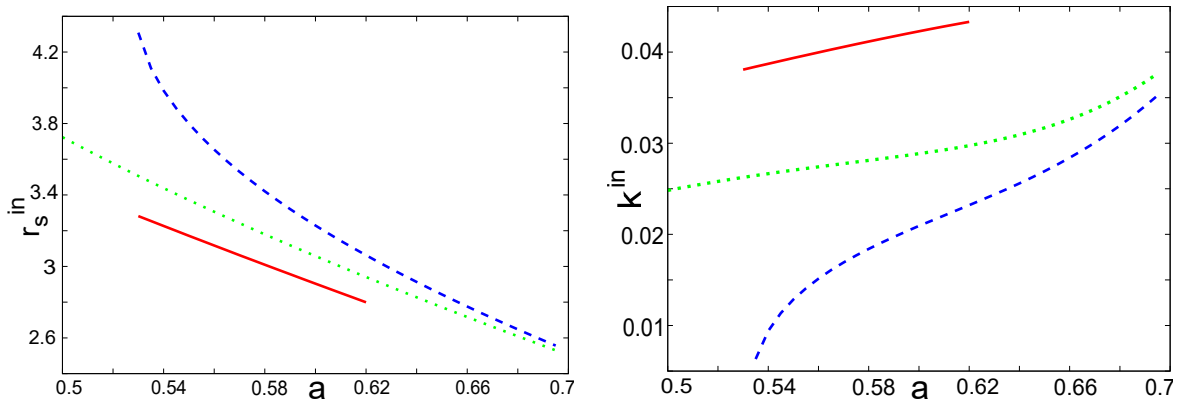


Figure 7.6: (a) $r_s^{in} - a$ and (b) $\kappa^{in} - a$ plots ($\mathcal{E} = 1.00025, \lambda = 3.0, \gamma = 4/3$) for multi-transonic polytropic accretion. Blue dashed curve, green dotted curve and red solid curve represent CH, CF and VE flows respectively.

In figure 7.6(a) and 7.6(b), we plot the variation of locations of the inner acoustic horizon $r_s^{in}$ and its corresponding $\kappa$, respectively, with $a$ for three different flow geometries. It is observed that

$$r_s^{in}(CH) > r_s^{in}(CF) > r_s^{in}(VE) \tag{7.88}$$

and

$$\kappa^{in}(VE) > \kappa^{in}(CF) > \kappa^{in}(CH), \tag{7.89}$$

as it was observed regarding the variation of $\kappa$ and $r_s$ with other parameters for accretion around a non-rotating black hole. It is also observed that $r_s^{in}$ and $\kappa$ anti-correlate and correlate respectively with $a$, thus once again solidifying the foundations of our arguments regarding the correlation of flow angular momentum $\lambda$ and the black hole spin $a$ in the

creation of an effective centrifugal potential barrier encountered by the flow. In figure 7.6(b), we observe the variation of $\kappa$ with $a$. As explained prebiously, first of all, it is first necessary to locate the shock forming region in the parameter space which is common to the three different disc geometries. Since, only a small portion of the parameter space is obtained through such procedure, hence the $\kappa - a$ relationship is obtained for a limited range of black hole spin, and for all the disc structures, the span of $a$ may not be exactly the same.

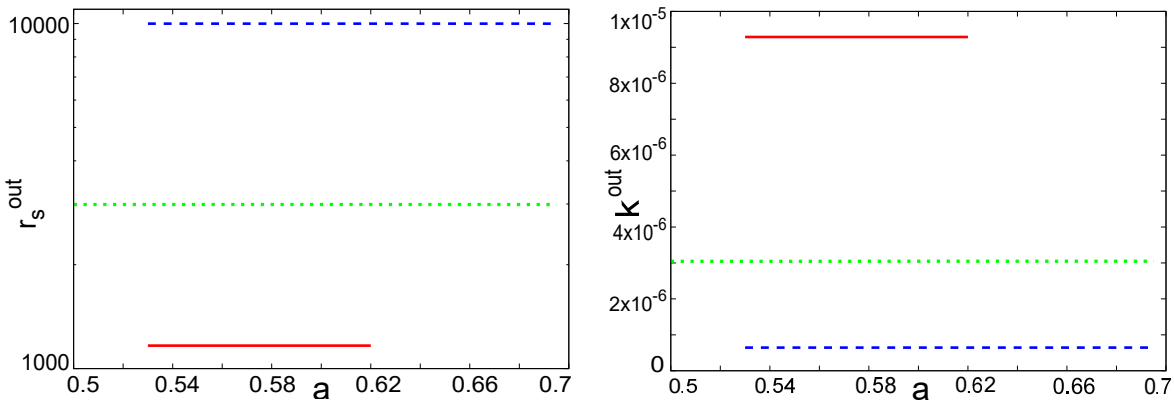


Figure 7.7: (a) $r_s^{out} - a$ and (b) $\kappa^{out} - a$ plots ($\mathcal{E} = 1.00025, \lambda = 3.0, \gamma = 4/3$) for multi-transonic polytropic accretion. Blue dashed curve, green dotted curve and red solid curve represent CH, CF and VE flows respectively.

In figure 7.7(a), one notes that although the relative trend

$$r_s(CH) > r_s(CF) > r_s(VE) \tag{7.90}$$

remains same for the $r_s^{out} - a$ plot, but the influence of the Kerr parameter in changing the values of the sonic point locations is more prominent for the inner horizons. This is somewhat obvious, since the outer sonic points form at a reasonably large distance from the black hole where the space-time is essentially Newtonian andthe black hole spin does not influence the flow properties significantly. From the comparision of figure 7.7(b) with figure 7.6(b), we find that the numerical value of $\kappa^{in}$ is always significantly large compared to the corresponding value of $\kappa^{out}$ for the same set of values of $[\mathcal{E}, \lambda, \gamma, a]$. It is once again observed that the variation of $\kappa$ with black hole spin gets significantly influenced by the geometric configuration of the flow as

$$\kappa^{out}(VE) > \kappa^{out}(CF) > \kappa^{out}(CH) \tag{7.91}$$

for the same value of black hole spin.

However, as of now, by plotting the $\kappa - a$ diagrams for shocked multi-transonic accretion, we have not been able to cover a reasonably large span of the Kerr parameter. We would like to observe how $\kappa$ varies over the entire astrophysically relevant range of $a$ from $-1$ to $+1$. In order to obtain such a plot, we shift our attention from multi-transonic to monotransonic accretion. In case of monotransonic flow, the three different disc structures overlap almost over the entire range of $a$. This task is absolutely essential for us to perform, in order to comment on the global variation of any quantity of our interest (in this case, $\kappa$) with black hole spin. It is also interesting to note that such variation covers both prograde and retrograde flows, and thus any asymmetry in the behavior of the plot on positive and negative sides of the a-axis shall point towards a possible instrument

to distinguish between the two different kinds of fluid flow around the rotating central massive compact objects.

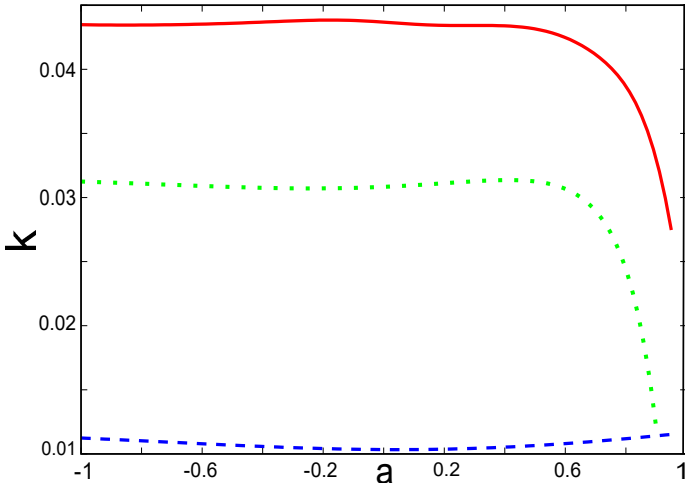


Figure 7.8: $\kappa - a$ plot ($\mathcal{E} = 1.2, \lambda = 2.0, \gamma = 4/3$) for monotransonic polytropic accretion. Blue dashed curve, green dotted curve and red solid curve represent CH, CF and VE flows respectively.

In figure 7.8, the variation of $\kappa$ with $a$ has been shown for all three flow geometries considering monotransonic accretion. The figure has been obtained for a given set of values for $[\mathcal{E}, \lambda, \gamma]$ corresponding to the stationary monotransonic accretion solutions. It is observed that the CH disc flow does not have any maxima or point of inflection, whereas the other two flow geometries manifest such peaks. This, however, does not necessarily indicate that the CH disc flow does not exhibit maxima in general. This artifact is solely attributed to the choice of $[\mathcal{E}, \lambda, \gamma]$ particularly for the given figure. As a matter of fact, $\kappa$ for all three flow geometries possesses an extrema in its dependence on black hole spin. However, this figure clearly indicates that there is a shift in the position of the peaks with variation of the other flow parameters. The figure also depicts a prominent asymmetry in the distribution of $\kappa$ over $a$ for prograde and retrograde flows.

## 7.6 Variation of $\kappa$ - isothermal accretion

In this section – along a similar line – we investigate the variation of $\kappa$ with various flow parameters and different disc geometries, for an isothermal fluid accreting onto both non-rotating and rotating black holes.

In figure 7.9(a), we plot the variation of the location of the acoustic horizon (the inner sonic point $r_s$) with the constant specific angular momentum of the flow $\lambda$. The value of flow temperature $T$ has been fixed at a high value of $2 \times 10^{11}$ K, in order to ensure monotransonic accretion for all three flow geometries. For the same reasons as stated in the previous section, $r_s$ anti-correlates with $\lambda$. For accretion discs in hydrostatic equilibrium along the vertical direction, the entire range of sonic points produced (for the given domain of $\lambda$) lie in the close proximity of the event horizon. This indicates that for a given set of the accretion parameters describing the flow, analogue Hawking effects will be most pronounced for such a flow model. The conclusion is further reinforced by the results presented in figure 7.9(b) where the acoustic surface gravity $\kappa$ has been plotted against the flow angular momentum $\lambda$ to obtain

$$\kappa(VE) > \kappa(CF) > \kappa(CH). \tag{7.92}$$

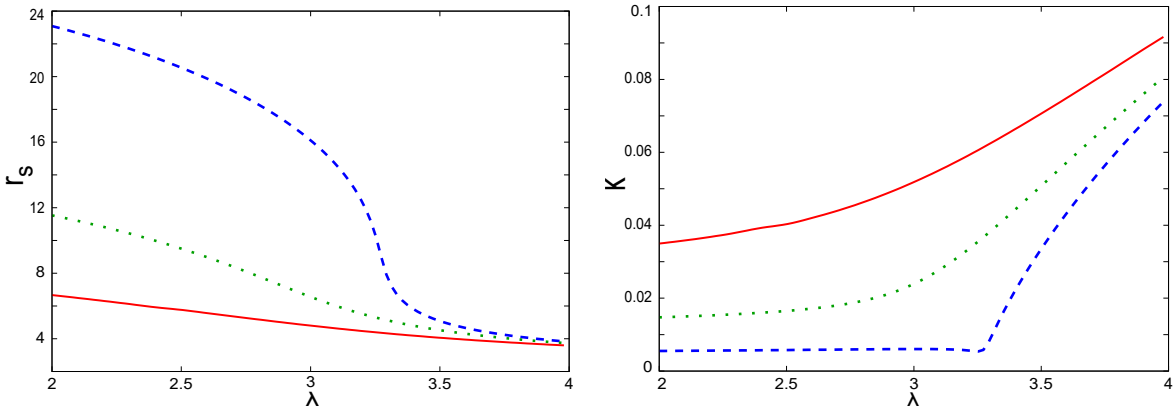


Figure 7.9: (a) $r_s - \lambda$ and (b) $\kappa - \lambda$ plots ($T = 2 \times 10^{11} K, a = 0$) for monotransonic isothermal accretion. Blue dashed curve, green dotted curve and red solid curve represent CH, CF and VE flows respectively.

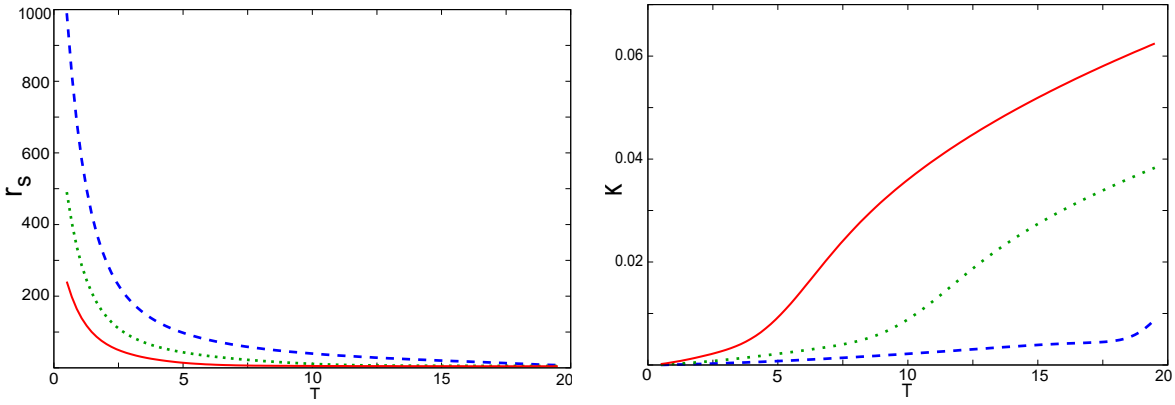


Figure 7.10: (a) $r_s - T$ and (b) $\kappa - T$ plots ($\lambda = 3.3, a = 0$) for monotransonic isothermal accretion. $T$ is in units of $10^{10}$ Kelvin. Blue dashed curve, green dotted curve and red solid curve represent CH, CF and VE flows respectively.

Figure 7.10(a) represents the variation of the location of the acoustic horizon ($r_s$) with constant flow temperatures $T$ in units of $10^{10}$ K. Since the position independent sound speed $c_s \propto T^{\frac{1}{2}}$, the sonic point $r_s$ anti-correlates with the flow temperature $T$. In figure 7.10(b), we plot the variation of the acoustic surface gravity $\kappa$ against $T$ in units of $10^{10}$ K. We observe that 'hotter' flows generate larger values of the analogue surface gravity at the acoustic horizon .

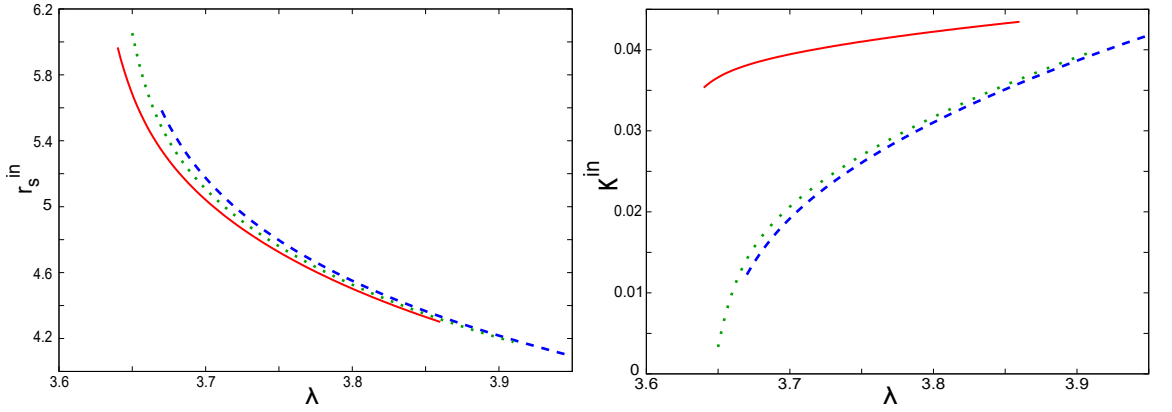


Figure 7.11: (a) $r_s^{in} - \lambda$ and (b) $\kappa^{in} - \lambda$ plots ($T = 10^{10} K, a = 0$) for multi-transonic isothermal accretion. Blue dashed curve, green dotted curve and red solid curve represent CH, CF and VE flows respectively.

Figure 7.11(a) and figure 7.11(b) we depict the dependence of the inner sonic point $r_s^{in}$ and its corresponding analogue surface gravity $\kappa^{in}$, respectively, on the specific angular momentum of shocked multi-transonic isothermal accretion flow around a non-rotating black hole. As, it was already seen from figure 5.8 in chapter 5, a significantly overlapping parameter region of shocked multi-transonic stationary flow solutions for different discs is available for Schwarzschild background space-time geometry. The considerable range of overlapping $\lambda$ for the given value of $T = 10^{10}$ K is also reflected in figure 7.11. It is once again evident that $r_s^{in}$ anti-correlates with $\lambda$ for the isothermal case as well, and consequently $\kappa^{in}$ correlates with $\lambda$. The usual comparative trends given by,

$$r_s^{in}(CH) > r_s^{in}(CF) > r_s^{in}(VE) \tag{7.93}$$

and

$$\kappa^{in}(VE) > \kappa^{in}(CF) > \kappa^{in}(CH), \tag{7.94}$$

are also observed.

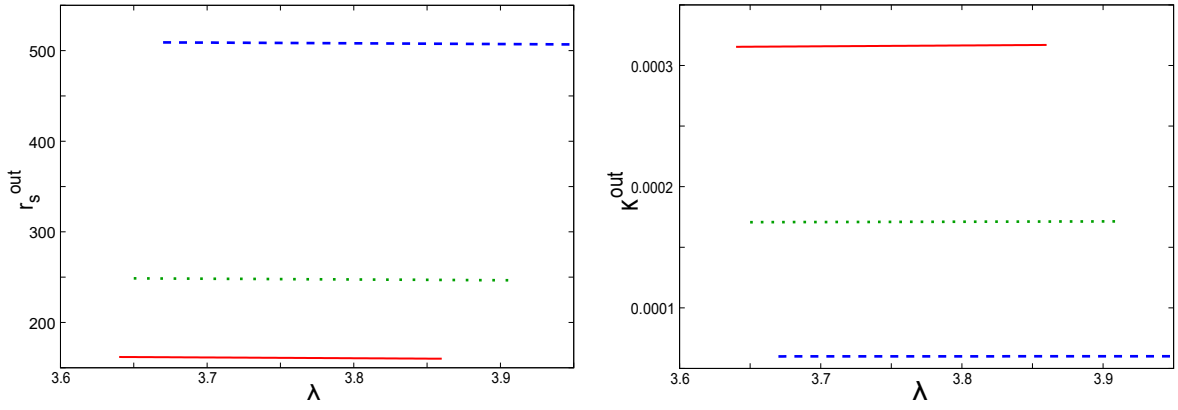


Figure 7.12: (a) $r_s^{out} - \lambda$ and (b) $\kappa^{out} - \lambda$ plots ($T = 10^{10}K, a = 0$) for multi-transonic isothermal accretion. Blue dashed curve, green dotted curve and red solid curve represent CH, CF and VE flows respectively.

Figure 7.12(a) and 7.12(b) depict the dependence of $r_s^{out}$ and $\kappa^{out}$, respectively, on $\lambda$ given $\left[T = 10^{10}K, a = 0\right]$ for CH, CF and VE discs. It is observed that VE discs correspond to the closest radial distances of the outer sonic points and the highest magnitudes of $\kappa$ at the outer acoustic horizons. The coupling of $G_{\mu\nu}$ and $g_{\mu\nu}$ is also clearly reflected in figure 7.12, where values of $\kappa$ corresponding to the outer sonic points – considerably far from the event horizon in a locality of effectively flat space-time – are extremely low compared to the magnitudes of $\kappa$ at the inner sonic points with significantly higher space-time curvatures.

The remaining content of this section deals with the investigation of variation of the location of the sonic points and the respective $\kappa$ with the black hole spin for relativistic, transonic, isothermal flows in Kerr space-time.

In figure 7.13(a) and 7.13(b), we plot the variation of locations of the inner sonic points $r_s^{in}$ and its corresponding $\kappa$, respectively, with $a$ for three different flow geometries. In accordance with the results for polytropic accretion, it is observed that

$$r_s^{in}(CH) > r_s^{in}(CF) > r_s^{in}(VE) \tag{7.95}$$

and

$$\kappa^{in}(VE) > \kappa^{in}(CF) > \kappa^{in}(CH), \tag{7.96}$$

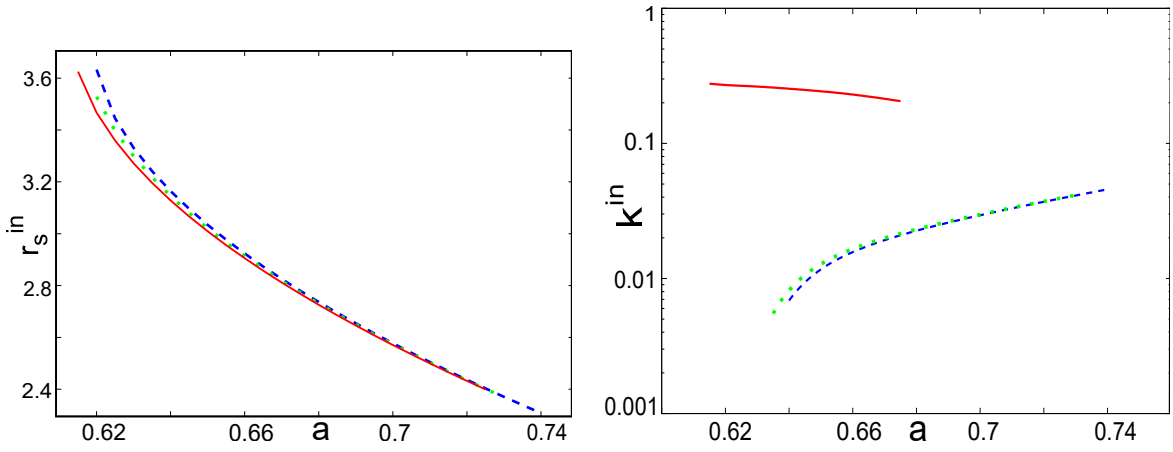


Figure 7.13: (a) $r_s^{in} - a$ and (b) $\kappa^{in} - a$ plots ($T = 10^{10}$ K, $\lambda = 3.0$) for multi-transonic isothermal accretion. Blue dashed curve, green dotted curve and red solid curve represent CH, CF and VE flows respectively.

as was the case for variation of $\kappa$ and $r_s$ with other isothermal flow parameters for accretion around a non-rotating black hole. It is also observed that $r_s^{in}$ anti-correlates with $a$. However, in figure 7.13(b) where we observe the variation of $\kappa^{in}$ with $a$, the individual trend of variation for the VE disc is found to be contrary to those of the other two disc models. In this context, we must remember that multi-transonic shocked accretion solutions offer a very narrow window of spin in which all the disc geometries overlap. Hence, behavior of a physical quantity in the given small range of $a$ may not be quite a reliable representation of the bigger picture. Thus, in order to resolve this discrepancy, we need to look at the global variation of acoustic surface gravity over the entire span of Kerr parameter.

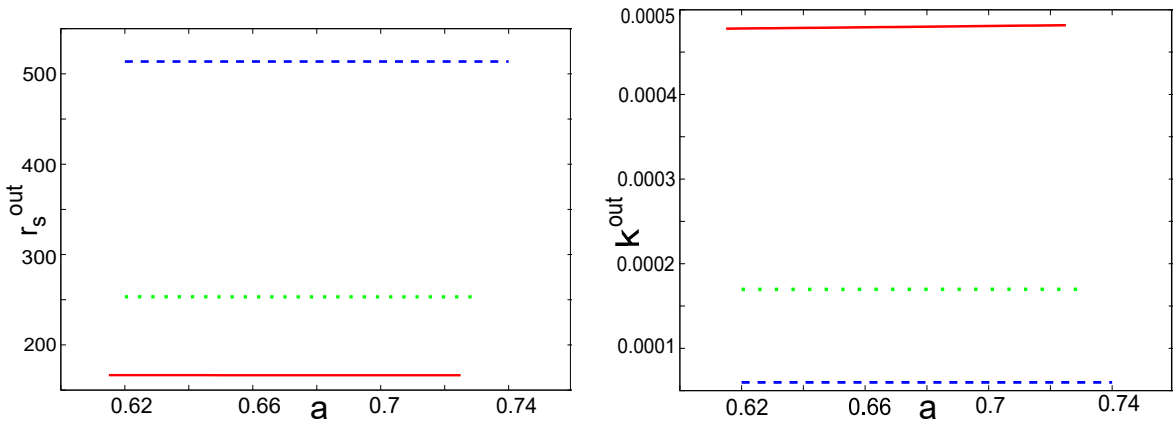


Figure 7.14: (a) $r_s^{out} - a$ and (b) $\kappa^{out} - a$ plots ($T = 10^{10}$ K, $\lambda = 3.0$) for multi-transonic isothermal accretion. Blue dashed curve, green dotted curve and red solid curve represent CH, CF and VE flows respectively.

In figure 7.14(a), we observe that although the relative trend

$$r_s(CH) > r_s(CF) > r_s(VE) \tag{7.97}$$

remains same for the $r_s^{out} - a$ plot, but the effect of the black hole spin on the values of sonic point locations is, once again, more prominent for the inner acoustic horizons. Comparision of figure 7.14(b) with figure 7.14(b) reveals the fact that the value of $\kappa^{in}$ is always several orders of magnitude larger than the corresponding $\kappa^{out}$ for the same set of

values of $[T, \lambda, a]$. It is also observed that

$$\kappa^{out}(VE) > \kappa^{out}(CF) > \kappa^{out}(CH) \tag{7.98}$$

for a given value of black hole spin.

As discussed in the previous section and also in this section regarding the discrepancy of variation of $\kappa^{in}$ with $a$ for VE discs, the only way to have a glimpse of the global dependence of a variable on flow parameters is to study the corresponding dependence for stationary monotransonic isothermal accretion solutions.

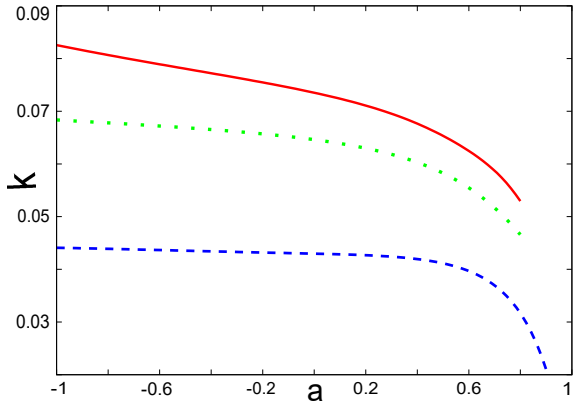


Figure 7.15: $\kappa - a$ plot ($T = 10^{12}$ K, $\lambda = 2.0$) for monotransonic isothermal accretion. Blue dashed curve, green dotted curve and red solid curve represent CH, CF and VE flows respectively.

Figure 7.15 depicts the global variational trend of $\kappa$ over the entire range of black hole spin for monotransonic isothermal accretion. It is observed that the trend of the dependence of $\kappa$ on the disc geometry remains the same as for polytropic accretion. The figure once again depicts a stark asymmetry in the distribution of $\kappa$ over $a$ for prograde and retrograde isothermal flows.

The principle motivation behind the investigation carried out in the present chapter has been our intention to study whether the emergence of gravity- like effects occurs in strongly gravitating physical systems. Conventional analogue models (Robertson [2012]) do not comprise of an actual horizon, which is necessary to conceive real physical Hawking effects. Such analogue configurations can offer no possibility for comparative studies of the corresponding analogue phenomena with actual Hawking effects within the same system. Therefore, we focus our work on an accreting astrophysical black hole, which seems to be the only possible system for investigating the influence of the physical black hole spacetime in constructing the analogue spacetime (Pu et al. [2012]). We demonstrate that the spin angular momentum (the Kerr parameter $a$), which is an explicit property of the black hole metric, influences the geometry and several other important features of the acoustic metric. It is expected that our findings will help in understanding the influences of gravitational field on the appearance of emergent gravity phenomena.

# Bibliography


H. Abraham, N. Bilić, and T. K. Das. *Classical & Quantum Gravity*, 23:2371, 2006.

M. A. Abramowicz. Physics of black hole accretion. In M. A. Abramowicz, G. Björnsson, and J. E. Pringle, editors, *Theory of Black Hole Accretion Disks*, pages 50–60, Jan 1998.

M. A. Abramowicz and S. K. Chakrabarti. *ApJ*, 350:281, 1990.

M. A. Abramowicz and S. Kato. *ApJ*, 336:304, 1989.

M. A. Abramowicz and W. H. Zurek. *ApJ*, 246:314, 1981.

M. A. Abramowicz, X. M. Chen, M. Granath, and J. P. Lasota. Advection-dominated Accretion Flows around Kerr Black Holes. *Astrophysical Journal*, 471:762, Nov 1996. doi: 10.1086/178004.

M. A. Abramowicz, A. Lanza, and M. J. Percival. *ApJ*, 479:179, 1997.

N. Afshordi and B. Paczyński. Geometrically Thin Disk Accreting into a Black Hole. *Astrophysical Journal*, 592:354–367, Jul 2003. doi: 10.1086/375559.

Arif Babul, Jeremiah P. Ostriker, and P. Meszaros. Self-consistent Spherical Accretion Shocks around Black Holes. *Astrophysical Journal*, 347:59, Dec 1989. doi: 10.1086/168096.

F. K. Baganoff, M. W. Bautz, W. N. Brandt, G. Chartas, E. D. Feigelson, G. P. Garmire, Y. Maeda, M. Morris, G. R. Ricker, L. K. Townsley, and F. Walter. Rapid X-ray flaring from the direction of the supermassive black hole at the Galactic Centre. *Nature*, 413: 45–48, September 2001. doi: 10.1038/35092510.

Steven A. Balbus and John F. Hawley. Instability, turbulence, and enhanced transport in accretion disks. *Reviews of Modern Physics*, 70(1):1–53, Jan 1998. doi: 10.1103/RevModPhys.70.1.

Cosimo Bambi. Testing black hole candidates with electromagnetic radiation. *Reviews of Modern Physics*, 89:025001, April 2017. doi: 10.1103/RevModPhys.89.025001.

P. Barai, T. K. Das, and P. J. Wiita. *ApJL*, 613:L49–L52, 2004.

Carlos Barceló, Stefano Liberati, and Matt Visser. Analogue gravity. *Living Reviews in Relativity*, 8(1):12, 2005. ISSN 1433-8351. doi: 10.12942/lrr-2005-12. URL `http://dx.doi.org/10.12942/lrr-2005-12`.

J. M. Bardeen, B. Carter, and S. W. Hawking. The four laws of black hole mechanics. *Communications in Mathematical Physics*, 31:161–170, Jun 1973. doi: 10.1007/BF01645742.

James M. Bardeen and Jacobus A. Petterson. The Lense-Thirring Effect and Accretion Disks around Kerr Black Holes. *Astrophysical Journal*, 195:L65, Jan 1975. doi: 10.1086/181711.

James M. Bardeen, William H. Press, and Saul A. Teukolsky. Rotating Black Holes: Locally Nonrotating Frames, Energy Extraction, and Scalar Synchrotron Radiation. *Astrophysical Journal*, 178:347–370, Dec 1972.

Soumen Basak. Analog of Superradiance effect in BEC. *arXiv e-prints*, art. gr-qc/0501097, Jan 2005.

Soumen Basak and Parthasarathi Majumdar. 'Superresonance' from a rotating acoustic black hole. *Classical and Quantum Gravity*, 20:3907–3913, Sep 2003. doi: 10.1088/0264-9381/20/18/304.

M. C. Begelman. Accretion of V > 5/3 Gas by a Schwarzschild Black Hole. *Astronomy & Astrophysics*, 70:583, Nov 1978.

Mitchell C. Begelman, Marta Volonteri, and Martin J. Rees. Formation of supermassive black holes by direct collapse in pre-galactic haloes. *MNRAS*, 370:289–298, Jul 2006.

J. D. Bekenstein. Statistical black-hole thermodynamics. *Physical Review D*, 12:3077–3085, Nov 1975. doi: 10.1103/PhysRevD.12.3077.

J. D. Bekenstein. Black-hole thermodynamics. *Physics Today*, 33:24–31, Jan 1980. doi: 10.1063/1.2913906.

Jacob D. Bekenstein. Nonexistence of Baryon Number for Black Holes. II. *Physical Review D*, 5:2403–2412, May 1972a. doi: 10.1103/PhysRevD.5.2403.

Jacob D. Bekenstein. Nonexistence of Baryon Number for Static Black Holes. *Physical Review D*, 5:1239–1246, Mar 1972b. doi: 10.1103/PhysRevD.5.1239.

Jacob D. Bekenstein. Black Holes and Entropy. *Physical Review D*, 7:2333–2346, Apr 1973. doi: 10.1103/PhysRevD.7.2333.

Emanuele Berti, Vitor Cardoso, and José P. Lemos. Quasinormal modes and classical wave propagation in analogue black holes. *Physical Review D*, 70:124006, Dec 2004. doi: 10.1103/PhysRevD.70.124006.

N. Bilic. *Classical & Quantum Gravity*, 16:3953, 1999.

N. Bilić, A. Choudhary, T. K. Das, and S. Nag. *Classical & Quantum Gravity*, 31:35002, 2014.

A. A. Bisikalo, V. M. Boyarchuk, V. M. Chechetkin, O. A. Kuznetsov, and D. Molteni. *MNRAS*, 300:39, 1998.

G. S. Bisnovatyi-Kogan, Y. B. Zel'dovich, and R. A. Syunyaev. Physical Processes in a Low-Density Relativistic Plasma. *Soviet Astronomy*, 15:17, August 1971.

O. Blaes. *MNRAS*, 227:975, 1987.

R. D. Blandford. Relativistic Accretion. In J. A. Sellwood and Jeremy Goodman, editors, *Astrophysical Discs - an EC Summer School*, volume 160 of *Astronomical Society of the Pacific Conference Series*, page 265, Apr 1999.

R. D. Blandford and R. L. Znajek. Electromagnetic extraction of energy from Kerr black holes. *MNRAS*, 179:433–456, May 1977. doi: 10.1093/mnras/179.3.433.

G. R. Blumenthal and W. G. Mathews. Spherical winds and accretion in general relativity. *Astrophysical Journal*, 203:714–719, Feb 1976. doi: 10.1086/154133.

T. Bohr, P. Dimon, and V. Putkaradze. Shallow-water approach to the circular hydraulic jump. *Journal of Fluid Mechanics*, 254:635–648, Jan 1993. doi: 10.1017/S0022112093002289.

D. A. Bollimpalli, S. Bhattacharya, and T. K. Das. *New Astronomy*, 51:153, 2017.

H. Bondi. On spherically symmetrical accretion. *Monthly Notices of the Royal Astronomical Society*, 112:195, Jan 1952. doi: 10.1093/mnras/112.2.195.

W. Brinkmann. Adiabatic accretion onto a Schwarzschild black hole. *Astronomy & Astrophysics*, 85(1-2):146–148, May 1980.

J. W. Broderick and R. P. Fender. Is there really a dichotomy in active galactic nucleus jet power? *MNRAS*, 417:184–197, October 2011. doi: 10.1111/j.1365-2966.2011.19060.x.

J. David Brown. Black hole entropy and the Hamiltonian formulation of diffeomorphism invariant theories. *Physical Review D*, 52:7011–7026, Dec 1995. doi: 10.1103/PhysRevD.52.7011.

David M. Caditz and Sachiko Tsuruta. Adiabatic Shocks in Accretion Flows. *Astrophysical Journal*, 501:242–251, Jul 1998. doi: 10.1086/305794.

Vitor Cardoso, José P. Lemos, and Shijun Yoshida. Quasinormal modes and stability of the rotating acoustic black hole: Numerical analysis. *Physical Review D*, 70:124032, Dec 2004. doi: 10.1103/PhysRevD.70.124032.

S. K. Chakrabarti. *ApJ*, 347:365, 1989.

S. K. Chakrabarti. *ApJ*, 471:237, 1996.

S. K. Chakrabarti. Accretion processes on a black hole. *Physics Reports*, 266:229–390, Jan 1996a. doi: 10.1016/0370-1573(95)00057-7.

Sandip K. Chakrabarti. Global solutions of viscous transonic flows in Kerr geometry - I. Weak viscosity limit. *MNRAS*, 283:325, Nov 1996b. doi: 10.1093/mnras/283.1.325.

Sandip K. Chakrabarti and Santabrata Das. Properties of accretion shock waves in viscous flows around black holes. *MNRAS*, 349:649–664, Apr 2004. doi: 10.1111/j.1365-2966.2004.07536.x.

K. M. Chang and J. P. Ostriker. Standing shocks in accretion flows onto black holes. *Astrophysical Journal*, 288:428–437, Jan 1985. doi: 10.1086/162809.

Soumini Chaudhury, Arnab K. Ray, and Tapas K. Das. Critical properties and stability of stationary solutions in multitransonic pseudo-Schwarzschild accretion. *MNRAS*, 373: 146–156, Nov 2006. doi: 10.1111/j.1365-2966.2006.11018.x.

C. Cherubini, F. Federici, S. Succi, and M. P. Tosi. Excised acoustic black holes: The scattering problem in the time domain. *Physical Review D*, 72:084016, Oct 2005. doi: 10.1103/PhysRevD.72.084016.

K. Choy, T. Kruk, M. E. Carrington, T. Fugleberg, J. Zahn, R. Kobes, G. Kunstatter, and D. Pickering. Energy flow in acoustic black holes. *Physical Review D*, 73:104011, May 2006. doi: 10.1103/PhysRevD.73.104011.

B. Czerny and B. You. Accretion in active galactic nuclei and disk-jet coupling. *Astronomische Nachrichten*, 337:73, February 2016. doi: 10.1002/asna.201512268.

B. Czerny, M. Mościbrodzka, D. Proga, T. K. Das, and A. Siemiginowska. Low angular momentum accretion flow model of Sgr A* activity. In S. Hledík and Z. Stuchlík, editors, *Proceedings of RAGtime 8/9: Workshops on Black Holes and Neutron Stars*, pages 35–44, December 2007.

B. Czerny, P. Lachowicz, M. Dovčiak, V. Karas, T. Pecháček, and T. K. Das. The model constraints from the observed trends for the quasi-periodic oscillation in RE J1034+396. *Astronomy & Astrophysics*, 524:A26, December 2010. doi: 10.1051/0004-6361/200913724.

T. K. Das and B. Czerny. *New Astronomy*, 17:254, 2012.

T. K. Das, J. K. Pendharkar, and S. Mitra. *ApJ*, 592:1078, 2003.

T. K. Das, N. Bilic, and S. Dasgupta. A black-hole accretion disc as an analogue gravity model. *JCAP*, 6:009, June 2007. doi: 10.1088/1475-7516/2007/06/009.

T. K. Das, S. Nag, S. Hegde, S. Bhattacharya, I. Maity, B. Czerny, P. Barai, P. J. Wiita, V. Karas, and T. Naskar. *New Astronomy*, 37:81, 2015.

Tapas K. Das. Generalized Shock Solutions for Hydrodynamic Black Hole Accretion. *Astrophysical Journal*, 577:880–892, Oct 2002. doi: 10.1086/342114.

Tapas K. Das. Behaviour of matter close to the event horizon. *MNRAS*, 349:375–384, Mar 2004. doi: 10.1111/j.1365-2966.2004.07528.x.

Tapas K. Das and B. Czerny. On the efficiency of the Blandford-Znajek mechanism for low angular momentum relativistic accretion. *MNRAS*, 421:L24–L28, March 2012. doi: 10.1111/j.1745-3933.2011.01199.x.

Tapas K. Das and A. Sarkar. Pseudo-Schwarzschild description of transonic spherical accretion onto compact objects. *Astronomy & Astrophysics*, 374:1150–1160, Aug 2001. doi: 10.1051/0004-6361:20010736.

M. Demianski and P. B. Ivanov. The dynamics of twisted accretion disc around a Kerr black hole. *Astronomy & Astrophysics*, 324:829–834, August 1997.

H. Falcke, F. Melia, and E. Agol. *American Institute of Physics Conference Series*, 522: 317–320, 2000.

F. Federici, C. Cherubini, S. Succi, and M. P. Tosi. Superradiance from hydrodynamic vortices: A numerical study. *Physical Review A*, 73:033604, Mar 2006. doi: 10.1103/PhysRevA.73.033604.

R. P. Fender, E. Gallo, and D. Russell. No evidence for black hole spin powering of jets in X-ray binaries. *MNRAS*, 406:1425–1434, August 2010. doi: 10.1111/j.1365-2966.2010.16754.x.

A. Ferrari, E. Trussoni, R. Rosner, and K. Tsinganos. On wind-type flows in astrophysical jets. I - The initial relativistic acceleration. *Astrophysical Journal*, 294:397–418, Jul 1985. doi: 10.1086/163307.

K. Ferrière. Interstellar magnetic fields in the Galactic center region. *Astronomy & Astrophysics*, 505:1183–1198, Oct 2009. doi: 10.1051/0004-6361/200912617.

P. Chris Fragile and Peter Anninos. Hydrodynamic Simulations of Tilted Thick-Disk Accretion onto a Kerr Black Hole. *Astrophysical Journal*, 623(1):347–361, Apr 2005. doi: 10.1086/428433.

J. Frank, A. King, and D. Raine. *Accretion power in astrophysics.*, volume 21. 1992.

J. Fukue. *PASJ*, 35:355, 1983.

J. Fukue. *PASJ*, 39:309, 1987.

K. Fukumara and S. Tsuruta. *ApJ*, 611:964, 2004.

C. F. Gammie and R. Popham. *ApJ*, 498:313, 1998.

David Garofalo. Retrograde versus Prograde Models of Accreting Black Holes. *Advances in Astronomy*, 2013:213105, January 2013. doi: 10.1155/2013/213105.

R. Genzel, R. Schödel, T. Ott, A. Eckart, T. Alexander, F. Lacombe, D. Rouan, and B. Aschenbach. Near-infrared flares from accreting gas around the supermassive black hole at the Galactic Centre. *Nature*, 425:934–937, October 2003. doi: 10.1038/nature02065.

Reinhard Genzel, Frank Eisenhauer, and Stefan Gillessen. The Galactic Center massive black hole and nuclear star cluster. *Reviews of Modern Physics*, 82:3121–3195, Oct 2010. doi: 10.1103/RevModPhys.82.3121.

A. M. Ghez, S. Salim, N. N. Weinberg, J. R. Lu, T. Do, J. K. Dunn, K. Matthews, M. R. Morris, S. Yelda, E. E. Becklin, T. Kremenek, M. Milosavljevic, and J. Naiman. Measuring Distance and Properties of the Milky Way's Central Supermassive Black Hole with Stellar Orbits. *Astrophysical Journal*, 689:1044–1062, Dec 2008. doi: 10.1086/592738.

S. Gillessen, F. Eisenhauer, T. K. Fritz, H. Bartko, K. Dodds-Eden, O. Pfuhl, T. Ott, and R. Genzel. The Orbit of the Star S2 Around SGR A* from Very Large Telescope and Keck Data. *ApJ*, 707:L114–L117, December 2009. doi: 10.1088/0004-637X/707/2/L114.

S. Goswami, S. N. Khan, A. K. Ray, and T. K. Das. *MNRAS*, 378:1407, 2007.

A. Gullstrand. *Arkiv for Matematik, Astronomi och Fysik*, 16:1–15, 1922.

Z. Haiman and E. Quataert. The Formation and Evolution of the First Massive Black Holes. In A. J. Barger, editor, *Supermassive Black Holes in the Distant Universe*, volume 308 of *Astrophysics and Space Science Library*, page 147, Aug 2004.

S. W. Hawking. Particle creation by black holes. *Communications in Mathematical Physics*, 43:199–220, Aug 1975. doi: 10.1007/BF02345020.

J. F. Hawley, L. L. Smarr, and J. R. Wilson. A numerical study of nonspherical black hole accretion. I Equations and test problems. *Astrophysical Journal*, 277:296–311, Feb 1984. doi: 10.1086/161696.

Friedrich W. Hehl, Claus Kiefer, and Ralph J. K. Metzler. *Black Holes: Theory and Observation*. 1998. doi: 10.1007/b13593.

Adam D. Helfer. Do black holes radiate? *Reports on Progress in Physics*, 66:943–1008, Jun 2003. doi: 10.1088/0034-4885/66/6/202.

Markus Heusler. *Black hole uniqueness theorems*. 1996.

K. Hioki and K.I. Maeda. *Physical Review D*, 80:024042, 2009.

L. C. Ho. *Observational Evidence For Black Holes in the Universe, ed. Chakrabarti, S. K.* Dordrecht: Kluwer, 1999.

R. Hōshi and N. Shibazaki. The Effect of Pressure Gradient Force on an Accretion Disk Surrounding a Black-Hole. *Progress of Theoretical Physics*, 58(6):1759–1765, Dec 1977. doi: 10.1143/PTP.58.1759.

F. Hoyle and R. A. Lyttleton. The evolution of the stars. *Proceedings of the Cambridge Philosophical Society*, 35(4):592, Jan 1939. doi: 10.1017/S0305004100021368.

L. Huang, M. Cai, Z. Q. Shen, and F. Yuan. *MNRAS*, 379:833–840, 2007.

Scott A. Hughes. Trust but verify: The case for astrophysical black holes. *arXiv e-prints*, art. hep-ph/0511217, Nov 2005.

S. Ichimaru. Bimodal behavior of accretion disks: theory and application to Cygnus X-1 transitions. *Astrophysical Journal*, 214:840–855, Jun 1977. doi: 10.1086/155314.

I. V. Igumenshchev and M. A. Abramowicz. *MNRAS*, 303:309, 1999.

A. F. Illarionov. *Soviet Astron.*, 31:618, 1988.

A. F. Illarionov and R. A. Sunyaev. *A & A*, 39:205, 1975.

Shamreen Iram. A dynamical systems analysis of axisymmetric accretion in a Schwarzschild black hole. *General Relativity and Gravitation*, 47:39, Apr 2015. doi: 10.1007/s10714-015-1874-8.

W. Israel. Thermo-field dynamics of black holes. *Physics Letters A*, 57:107–110, May 1976. doi: 10.1016/0375-9601(76)90178-X.

T. Jacobson. Trans-Planckian Redshifts andthe Substance of the Space-Time River. *Progress of Theoretical Physics Supplement*, 136:1–17, Jan 1999. doi: 10.1143/PTPS.136.1.

Theodore Jacobson. Black-hole evaporation and ultrashort distances. *Physical Review D*, 44:1731–1739, Sep 1991. doi: 10.1103/PhysRevD.44.1731.

Frank C. Jones and Donald C. Ellison. The plasma physics of shock acceleration. *Space Science Review*, 58(1):259–346, Dec 1991. doi: 10.1007/BF01206003.

D. W. Jordan and P. Smith. *Nonlinear Ordinary Differential Equations*. Oxford University Press, Oxford, 1999.

M. Kafatos and R. X. Yang. *MNRAS*, 268:925, 1994.

G. D. Karssen, M. Bursa, A. Eckart, M. Valencia-S, M. Dovčiak, V. Karas, and J. Horák. Bright X-ray flares from Sgr A*. *MNRAS*, 472:4422–4433, December 2017. doi: 10.1093/mnras/stx2312.

S. Kato, J. Fukue, and S. Mineshige. *Black Hole Accretion Disc*. Kyoto University Press, 1998.

D. Kazanas and D. C. Ellison. The Central Engine of Quasars and Active Galactic Nuclei: Hadronic Interactions of Shock-accelerated Relativistic Protons. *Astrophysical Journal*, 304:178, May 1986. doi: 10.1086/164152.

Wontae Kim, Young-Jai Park, Edwin J. Son, and Myung Seok Yoon. Statistical Entropy and Superradiance in 2+1 Dimensional Acoustic Black Holes. *arXiv e-prints*, art. gr-qc/0504127, Apr 2005.

S. Kumar. Twisted accretion discs - IV. Alignment in polytropic discs and low alpha limit. *MNRAS*, 233:33, Jul 1988. doi: 10.1093/mnras/233.1.33.

L. D. Landau and E. M. Lifshitz. *Fluid Mechanics*. Pergamon Press, Course of Theoretical Physics, Volume 6, 1959.

L. D. Landau and E. M. Lifshitz. *Classical Theory of Fields*. Pergamon Press, Course of Theoretical Physics, Volume 2, 1994.

Antonio Lanza. Self-gravitating Thin Disks around Rapidly Rotating Black Holes. *Astrophysical Journal*, 389:141, Apr 1992. doi: 10.1086/171193.

J. P. Lasota and M. A. Abramowicz. *Classical & Quantum Gravity*, 14:A237, 1997.

Georges Lemaître. L'Univers en expansion. *Annales de la Société Scientifique de Bruxelles*, 53:51, Jan 1933.

Josef Lense and Hans Thirring. Über den Einfluß der Eigenrotation der Zentralkörper auf die Bewegung der Planeten und Monde nach der Einsteinschen Gravitationstheorie. *Physikalische Zeitschrift*, 19:156, Jan 1918.

Samuel Lepe and Joel Saavedra. Quasinormal modes, superradiance and area spectrum for 2+1 acoustic black holes [rapid communication]. *Physics Letters B*, 617:174–181, Jun 2005. doi: 10.1016/j.physletb.2005.05.021.

E. P. T. Liang and P. L. Nolan. *Space Sc. Rev.*, 38:353, 1984.

E. P. T. Liang and K. A. Thomson. *ApJ*, 240:271, 1980.

D. N. C. Lin and J. C. B. Papaloizou. Theory of Accretion Disks II: Application to Observed Systems. *Annual Review of Astronomy and Astrophysics*, 34:703–748, Jan 1996. doi: 10.1146/annurev.astro.34.1.703.

J. F. Lu, K. N. Yu, F. Yuan, and E. C. M. Young. *A & A*, 321:665, 1997.

Ju-Fu Lu and Bo-Yan Zhou. Observational Evidence of Jet Precession in Galactic Nuclei Caused by Accretion Disks. *Astrophysical Journal*, 635(1):L17–L20, Dec 2005. doi: 10.1086/499333.

D. Lynden-Bell. Galactic Nuclei as Collapsed Old Quasars. *Nature*, 223(5207):690–694, Aug 1969. doi: 10.1038/223690a0.

Thomas J. Maccarone. On the misalignment of jets in microquasars. *MNRAS*, 336(4): 1371–1376, Nov 2002. doi: 10.1046/j.1365-8711.2002.05876.x.

Edward Malec. Fluid accretion onto a spherical black hole: Relativistic description versus the Bondi model. *Physical Review D*, 60(10):104043, Nov 1999. doi: 10.1103/PhysRevD.60.104043.

Ipsita Mandal, Arnab K. Ray, and Tapas K. Das. Critical properties of spherically symmetric black hole accretion in Schwarzschild geometry. *MNRAS*, 378:1400–1406, Jul 2007. doi: 10.1111/j.1365-2966.2007.11898.x.

D. P. Marrone, F. K. Baganoff, M. R. Morris, J. M. Moran, A. M. Ghez, S. D. Hornstein, C. D. Dowell, D. J. Muñoz, M. W. Bautz, G. R. Ricker, W. N. Brandt, G. P. Garmire, J. R. Lu, K. Matthews, J. H. Zhao, R. Rao, and G. C. Bower. An X-Ray, Infrared, and Submillimeter Flare of Sagittarius A*. *ApJ*, 682:373–383, July 2008. doi: 10.1086/588806.

Daniel P. Marrone, James M. Moran, Jun-Hui Zhao, and Ramprasad Rao. An Unambiguous Detection of Faraday Rotation in Sagittarius A*. *Astrophysical Journal*, 654: L57–L60, Jan 2007. doi: 10.1086/510850.

R. Matsumoto, Fukue Kato, S., J., and A. T. Okazaki. *PASJ*, 36:71, 1984.

F. Melia, S. Liu, and R. Coker. A Magnetic Dynamo Origin for the Submillimeter Excess in Sagittarius A*. *Astrophysical Journal*, 553:146–157, May 2001. doi: 10.1086/320644.

Fulvio Melia. An Accreting Black Hole Model for Sagittarius A *. *Astrophysical Journal*, 387:L25, Mar 1992. doi: 10.1086/186297.

P. Meszaros and J. P. Ostriker. Shocks in spherically accreting black holes : a model for classical quasars. *Astrophysical Journal*, 273:L59–L63, Oct 1983. doi: 10.1086/184130.

F. Curtis Michel. Accretion of Matter by Condensed Objects. *Astrophysics & Space Sc.*, 15(1):153–160, Jan 1972. doi: 10.1007/BF00649949.

A. G. Mikhailov, M. Yu Piotrovich, Yu N. Gnedin, T. M. Natsvlishvili, and S. D. Buliga. Criteria for retrograde rotation of accreting black holes. *MNRAS*, 476:4872–4876, June 2018. doi: 10.1093/mnras/sty643.

Charles W. Misner, Kip S. Thorne, and John A. Wheeler. *Gravitation*. 1973.

V. Moncrief. Stability of stationary, spherical accretion onto a Schwarzschild black hole. *Astrophysical Journal*, 235:1038–1046, Feb 1980. doi: 10.1086/157707.

M. Moscibrodzka. Spherical accretion in nearby weakly active galaxies. *Astronomy & Astrophysics*, 450(1):93–103, Apr 2006. doi: 10.1051/0004-6361:20054165.

M. Moscibrodzka, T. K. Das, and B. Czerny. *MNRAS*, 370:219, 2006.

Enmanuelle Mossoux and Nicolas Grosso. Sixteen years of X-ray monitoring of Sagittarius A*: Evidence for a decay of the faint flaring rate from 2013 August, 13 months before a rise in the bright flaring rate. *Astronomy and Astrophysics*, 604:A85, August 2017. doi: 10.1051/0004-6361/201629778.

B. Muchotrzeb. Transonic accretion flow in a thin disk around a black hole. II. *Acta Astronomica*, 33(1):79–87, Jan 1983.

B. Muchotrzeb and B. Czerny. *Acta Astron.*, 36:1, 1986.

B. Muchotrzeb and B. Paczynski. *Acta Astron.*, 32:1, 1982.

S. Nag, S. Acharya, A. K. Ray, and T. K. Das. *New Astronomy*, 17:285, 2012.

R. Narayan and I. Yi. Advection-dominated Accretion: A Self-similar Solution. *Astrophysical Journal*, 428:L13, Jun 1994. doi: 10.1086/187381.

R. Narayan and I. Yi. Advection-dominated Accretion: Underfed Black Holes and Neutron Stars. *Astrophysical Journal*, 452:710, Oct 1995. doi: 10.1086/176343.

Richard P. Nelson and John C. B. Papaloizou. Hydrodynamic simulations of the Bardeen-Petterson effect. *MNRAS*, 315(3):570–586, Jul 2000. doi: 10.1046/j.1365-8711.2000.03478.x.

I. Novikov and K. S. Thorne. *Black Holes, ed. De Witt C. & De Witt B.* Gordon and Breach, New York, 1973.

Michael O' Riordan, Asaf Pe'er, and Jonathan C. McKinney. Effects of Spin on High-energy Radiation from Accreting Black Holes. *ApJ*, 831:62, November 2016. doi: 10.3847/0004-637X/831/1/62.

T. Okuda and D. Molteni. Low angular momentum flow model for Sgr A*. *Monthly Notices of the Royal Astronomical Society*, 425:2413–2421, Oct 2012. doi: 10.1111/j.1365-2966.2012.21571.x.

B. Paczynski and G. Bisnovatyi-Kogan. A Model of a Thin Accretion Disk around a Black Hole. *Acta Astronomica*, 31:283, Jan 1981.

B. Paczyński and P. J. Wiita. *A & A*, 88:23, 1980.

T. Padmanabhan. Gravity and the thermodynamics of horizons. *Physics Reports*, 406: 49–125, Jan 2005. doi: 10.1016/j.physrep.2004.10.003.

Don N. Page. Hawking radiation and black hole thermodynamics. *New Journal of Physics*, 7:203, Sep 2005. doi: 10.1088/1367-2630/7/1/203.

P. Painlevé. La mécanique classique et la théorie de la relativité. *Comptes Rendus Academie des Sciences (serie non specifiee)*, 173:677–680, Jan 1921.

Renaud Parentani. What did we Learn from Studying Acoustic Black Holes? *International Journal of Modern Physics A*, 17:2721–2725, Jan 2002. doi: 10.1142/S0217751X02011679.

V. I. Pariev. *MNRAS*, 283:1264, 1996.

Myeong-Gu Park. Self-consistent Models of Spherical Accretion onto Black Holes. II. Two-Temperature Solutions with Pairs. *Astrohysical Journal*, 354:83, May 1990a. doi: 10.1086/168669.

Myeong-Gu Park. Self-consistent Models of Spherical Accretion onto Black Holes. I. One-Temperature Solutions. *Astrophysical Journal*, 354:64, May 1990b. doi: 10.1086/168668.

J. Peitz and S. Appl. *MNRAS*, 286:681, 1997.

J. A. Petterson. Twisted accretion disks. I. Derivation of the basic equations. *Astrophysical Journal*, 214:550–559, Jun 1977. doi: 10.1086/155280.

G. Ponti, B. De Marco, M. R. Morris, A. Merloni, T. Muñoz-Darias, M. Clavel, D. Haggard, S. Zhang, K. Nandra, S. Gillessen, K. Mori, J. Neilsen, N. Rea, N. Degenaar, R. Terrier, and A. Goldwurm. Fifteen years of XMM-Newton and Chandra monitoring of Sgr A<SUP>?</SUP>: evidence for a recent increase in the bright flaring rate. *MNRAS*, 454:1525–1544, December 2015. doi: 10.1093/mnras/stv1537.

R. Popham and C. F. Gammie. *ApJ*, 504:419, 1998.

K. H. Prendergast and G. R. Burbidge. On the Nature of Some Galactic X-Ray Sources. *Astrophysical Journal*, 151:L83, Feb 1968. doi: 10.1086/180148.

J. E. Pringle. Accretion discs in astrophysics. *Annual Review of Astronomy and Astrophysics*, 19:137–162, Jan 1981. doi: 10.1146/annurev.aa.19.090181.001033.

R. J. Protheroe and D. Kazanas. On the origin of relativistic particles and gamma-rays in quasars. *Astrophysical Journal*, 265:620–624, Feb 1983. doi: 10.1086/160707.

H. Y. Pu, I. Maity, T. K. Das, and H. K. Chang. *Classical & Quantum Gravity*, 29:245020, 2012.

Arnab K. Ray and J. K. Bhattacharjee. Realizability of stationary spherically symmetric transonic accretion. *Physical Review E*, 66:066303, Dec 2002. doi: 10.1103/PhysRevE.66.066303.

Martin J. Rees. Black Hole Models for Active Galactic Nuclei. *Annual Review of Astronomy and Astrophysics*, 22:471–506, Jan 1984. doi: 10.1146/annurev.aa.22.090184.002351.

Martin J. Rees. Formation and Growth of Supermassive Black Holes. In Marat Gilfanov, Rashid Sunyeav, and Eugene Churazov, editors, *Lighthouses of the Universe: The Most Luminous Celestial Objects and Their Use for Cosmology*, page 345, Jan 2002.

H. Riffert and H. Herold. *ApJ*, 450:508, 1995.

S. J. Robertson. The theory of Hawking radiation in laboratory analogues. *Journal of Physics B Atomic Molecular Physics*, 45(16):163001, August 2012. doi: 10.1088/0953-4075/45/16/163001.

E. L. Robinson. The structure of cataclysmic variables. *Annual Review of Astronomy and Astrophysics*, 14:119–142, Jan 1976. doi: 10.1146/annurev.aa.14.090176.001003.

K. Sawada, T. Matsuda, and I. Hachisu. Accretion shocks in a close binary system. *MNRAS*, 221:679–686, Aug 1986. doi: 10.1093/mnras/221.3.679.

P. A. G. Scheuer and R. Feiler. The realignment of a black hole misaligned with its accretion disc. *MNRAS*, 282:291, Sep 1996. doi: 10.1093/mnras/282.1.291.

N. I. Shakura and R. A. Sunyaev. *A & A*, 500:33–51, 1973.

Stuart L. Shapiro. Accretion onto Black Holes: the Emergent Radiation Spectrum. II. Magnetic Effects. *Astrophysical Journal*, 185:69–82, Oct 1973a. doi: 10.1086/152396.

Stuart L. Shapiro. Accretion onto Black Holes: the Emergent Radiation Spectrum. *Astrophysical Journal*, 180:531–546, Mar 1973b. doi: 10.1086/151982.

V. F. Shvartsman. Neutron Stars in Binary Systems Should Not Be Pulsars. *Soviet Astronomy*, 15:342, Oct 1971a.

V. F. Shvartsman. Halos around "Black Holes". *Soviet Astronomy*, 15:377, Dec 1971b.

T. R. Slatyer and C. M. Savage. Superradiant scattering from a hydrodynamic vortex. *Classical and Quantum Gravity*, 22:3833–3839, Oct 2005. doi: 10.1088/0264-9381/22/19/002.

H. C. Spruit. Stationary shocks in accretion disks. *Astronomy & Astrophysics*, 184:173–184, Oct 1987.

O. Straub, F. H. Vincent, M. A. Abramowicz, E. Gourgoulhon, and T. Paumard. *Astronomy & Astrophysics*, 543:A83, 2012.

S. H. Strogatz. *Nonlinear Dynamics And Chaos: With Applications To Physics, Biology, Chemistry, And Engineering*. Westview Press, 2001.

M. Takahashi, D. Rilett, K. Fukumura, and S. Tsuruta. *ApJ*, 572:950, 1992.

R. Takahashi. *IAU Symposium Proccedings*, 222:115–116, 2004.

P. Tarafdar and T. K. Das. *IJMPD*, 24:1550096, 2015.

P. Tarafdar, D. A. Bollimpalli, S. Nag, and T. K. Das. *arXiv:1612.06882*, 2017.

Pratik Tarafdar and Tapas K. Das. Influence of the geometric configuration of accretion flow on the black hole spin dependence of relativistic acoustic geometry. *International Journal of Modern Physics D*, 27:1850023-298, Jan 2018a. doi: 10.1142/S0218271818500232.

Pratik Tarafdar and Tapas K. Das. Influence of matter geometry on shocked flows-I: Accretion in the Schwarzschild metric. *New Astronomy*, 62:1–14, July 2018b. doi: 10.1016/j.newast.2017.12.007.

A. H. Taub. Relativistic Fluid Mechanics. *Annual Review of Fluid Mechanics*, 10:301–332, Jan 1978.

Kip S. Thorne. Disk-Accretion onto a Black Hole. II. Evolution of the Hole. *Astrophysical Journal*, 191:507–520, Jul 1974. doi: 10.1086/152991.

G. Tóth, R. Keppens, and M. A. Botchev. *Astronomy & Astrophysics*, 332:1159, 1998.

W. G. Unruh. Experimental black-hole evaporation. *Physical Review Letters*, 46:1351–1353, May 1981. doi: 10.1103/PhysRevLett.46.1351.

W. G. Unruh. Sonic analogue of black holes and the effects of high frequencies on black hole evaporation. *Physical Review D*, 51:2827–2838, Mar 1995. doi: 10.1103/PhysRevD.51.2827.

M. Visser. Acoustic black holes: horizons, ergospheres and Hawking radiation. *Classical and Quantum Gravity*, 15:1767–1791, June 1998. doi: 10.1088/0264-9381/15/6/024.

R. M. Wald. *General relativity.* 1984.

R. M. Wald. *Quantum field theory in curved spacetime and black hole thermodynamics.* 1994.

Robert M. Wald. The Thermodynamics of Black Holes. *Living Reviews in Relativity*, 4:6, Jul 2001. doi: 10.12942/lrr-2001-6.

Q. D. Wang, M. A. Nowak, S. B. Markoff, F. K. Baganoff, S. Nayakshin, F. Yuan, J. Cuadra, J. Davis, J. Dexter, A. C. Fabian, N. Grosso, D. Haggard, J. Houck, L. Ji, Z. Li, J. Neilsen, D. Porquet, F. Ripple, and R. V. Shcherbakov. Dissecting X-ray-Emitting Gas Around the Center of Our Galaxy. *Science*, 341:981–983, August 2013. doi: 10.1126/science.1240755.

P. J. Wiita. Physical properties of thick supercritical accretion disks. *Astrophysical Journal*, 256:666–680, May 1982. doi: 10.1086/159941.

Paul J. Wiita. Accretion Disks around Black Holes. In Bala R. Iyer and Biplab Bhawal, editors, *Black Holes, Gravitational Radiation, and the Universe: Essays in Honor of C.V. Vishveshwara*, page 249, Jan 1999.

R. X. Yang and M. Kafatos. *A & A*, 295:238, 1995.

Qiang Yuan, Q. Daniel Wang, Siming Liu, and Kinwah Wu. A systematic Chandra study of Sgr A<SUP>⋆</SUP>: II. X-ray flare statistics. *MNRAS*, 473:306–316, January 2018. doi: 10.1093/mnras/stx2408.

A. F. Zakharov, F. D. Paolis, G. Ingrosso, and A. A. Nucita. *New Astronomy Reviews*, 56:64–73, 2012.